Vortex-induced vibrations of a circular cylinder in elevated turbulence and unsteady freestream conditions

by

Nikhilesh Tumuluru Ramesh

A thesis
presented to the University of Waterloo
in fulfillment of the
thesis requirement for the degree of
Doctor of Philosophy
in
Mechanical and Mechatronics Engineering

Waterloo, Ontario, Canada, 2024

Examining Committee Membership

The following served on the Examining Committee for this thesis. The decision of the Examining Committee is by majority vote.

External Examiner	Dr. G. Assi Professor Dept. of Naval Architecture and Ocean Engineering The University of São Paulo, Brazil
Supervisor	Dr. S. Yarusevych Professor Dept. of Mechanical and Mechatronics Engineering University of Waterloo, Canada
Supervisor	Dr. C. Morton Associate Professor Dept. of Mechanical Engineering McMaster University, Canada
Internal Members	Dr. X. Li Professor Dept. of Mechanical and Mechatronics Engineering University of Waterloo, Canada
	Dr. S. Peterson Professor Dept. of Mechanical and Mechatronics Engineering University of Waterloo, Canada
Internal-External Member	Dr. S. Narasimhan Professor Dept. of Civil and Environmental Engineering University of California Los Angeles, the Unites States of America

Author's Declaration

This thesis consists of material all of which I authored or co-authored: see Statement of Contributions included in the thesis. This is a true copy of the thesis, including any required final revisions, as accepted by my examiners.

I understand that my thesis may be made electronically available to the public.

Statement of Contributions

I, Nikhilesh Tumuluru Ramesh, was the sole author of Chapters 1,2,3, and 7 which were written under the supervision of Dr. Serhiy Yarusevych and Dr. Chris Morton, and were not written for publication. Chapters 4-6 were adapted from manuscripts that are published, under review, or are being prepared for publication as follows:

1. Chapter 4: Tumuluru Ramesh, N., Morton, C., & Yarusevych, S. 2024 Vortex-induced vibrations in the presence of moderate freestream turbulence. *Physics of Fluids 36(2).*

2. Chapter 5: Tumuluru Ramesh, N., Yarusevych, S., & Morton, C. 2024 Transient vortex-induced vibrations of a cylinder released from rest. Under review

3. Chapter 6: Tumuluru Ramesh, N., Yarusevych, S., & Morton, C. 2024 Transient vortex-induced vibrations of a cylinder subjected freestream velocity changes. Manuscript under preparation

Funding was provided by the Natural Sciences and Engineering Research Council of Canada.

Abstract

This thesis presents the results of a series of experimental investigations focused on exploring one degree of freedom (1-DOF) vortex-induced vibrations (VIV) of a rigid, circular cylinder in two practical flow conditions: elevated freestream turbulence (eFST) and unsteady incoming flow. Elevated FST was generated by placing a turbulence grid upstream of the VIV setup. Unsteady freestream conditions were achieved by ramping the freestream velocity in sigmoidal profiles between end states corresponding to adjacent VIV response branches. A key novelty of the present work is the simultaneous consideration of the structure and wake dynamics to better elucidate the physical mechanisms at play.

First, VIV in moderate levels of eFST (Tu = 2.7%) were examined. Notable deviations of both structure and wake behavior are observed towards the end of the lower response branch. In particular, an earlier onset of desynchronization is observed in the presence of eFST. Conversely, minimal changes are observed within the initial and upper response branches. The underlying mechanisms resulting in the general robustness of VIV to eFST were investigated by comparing eFST effects on the wake of a stationary cylinder and an elastically-mounted cylinder vibrating with minor oscillation amplitudes (less than 1% of cylinder diameter). For stationary cylinders, eFST promotes transition in the separated shear layers, precipitating several changes to the near wake characteristics. Conversely, the shear layers in the VIV cases are desensitized to the perturbations of eFST. This change in shear layer behavior in VIV is linked to the coupling between the fluid and cylinder, featuring small perturbations to the shear layer induced by cylinder oscillations. The fluid-structure coupling is evidenced by a slight modification of the von Kármán shedding frequency in the wake and the emergence of this modified shedding frequency in the cylinder displacement spectra in addition to the structure's natural frequency. Additionally, analysis of the wake in the lower branch revealed subtle changes to the vortex dynamics in the presence of eFST that are reflective of the system transitioning to a premature desynchronized state.

VIV in unsteady flows typically feature *transient* changes to the structural and wake dynamics. Transient dynamics are encountered when the energy gained by the structure from the fluid is not balanced by the energy lost to damping, leading to a change in the state of the system. Transient VIV dynamics are also encountered in steady flow conditions when the system experiences changes to its structural properties. Thus, owing to fewer experimental challenges, transient VIV was first studied in steady flow by releasing a cylinder from rest and observing its transient progression until it converges on *quasi-steady* oscillations. The results indicate notably different dynamics across the response branches, including a distinct overshoot of oscillation amplitudes for reduced velocities in the initial branch and a gradual increase in oscillation amplitudes, with the envelopes resembling sigmoidal curves, for reduced velocities in the upper and lower branches. The oscillation amplitude growth rate was found to decay with increasing reduced velocities. This is associated with the differences in the forcing characteristics (and consequently the energy transfer between the fluid and structure) on the cylinder, with the phase difference between forcing and cylinder

displacement playing a prominent role. Analysis of the wake revealed the different coherent structures encountered as the system transitions from initial von Kármán shedding to the final vortex shedding patterns characteristic to each branch. Additionally, quantitative wake analysis revealed a close relationship between the forcing phase difference and the timing of vortex shedding with respect to the oscillation cycle. Finally, key insights are gained into the onset of lock-in, featuring distinct changes to the forcing characteristics that are associated with a modification of the vortex shedding mechanism. Specifically, cylinder oscillation promotes the deflection and mutual interaction of oppositely-signed shear layers, resulting in a progressive disruption of the von Kármán shedding mechanism.

The final set of experiments considered transient VIV in unsteady incoming flow conditions. Two distinct freestream accelerations were considered including a "fast ramp", where the change in freestream velocity occurs within 45 cylinder oscillation cycles, and a "slow ramp" where the freestream velocity change is within 900 oscillation cycles. A total of six cases were considered that correspond to transitions between adjacent response branches. Analysis of the structure and wake response for the fast ramp indicate a relatively rapid initial response to the changing freestream velocity (within 20 oscillation cycles) for all cases, however, the transient progression between the two end states varies significantly between the different cases considered. Similar to the findings from the release from rest experiments, the transient dynamics were closely related to the energy transfer mechanisms between the fluid and structure, with significant influence from the phase difference between forcing and displacement. The slowest rates of oscillation amplitude change were observed at larger reduced velocities near the lower branch, while the largest rates of amplitude change occurred near the initial-upper branch transition. Overall, the transient dynamics for the fast ramp deviated significantly from the expected quasi-steady response, with the slowest transient exceeding six times the expected quasi-steady response based on the instantaneous freestream velocity. Analysis of the slow ramp cases revealed the transient dynamics approaching quasi-steady behavior, while the nature of the responses remained similar to those from the fast ramp. Comparisons between the present results and those from previous studies suggest a significant dependence of system behavior on the mass ratio. In particular, an approximately inverse relationship was found between the mass ratio and the mean freestream acceleration required to elicit quasi-steady behavior.

Acknowledgements

The past four and a half years have truly tested me in ways I did not anticipate. It took a village to get me to this point.

First and foremost, I would like to sincerely thank my supervisors, Dr. Serhiy Yarusevych and Dr. Chris Morton. I greatly appreciate your patience through the years. Serhiy, your unwavering commitment to excellence is inspiring. The "moment of clarity" you had on the way back from APS 2022 helped steer me back on track. Chris, I am deeply grateful for your personal involvement in the LTRAC experiments. I hope to emulate your work ethic as I move forward. I am also very grateful to Dr. Gustavo Assi, Dr. Sean Peterson, Dr. Xianguo Li, and Dr. Sriram Narasimhan for accepting to evaluate my thesis and for the useful suggestions provided by the comprehensive committee members during my proposal that helped shape this thesis. Thank you to all the technical staff in MME, particularly Jason Benninger and Neil Griffet, for the guidance and help during the setup of my experiments. I owe special thanks to Dr. Zhao Pan for entrusting me with multiple teaching opportunities and helping me grow my confidence!

To all the fluids family I have crossed paths with, thank you for enriching my experience both inside and outside the lab. Thank you, Yash, Caddie, John, Supun, Nianhua, Kaycee, Connor, Deep, Hicham, Olena, Florian, and Thomas. Special thanks to Yash and Caddie for laying the groundwork for me to come to Waterloo and for continuous guidance to this day. John, your enthusiasm and wit helped ease my transition to Canada. Supun, you continue to inspire me with your refreshing perspectives and willingness to always lend an ear. We have witnessed each other's growth right from the early days of the pandemic. I am excited for the next phases for both of us, my friend! Nianhua and Kaycee, you both know the bond we forged is deeper than words can express! To all those outside FMRL who were critical to my well-being: Mercy, Pratishtha, and Nikolai, thank you for all the good times in bluff and basketball! To all the friends I was lucky to make outside work: Yash Abhang, Bharat, Vamshi, Manu, Paaji, Kiran, Vishesh, Shashi, Shiva, and Sunidhi, thank you for keeping me grounded and sane. Special mention to Vamshi for tolerating me the longest as a roommate!

My family remains the bedrock behind my efforts. To my in-laws: Mava and Atte, you have provided me with a blueprint of an ideal family. Sowmya didi, you are the sister I never had! Indira atta, Srinivas mama, Hemanth anna, and Vasanth, it's impossible to express my gratitude. All of you have set an example of how to strive for excellence in anything you pursue. To my parents, Amma and Nana, I would not be where I am today without your constant support in the face of all odds. I am grateful you stuck by me despite my choices leading me away from the conventional norm of "settling down". You will not have to wait much longer. To my wife Dr. Sushma Indrakumar, you remain the center of my small universe, papa. Thank you for choosing me as your life partner! I am infinitely better for it.

Table of Contents

List of Figures x

List of Tables xvii

List of Abbreviations xviii

List of Symbols xix

1 Introduction 1

1.1 Motivation and thesis outline 4

2 Background 5

2.1 Crossflow over a stationary cylinder 6

2.2 Quasi-steady vortex-induced vibrations 7

2.3 Freestream turbulence effects on stationary and oscillating cylinders 13

2.3.1 Effect of eFST on stationary cylinders 15

2.3.2 Effect of eFST on VIV 16

2.4 Transient vortex-induced vibrations 18

2.4.1 Transient VIV in steady freestream conditions 20

2.4.2 Transient VIV in unsteady freestream conditions 22

3 Methodology 26

3.1 Experimental setups 27

3.1.1 FMRL water tunnel, VIV setup, and eFST generation 27

3.1.2 LTRAC water tunnel and VIV setup 31

3.2 Data Collection 33

3.2.1 Particle image velocimetry 33

3.2.2 Quasi-steady VIV in eFST (FMRL) 34

3.2.3 Transient VIV in steady freestream conditions (FMRL) 36

3.2.4 Transient VIV in unsteady freestream conditions (LTRAC) 37

3.3 Data Analysis Techniques 39

3.3.1 Proper orthogonal decomposition 39

3.3.2 Time-frequency analysis 40

3.3.3 Numerical force estimation 41

3.3.4 Vortex Identification 41

4 Freestream turbulence effects on quasi-steady vortex-induced vibrations 43
4.1 Amplitude and frequency response . . . 44
4.2 Mean flow topology and vortex shedding modes . . . 46
4.3 Wake reorganization with small-amplitude cylinder vibrations . . . 48
4.4 Desynchronization analysis . . . 52
4.5 Concluding remarks . . . 55

5 Transient vortex-induced vibrations of a cylinder released from rest in a steady freestream 57
5.1 Quasi-steady state system characteristics . . . 58
5.2 Transient amplitude response . . . 60
5.3 Transient frequency response and the onset of lock-in . . . 63
5.4 Transient forcing characteristics and energy analysis . . . 67
5.5 Attendant transient wake dynamics . . . 71
5.6 Discussion . . . 79
5.7 Concluding remarks . . . 83

6 Transient vortex-induced vibrations of a cylinder in unsteady freestream conditions 85
6.1 Quasi-steady state system characteristics . . . 86
6.2 Transient amplitude response . . . 86
6.3 Transient forcing characteristics . . . 95
6.4 Attendant transient wake characteristics . . . 102
6.4.1 UB-IB dual response . . . 112
6.5 Discussion . . . 116
6.6 Concluding remarks . . . 119

7 Conclusions & Recommendations 121
7.1 Conclusions . . . 122
7.2 Recommendations . . . 124

References 126

Appendices 141

A Uncertainty analysis 142
A.1 Uncertainty in vortex shedding dynamics . . . 145

B Additional measurements of the hysteresis in the initial↔upper branch transition 148

List of Figures

2.1 Schematic of a cylinder modeled as a spring-mass-damper system free to oscillate transversely to the oncoming fluid. The z-axis is into the page. . . 8

2.2 (a) Amplitude and (b) frequency response for low (black markers) and high (red markers) mass-damping systems, respectively. The dashed slanted line in the frequency response represents von Kármán shedding frequency. Figures adapted from [62, 83]. 10

2.3 (a) Map of vortex shedding patterns across a wide range of A^*, U^*. Adapted from [123]. (b-d) Illustrations of vortex shedding patterns observed in 1-DOF free vibration. 11

2.4 Illustration of the parameter space for various applications susceptible to VIV with ranges provided for the estimated ratio of freestream time scales to the dominant system time scales. 20

2.5 (a) Envelope of the amplitudes for a sinusoidally varying freestream velocity (shown in blue) with mean $U^* = 5.65$. (b) Quasi-steady system response (black markers) along with the unsteady system responses (colored markers) with the quasi-steady amplitude of the mean U^* in the unsteady cases highlighted on the quasi-steady curve. Adapted from [94] 23

2.6 Time spent in the lock-in region ($\Delta t f_n$) vs γ with the vertical dashed lines representing the boundaries between regions exhibiting different behavior. A- System response is similar to quasi-steady response, B- System shows significant response that may or may not resemble quasi-steady response, and C- system shows minimal response owing to the limited time spent in the lock-in regime. Adapted from [150]. 25

3.1 Water tunnel facility inside FMRL at the University of Waterloo. 28

3.2 VIV setup on water flume. The right top inset shows components of the VIV setup. The right bottom inset shows a schematic of the turbulence grid, and the left inset shows the release mechanism. The origin of the coordinate system shown in the figure is at the center of the cylinder at its equilibrium position. The PIV schematics are included with the camera under the channel and the green laser sheet at the submerged cylinder midspan. 29

3.3 Spectra of the streamwise velocity fluctuations at the cylinder location with and without the grid. 31

3.4 Water tunnel facility inside LTRAC at the University of Calgary. 32

3.5 Air bearing VIV setup at LTRAC. The camera is shown positioned under the water channel. The green plane indicates the laser sheet with the gray shaded region showing the shadowed regions. 33

3.6 Imposed change in variable drive frequency (dashed lines) and the associated change in measured freestream velocity (solid lines) for all six cases considered. 38

3.7 Contours of identified vortex boundaries overlaid on contours of spanwise vorticity. (a) Contours using aggressive λ_{2_0} (dotted line) and the associated last continuous contours (solid line), and (b) contours using relaxed λ_{2_0} and associated last continuous contours. 42

4.1 (a) Amplitude response of system. Green and yellow circled markers indicate locations where PIV data were collected for the eFST and baseline cases, respectively. Blue open markers correspond to data from [62] for comparison at similar mass-damping. (b) Frequency response of the system. The dashed line represents a Strouhal number of $St = 0.205$. 44

4.2 Histograms of peak amplitudes across the synchronization region. Insets show typical time traces of response along with the corresponding color coded standard deviation. The peaks are normalized by the mean of all peaks in the dataset. 46

4.3 Mean streamwise velocity and phase averaged spanwise vorticity contours. 47

4.4 Effect of eFST on the mean streamwise velocity for (a) stationary cylinder, (b) low-amplitude cylinder vibration at $U^* \approx 4.0$, and (c) low-amplitude cylinder vibration at $U^* \approx 11.2$. Bottom row depicts the differential wake (eFST-baseline) to better illustrate the changes. 50

4.5 Velocity statistics along wake centerline (a)Mean streamwise velocity, (b) rms streamwise velocity fluctuations, and (c) rms transverse velocity fluctuations. 51

4.6 (a) PSDF of transverse velocity along wake centerline for baseline cases. (b) Spectra of cylinder displacement at $U^* \approx 4.0$ (c) Spectra of cylinder displacement at $U^* \approx 11.2$. Red dotted lines indicate the modified vortex shedding frequency. 51

4.7 Reynolds shear stress in the wake for (a) stationary cylinder, (b) low-amplitude cylinder vibration at $U^* \approx 4.0$, and (c) low-amplitude cylinder vibration at $U^* \approx 11.2$. 52

4.8 POD streamwise spatial mode contours of the first and third mode for (a) baseline and (b) eFST cases. 53

4.9 Relative energy of first six POD modes associated with 2P shedding near the onset of desynchronization at $U^* \approx 9.5$. 54

4.10 Phase-averaged spanwise vorticity with the cylinder at maximum positive amplitude for (a) baseline and (b) eFST cases using a LOM of six modes at $U^* \approx 9.5$. 55

5.1 Quasi-steady state system characteristics. (a) Mean amplitude response calculated as the mean of all peaks in a time series, (b) frequency response calculated using spectral analysis of the displacement signal, and (c) mean vortex force phase difference obtained through the application of the Hilbert transform [83]. The uncertainty in all quantities is accommodated by the marker sizes. The red, green, and blue markers indicate U^* which are analyzed in further detail using both PIV measurements and detailed force analysis. 59

5.2 Phase-averaged spanwise vorticity contours at locations marked by the colored symbols (figure 5.1 in the (a) initial, (b) upper, and (c) lower branches, respectively. The cylinder is at top dead center of oscillation cycle in all cases. 60

5.3 Transient amplitude response across the branches. (a) Representative time series response at marked locations in figure 5.1, (b) envelope of peak amplitudes across 15 trials, and (c) ensemble average of all trials shifted by estimated time lag τ. 61

5.4 (a) Ensemble-average of all trials across the synchronization regime, and (b) associated settling time at each U^*. The settling time is determined as per the algorithm described in text. 62

5.5 Ensemble-averaged normalized wavelet scalograms of force at (a) $U^* \approx 5.2$ (initial), (b) $U^* \approx 6.0$ (upper), and (c) $U^* \approx 7.2$ (lower branches). The green solid lines represent locus of maximum in force scalogram magnitude, red represents the locus of maximum in displacement scalogram magnitude, dashed black indicates von Kármán frequency, and the dashed-dotted black line represents the structure's natural frequency. 64

5.6 Onset of nonlinear behavior for a single trial at $U^* \approx 7.2$. (a) Nondimensional displacement and vortex force and (b) normalized wavelet scalogram of vortex force. The left inset displays the time period featuring periodic forcing at predominantly von Kármán frequency and the right inset displays a period of noisy forcing signal characterized by frequency components around both von Kármán and structure natural frequency along with the associated growth in oscillation amplitudes. 66

5.7 Time history of energy concentrated around a band of ±10% of the von Kármán and natural frequency components at $U^* \approx 7.2$ for a single trial (figure 5.6). 67

5.8 Ensemble-averaged nondimensional vortex force (top row, C_{Lv}), vortex force phase difference (middle row, ϕ_v), and nondimensional energy transfer to the cylinder over each oscillation cycle (bottom row, E^*) for representative U^* in (a) initial, (b) upper, and (c) lower branches, respectively. The force plots are overlaid with ensemble-averaged amplitude, and the phase plots are overlaid with loci of force and displacement frequencies from figure 5.5. 69

5.9 Vortex force phase difference ϕ_v immediately after lock-in for all tested U^*. The dotted line represents 90°. 70

5.10 (a) Ensemble-averaged time series and spanwise vorticity at $U^* \approx 7.2$ for (b) $(t-\tau)f_n \approx 3$, (c) $(t-\tau)f_n \approx 6$, (d) $(t-\tau)f_n \approx 10$, and (e) $(t-\tau)f_n \approx 15$. The solid black lines in (b-e) indicate the vortex boundaries identified through the methodology outlined in 3.3.4. 73

5.11 Transient wake characteristics at $U^* \approx 5.2$. (a) Vortex formation lengths and (b) phase of oscillation at vortex shedding. Dashed, dotted lines in (a) represent the formation lengths obtained from the stationary cylinder and quasi-steady, phase-averaged VIV cases, respectively. Dashed lines in (b) indicate the quasi-steady, phase-averaged θ with the shaded regions indicating the methodological uncertainty. Gray areas identify regions where estimations are unreliable due to the absence of lock-in and/or low-amplitude oscillation preventing accurate phase estimation. 74

5.12 (a) Ensemble-averaged time series and spanwise vorticity at $U^* \approx 6.0$ for (b) $(t-\tau)f_n \approx 8$, (c) $(t-\tau)f_n \approx 10$, (d) $(t-\tau)f_n \approx 13$, and (e) $(t-\tau)f_n \approx 18$. The black solid lines in (b-e) indicate the vortex boundaries identified through the methodology outlined in 3.3.4. 75

5.13 Transient wake characteristics at $U^* \approx 6.0$. (a) Vortex formation lengths and (b) phase of cylinder oscillation at the instant of vortex shedding. Refer to figure 5.11 for interpretation of lines and shaded regions. 76

5.14 (a) Ensemble-averaged time series and spanwise vorticity at $U^* \approx 7.2$ for (b) $(t-\tau)f_n \approx 10$, (c) $(t-\tau)f_n \approx 18$, (d) $(t-\tau)f_n \approx 27$, and (e) $(t-\tau)f_n \approx 33$.The black solid lines in (b-e) indicate the vortex boundaries identified through the methodology outlined in 3.3.4. 77

5.15 Transient wake characteristics at $U^* \approx 7.2$. (a) Vortex formation lengths and (b) phase of cylinder oscillation at the instant of vortex shedding. Refer to figure 5.11 for interpretation of lines and shaded regions. 78

5.16 Single realization transient of the normalized wavelet scalogram of vortex forcing (top row), and normalized wavelet scalogram of transverse velocity signal (bottom row) at $X/D \approx 4$ for (a) $U^* \approx 5.2$, (b) $U^* \approx 6.0$, and (c) $U^* \approx 7.2$, respectively. 79

5.17 Energy transferred over one cycle through the cylinder's trajectory in the amplitude-wavelength plane. (a) Trajectory at all representative U^* with the start identified through blue markers and (b-d) comparison of energy extracted with forced vibration data from [124]. 82

6.1 Quasi-steady state system characteristics. (a) Mean amplitude response calculated as the mean of all peaks in a time series, (b) frequency response calculated using spectral analysis of the displacement signal, and (c) mean vortex force phase difference obtained through the application of the Hilbert transform [83]. The uncertainty in all quantities is accommodated by the marker sizes. Black markers signify increasing U^* while gold markers signify decreasing U^*. 87

6.2 Transient amplitude envelopes across all trials for the fast ramp cases (see section 3.2.4 for details on the fast ramp). The red lines represent the quasi-steady amplitudes at the corresponding freestream velocities. The green lines represent the ensemble averages of all trials. The vertical dashed lines demarcate the period of freestream velocity change (freestream transient). . 88

6.3 Transient amplitude envelopes for all trials across the branches for slow ramp cases (see section 3.2.4 for details on the slow ramp). The red lines represent the quasi-steady amplitudes at the corresponding freestream velocities. The green lines represent the ensemble averages of all trials. The vertical dashed lines demarcate the freestream transient period. 90

6.4 Estimations of transient start (open symbols) and end times (filled symbols) for (a) fast ramp and (b) slow ramp cases, respectively. The shaded regions indicate the freestream transient period with the yellow representing the fast ramp and the magenta representing the slow ramp. The dashed-dotted lines indicate the transient time of the quasi-steady response, estimated using the same methodology. (c) The total nondimensional transient time for each case, and (d) transient time as a percentage of the associated quasi-steady transient time. 93

6.5 Transient system trajectories in the $A^* - U^*$ plane. The yellow lines depict the fast ramp cases while the magenta lines depict the slow ramp cases. . . 94

6.6 Forcing characteristics for all cases except the UB-IB transition. The left column depicts the ensemble-averaged normalized force magnitude in blue along with the ensemble-averaged cylinder displacement in gray. The middle column depicts the vortex force phase difference, and the right column depicts the ensemble-averaged and normalized signal energy of vortex forcing. The vertical dashed lines in all plots demarcate the freestream transient period. 97

6.7 Forcing characteristics of individual realizations for the UB-IB transition with (a) remaining in the high-amplitude state and (b) returning to the initial branch. 100

6.8 Forcing magnitude (top row) and phase difference (bottom row) of individual realizations for the (a) UB-LB and (b) LB-UB cases, respectively. 101

6.9 (a) Ensemble-averaged time series and spanwise vorticity for the IB-UB case at (b) $(t-\tau)f_n \approx 46$, (c) $(t-\tau)f_n \approx 56$, (d) $(t-\tau)f_n \approx 62$, and (e) $(t-\tau)f_n \approx 70$. 104

6.10 Transient wake dynamics for the IB-UB case. (a) Ensemble-averaged normalized signal energy of the transverse velocity along the wake centerline at $X/D \approx 2.5$ and (b) ensemble-averaged rms error of the near wake with respect to the initial quasi-steady state. 105

6.11 (a) Ensemble-averaged time series and spanwise vorticity for the UB-LB case at (b) $(t-\tau)f_n \approx 40$, (c) $(t-\tau)f_n \approx 48$, (d) $(t-\tau)f_n \approx 55$, and (e) $(t-\tau)f_n \approx 62$. 106

6.12 Transient wake dynamics for the UB-LB case. (a) Ensemble-averaged normalized signal energy of the transverse velocity along the wake centerline at $X/D \approx 2.5$ and (b) ensemble-averaged rms error of the near wake with respect to the initial quasi-steady state. 107
6.13 (a) Ensemble-averaged time series and spanwise vorticity for the LB-UB case at (b) $(t-\tau)f_n \approx 63$, (c) $(t-\tau)f_n \approx 70$, (d) $(t-\tau)f_n \approx 76$, and (e) $(t-\tau)f_n \approx 83$. 108
6.14 Transient wake dynamics for the LB-UB case. (a) Ensemble-averaged normalized signal energy of the transverse velocity along the wake centerline at $X/D \approx 2.5$ and (b) ensemble-averaged rms error of the near wake with respect to the initial quasi-steady state. 108
6.15 (a) Ensemble-averaged time series and spanwise vorticity for the LB-Dsnc case at (b) $(t-\tau)f_n \approx 44$, (c) $(t-\tau)f_n \approx 60$, (d) $(t-\tau)f_n \approx 70$, and (e) $(t-\tau)f_n \approx 89$. 109
6.16 Transient wake dynamics for the LB-Dsnc case. (a) Ensemble-averaged normalized signal energy of the transverse velocity along the wake centerline at $X/D \approx 2.5$ and (b) ensemble-averaged rms error of the near wake with respect to the initial quasi-steady state. 110
6.17 (a) Ensemble-averaged time series and spanwise vorticity for the Dsnc-LB case at (b) $(t-\tau)f_n \approx 50$, (c) $(t-\tau)f_n \approx 70$, (d) $(t-\tau)f_n \approx 90$, and (e) $(t-\tau)f_n \approx 107$. 111
6.18 Transient wake dynamics for the Dsnc-LB case. (a) Ensemble-averaged normalized signal energy of the transverse velocity along the wake centerline at $X/D \approx 2.5$ and (b) ensemble-averaged rms error of the near wake with respect to the initial quasi-steady state. 112
6.19 (a) Ensemble-averaged time series and spanwise vorticity for the UB-IB. case that remains at a high-amplitude state at (b) $(t-\tau)f_n \approx 40$, (c) $(t-\tau)f_n \approx 46$, (d) $(t-\tau)f_n \approx 62$, and (e) $(t-\tau)f_n \approx 72$. (f) Ensemble-averaged time series and spanwise vorticity for the UB-IB. case that returns to the initial branch at (g) $(t-\tau)f_n \approx 120$, (h) $(t-\tau)f_n \approx 135$, (i) $(t-\tau)f_n \approx 160$, and (j) $(t-\tau)f_n \approx 180$. 114
6.20 Transient wake dynamics for the UB-IB. cases. The top row depicts the trials the remain in high-amplitude oscillations, while the bottom row depicts trials that returned to the initial branch. (a) Ensemble-averaged normalized signal energy of the transverse velocity along the wake centerline at $X/D \approx 2.5$ and (b) ensemble-averaged rms error of the near wake with respect to the initial quasi-steady state. 116

A.1 Vortex boundaries identified using the last continuous threshold method (see section 3.3.4) employing contours of (a) λ_2 criterion and (b) Q criterion. . . 146
A.2 Circulation estimates from phase-averaged vorticity contours versus cylinder oscillation phase. 147

B.1 Measurements between $4.7 \lessapprox U^* \lessapprox 5.5$.(a) Top ten percent of amplitude peaks, (b) rms vortex force coefficient, and (c) nondimensional frequency ratio with the dashed-dotted line demarcating system natural frequency. 149

B.2 System characteristics in the upper branch (left column) and the high-amplitude hysteresis state (right column). (a) Time series of cylinder displacement, (b) Time series of the vortex forcing, (c), (d) vortex force phase difference, and (e) normalized signal energy of the vortex force overlaid with the maximum locus of the forcing (green) and displacement (red) signal energies, respectively. 151

B.3 Phase-averaged spanwise vorticity contours (top row) for the (a) upper branch and (b) high-amplitude hysteresis cases. 153

B.4 Mean streamwise velocity contours (top row) for the (a) upper branch and (b) high-amplitude hysteresis cases. 153

List of Tables

2.1 Parameter space estimation for the ratio of freestream time scales to the dominant system time scales. 20

3.1 Parameters of the experimental VIV system. 30
3.2 Parameters for eFST PIV experiments. 36
3.3 Parameters for PIV experiments. 37
3.4 Parameters for unsteady freestream experiments. 38
3.5 Parameters for PIV experiments. 39

A.1 Maximum uncertainty estimates of measured and derived quantities. All uncertainty estimates are provided over a 95% confidence interval. 145

List of Abbreviations

VIV	Vortex Induced Vibrations
DOF	Degree of Freedom
eFST	elevated Freestream Turbulence
PIV	Particle Image Velocimetry
ABL	Atmospheric Boundary Layer
FMRL	Fluid Mechanics Research laboratory
LTRAC	Laboratory for Turbulence Research and flow Control
DC	Direct Current
CCD	Charge Coupled Device
IB	Initial Branch
UB	Upper Branch
LB	Lower Branch
Dsnc	Desynchronization
POD	Proper Orthogonal Decomposition
PCA	Principal Component Analysis
STFT	Short Time Fourier Transform
LOM	Low Order Model

List of Symbols

Accents and Subscripts

Example	Description
$\overline{a}$	Time-averaged quantity
$\vec{a}$	Vector quantity
a'	Fluctuating quantity
a''	Fluctuations arising from small-scale turbulence
a_{rms}	Root-mean-squared quantity
a_{mean}	Mean of all quantities
a_{σ}	Standard deviation of all quantities
a_{10}	Mean of top 10% of all quantities
a_{max}	Maximum of all quantities
a_x	Quantity along streamwise direction
a_a	Quantity related to the added mass
a_v	Quantity related to the vortex forcing
$\dot{a}$	First derivative of a with respect to time
$\ddot{a}$	Second derivative of a with respect to time

Dimensionless Quantities

Symbol	Description	Definition
Re	Reynolds number; length scale a	$U_0 a/\nu$
St	Strouhal number; length scale a	fa/U_0
U^*	Reduced velocity	$U_0/f_n D$
A^*	Nondimensional amplitude	A/D
f^*	Nondimensional frequency	f/f_n
m^*	Mass ratio	$4m/(\rho\pi D^2 L)$

ζ	Damping constant	$c/(2\sqrt{km})$
Tu	Turbulence intensity	u'_{rms}/U_0
γ	Flow unsteadiness parameter	$T_n \frac{\lvert dU_0/dt \rvert}{U_0}$
C_{Lv}	Vortex force coefficient, submerged length L, diameter D	$\frac{F_{0v}}{(0.5\rho U_0^2 LD)}$
E^*	Nondimensional energy input to cylinder over a cycle	$\int_t^{t+T} C_{Lv} \cdot \frac{\dot{y}}{D}\, dt$

Roman Symbols

Symbol	Description	Units
A	Oscillation amplitude	m
f	Oscillation frequency	Hz
f_n	Natural frequency in still water	Hz
f_d	Damped natural frequency	Hz
D	Cylinder diameter	m
L	Cylinder submerged length	m
U_0	Freestream velocity	$\mathrm{m\,s^{-1}}$
m	Oscillating mass	kg
c	System damping	$\mathrm{kg\,s^{-1}}$
k	Spring constant	$\mathrm{kg\,s^{-2}}$
F, F_v	Total force, Vortex force	$\mathrm{kg\,m^2\,s^{-2}}$
X, Y, Z	Streamwise, transverse, and spanwise coordinates	m
W_ψ	Wavelet transform	$\mathrm{m\,s^{-1}}$
y	Cylinder position	m
u, v	Streamwise, transverse velocity	$\mathrm{m\,s^{-1}}$
t_{gr}, t_{gd}, t_{gl}	Gust rise time, gust duration, gust lapse time	s
t_f, t_{vs}	Freestream transient period, vortex shedding period	s
τ	Temporal shift for ensemble averaging	s
t_s, t_t, t^*	System settling time, system transient time, transient start/end time	s

M	Mesh width	m
Q	Vortex identification criterion [70]	s^{-2}
L_f	Vortex formation length	m

Greek Symbols

Symbol	Description	Units
θ	Cylinder oscillation phase angle. Presented in degrees	rad
ϕ	Phase difference between total forcing and cylinder displacement. Presented in degrees	rad
ϕ_v	Phase difference between vortex forcing and cylinder displacement. Presented in degrees	rad
Γ	Vortex circulation	$m^2\,s^{-1}$
ϕ_n^u	Streamwise n^{th} POD mode	-
Λ_x	Integral length scale in streamwise direction	rad
λ_2	Vortex identification criterion [77]	s^{-2}
ν	Kinematic viscosity	$m\,s^{-2}$
ρ	Density	$kg\,m^{-3}$
κ	Logarithmic decrement	-
ϵ	Root-mean-squared error of velocity field	$m\,s^{-1}$
ω	Spanwise vorticity	s^{-1}

Chapter 1

Introduction

Vortex-induced vibrations are introduced and the key motivations for this work are outlined following a brief outlook of the current state of the art. Finally, the objectives for this thesis are set.

Vortex-induced vibrations (VIV) are a class of fluid-structure interactions that may result in significant structural oscillations for bluff bodies exposed to fluid flow. The oscillations are a consequence of periodic loads imposed by the regular shedding of vortices at frequencies near the structure's natural frequency. VIV have serious implications for many engineering structures exposed to fluid flow, including ocean risers [79], chimneys [128], transmission tower tubes [43], and towers/masts [106]. Conversely, VIV can also be leveraged for energy harvesting applications [187]. Physically, the oscillations of the structure modify the vortex shedding characteristics, resulting in coupled nonlinear interactions between the oscillating body and the surrounding fluid flow. The complex physics engendered by these interactions, in conjunction with the critical practical implications, have resulted in VIV receiving widespread attention in research studies.

Many early studies of VIV considered a relatively simple but fundamental model of VIV consisting of a rigid cylinder constrained to oscillate in 1 degree of freedom (1-DOF) transverse to the incoming freestream with uniform amplitude along the cylinder's span (e.g, [54, 185]). The direction transverse to the freestream is where the largest amplitudes of oscillation are typically observed owing to the dominance of fluctuating forces along that direction [23]. Since the early studies, significant progress has been made toward the exploration of both the structural and wake dynamics of the 1-DOF uniform amplitude case (e.g., [62, 123]). Building on this foundation, recent studies on VIV have investigated increasingly complex cases of VIV that are more representative of real-world applications. These include rigid cylinders exhibiting 2-DOF motion (transverse to and in-line with the freestream) with uniform amplitude [75], 2-DOF motion with spanwise variation in amplitude [55, 112], and flexible cylinders exhibiting 2-DOF motions [30]. In addition to uniform circular cylinders, different studies have considered VIV of elliptical cylinders [194], curved and wavy cylinders [10, 11], tapered cylinders [80], and square cylinders [217], among others.

While rapid progress continues to be made on VIV, comprehensive characterization of real-world VIV needs to incorporate the effects of various non-uniform and/or unsteady inflow conditions that may be encountered in diverse operational environments. To this end, notable research directions include the effects of shear flow on VIV [36, 102] and VIV in oscillatory flows [184, 218]. However, there has been surprisingly little research related to two incoming flow conditions commonly encountered in real-world flows: (i) incoming flow with elevated levels of freestream turbulence (eFST) and (ii) unsteady incoming flows. Elevated FST encompasses a variety of incoming flow disturbances that span a wide range of length and time scales, whereas unsteady incoming flows are characterized by transient changes in the incoming flow velocity. Both these flow conditions feature prominently in environments where VIV are observed [39, 209].

Pertinent to the dynamics of VIV in eFST and unsteady freestream conditions is the concept of energy transfer between the fluid and the structure. For a system to exist at an equilibrium state, the energy gained by the structure from the flow over one oscillation cycle has to be balanced by the energy lost due to structural damping [115, 123]. The majority

of prior VIV studies have focused on structures exhibiting *quasi-steady* vibrations near a stable equilibrium state. Conversely, changes in the quasi-steady energy balance may result in *transient* changes to the system state (amplitude and/or frequency of oscillations), with minimal focus on such cases in literature. Intuitively, transient VIV behavior is expected in unsteady freestream conditions due to the constant change in operating conditions. However, transient VIV behavior can also be observed in steady flow conditions. A case in point is a system subject to changing structural properties (e.g., due to a structural component failure, such as a supporting cable) that triggers the onset of VIV. Irrespective of the way transient VIV is initiated (changing freestream/structural conditions), the growth/decay of vibrations is closely related to the energy transfer between the fluid and the structure. This allows for examination of transient VIV in steady flows (that are easier to replicate at a lab scale), thereby serving as a useful first step towards characterizing transient VIV in unsteady flows. Overall, while transient VIV may be induced in steady flows, unsteady flows, and eFST conditions, the effects of eFST considered in this thesis are found to primarily affect the quasi-steady response of the system due to the characteristics of the incoming flow disturbances (more details on this are provided in section 2.3).

Prior research on quasi-steady VIV in eFST conditions and transient VIV in steady and unsteady conditions are relatively scarce. Studies that investigated quasi-steady VIV in eFST conditions have considered notably different configurations (1-DOF rigid, 2-DOF flexible, etc.) and different operating conditions with minimal to no flow field information (e.g., [139, 173]). Consequently, limited insights can be gained about the underlying physical mechanisms at play. Studies that have explored transient VIV (e.g., [7, 150]) report dynamics that are distinct from the quasi-steady cases. However, unlike the generally steady progression in problem complexity for quasi-steady VIV of various geometries, transient VIV studies have examined more complex configurations and geometries (e.g., 2-DOF flexible) without a consistent bottom-up approach. Moreover, most of the studies do not provide flow measurements in conjunction with structural responses, thereby providing limited insight into the underlying mechanisms. Overall, the two incoming flow conditions being studied in the thesis, eFST, and unsteady incoming freestream, result in significant changes to both quasi-steady and transient VIV behavior. However, notable gaps remain in our understanding of VIV under such conditions.

1.1 Motivation and thesis outline

This thesis is motivated by the imperative to advance the current state of the art in vortex-induced vibrations within the context of two key practical flow conditions encompassing both quasi-steady and transient system behaviors. Furthermore, the author contends that such an endeavor necessitates the concurrent examination of wake and structural dynamics, helping to form a holistic understanding of the underlying physical mechanisms. A series of experimental investigations are carried out to address the knowledge gaps while employing techniques that enable the measurement of structural displacement and forces on carefully manufactured VIV setups. Additionally, flow information is simultaneously acquired with force and displacement through a minimally invasive flow measurement technique, particle image velocimetry (PIV). The 1-DOF rigid cylinder is adopted as the standard model throughout this thesis given the gaps in the literature even for this relatively simple case in both eFST and unsteady freestream conditions. In light of this motivation, the following research objectives are put forth:

- Characterize the response of a cylinder undergoing quasi-steady VIV in eFST conditions and associate the modified structural response to changes in the wake dynamics when compared to baseline (low FST) conditions.
- Examine the transient structural and wake dynamics of a cylinder released from rest in steady flow conditions and identify the system characteristics associated with the onset of nonlinear behavior.
- Examine the transient wake and structural response of a cylinder undergoing quasi-steady VIV subject to unsteady incoming freestream conditions. Additionally, associate the system dynamics to the different energy transfer mechanisms responsible for the growth/decay of oscillations in the transient VIV cases for both the steady and unsteady freestream cases.

This thesis is organized as follows. Chapter 2 presents the relevant literature pertaining to the aforementioned objectives. Specifically, brief overviews of flow across stationary cylinders and the dynamics of quasi-steady VIV are presented. This is followed by detailed reviews of previous works on the influence of eFST on VIV, and transient VIV in both steady and unsteady flow conditions. Chapter 3 describes the different experimental facilities, VIV setups, and data analysis techniques employed in the thesis. This chapter is followed by the results from experiments on VIV in eFST conditions in Chapter 4. Comparisons are made to the stationary cylinder case to elucidate similarities and differences in the wake dynamics in eFST conditions. Chapter 5 details the outcome of experiments conducted on a cylinder released from rest in a steady freestream and the associated transient structure and wake characteristics. Following this, transient VIV characteristics in unsteady freestream conditions are explored in Chapter 6. Finally, the conclusions from the experimental studies and recommendations are provided in Chapter 7.

Chapter 2

Background

Pertinent research studies essential to the current thesis are discussed in this chapter. First, flow across the stationary cylinder is described, forming a baseline for the basics of quasi-steady VIV which are discussed next. Following this, previous studies on the effects of eFST on stationary cylinders and VIV are detailed along with a brief outlook of the expected FST in VIV environments. Lastly, transient VIV are discussed for both steady and unsteady freestream cases based on a defined parameter space representative of environmental conditions.

Owing primarily to the geometric similarity, the flow over oscillating cylinders and stationary cylinders share several commonalities, including the formation of shear layers and the periodic shedding of large-scale coherent structures into the wake. It is thus instructive to examine the flow across stationary cylinders before moving on to the oscillating cylinder cases.

2.1 Crossflow over a stationary cylinder

The dynamics of the stationary cylinder wake have been the primary focus of numerous studies (e.g., [18, 133, 159]). The Reynolds number Re demarcates different wake flow regimes.

For Re between 30 and 50 depending on experimental conditions, the separated shear layers roll-up into a staggered arrangement of laminar vortices, also known as the Kármán vortex street [146]. The flow in the regime between $50 \lessapprox Re \lessapprox 180$ can be considered two-dimensional as the vortices are shed parallel to the cylinder (spanwise invariant under controlled conditions [59, 201]). The onset of three-dimensionality in the flow is first identified between $180 \lessapprox Re \lessapprox 300$ through two distinct instabilities [202, 205] called Mode A and Mode B instabilities. These instabilities are characterized by the appearance of small-scale streamwise vortices. Farther downstream of the vortex formation region, the flow transitions into turbulence. With increasing Re, the transition region moves upstream. When this upstream movement approaches the vortex formation region, turbulent vortex shedding ensues [60]. However, the separated shear layers and the boundary layer remain laminar throughout this regime ($180 \lessapprox Re \lessapprox 300$).

Transition to turbulence is observed within the separated shear layers over a wide range of Reynolds numbers ($300 \lessapprox Re \lessapprox 200{,}000$) [216]. This regime, relevant to many engineering applications, is commonly referred to as the transition in the shear layer regime [215]. It can be divided into three sub-regimes. The first of these, ($300 \lessapprox Re \lessapprox 1{,}200$) is where transition waves are observed along the separated shear layers [26]. The formation length steadily increases in this regime before reaching a maximum. In the second sub-regime ($1{,}200 \lessapprox Re \lessapprox$ 20,000-50,000 depending on the freestream turbulence), small-scale vortices are observed in the separated shear layers [196]. The vortex formation length continually reduces in the second shear layer transition regime. Beyond $Re \approx 20{,}000$, the length of the formation region remains unchanged [215]. The final sub-regime of shear layer transition ($Re \gtrapprox$ 20,000-50,000) is characterized by a steady upstream movement of the transition region with increasing Re and the three-dimensional flow in the near wake [41].

Following the shear layer transition, the next regime is characterized by a transition in the boundary layer [215]. This is typically accompanied by a downstream movement of the separation line leading to the "drag crisis", characterized by a sudden reduction in the drag

at $Re \approx 120{,}000$. The transition location then moves upstream with increasing Re until it reaches the front stagnation point, and this marks the end of the boundary layer transition regime. Different regimes of flow exist beyond boundary layer transition but will not be discussed here as they are of little interest to the current work.

The mechanics of turbulent vortex shedding can be categorized into different stages including vortex formation, saturation, and downstream advection [157]. During formation, the vortex is fed by circulation from the shear layer and grows in size. Vorticity for this process is provided by the tangential acceleration of fluid over the cylinder surface [126]. The saturation stage is characterized by a peak in the vortex circulation and a subsequent pinch-off from the separated shear layer as the vortex sheds [76]. The shed vortex then advects away from the cylinder. Not all of the vorticity generated at the surface is shed as a vortex [21]. Some of the vorticity is annihilated by oppositely-signed vorticity as it is entrained across the wake by the shear layers [3, 126, 212]. The ratio between the circulation contained in the shed vortices to that generated at the surface, known as the deficit ratio, varies between 0.4 and 0.7 depending on the experimental conditions [158, 207].

2.2 Quasi-steady vortex-induced vibrations

As discussed above, periodic vortex shedding is a key feature of flow across stationary cylinders for $Re \gtrapprox 50$. Vortex shedding results in periodic fluctuating forces on the cylinder with forces in the lift direction typically being more dominant [23]. For an elastically-mounted cylinder in crossflow, if the vortex shedding frequency approaches the structure's natural frequency, significant vortex-induced vibrations may ensue [203]. The cylinder motion in turn modifies the vortex shedding characteristics, resulting in a coupled interaction between the wake and the cylinder motion [62]. Partly owing to the significant practical relevance, multiple studies have explored the structure and wake dynamics of VIV, several of which are summarized in extensive reviews on the subject (e.g., [19, 166, 203]). The majority of prior VIV studies have focused on systems exhibiting *quasi-steady* vibrations near a stable equilibrium state. At equilibrium, the energy gained by the structure from the flow over one oscillation cycle is balanced by the energy lost to structural damping [91, 115, 123]. Conversely, changes in the quasi-steady energy balance may result in a *transient* change in VIV dynamics. It must be noted that even under ideal conditions, systems undergoing VIV may not be in perfect equilibrium owing to small cycle-to-cycle variations in system dynamics. Consequently, the system "hovers" near the stable equilibrium state. First, a brief overview of quasi-steady structure and wake characteristics is presented.

Irrespective of its state (quasi-steady/transient), a structure undergoing VIV can be represented as a spring-mass-damper subjected to external forcing [203] (figure 2.1). When the structure is restricted to move in one degree of freedom (1-DOF) transverse to the

freestream, the equation of motion is:

$$m\ddot{y} + c\dot{y} + ky = F(t) \tag{2.1}$$

where m is the mass of the structure, c is the structural damping, and k is the spring constant. Systems undergoing quasi-steady VIV exhibit the phenomenon of "lock-in" [18], where the dominant wake (shedding) frequency matches the structure oscillation frequency, and the structural response and forcing are well approximated by single harmonic periodic functions [83] as:

$$y(t) = Asin(2\pi ft), F(t) = F_0 sin(2\pi ft + \phi) \tag{2.2}$$

where A is the amplitude of oscillations, f is the lock-in frequency, and ϕ is the phase difference between forcing and displacement. The structural response is typically characterized by a nondimensional amplitude $A^* = A/D$ and a nondimensional frequency $f^* = f/f_n$, where D is the cylinder diameter and f_n is the natural frequency of the structure in the operational medium at quiescent conditions[1] [166]. These parameters are primarily influenced by the reduced velocity $U^* = U_0/(f_n D)$, where U_0 is the freestream velocity. Other influencing parameters include the mass ratio $m^* = 4m/(\rho\pi D^2 L)$, damping ratio $\zeta = c/(2\sqrt{mk})$, and Reynolds number Re. A more comprehensive list of influencing parameters that account for different geometrical and/or flow conditions (e.g., spanwise taper, shear flow) may be found in other studies (e.g.,[166, 190]).

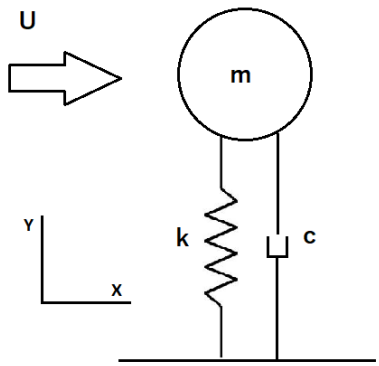

Figure 2.1: Schematic of a cylinder modeled as a spring-mass-damper system free to oscillate transversely to the oncoming fluid. The z-axis is into the page.

A typical quasi-steady amplitude and frequency response of a 1-DOF system (data from [62, 83]) is depicted in figure 2.2 against the reduced velocity U^*. Here, the amplitude response is quantified as the maximum nondimensional amplitude (A^*_{max}) peak in a time series of cylinder oscillation[2]. The frequency response is typically extracted by identifying

[1]Throughout this thesis, structural natural frequency refers to that obtained in still water as the operational medium

[2]The amplitude response is quantified using different metrics in various studies (e.g., [83, 154]) with the current work adopting the mean of all amplitude peaks A^*_{mean} in a given time series for better statistical representation.

the dominant frequencies in a spectral analysis of the displacement signal. Two distinct types of responses are observed in figure 2.2 with markers that correspond to low mass-damping (black markers) and high mass-damping (red markers), respectively[3]. Unlike a linear oscillator, the amplitude response of both low and high mass-damping systems reveals the existence of different regions, or "branches", of response. For low mass-damping systems (figure 2.2(a), black markers), four response branches can be identified. These regions are commonly referred to as the initial, upper, and lower branches as well as desynchronization (see annotations in figure 2.2(a)) [203]. In contrast, high mass-damping systems exhibit only the initial and lower response branches along with desynchronization [203].

The initial branch is typically characterized by relatively low oscillation amplitudes (figure 2.2(a)). A dual frequency response centered around the von Kármán shedding frequency and cylinder natural frequency [83] is observed in the early initial branch. This is represented by two black markers at the same U^* in figure 2.2(b). This is followed by a switch to a single lock-in frequency towards the end of the initial branch (figure 2.2(b)) [83]. The dual frequency response is associated with a beating-type amplitude response [166]. For low mass-damping systems, the phase difference between forcing and displacement ϕ (equation 2.2) remains close to 0° in the initial branch. The switch to the upper branch for low mass-damping systems is characterized by an abrupt jump in amplitude. The phase difference remains near 0° and a single lock-in frequency near the system's natural frequency [62] is observed. The transition between the initial and upper branches is hysteretic [84]. Additionally, the largest amplitudes of oscillation are generally found in the upper branch. The lower branch continues to exhibit a single lock-in frequency along with a switch in the phase difference ($\phi \approx 180°$). The amplitudes, while still relatively large, are smaller than those in the upper branch. Finally, the onset of desynchronization is marked by a substantial decrease in the oscillation amplitudes [132]. This is associated with the wake desynchronizing from the structural oscillation (hence the name) and is characterized by the re-emergence of the von Kármán component (figure 2.2(b), $U^* \gtrapprox 8$) [132]. High mass-damping systems also exhibit some similar characteristics in the initial and lower compared to low mass-damping systems albeit with some key differences. Apart from lower oscillation amplitudes, high mass-damping systems also exhibit more narrow ranges of synchronization (lock-in) [54] (compare the red and black markers in figure 2.2).

[3]No specific cutoff demarcating high and low mass-damping systems are used in literature

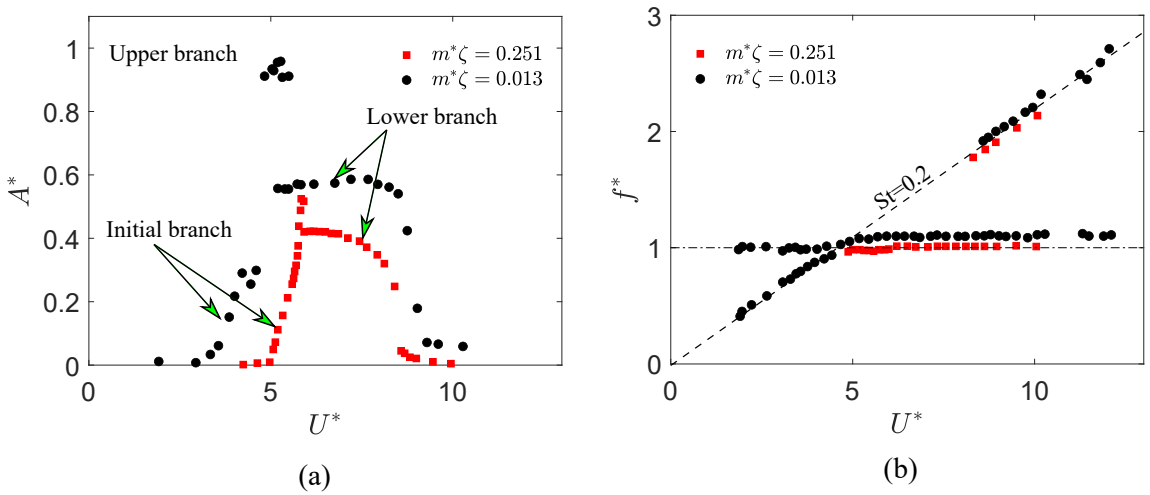

Figure 2.2: (a) Amplitude and (b) frequency response for low (black markers) and high (red markers) mass-damping systems, respectively. The dashed slanted line in the frequency response represents von Kármán shedding frequency. Figures adapted from [62, 83].

Each response branch is associated with unique vortex dynamics. A detailed study on the effect of cylinder oscillations on the wake was conducted by Williamson and Roshko [204] using flow visualization. They employed forced (controlled) vibrations of the cylinder at different amplitude ratios and reduced velocities to create a map of the different vortex shedding patterns observed across a large parameter space that also encompasses the expected regions of possible free vibrations for a 1-DOF system. An updated map was provided by Morse and Williamson [123] who used PIV to study the wake. The vortex shedding patterns associated with the main branches of oscillation along with the corresponding map are shown in figure 2.3. Vortex shedding in the initial branch resembles that in the wake of a stationary cylinder, characterized by the alternate shedding of oppositely signed vortices into the wake (figure 2.3(b)). This mode of shedding is commonly referred to as 2S [204]. The switch to the upper branch is accompanied by a change in the wake topology where two vortices, one primary, and one weaker counter-rotating secondary vortex, are shed in each half cycle ($2P_0$ mode, figure 2.3(c)). The lower branch wake topology features a modified version of $2P_0$ with primary and secondary vortices of similar strengths (2P mode, figure 2.3(d)) [204].

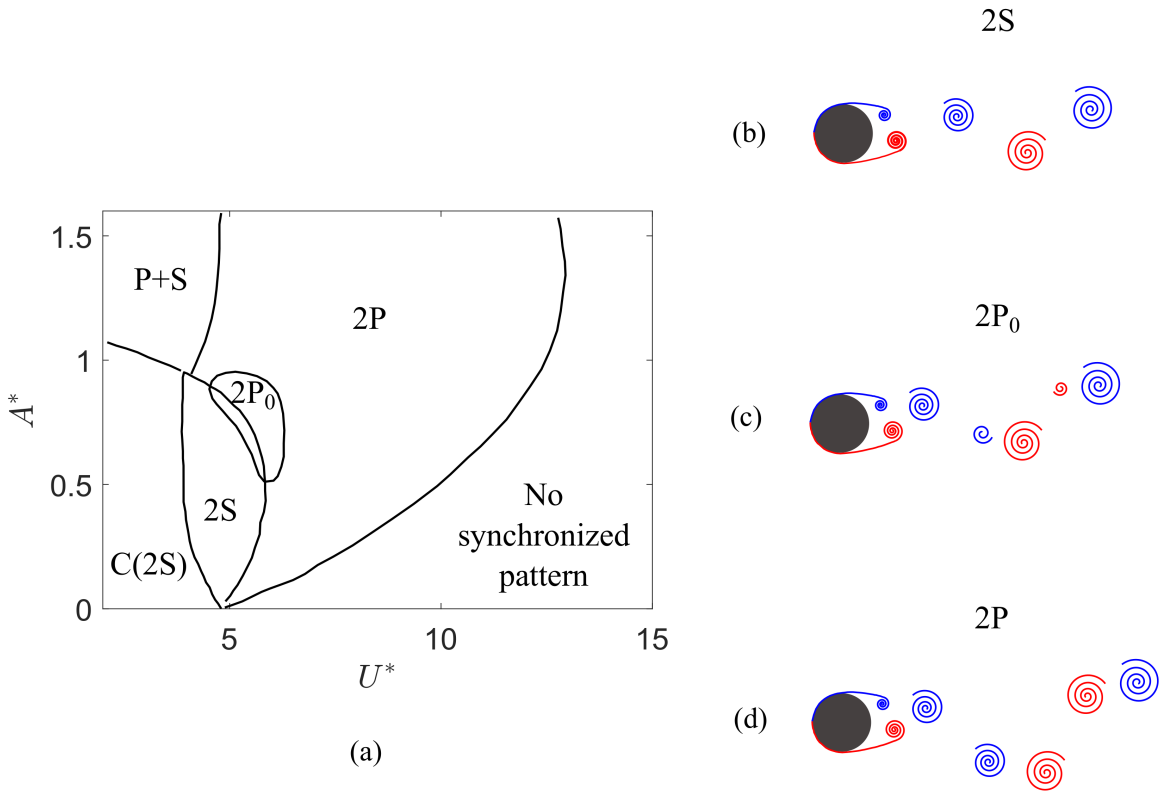

Figure 2.3: (a) Map of vortex shedding patterns across a wide range of A^*, U^*. Adapted from [123]. (b-d) Illustrations of vortex shedding patterns observed in 1-DOF free vibration.

Knowledge of the associated vortex dynamics in VIV allows for a better understanding of the mechanisms underlying system behavior. Govardhan and Williamson [62] modified the equation of motion (equation 2.1) to explore a more direct relationship between the structure and the wake. Following the work of Lighthill [103], the total force can be decomposed into an added mass force and a vortex force. For circular cylinders exhibiting periodic motion, the added mass component, given by $F_a(t) = -m_a\ddot{y}$ (where m_a is the added mass), is in phase with the cylinder motion [62, 116]. Equation 2.1 can now be represented as:

$$m\ddot{y} + c\dot{y} + ky = F(t) = F_a(t) + F_v(t) \tag{2.3}$$

$$(m + m_a)\ddot{y} + c\dot{y} + ky = F_v(t) \tag{2.4}$$

The vortex force can be represented as a periodic function $F_v = F_{0v}sin(2\pi ft + \phi_v)$, where ϕ_v is the phase difference between the vortex force and the cylinder displacement [62]. This decomposition helps in correlating the phase jumps between the branches with changes in

the vortex shedding mode. Specifically, the transition between 2S and $2P_0$ shedding accompanying the initial-upper branch transition is associated with a nearly 180° phase jump in the vortex force phase difference[4] ϕ_v, and minimal change to the total phase difference ϕ. The jump in the vortex phase is also related to a switch in the timing of vortex shedding with respect to the oscillation cycle [100]. Conversely, the second transition between the upper and lower branches is characterized by a large jump in the total phase difference, and an insignificant change in the vortex force phase difference (timing of shedding), since both upper and lower branches are associated with similar shedding topologies ($2P_0$ and 2P, respectively) [62].

VIV characteristics can also be examined through the lens of an energy transfer between fluid flow and the structure. For a system at equilibrium undergoing VIV, the energy transfer from the fluid to the structure over an oscillation cycle can be calculated as:

$$E = \int_t^{t+T} F(t) \cdot \dot{y}(t)\, dt = \int_t^{t+T} [F_a(t) + F_v(t)] \cdot \dot{y}(t)\, dt \tag{2.5}$$

where $T = 1/f$ is defined using the oscillation (lock-in) frequency. The added mass component does not contribute to the energy transferred to the structure over a cycle [75, 116], leaving the vortex-induced force as the sole contributor. Approximating the vortex-induced force as $F_v(t) = F_{0v} sin(2\pi f t + \phi_v)$ and displacement from equation 2.2, energy transfer to the cylinder over one oscillation cycle can be calculated as [123]:

$$E = \pi A F_{0v} sin(\phi_v) \tag{2.6}$$

The vortex force phase difference ϕ_v in equation 2.6 assumes a prominent role in determining the system response characteristics. Positive energy transfer to the structure, and subsequently, the condition for the existence of free vibrations, necessitates the phase difference to lie within $0 < \phi_v < 180$ [123]. Additionally, any value of ϕ_v other than 90°, results in a component of forcing in phase with the cylinder acceleration, thereby contributing to an effective added mass [83].

Menon and Mittal [116] employed energy transfer analysis to investigate the mechanisms responsible for initiating and sustaining VIV of elliptical cylinders operating in the laminar shedding regime. A force partitioning method [35, 147] was used to isolate individual contributors to the total force experienced by the structure including added mass force, viscous force, and vorticity-induced force (see [116] for details). The authors show that vorticity-induced forces dominate for both the onset of vibrations and at quasi-steady state, with added mass force and viscous forces contributing negligibly. The study also utilizes the concept of "energy maps" to analyze free vibrations. Energy maps have also been explored in other studies (e.g., [115, 123]). The map is created by employing forced oscillations at multiple prescribed amplitudes and frequencies and calculating the energy transferred to

[4]Also referred to as vortex phase moving forward

the structure over an oscillation cycle across the amplitude-frequency plane. Iso-contours of zero energy transfer on the map are used to identify the boundaries for free vibration at zero damping and have been shown to accurately predict quasi-steady state response under carefully matched kinematic conditions [115, 123].

2.3 Freestream turbulence effects on stationary and oscillating cylinders

In addition to the inherent variation in key nondimensional parameters known to influence VIV, practical applications subjected to VIV encounter varying levels of incoming flow disturbances, commonly referred to as freestream turbulence (FST) or elevated FST (eFST) [39, 209, 216]. eFST is typically characterized by a turbulence intensity $Tu = u'_{rms}/U_0$, and a characteristic length (integral) scale Λ_x [143], where x denotes the streamwise (longitudinal) direction. The integral scale approximately characterizes the size of the most energetic turbulent structures [183]. Turbulent flow typically contains structures of varying length and time scales. Energy is transferred from the larger to smaller scales in a process known as the energy cascade, eventually dissipating into heat at the Kolmogorov scales [143].

The size of the most energetic turbulent flow features (integral scales) relative to the characteristic geometry length scale (e.g., cylinder diameter) of a structure susceptible to VIV is relevant to the effect of the incoming freestream perturbation on system characteristics. In general, the time scales of turbulent flow structures typically scale with the size of the structures [144]. Thus, for engineering structures of relatively small characteristic lengths (diameters of $O(0.01)m - O(1)m$)[5], flow features with integral scales on the order of tens or even hundreds of meters are likely to be perceived as relatively slow changes in the global freestream velocity. These situations are outlined in more detail in section 2.4. Conversely, integral scales less than or on the order of the structure characteristic length scale (typically cylinder diameter) are likely perceived as localized short-term unsteady fluctuations in velocity. If the time scales associated with these fluctuations are much smaller than the dominant system time scales (such as lock-in or shedding frequency), then it is expected that the flow unsteadiness will primarily affect the quasi-steady system behavior with minimal effect on the long-term (transient) VIV response. The spatial and temporal scales associated with eFST considered in this thesis are smaller than the dominant length and time scales associated with VIV. Consequently, the effects of eFST on VIV are adequately captured through examination of the mean (quasi-steady) VIV characteristics, with insignificant influence on the transient (long-term) behavior of the system.

Two notable operational environments where structures susceptible to VIV operate are large water bodies (ocean risers, oil pipelines) and the atmosphere (towers/masts, chimneys, e.t.c).

[5]examples include transmission tower tubes, ocean risers or towers/masts

Turbulence in the ocean arises from a number of flow phenomena including ocean waves and Langmuir circulations [32]. However, turbulence measurement in the oceans is still in a relatively nascent stage compared to atmospheric measurements. Most previous studies have focused on the mixed and upper ocean layers (first few hundred meters in depth) where interactions with the atmosphere and various instabilities are primarily responsible for a higher degree of unsteadiness [58]. Turbulent motions have been found to range in integral scales from a few centimeters to hundreds of meters and are often superimposed on wave motions with wavelengths on the order of a few meters to hundreds of meters [39]. Direct measurements of the turbulence intensities from different studies conducted primarily near coastal regions indicate a wide range of values from approximately $Tu = 3\%$ to over 15 % [110, 117, 136, 137].

Atmospheric flows are inherently turbulent, with flow features spanning length scales ranging from millimeters to the order of the Earth's circumference, and time scales ranging from fractions of a second to years [14]. Further, atmospheric flows are subject to the no-slip condition at the Earth's surface, resulting in the formation of an atmospheric boundary layer (ABL) that typically spans hundreds of meters in the wall-normal direction [121]. Complex terrain features over urban and suburban regions further influence the boundary layer development. Numerous studies have been conducted to characterize the structure and characteristics of the ABL (e.g., [65, 72, 122]). Of interest to the present work is an estimation of the turbulence intensities and integral length scales inherent to atmospheric flows that can potentially affect VIV response of structures operating in such environments. Recommended values for modeling the turbulence intensity and/or integral length scales have been proposed in different international standards (e.g., ESDU 85020 [188], Eurocode EN 1991-1-4 [1], ASCE 7-05 [134]). For example, the turbulence intensities for a reference velocity of 10 m/s and roughness height of 0.3 m from ESDU 85020 range between approximately 7 and 12% at a height of 300 m to between approximately 15 and 25% at a height of 20 m [88]. The roughness height chosen corresponds to that recommended for small towns and suburbs of large towns and cities. For the same parameters, the integral length scale varied between approximately 150-200 m at a height of 20 m to between 300 and 650 m at a height of 300 m. The turbulence intensity and integral length scales reduce for smaller values of the roughness height. For example, a roughness height of 0.002 m and the same reference velocity from ESDU 85020 results in estimated turbulence intensities between approximately 5 and 11% for the same height ranges, and corresponding integral scales between 70 and 125 m [50].

In laboratory settings, grids have typically been used to generate nearly isotropic turbulence (e.g., [92, 95–97, 119, 156]). Grids generally consist of monoplane or biplane rods that form a mesh pattern. If the Reynolds number based on the rod diameter is sufficiently large, the turbulence intensity in a facility can be increased from its baseline levels [97]. Due to a lack of turbulence-generating mechanisms downstream of the grid, the turbulence intensity decays while the integral length scales increase with the downstream distance from the grid [156] as per:

$$Tu^2 = C\left(\frac{x - x_0}{M}\right)^b \tag{2.7}$$

$$\frac{\Lambda_x}{M} = C_\Lambda (x - x_0)^{1/2} M^{-1/2} \tag{2.8}$$

Here, C, b and C_Λ are constants that depend on initial conditions (e.g., rod geometry) [95]. Additionally, Λ_x is the longitudinal integral scale, x, x_0 are the distance from the grid and the imaginary center of the grid, and M is the mesh width. Previous studies have shown that nearly isotropic turbulence may be achieved approximately $20M$ downstream of the grid [64, 90, 95].

Turbulent incoming flow can be considered as a perturbation to various regions of flow around a cylinder including the boundary layers, shear layers, and the wake. These perturbations may result in changes to the wake dynamics that affect the forces experienced by the structure. Although the flow dynamics are typically different between stationary and vibrating cylinders, some similarities in wake development, particularly at low amplitudes of vibrations, warrant a brief overview of the research focused on eFST effects on flow over stationary cylinders.

2.3.1 Effect of eFST on stationary cylinders

Freestream turbulence effects on stationary cylinders have been widely investigated in literature. Due to the sensitivity of the flow across a cylinder to the operational Re (see section 2.1), studies on eFST effects on a cylinder have typically focused on specific regimes ranging from the transition in wake regime ($180 \lessapprox Re \lessapprox 300$) [2] to the critical and post critical regimes ($Re \gtrapprox 120{,}000$) [213]. For this overview, the results pertaining to the shear layer transition regime are presented due to their relevance to a wide range of engineering applications.

Maryami et al. [113] conducted experiments at $Re = 14{,}500$, corresponding to the early shear layer transition regime. The turbulent intensity varied between 3.1 and 5.1 % with corresponding integral length scales between 0.66 and $1.1D$. The results show that eFST delays boundary layer separation on the cylinder by up to 10° and increases the rms surface pressure coefficient by up to 25%. Khabbouchi et al. [82] studied the effect of eFST on the separated shear layer for $4{,}500 < Re < 47{,}000$ using turbulence intensities ranging from 0.2 to 6.2 %. The integral scales were maintained at approximately $2D$. Hotwire measurements were acquired at multiple streamwise and spanwise locations across the shear layer and near wake. The results indicate an upstream movement of the shear layer transition with eFST and a decrease in the vortex formation length from $X/D \approx 2.2$ to 1.6. An increase in the transverse extent of the shear layer (width of the shear layer) was promoted with eFST. Additionally, the presence of high-frequency fluctuations associated with the shear layer vortices was observed to diminish with increasing eFST. The authors conclude that eFST promotes the breakdown of shear layer structures into turbulence, thus precipitating the outlined effects on the shear layer and near wake characteristics.

Arie et al. [9] investigated the effect of both the turbulence intensity and the integral length scale on cylinders for 8,000 $< Re <$ 54,000. Cylinders of varying diameter were used with different grids to achieve desired combinations of intensities and relative length scales (0.9 % $< Tu <$ 12 %, and $0.1 < \frac{\Lambda_x}{D} < 10$). The introduction of eFST was found to minimally affect the Strouhal number St. For relatively constant turbulence intensities, the authors found that decreasing the integral scales resulted in lower drag coefficients. Overall, increasing the turbulence intensity and decreasing the integral scale were found to induce premature drag crisis. Additionally, eFST was found to decrease the spanwise correlation lengths, in some cases to approximately 0.1 times the baseline value. Surry [179] studied the effect of high-intensity turbulence on stationary cylinders for 33,000 $< Re <$ 44,000. Freestream turbulence intensity of $Tu \gtrapprox 10$ % and integral length scales varying between 0.36 to 4 D were considered. Similar to other studies (e.g., [9]), eFST minimally affected St. Overall, the authors describe the effects of eFST as similar to increasing the operational Re.

Several studies (e.g., [52, 53, 162]) have found that eFST modifies the boundary layer characteristics to varying extents depending on the intensity and length scale of turbulence. In particular, studies conducted for Re corresponding to the later stages of shear layer transition ($Re \gtrapprox$ 30,000) indicate that the boundary layers are prone to transition when exposed to eFST. One mechanism responsible for boundary layer transition in the presence of eFST is vorticity amplification [161, 162, 180]. Turbulent fluctuations present in the incoming flow, are susceptible to undergoing significant amplification as they are conveyed by the diverging mean flow toward the body stagnation zone. Selective stretching of vortex filaments is proposed as the mechanism responsible for the amplification of vorticity and, hence, of streamwise turbulence. The amplified turbulence, in particular, those eddies of scales on the order of the boundary layer thickness, interact with the boundary layer to induce a premature transition and the onset of the drag crisis [93].

In conclusion, the effect of eFST on cylinders has been shown to depend strongly on the operational Re regime, the freestream turbulence intensity, and the integral length scale. A common thread among all tested regimes is the significant influence of eFST on the wake characteristics. In the early shear layer transition regime ($1,000 \lessapprox Re \lessapprox 10,000$), the shear layers and near wake are modified, including premature shear layer transition, a significant reduction in the extent of the recirculation region behind the cylinder, and an increase in structural loading [82, 113, 130]. For higher Re, eFST can induce earlier boundary layer transition, resulting in narrower wakes, and decreased structural loading associated with the drag crisis [24, 86, 214].

2.3.2 Effect of eFST on VIV

Comparing to the case of a stationary cylinder, a limited number of investigations have considered the effect of eFST on VIV of circular cylinders, making it difficult to draw general conclusions. Goswami et al. [61] conducted experiments in a wind tunnel for a cylinder with

a large mass ratio (m^* >100) and $\zeta = 0.0015$ with one degree of freedom (1-DOF) transverse to the flow. They conducted measurements at $Tu = 2.5\%$ for 5,000 < Re < 6,500. The results show that eFST induces notable modulations in the amplitude response and a more broadband frequency response, however, there are minimal changes to the overall nature of the amplitude response curve. Pasto [139] conducted experiments on a cylinder with relatively large mass-damping ($m^*\zeta$=0.321-0.78) constrained to 1-DOF and in three different freestream conditions – smooth flow (no baseline characteristics provided), $Tu = 3\%$, and $Tu = 13.5\%$ with longitudinal integral scales of $\Lambda_x/D = 0.2$ and 1 for the low and high Tu cases, respectively. The Reynolds number varied between 34,000 and 50,000. The results show a departure from normal amplitude response for both the low and high turbulence cases. For $Tu = 3$ %, peak amplitude of oscillations decreased. This was more pronounced for $Tu = 13.5\%$, along with a smoother transition between the initial and lower branches. Further, increasing FST intensity produced earlier desynchronization (reduced range of synchronization). Finally, an effective Re formulation suggested in [98] for stationary cylinders was used to interpret the results. The formulation translates the effect of elevated freestream turbulence and/or surface roughness into an increased perceived Reynolds number. Depending on the case, this resulted in the cylinder operational Re regime changing from sub-critical to either transitional or critical, which the author related to the observed changes in system response. Recently, a study by Bourguet and Mathis [29] on the VIV of a cylinder of large mass ratio ($m^* \approx 1000$) at $Re \approx 10{,}000$ reported an increase of up to 45% in peak oscillation amplitudes in the presence of freestream turbulence with intensities up to 10 %. Notably, owing to the large mass ratio, the peak oscillation amplitudes were relatively small ($\approx 0.1D$).

Previous studies have also investigated the effect of eFST on circular cylinders undergoing 2-DOF VIV. So et al. [173] conducted experiments with an elastic acrylic cylinder with $m^*\zeta = 23.4$ between $5,000 < Re < 41,000$ and Tu ranging from 9.8 to 13.3 % compared to a baseline $Tu = 0.2\%$. A significant increase in oscillation amplitudes was observed, with no appreciable change in the range of synchronization. Deng et al. [43] conducted full-scale experiments on cylinders hinged at the end with various joints to mimic those used in transmission tower tubes for 10,000 < Re < 80,000 and $1.49 < m^*\zeta < 15$. For eFST of different intensities ($Tu = 5.7\%, 10.1\%$), a decrease in peak amplitudes was observed. Furthermore, increasing Tu was found to result in lower amplitudes of oscillation. Apart from experimental studies, wake oscillator models have been employed to study eFST effects on VIV [12, 13]. In particular, eFST is introduced as a stochastic disturbance to the input and the results are compared to a baseline case with smooth flow. However, the results from wake oscillator models are typically limited in their scope and rely on experimental data to tune their models. Hence they are not used to draw any conclusions for the present work. Other studies of possible interest to the reader but with limited overlap to the current scope include studies examining eFST effects on VIV and galloping of rectangular cylinders and flexible side-by-side cylinders (e.g., [40, 111, 195, 208]).

The prior studies on eFST effects on VIV have reported varying results. While some of this may be attributed to the different configurations (1/2-DOF, rigid/elastic) and parameter

ranges employed, the lack of flow field data makes it difficult to identify the underlying mechanisms governing the reported responses. Moreover, considering the sensitivity of stationary cylinder wakes to both the Reynolds number and eFST, it is important to provide independent control of these two parameters, which has not been undertaken in the mentioned studies.

2.4 Transient vortex-induced vibrations

Quasi-steady VIV are typically attained under controlled laboratory conditions where the freestream is steady and uniform. However, changes in the quasi-steady energy balance resulting in transient VIV is a more realistic representation of real-world VIV. Transient VIV may be encountered in different situations. One common example is a change in incoming freestream velocity that positions the vortex shedding frequency near the structural natural frequency thereby triggering vibrations and the subsequent transient progression to a quasi-steady (equilibrium) state. Conversely, changes in the global mean freestream velocity (unsteady freestream) may perturb a system from a prevailing quasi-steady state. Transient VIV may also be encountered in steady flow conditions as a result of changing structural properties (e.g., due to a structural component failure, such as a supporting cable) that triggers the onset of VIV. The outlined situations, among others, should be considered during the design of engineering structures susceptible to VIV, particularly due to their operation in inherently unsteady environments such as oceans and the atmosphere [39, 209]. It is reiterated here that, in the present work, the discussion of freestream turbulence effects on VIV is limited to the cases where the integral scales are smaller than the structure size. Consequently, eFST does not appreciably modify the transient VIV characteristics.

In the atmosphere, coherent motions may result in unsteady freestream conditions (commonly known as gusts). A gust is typically characterized as a relatively rapid excursion of the freestream velocity from its mean value. Various parameters are used to describe gust characteristics including the gust factor (G), rise time (t_{gr}), lapse time (t_{gl}), and gust duration (t_{gd}) [67]. The gust factor is defined as the ratio between a short-term, time-averaged wind speed $\overline{U_g}$ and a long-term, time-averaged wind speed $\overline{U_h}$ as $G = \overline{U_g}/\overline{U_h}$. The time periods used to define the two time scales vary in literature. The World Meteorological Organization and North American building code recommend 3 s for the short-term average and 10 mins for the long-term average [174, 206]. Measured gust factors at different locations worldwide typically fall between $1 < \mathrm{G} < 4$ barring some extreme gust events [67, 78, 211]. The gust rise time t_{gr} is the time taken for the wind speed to increase from a steady value to a local peak value. The gust duration t_{gd} is the length of time when the velocity remains elevated, and the gust lapse time t_{gl} is the time taken from the peak amplitude to the next local minimum in velocity. The gust factor (magnitude) and rise/lapse times are important parameters that govern the transient structural loading and response on structures [142]. Compared to the relatively rapid wind speed changes caused by atmospheric gusts, the time scales of various oceanic processes that may result in changing freestream

conditions are typically significantly larger [31]. Of the different oceanic processes, those with timescales of possible relevance to transient VIV include turbulent patches [210], Langmuir cells [32], and surface waves, with the timescales ranging from $\mathcal{O}(10)s$ to $\mathcal{O}(1000)s$ [45].

Pertinent to bluff body flows, the ratio between the freestream time scales (gusts, oceanic processes) and the dominant system time scales (natural time period/vortex shedding time period) plays a prominent role in determining the transient structure/wake dynamics [151, 165]. For instance, consider that the freestream time scale (e.g., gust rise time) is much larger than the structure/wake time scale ($t_f/t_{vs} >> 1$, where t_f represents the freestream timescale and t_{vs} is the vortex shedding period). In this case, the slow variation in the freestream relative to system time scales allows for the system to approach quasi-steady state at each new operating condition. This allows the resulting transient behavior to potentially be modeled using quasi-steady response characteristics. Conversely, relatively rapid changes to the freestream ($t_f/t_{vs} << 1$) may be considered impulsive, thereby eliciting distinct dynamics [165].

A brief examination of the ratio between typical freestream time scales and the dominant system timescales of structures susceptible to VIV provides an insight into the relevant parameter space. Table 2.1 provides a list of different applications susceptible to VIV along with relatively simple approximations of their characteristic lengths (diameters), expected vortex shedding periods, and the ratio between the freestream timescale and the shedding period (t_f/t_{vs}). The use of the shedding period instead of the natural frequency as the dominant system timescale is considered a reasonable assumption given that the largest oscillation amplitudes (upper branch) are typically achieved when the structural natural frequency is within approximately 20% of the vortex shedding frequency [83]. Strouhal numbers of 0.2 were used to calculate the range of vortex-shedding periods as expected for circular cylinders that typically approximate the shapes of the examined structures [5, 135]. Gust rise times are employed as a representative time scale for gusts with a range of 5-40 s considered as the gust rise time scale, derived from reported values in various studies [16, 67, 211]. This range corresponds to a minimum probability exceeding 1 % on a probability distribution of rise times. While mean wind speeds vary significantly across the globe based on region and height above sea level [8], a conservative range of speeds was adopted (2-12 m/s) for the calculation of shedding periods based on reported values (e.g, [15, 67, 160, 211]). For oceanic flows, current speeds typically range from $\mathcal{O}(0.1)m/s$ to $\mathcal{O}(1)m/s$ [73, 81, 164] and a range of 0.1 to 10 m/s is employed for the present analysis.

Figure 2.4 depicts the ratio of freestream to system timescales on a semi-log plot as obtained from the above analysis. Even from this simplified analysis, it is apparent that changing freestream conditions occur over a wide range of relevant system timescales. Chimneys are found on the lower end of this range where the freestream changes occur relatively rapidly compared to the dominant system time periods, while ocean risers and transmission tower tubes fall farther to the right with changes in freestream occurring over tens or hundreds of system time periods.

Application	Diameter(m)	Shedding period(s)	t_f/t_{vs}
Chimney [49, 128, 149]	$O(1) - O(10)$	0.3-250	0.04-130
Transmission tower tubes [43, 68, 101]	$O(0.01) - O(0.1)$	0.002-0.25	20-15000
Tower/mast [38, 48, 106, 192]	$O(0.1) - O(1)$	0.04-25	0.2-1300
Ocean riser [79, 186, 191]	$O(0.01) - O(0.1)$	0.005-5	2-200000

Table 2.1: Parameter space estimation for the ratio of freestream time scales to the dominant system time scales.

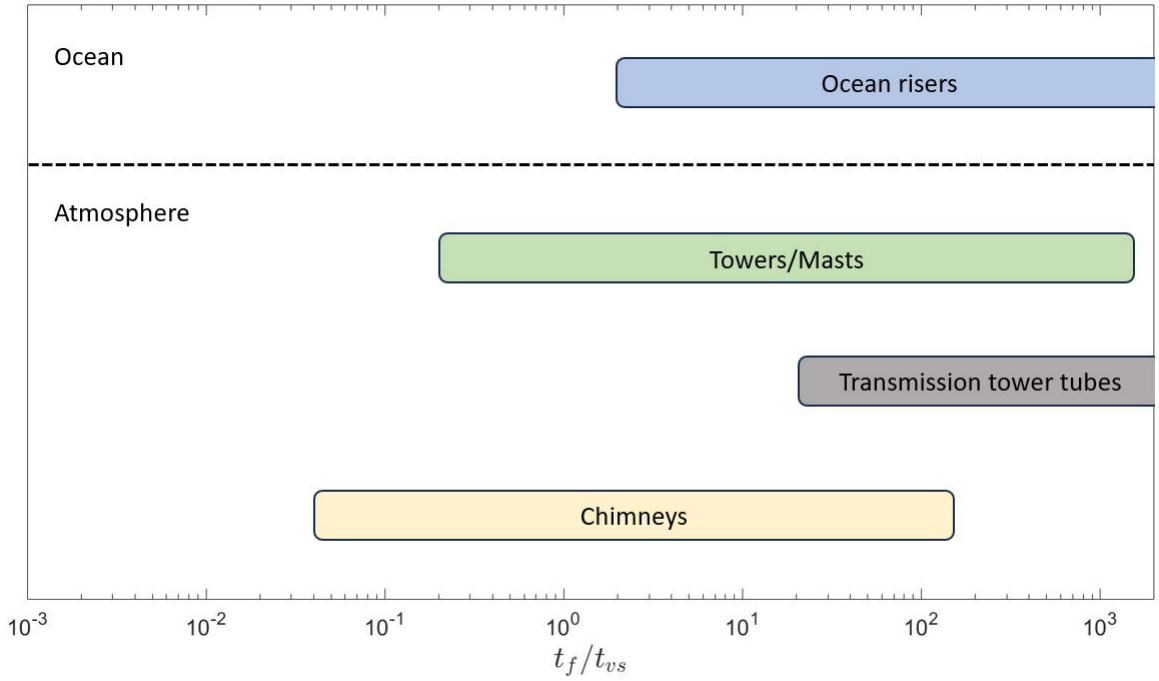

Figure 2.4: Illustration of the parameter space for various applications susceptible to VIV with ranges provided for the estimated ratio of freestream time scales to the dominant system time scales.

The following sections provide an overview of the relevant literature for transient VIV in steady and unsteady freestream conditions.

2.4.1 Transient VIV in steady freestream conditions

An elastically-mounted cylinder released from rest in a steady freestream is considered a representative case of a system following an impulsive change in structural characteristics that give rise to the onset of VIV. Anagnostopoulos and Bearman [7] conducted an early study that considered transient VIV development from rest, where a cylinder was released into a steady freestream in laminar vortex shedding conditions ($90 < Re < 150$). The cylinder had a mass ratio $m^* \approx 149$, damping ratio $\zeta \approx 0.0015$, and was restricted to move

in 1-DOF transverse to the freestream. For reduced velocities corresponding to the lower branch, the cylinder exhibited a steady increase in oscillation amplitudes up to quasi-steady state. In particular, for $U^* \approx 5.8$, the cylinder reached quasi-steady state ($A^* \approx 0.53$) in around 70 oscillation cycles. At a larger reduced velocity ($U^* \approx 6.3$), a significant reduction (>50%) in the amplitude growth rate was observed despite similar final quasi-steady state amplitudes ($A^* \approx 0.5$).

Leontini et al. [100] conducted a numerical study of VIV in a laminar shedding regime ($Re = 200$) with $m^* = 10$ and $\zeta = 0.01$. The simulations included the transient build-up from rest and continued through quasi-steady state. The lower branch transient behavior exhibited a steady growth of amplitudes with the envelope of oscillation amplitudes resembling a sigmoid curve. In contrast to quasi-steady state, where the phase difference ϕ is relatively constant, a consistent increase in ϕ was observed during the transient amplitude growth. The transient response in the initial branch revealed a beating-type behavior with the instantaneous phase difference ϕ (equation 2.2) modulating between positive and negative values. A number of other studies pertaining to transient VIV development from rest have also been conducted within laminar vortex shedding regimes (e.g., [6, 116, 145]). While the findings from these studies provide further support to the discussed response, including varying amplitude growth rates and non-stationary instantaneous phase differences, structural response characteristics and wake dynamics for laminar shedding regimes are different from turbulent regimes [203].

Brika and Laneville [30] conducted experiments (including release from rest) on a long flexible cylinder free to move in 2-DOF for $3,400 < Re < 11,800$. The flexible cylinder had an aspect ratio of 52.7 and mass damping $m^*\zeta$ varied between 0.013 and 0.3. When released from rest for reduced velocities in the initial branch, the cylinder exhibited a distinct overshoot in oscillation amplitudes above quasi-steady values before settling into quasi-steady state. The instantaneous phase difference ϕ exhibited an abrupt drop (exact values not specified in [30]) near the instant where the amplitude overshoot reached its maximum. For U^* in the lower branch, amplitudes continuously increased to quasi-steady state values, with the envelope exhibiting a sigmoid shape. The authors further show that the time required to attain quasi-steady state (settling time) in the lock-in regime increases nearly exponentially with reduced velocity, with the shortest settling time near the initial branch (approximately $3,000$ cycles) and the longest settling times in the lower branch (approximately $50,000$ cycles). Notably, wake measurements were not reported for the transient build-up.

To the best of the author's knowledge, despite recurring themes emerging from the different studies regarding the transient response of the system at the onset of VIV, a comprehensive investigation focused on characterizing transient VIV development from rest across all response branches and at turbulent shedding conditions has not been undertaken.

2.4.2 Transient VIV in unsteady freestream conditions

Transient VIV response may also be initiated through a change in freestream velocity. However, the number of studies that explore this topic is limited compared to the vast number of studies on stationary cylinders in changing freestream conditions (e.g., [28, 66, 99, 165, 175]). Further, to the best of the author's knowledge, no studies examine the case of a rigid elastically-mounted cylinder under unsteady freestream conditions. Laguë and Laneville [94] conducted experiments on a flexible cylinder in time-varying flow using the same 2-DOF setup as Brika and Laneville [30]. Briefly, the mass ratio of the system $m^* \approx 1590$ and ζ varied between 0.83×10^{-4} and 2×10^{-4}. The freestream velocity was modified by superimposing a sinusoidally varying ΔU_0 with differing periods on U_0. The associated change in the reduced velocity is represented as:

$$U^*(t) = U^* + \Delta U^* sin(t/P) \tag{2.9}$$

where P is the period of the freestream, and was varied between 10 and 150 s. Further, ΔU^* varied between 0 and 1.88. The results of the study are primarily focused on the $P = 100s$ and $\Delta U^* = 1.25$ case. Comparing the sinusoidal variation in freestream to the definition of gusts, the quarter time period $P/4$ is analogous to the gust rise time t_{gr}. The change in velocity for $P/4 = 25s$ occurs over approximately 437 cycles of the cylinder oscillation, which would fall in the range of conditions experienced by transmission tower tubes, towers, and risers based on figure 2.4. The results show significant modulations in the cylinder amplitude with the envelopes exhibiting sawtooth and/or sinusoidal shapes depending on the operational reduced velocity (U^* on the right-hand side of equation 2.9). Further, the modulations in amplitude are periodic with the period synchronized with the change in freestream conditions, but with a time lag of approximately $P/3 - P/4$. One such example is shown in figure 2.5(a) where the blue lines show freestream variation and the black lines show the envelope of the cylinder amplitude time series for mean $U^* = 5.65$. This unsteady amplitude modulation is mapped as a trajectory of points in the $A^* - U^*$ plane as shown in blue markers in figure 2.5(b). The black markers show the quasi-steady system response. The unsteady responses for other mean U^* values are also plotted using different colors. It can be seen that, in all cases, the trajectories loosely resemble ellipses around the quasi-steady response at the mean U^* (large colored markers on the quasi-steady response plot), with the exception of the red dots ($U^* = 6.3$), where the unsteady response amplitudes are significantly smaller than the corresponding quasi-steady state. It is worth noting that the freestream change in this case falls in the region of mode transition between the initial and upper branches.

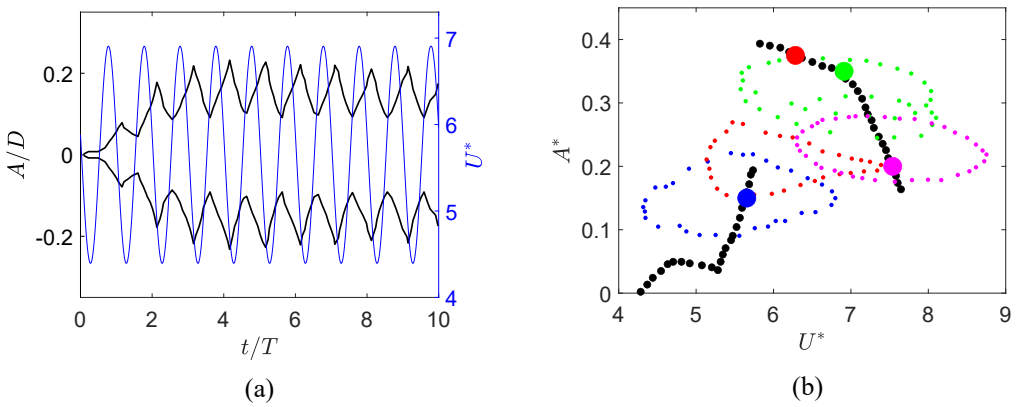

Figure 2.5: (a) Envelope of the amplitudes for a sinusoidally varying freestream velocity (shown in blue) with mean $U^* = 5.65$. (b) Quasi-steady system response (black markers) along with the unsteady system responses (colored markers) with the quasi-steady amplitude of the mean U^* in the unsteady cases highlighted on the quasi-steady curve. Adapted from [94]

For fixed ΔU^*, increasing the period of the velocity variation P resulted in the oscillation amplitudes approaching those of quasi-steady state, which the authors attributed to increased time for amplitude build-up. Increasing the magnitude of ΔU_0 resulted in larger changes to the reduced velocity within the same period, in some cases allowing for a switch in the response branch. Overall, the unsteady responses indicate that the changes in freestream velocity are not slow enough to allow the transient response to approach the quasi-steady state system response.

Resvanis et al. [150, 151] conducted experiments on a flexible 2-DOF cylinder exposed to time-varying flows. The aspect ratio of the cylinder model was 166, with a mass ratio of 1.53. The cylinder was towed from rest with varying ramp (up/down) profiles for Reynolds numbers up to 60,000. A nondimensional parameter to quantify unsteadiness is introduced as $\gamma = T_n \frac{|dU_0/dt|}{U_n}$, where n is the mode of response, and U_n, T_n are the freestream velocity required to excite the mode and the time period of the mode, respectively. This parameter is interpreted as the fractional change in flow velocity during one oscillation cycle. The experiments consisted of sweeping the entire lock-in range using different accelerations (γ) with the cylinder starting from rest. The amount of time spent by the system in the synchronization (lock-in) region can be estimated. In particular, assuming that the system is excited when the freestream velocity is within ±20% of U_n, then [151]:

$$\gamma \approx T_n \frac{\Delta U/\Delta t}{U_n} = T_n \frac{1.2U_n - 0.8U_n}{U_n} = \frac{2T_n}{5\Delta t} \tag{2.10}$$

From this, the time spent in the synchronization region Δt, which is loosely analogous to the freestream timescale t_f, can be represented as $\Delta t = 2T_n/5\gamma$. Thus, for larger γ, the system spends less time in the lock-in region and vice-versa. The results show that, for

slow accelerations ($\gamma < 0.02$), the system response approached quasi-steady levels. For moderate accelerations ($0.02 < \gamma < 0.1$), the cylinder exhibited significant oscillations, which in some cases were found to exceed quasi-steady state values. For large accelerations ($\gamma > 0.1$), insignificant oscillations were observed, owing to the limited time spent in the lock-in regime. This is depicted in figure 2.6, where the discussed slow, moderate, and fast acceleration regions are classified as A, B, and C, respectively.

The experiments of Laguë and Laneville [94] with the flexible cylinder in sinusoidally varying flow indicate that quasi-steady behavior is not observed despite the relatively slowly varying freestream. Assuming the quarter period as the freestream time scale (analogous to the gust rise time), $t_f f_n = \frac{P}{4} f_n \approx 437$, when $P/4 = 25s$. Conversely, in the experiments of Resvanis [150], quasi-steady system behavior is observed when $t_f f_n = \Delta t f_n \gtrapprox 20$. The contrasting behavior is most likely due to the significant difference in mass ratios ($m^* \approx 1590$ in the experiments of Lague and Laneville and $m^* = 1.53$ in the experiments of Resvanis). A high mass ratio implies that the system requires a much longer time (more oscillation cycles) to reach quasi-steady state. In particular, for the cylinder model used by Lague and Laneville, the minimum time required to reach quasi-steady state when the cylinder was released from rest was approximately 3,000 cycles as shown in a different study using the same facility and model [30]. This is an order of magnitude higher than the change in freestream velocity timescale. In the experiments of Resvanis [150], the cylinder converged on quasi-steady state in approximately four cycles when subjected to an impulse change in velocity. The effect of mass ratio on the classification of system response based on γ is also proposed as a future research question.

Other studies that explore unsteady freestream conditions on VIV have focused on oscillating flows with zero mean velocity (e.g., [34, 56, 87, 177]). However, in all these studies, the cylinder is forced to cross its own wake when the flow direction is reversed, thus eliciting distinct behaviors and, as such, are not the primary interest for the present work.

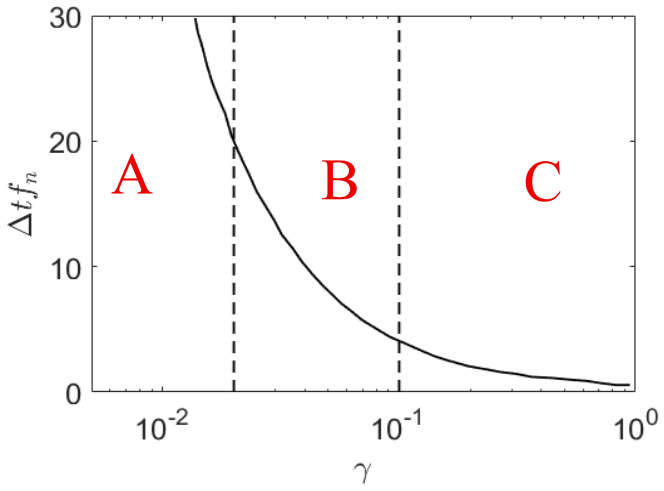

Figure 2.6: Time spent in the lock-in region ($\Delta t f_n$) vs γ with the vertical dashed lines representing the boundaries between regions exhibiting different behavior. A- System response is similar to quasi-steady response, B- System shows significant response that may or may not resemble quasi-steady response, and C- system shows minimal response owing to the limited time spent in the lock-in regime. Adapted from [150].

Chapter 3

Methodology

Experimental facilities and VIV setups for the three main campaigns are detailed along with the associated measurement techniques. Key data processing methods are also discussed.

3.1 Experimental setups

The experiments conducted as part of this thesis were performed at the University of Waterloo in the Fluid Mechanics Research Laboratory (FMRL) and at the University of Calgary in the Laboratory for Turbulence Research in Aerodynamics and flow Control (LTRAC), respectively. The experiments at FMRL addressed the objectives related to (i) the effect of eFST on VIV and (ii) transient VIV development from rest, while the experiments at LTRAC were performed to (iii) explore the effects of changes in freestream on VIV. Herein, an overview of the experimental facilities and VIV setups is provided. Chapters 4 and 5 contain the results for the experiments conducted at FMRL while Chapter 6 contains the results of the experimental campaign at LTRAC. The associated uncertainties in all quantities are presented in Appendix A.

3.1.1 FMRL water tunnel, VIV setup, and eFST generation

FMRL houses an open channel, closed-loop water tunnel facility that is shown in figure 3.1. The flow in the water tunnel at FMRL is driven by a constant head developed in an overhead tank that is supplied with water from two centrifugal pumps. The velocity in the test section is set by a combination of a gate valve and a variable porosity back gate placed approximately 1 m downstream of the test section. The settling chamber houses the flow conditioning elements including a square grid (12.7 mm spacing), a honeycomb (12.7 mm cell), and four wire meshes, with all the elements following the design recommendations of Mehta and Bradshaw [114] and Derbunovich et al. [44]. The flow enters the test section through a contraction which has an area ratio of 5:9. An entrance length equivalent to the width of the contraction is allowed before the start of the glass test section. The 2.5 m long test-section is 0.5 m in width and is designed for a water height of 0.8 m. The walls and floor of the test sections are constructed from glass to facilitate optical access. For all experiments at FMRL, the freestream velocity in the test section was held fixed at U_0=0.155 m/s and was uniform to within $0.01U_0$ outside of the wall boundary layers. The corresponding water height was 0.26 m. The baseline freestream turbulence intensity in the streamwise direction is 0.9% of the mean velocity.

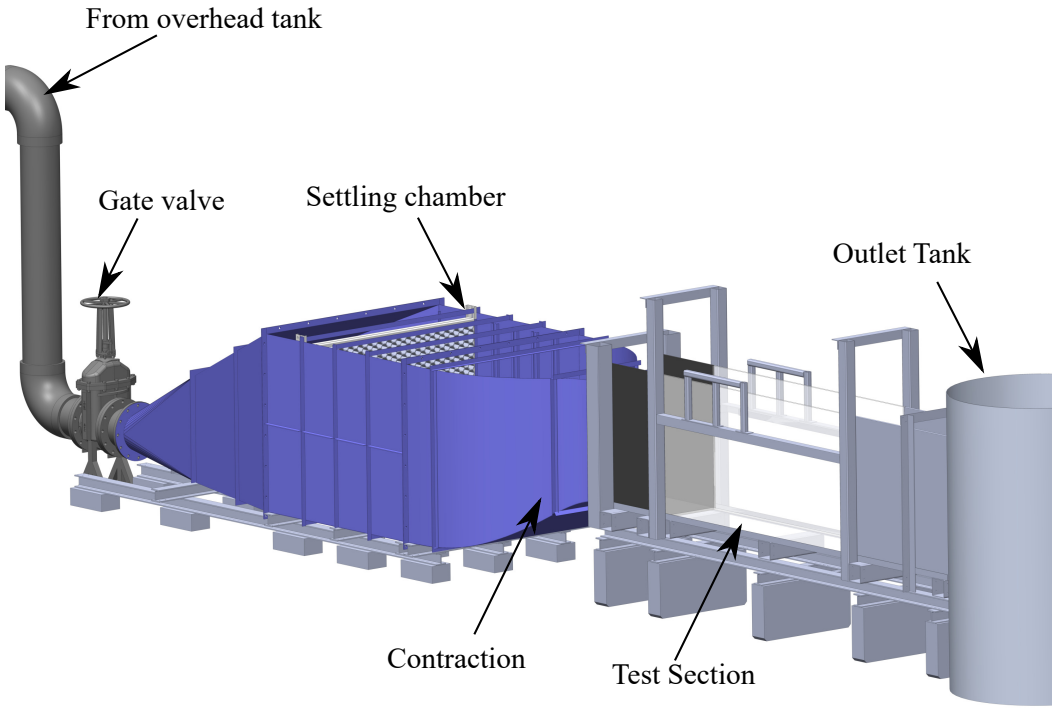

Figure 3.1: Water tunnel facility inside FMRL at the University of Waterloo.

In contrast to most traditional VIV setups, the experimental setup at FMRL was designed to examine VIV at constant Reynolds numbers. The VIV setup employs a method of modifying the natural frequency to produce a wide range of reduced velocities while maintaining a constant freestream velocity. This experimental arrangement is inspired by previous approaches [25, 75] and is shown in figure 3.2. A 2.54 cm diameter solid acrylic cylinder of length 73.00 cm is mounted at the end of a 182.00 cm long rigid hollow aluminum pendulum arm with an outer diameter of 2.54 cm. The pendulum arm is hinged to a support frame using a pair of ball bearings and is free to move in 1-DOF transverse to the freestream. Four springs, each with a stiffness of 367 N/m are attached using a collar that can slide along the length of the pendulum arm in order to modify the cylinder's natural frequency. Additionally, a system was devised to enable automated release from rest as described below. This system was only used for the study on transient VIV development from rest (Chapter 5).

To ensure repeatable cylinder release from rest, a plunging mechanism was used (shown in the left inset of figure 3.2). Specifically, the pendulum arm was held at its equilibrium position ($Y = 0$) between two prongs of a plunger that is mounted on a sliding rail, with the end of the plunger attached to a pull-type solenoid. The solenoid was powered through a 24 V DC power supply and triggered using a 5 V DC signal from an external circuit controlled through LabVIEW software. When activated, the solenoid initiates a rapid recoil of the plunger (recoil time $< 5\%$ of the von Kármán vortex shedding period), thus freeing the cylinder to vibrate. The release mechanism was verified to minimally influence the cylinder.

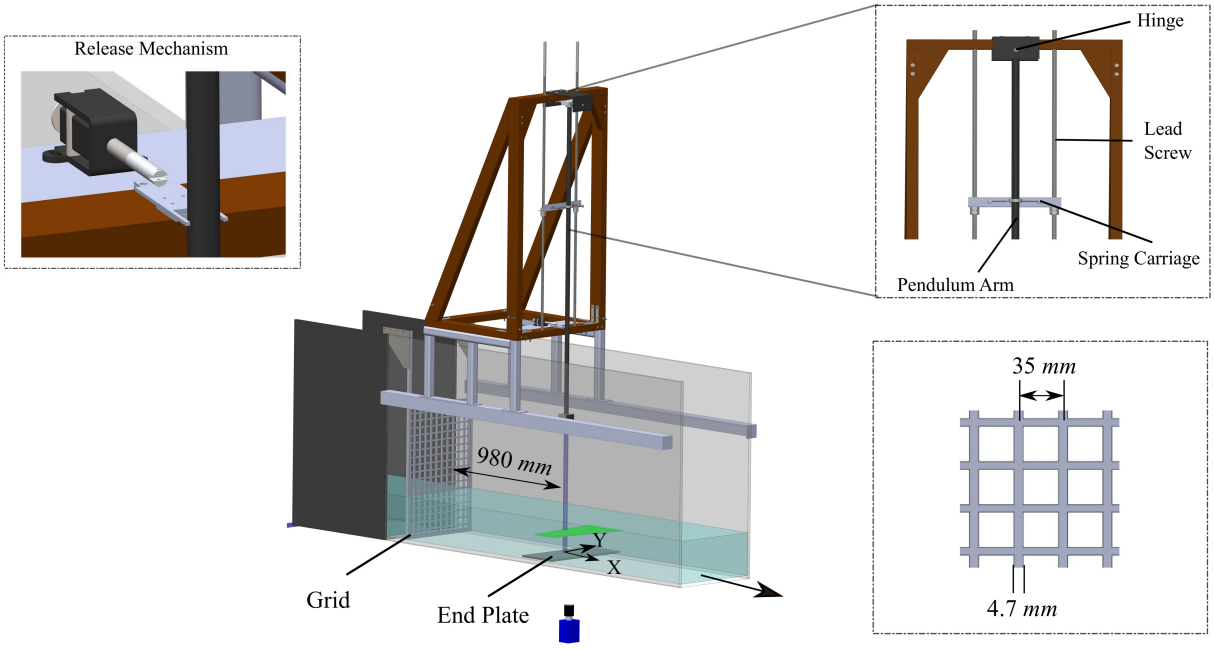

Figure 3.2: VIV setup on water flume. The right top inset shows components of the VIV setup. The right bottom inset shows a schematic of the turbulence grid, and the left inset shows the release mechanism. The origin of the coordinate system shown in the figure is at the center of the cylinder at its equilibrium position. The PIV schematics are included with the camera under the channel and the green laser sheet at the submerged cylinder midspan.

The relevant parameters of the VIV system are presented in table 3.1. The cylinder's natural frequency was determined from spectral analysis of free vibration tests in quiescent water, while free vibration tests in air were used to estimate the structural damping, by applying the log-decrement method [74] as shown in equation 3.1. Minor differences in the damping ratio across the range of natural frequencies investigated as seen here are found to minimally affect system response characteristics [176]. The maximum expected peak-to-peak VIV oscillation amplitude ($O(2D)$) results in less than 1° of angular displacement of the pendulum, negligible vertical displacement, and less than $0.1D$ oscillation amplitude disparity between the top and bottom portion of the submerged cylinder.

$$\begin{aligned} \kappa_i &= ln(\frac{A_{i-1}}{A_i}) \\ \zeta_i &= \frac{\kappa_i}{2\pi} \\ \zeta &= 1/N \sum_{i=1}^{N=10} \zeta_i \end{aligned} \tag{3.1}$$

Parameter	m^*	ζ ($\times 10^{-4}$)	$f_n(Hz)$	U^*
Value	18.2	6.5-3.4	0.48-1.55	3.9-12.7

Table 3.1: Parameters of the experimental VIV system.

To minimize end effects, a rectangular end plate, spanning the width of the tunnel and with length $9D$, was placed less than 1 mm from the tip of the cylinder. The end plate has a sharp tapered leading edge that is $3D$ upstream of the cylinder edge. It was mounted outside of the wall boundary layer to ensure uniform freestream conditions across the span of the submerged cylinder model. The height of the submerged cylinder was 21.0 cm, resulting in an aspect ratio of 8.26, and a blockage ratio of less than 5 %. The Reynolds number was maintained constant at approximately 4,400. This value is within the shear layer transition regime for a stationary cylinder, of relevance to many practical applications, and was selected due to the availability of reference data (e.g., [63]).

The incoming flow turbulence characteristics were varied from the baseline case through the use of a bi-planar grid [92, 95]. The grid has a mesh width $M = 35.0$ mm, and a square rod width $d = 4.7$ mm, resulting in a solidity $\sigma \approx 25\%$, well below the maximum recommended solidity of $\sigma \approx 50\%$ in order to achieve homogeneous and isotropic turbulence [156]. Previous studies have shown that nearly homogeneous and isotropic turbulence may be achieved approximately $20M$ downstream of the grid [64, 90, 95]. In the present study, the grid was placed $28M$ upstream of the cylinder in a frame attached to the water flume as seen in figure 3.2. The turbulence characteristics were evaluated through Particle image velocimetry (PIV) measurements (detailed in section 3.2.2). Figure 3.3 presents the power spectral density of the streamwise velocity fluctuations at the cylinder location in an empty test section with and without the grid. A clear increase in energy content across the entire range of frequencies is observed, and the inertial subrange can be identified in the spectrum [144]. The produced flow at the cylinder location has a turbulence intensity $Tu = 2.7\%$ with the longitudinal integral scale $\Lambda_x/D = 0.33$, determined by integrating an exponential curve fit to the spatial auto-correlation function of the fluctuating velocity [183].

It must be noted that, apart from the presented case, two other eFST conditions were studied by moving the grid further upstream and employing another grid with a smaller mesh width. However, both additional cases had lower turbulence intensities and had a similar but less pronounced effect on VIV response. Thus, results are presented only for the largest intensity case ($Tu = 2.7\%$) where the most prominent effects were observed. While investigating the effects of higher intensities on VIV is desirable, the use of a passive grid in conjunction with typical experimental facility restrictions (e.g., size), the desired parameters (e.g., cylinder diameter and freestream velocity), and requirement for homogeneous and isotropic turbulence limit the maximum intensity that can be generated. More details are provided in chapter 4.

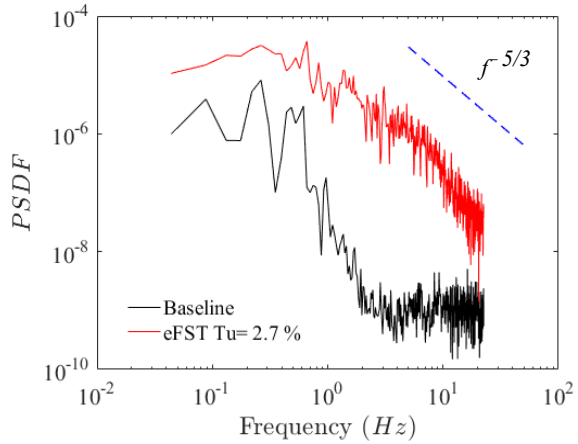

Figure 3.3: Spectra of the streamwise velocity fluctuations at the cylinder location with and without the grid.

3.1.2 LTRAC water tunnel and VIV setup

The open channel, closed-loop water tunnel at LTRAC is show in figure 3.4. Water is introduced into the primary plenum and guided through a sequence of flow conditioning elements comprising a singular honeycomb flow straightener and three fine screens. The flow is then accelerated to the test section by a contraction with a 6:1 ratio. A reservoir located at the terminus of the test section facilitates water recirculation back to the plenum. This process is managed through an axial pump regulated by a variable frequency drive. For optimal optical access, both the walls and floor of the test sections are constructed from glass. The test section spans 4 m in length and features a cross-section of 0.385 m width and 0.45 m height. The water velocity can be varied between approximately 7 and 40 cm/s in increments of 0.07 cm/s. The flow within the test section is uniform to within $0.01U_0$ outside of the wall boundary layers and the baseline freestream turbulence intensity is less than 1% of the mean freestream velocity.

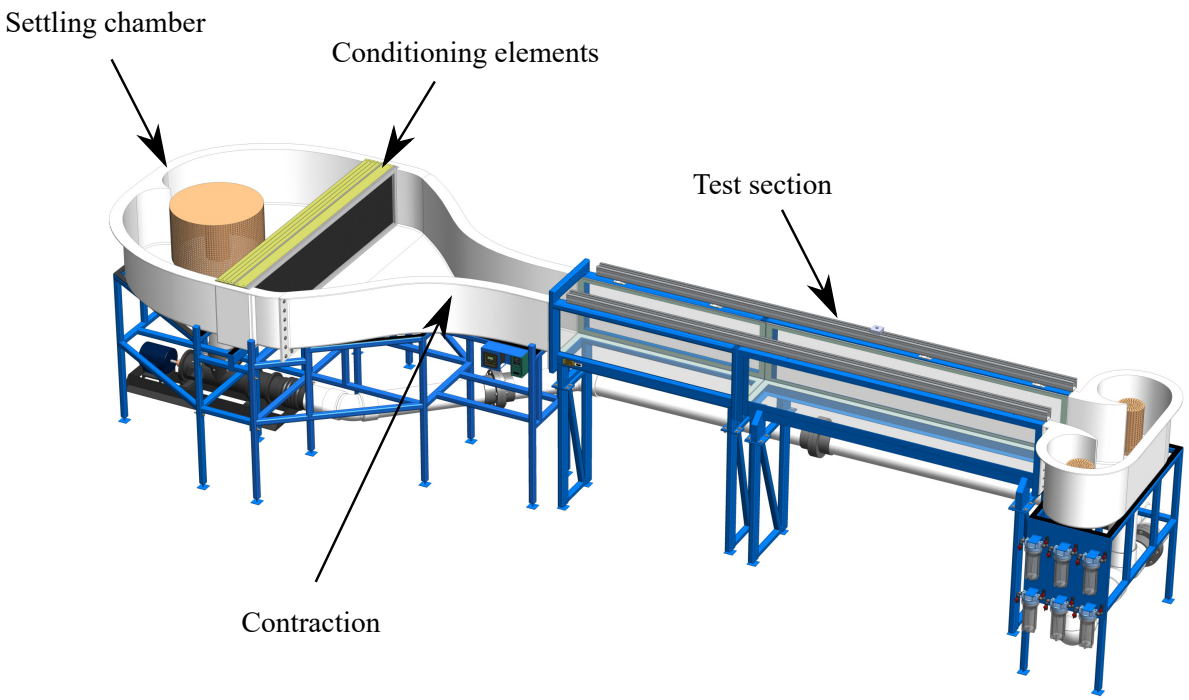

Figure 3.4: Water tunnel facility inside LTRAC at the University of Calgary.

The VIV setup at LTRAC comprised a more traditional spring-mounted, air-bearing apparatus. A 1.905 cm hollow carbon fiber cylinder was mounted onto two OAV 13 mm air bushings, as shown in figure 3.5, to facilitate low friction 1-DOF movement transverse to the freestream. A plate fixed to the ends of the bushings was connected to two identical linear springs with a spring constant 193 N/m. The other ends of the springs were connected to fixed frames such that they were extended when the cylinder was at its equilibrium position. The cylinder was connected to the plate through an ATI Mini40 force transducer (details in section 3.2.4). The natural frequency of the structure in still water, measured through spectral analysis of impulse tests, was 1.7 Hz. The structural damping in air was $\zeta = 0.0013$, as calculated through the log decrement method. The mass ratio of the system was 9.37.

A rectangular end plate spanning the width of the tunnel and with length $23D$ was placed within 2 mm from the tip of the cylinder model. The leading edge of the plate has a super-elliptic profile and was placed $7D$ upstream of the cylinder center. The end plate was mounted approximately 4 cm from the bottom wall to minimize boundary layer effects. Thin rubber inserts were used to seal the gaps between the plate and the water tunnel side walls. The blockage ratio presented by the cylinder was less than 5%. The aspect ratio of the submerged cylinder was held fixed at 21, while the Reynolds number based on cylinder diameter was varied between approximately 2,300 and 6,800.

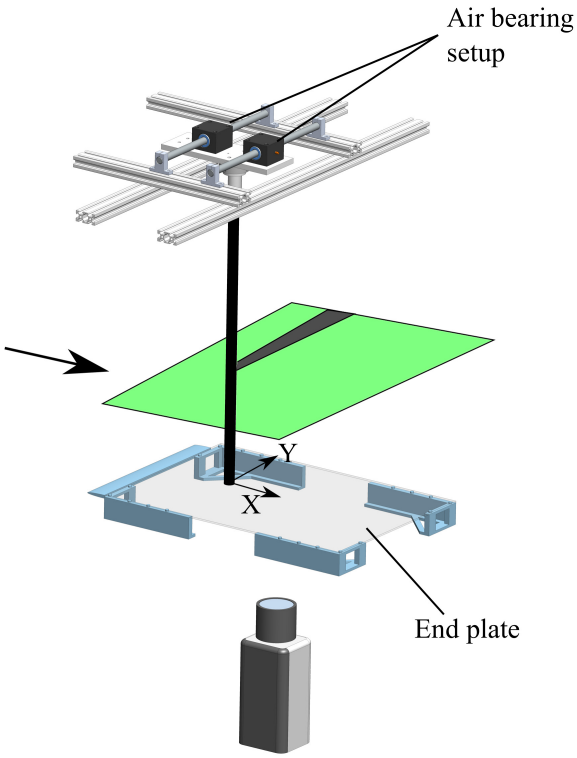

Figure 3.5: Air bearing VIV setup at LTRAC. The camera is shown positioned under the water channel. The green plane indicates the laser sheet with the gray shaded region showing the shadowed regions.

3.2 Data Collection

3.2.1 Particle image velocimetry

Particle image velocimetry (PIV) was the primary flow measurement technique employed in this work. PIV offers the advantage of non-intrusive acquisition of instantaneous velocity field data, thus holding significant appeal. Briefly, PIV involves imaging tracer particles, illuminated by pulsed light sources, to derive velocity vector fields via statistical image processing techniques. Comprehensive insights into PIV techniques and useful recommendations can be found in several works (e.g, [148, 168, 198, 200]). Here, a brief overview of the general procedures employed in this thesis is provided, with experiment-specific details provided in the subsequent sub-sections.

To enable imaging, tracer particles are introduced into the flow. Apart from the requirements of these particles being non-toxic, non-corrosive, non-abrasive, non-volatile, and chemically inert, the particles must conform to the flow without experiencing notable inertial effects.

Compared to gaseous flows[1], PIV experiments in water afford the luxury of a significantly higher-density medium, in which relatively large tracer particles can adequately follow the flow. For all experiments in this thesis, the flow was seeded with hollow glass spheres with a mean particle diameter of 10 μm, and a specific gravity of 1.1. The hollow glass spheres were first thoroughly mixed into a container of water and then added to the water tunnels. Since both water tunnel facilities are closed-loop, minimal decay in the seeding densities was observed throughout each campaign.

To illuminate the tracer particles, laser light is typically employed. All flow field measurements conducted within this thesis constituted measurements of two velocity vector components in a plane, i.e., two-component PIV. Thus, the laser beam was formed into a thin diverging sheet, using a combination of spherical and cylindrical lenses. Imaging was then performed by placing cameras at orthogonal viewing angles to the laser sheet. Calibration was performed by imaging a submerged target comprising a square grid of 10 mm at the laser sheet location and performing a scaling. To minimize reflections, the regions where the laser sheet impacted the cylinder were painted black.

3.2.2 Quasi-steady VIV in eFST (FMRL)

Quasi-steady measurements for both baseline and eFST cases were acquired at 45 reduced velocities (U^*) throughout the synchronization (lock-in) region spaced approximately $\Delta U^* = 0.15$ apart. Prior to measurement at each U^*, the natural frequency of the structure was modified by changing the spring position (see section 3.1.1). Following this, the system was allowed to settle at its quasi-steady state for a sufficiently long time before data acquisition. Cylinder position was measured using a Hoskin CP24MHT80 laser-based displacement sensor secured to a mounting frame at a sampling frequency of 500 Hz, which is more than 50 times greater than the highest natural frequency of the structure considered in the present study. The sensor has a measuring range of 120 mm, equivalent to $4.72D$, a resolution of 20 μm, and a measuring rate of 1500 Hz. The sensors were powered through a 24 V DC power supply. The calibration of the sensors was verified using a Velmex BiSlide traverse. The uncertainty associated with cylinder displacement measurements is estimated to be $\pm$ $0.003D$. For cases where PIV measurements were acquired simultaneously with displacement, analog signals were acquired at a sampling frequency of 100,000 Hz. The oversampled data were then resampled to 500 Hz. At each U^*, data were collected for a total of 120 s enabling the capture of at least 80 cycles of oscillation. In addition to the VIV experiments, flow measurements were acquired for a reference stationary cylinder case. To achieve stationary conditions, the tip of the cylinder was anchored to the end plate at its equilibrium position.

Flow velocity measurements for the VIV experiments, reference stationary cylinder, and eFST characterization were performed using two-component PIV. Wake measurements

[1]Recently, the development of sub-millimetre helium/air-filled soap bubbles have emerged as a viable candidate for relatively large and nearly neutrally buoyant tracer particles in air flows [17, 27, 167].

were performed at a horizontal plane (XY plane) at the midspan of the cylinder, with background flow characterization performed in the same plane without the cylinder in place. The flow was seeded with hollow glass spheres with a mean particle diameter of 10 μm, and specific gravity of 1.1. Illumination was provided by a dual cavity 532 nm Nd:YAG laser (Quantel EverGreen 70), whose light was formed into a sheet with an approximate thickness of 2 mm at the cylinder location. Images for the stationary and vibrating cylinder were acquired using an Imager Pro X CCD camera with a sensor size of 2560 x 2160 px, equipped with a Nikon 50 mm lens and set to an aperture $f_{\#}$= 2.8. The full sensor was used to capture a field of view of approximately 6.7 $\times$ 6.2D. 2,350 particle images were acquired for each case in a dual-frame mode at a frequency of 22 Hz (more than 17 times the highest vortex shedding frequency), with frame separation of 5,500 μs, resulting in average particle displacements of approximately 10 px in the freestream. For background flow measurements, the camera was outfitted with a Nikon 105 mm lens, set to an aperture $f_{\#}$= 5.6, resulting in a full-sensor field of view of approximately 3.3 $\times$ 2.8D. 4,100 images were acquired in single frame mode at a frequency of 45 Hz. For all cases, the laser and camera were synchronized by a programmable timing unit and controlled via LaVision DaVis 10.0 software. The essential parameters used for the different experiments are summarized in table 3.2.

The PIV images were processed using the LaVision DaVis 10.0 software. The images were first preprocessed by minimum subtraction across the entire ensemble, followed by the application of a geometric mask over the cylinder and any shadowed regions. Intensity normalization was then applied across all the images. Following the prepossessing, velocity fields were obtained using a multi-pass cross-correlation algorithm [4], with a final interrogation window size of 48X48 px and 75 % overlap, resulting in a final vector pitch of approximately 0.02D. The results were post-processed using universal outlier detection [199] with vector removal. The measurement uncertainty in instantaneous velocity magnitude due to random errors was estimated using the correlation statistics method [170], and is less than approximately 1.5% and 12% of U_0 in the freestream and wake, respectively.

For the estimation of turbulence intensity from PIV, the methods outlined by Scharnowski et al. [169] and Lavoie et al. [95] were adopted. In particular, the field of view was reduced by approximately 50 % compared to the cylinder cases by employing a 105 mm Nikon lens. This ensured that the field of view was approximately ten times the integral length scale while still ensuring good spatial resolution from the final interrogation window. Specifically, the final vector pitch (0.25 mm/vector) was deemed sufficiently small when compared to the integral length scales. Additionally, large particle displacements between image pairs were ensured (around 100 px) to reduce relative uncertainty, and a larger number of samples were acquired compared to wake measurements to ensure sufficient statistical convergence. The resulting turbulence intensity was estimated to be Tu = 0.9 and 2.7 $\pm$ 0.05%, for the baseline and eFST cases, respectively.

Parameter	eFST characterization	Cylinder	Units
Plane	XY	XY	
Lens focal length	105	50	mm
Lens aperture	2.8	5.6	-
Sensor resolution	1560 X 2560	2160 X 2560	px
Field of view	71 X 85	158 X 172	mm
PIV mode	Single frame	Double frame	-
Sample rate	45	22	Hz
Frame separation	-	5500	μs
Final vector pitch	0.25	0.52	mm/vector
Number of images	4100	2350	-

Table 3.2: Parameters for eFST PIV experiments.

3.2.3 Transient VIV in steady freestream conditions (FMRL)

The transient response of an elastically-mounted cylinder released from rest was investigated at six U^* values spanning the lock-in regime including two U^* values in each of the initial, upper, and lower response branches. A minimum of fifteen release-from-rest trials were conducted for each case. Of these six cases, three U^* (one in each of the initial, upper, and lower branches and highlighted in section 5.1) included simultaneous cylinder position and wake velocity measurements for five of the fifteen trials. After each trial, the structure was brought to rest and allowed to settle for a period of at least 30 shedding cycles before the next trial. Additionally, quasi-steady system response (data recorded after allowing sufficient time for the system to settle) was obtained over the entire lock-in regime using incremental variations in U^*. Cylinder position was measured using a Hoskin CP24MHT80 laser-based displacement sensor. For each case, data were recorded for 120 s. For transient cases, both displacement and flow measurements were started ten seconds prior to the release of the cylinder, and the signals were acquired at a sampling frequency of 100,000 Hz. The oversampled data were then resampled to 500 Hz.

Flow velocity measurements were performed using two-component PIV in a horizontal plane (XY plane) at the midspan of the cylinder. The flow seeding, illumination, image acquisition procedure, and PIV processing procedure were the same as described for the eFST experiments (section 3.2.2), and the essential PIV parameters are summarized in table 3.3.

Parameter	Value	Unit
Plane	XY	
Lens focal length	50	mm
Lens aperture	2.8	-
Sensor resolution	2160 X 2560	px
Field of view	156 X 185	mm
PIV mode	Double frame	-
Sample rate	22	Hz
Frame separation	5500	μs
Final vector pitch	0.7	mm/vector
Number of images	1350 +	-

Table 3.3: Parameters for PIV experiments.

3.2.4 Transient VIV in unsteady freestream conditions (LTRAC)

For the experiments at LTRAC, six cases of changing freestream conditions were considered. These cases were chosen to assess transient system characteristics during the transition between the main response branches. The changes in velocity were achieved through the input of sigmoid ramp signals to the variable frequency drive. This in turn resulted in a similar ramp in freestream velocity. Velocity measurements for the ramp cases were conducted using PIV at the cylinder location in an empty test section. The drive input along with the associated velocity changes are depicted in figure 3.6, where the velocity is averaged over three PIV trials. Overall, the velocity profiles in all cases were seen to follow the imposed frequency changes relatively closely. Small overshoots/undershoots in the velocity profiles are observed in almost all cases near the end of the velocity change and are a result of oscillations introduced by surface waves. However, these oscillations are within 5% of the mean freestream velocity at the end state and do not affect the results or conclusions appreciably. The final ramp profiles were selected after multiple tests focused on minimizing the generation of surface waves following the conclusion of the velocity ramp. The total ramp time was scaled based on the difference between the initial and final quasi-steady state velocities to maintain nearly constant mean freestream accelerations across all cases. This resulted in the total period of the freestream transient varying between approximately 28 and 45 cycles of cylinder oscillation depending on the case. Shortening the ramp time further resulted in notable velocity oscillations following the ramp (greater than approximately 5% of the quasi-steady velocity). Hereafter, the velocity changes described above are referred to as the "fast ramp" cases.

In addition to the fast ramp cases, significantly slower variations in velocity were also considered for all the cases investigated. Specifically, for these "slow ramp" cases, the total period of the freestream transient was between approximately 13 and 20 times longer than the fast ramp cases. Freestream velocity measurements using PIV were not collected for the slow ramp cases since the frequency changes were tracked well by the velocity for the fast ramp cases (figure 3.6), they are expected to match even better for the slow ramp cases.

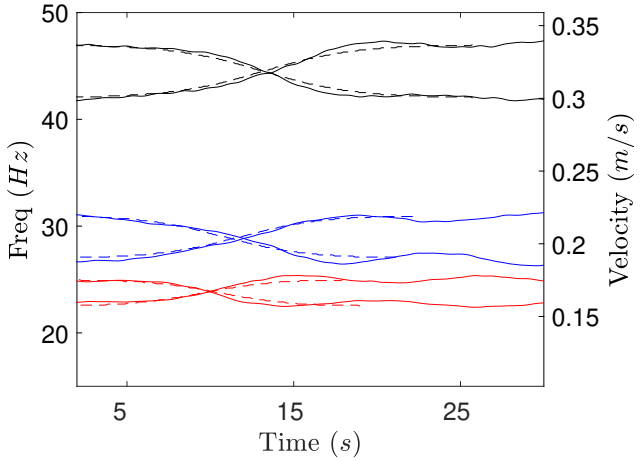

Figure 3.6: Imposed change in variable drive frequency (dashed lines) and the associated change in measured freestream velocity (solid lines) for all six cases considered.

A minimum of twenty repeated trials were conducted for each fast ramp case involving cylinder displacement measurements. These included initial branch (IB) ↔ upper branch (UB), upper branch (UB) ↔ lower branch (LB), and lower branch (LB) ↔ desynchronization (Dsnc). An additional minimum of five trials were acquired simultaneously with PIV, and a minimum of ten trials were conducted for the slow ramp cases without PIV acquisition. Details of the different cases are provided in table 3.4.

Case	# trials (fast,slow)	# PIV trials (fast ramp)	Velocity change (m/s)	Ramp time (fast,slow tf_n)
IB to UB	20,10	5	0.159-0.178	28, 360
UB to IB	40,10	8	0.178-0.159	28, 360
UB to LB	20,10	5	0.191-0.220	37, 646
LB to UB	20,10	5	0.22-0.191	37, 646
LB to Dsnc	20,10	5	0.3-0.335	45, 890
Dsnc to LB	20,10	7	0.35-0.3	45, 890

Table 3.4: Parameters for unsteady freestream experiments.

The cylinder position was measured using a Wengler CP24MHT80 laser-based displacement sensor at a sampling frequency of 1,000 Hz. For cases where particle image velocimetry measurements were acquired simultaneously with displacement, analog signals were acquired at a sampling frequency of 50,000 Hz. The oversampled data were then resampled to 1,000 Hz. Direct force measurements were performed using a 6-axis ATI Mini40 sensor with a resolution of 0.005 N. The fluid forcing was obtained by subtracting the inertial force (inertial mass times the acceleration) associated with the accelerating cylinder and the

mounting apparatus from the force measurements. For all cases, force and position acquisition were acquired 20 s prior to the initiation of the ramp and continued for a total of 180 s.

Flow velocity measurements were performed using two-component PIV in a horizontal plane (XY plane) at the midspan of the cylinder. The flow was seeded with 10 micron hollow glass spheres. Illumination was provided by a Photonics 20 mJ Nd:YLF high repetition rate pulsed laser with a wavelength of 527 nm, whose light was formed into a sheet of approximately 2 mm thickness at the cylinder location. Images were acquired using a Phantom Miro M340 digital camera with sensor resolution 2560 $\times$ 1600 px equipped with a 24 mm Nikon AF Nikkor lens located underneath the water channel (figure 3.5). Images were acquired in dual-frame mode at 30 Hz. The frame separation was varied between 3,000 and 7,000 μs based on the freestream velocity to achieve a pixel displacement of approximately 10 px in the freestream. The sensor was cropped to 1216 $\times$ 1200 px to enable longer acquisition times that can accommodate cases with slower transients (LB $\leftrightarrow$ Dsnc). This resulted in a final field of view of approximately 136 $\times$ 136 mm. At least 2300 images were acquired for each case. The laser and camera were synchronized by a programmable timing unit and controlled through LaVision Davis 10.0 software. Additionally for the PIV cases, position and force measurements were initiated 15 s prior to the start of the PIV acquisition. Further, the ramp started 15 s after the PIV image acquisition was initiated. The processing steps after image acquisition were the same as those used in the previous two experiments (see section 3.2.2) with the final relevant parameters shown in table 3.5.

Parameter	Value	Unit
Plane	XY	
Lens focal length	24	mm
Lens aperture	2.8	-
Sensor resolution	2560 $\times$ 1600	px
Field of view	136 $\times$ 136	mm
PIV mode	Double frame	-
Sample rate	30	Hz
Frame separation	3,000-7,000	μs
Final vector pitch	1.1	mm/vector
Number of images	2300 +	-

Table 3.5: Parameters for PIV experiments.

3.3 Data Analysis Techniques

3.3.1 Proper orthogonal decomposition

Proper orthogonal decomposition (POD), also commonly known as principal component analysis (PCA) among other names [182], is a modal decomposition technique that extracts

modes based on optimizing the mean square of the field variable being examined. POD was introduced to the fluid mechanics community by Lumley [108] as a tool to study coherent structures in turbulent flows with a detailed methodology outlined by Berkooz et al. [22]. POD has since been used extensively in the analysis of bluff body flows (e.g., [127, 141, 153, 189]). The turbulent velocity field in the wake of a bluff body can be decomposed into mean and fluctuating components, where the latter is composed of quasi-periodic coherent motions and residual small-scale turbulence. This triple decomposition can be expressed as [71, 152]:

$$\vec{u}(\vec{X},t) = \overline{\vec{u}(\vec{X})} + \vec{u}'(\vec{X},t) + \vec{u}''(\vec{X},t) \tag{3.2}$$

where the overbar represents an ensemble average, $\vec{u}'(\vec{X},t)$ represent the coherent motions, and $\vec{u}''(\vec{X},t)$ represents the small-scale turbulence. Application of POD to a fluctuating velocity component field will yield an energy-based decomposition into a set of spatial modes $\vec{\phi}_n(\vec{X})$ and temporal coefficients b_n. The velocity field can now be represented as:

$$\vec{u}(\vec{X},t) = \overline{\vec{u}(\vec{X})} + \sum_{n=1}^{N} b_n(t)\vec{\phi}_n(\vec{X}), \tag{3.3}$$

The modes are spatially orthogonal and the temporal coefficients are uncorrelated in time. The spatial modes are obtained as eigenmodes of the velocity autocorrelation matrix, while the eigenvalues represent the contribution of the corresponding mode to the total fluctuating kinetic energy. Consequently, the most dominant modes can be identified by sorting the modes in descending order of their eigenvalues. Further, truncating the POD series (equation 3.3) to the modes that contain a significant portion of the total fluctuating energy enables the construction of a reduced-order model of the flow that includes contributions from only the most dominant coherent structures. For flows dominated by large-scale convective features, such as flow past oscillating and stationary cylinders, the most energetic POD modes are paired [109, 189]. The present study employs the snapshot method of computing POD modes [172].

3.3.2 Time-frequency analysis

For non-stationary signals, time-frequency analysis is essential to capture dynamic signal characteristics and identify frequency transitions and modulations that spectral analysis may overlook. Two common techniques are the short-time fourier transform (STFT) and Wavelets [171]. STFT divides the signal into short segments and computes Fourier transforms for each segment, facing challenges in representing varying frequency content within a single window. In contrast, wavelet analysis uses adaptive windows, providing better temporal localization for transient features compared to STFT. To this end, wavelet analysis is employed in this thesis for time-frequency analysis. For a continuous function $y(t)$, the wavelet transform is given by [104]:

$$W_\psi(t,s) = \frac{1}{\sqrt{s}} \int_{-\infty}^{\infty} \psi^*\left(\frac{\eta - t}{s}\right) y(\eta) d\eta \tag{3.4}$$

where ψ^* is the complex conjugate of the wavelet function and s is the scale parameter. Throughout this work, a Morse wavelet [105] with a symmetry parameter $\gamma = 3$ and time-bandwidth parameter $\beta = 60$ was used. The modulus square of the resulting wavelet transform $|W_\psi(t,s)|^2$ expresses the local energy density of the signal at time t and wavelet scale s.

3.3.3 Numerical force estimation

For experiments conducted at FMRL, instantaneous forcing on the cylinder was estimated through the substitution of known variables into the system equation of motion (equation 2.1). The displacement signal was low-pass filtered to remove high-frequency noise using a cutoff frequency where the spectral energy has decayed to 3 orders of magnitude from its peak value. Following this, the velocity and acceleration terms were calculated through numerical differentiation of the displacement signal using the fourth-order central finite difference scheme for the interior points and first-order schemes at the boundaries. With known structural parameters m, k, and c, the estimation of kinematic variables on the left-hand side of equation 2.1 provides a direct estimate of the forcing term at a given time. While the forcing estimate is sensitive to the uncertainties in the measured variables (see appendix A for uncertainties), the approach was verified to produce reliable estimates based on the comparison against experimental force balance measurements in LTRAC.

3.3.4 Vortex Identification

Coherent structures (vortices) of varying patterns feature prominently in the wakes of cylinders undergoing VIV (section 2.2). Robust identification of vortices enables a more detailed qualitative and quantitative analysis of wake dynamics. Despite the routine occurrence of vortices in a wide variety of fluid mechanics problems, a universal definition of a vortex has not been adopted through the fluid mechanics community [51]. A common challenge in vortex identification stems from the lack of a sharp boundary between the rotational and irrotational regions of a fluid.

A relatively simple vortex identification method is based on vorticity [85, 120, 163]. However, this method fails to distinguish between a rotational region with swirl and a shear-dominated region of the flow [51, 77]. Other more advanced methods that partly address this issue have been developed that employ the velocity gradient tensor to identify vortices. These include the Δ criterion [37, 193], Q criterion [70, 197], λ_{ci} [20, 219] and its extension $\lambda_{cr}/\lambda_{ci}$ [33], among others. In the present study, coherent structures in the wake were identified through an iterative vortex identification routine based on the λ_2 criterion [77], in part due to its relatively simple implementation and widespread use for bluff body wakes (e.g., [42, 57, 178]).

Figure 3.7 demonstrates the application of the iterative procedure to an example flowfield associated with the initial branch of VIV. Each PIV snapshot was spatially averaged using a 4×4 window and contours of λ_2 at an initial threshold λ_{2o} were chosen to identify vortex cores downstream of the cylinder (dotted lines in figure 3.7(a)). Following this, the threshold was iteratively relaxed up to the last continuous contours that completely enclosed contours at λ_{2o} (solid lines in figure 3.7(a)) while any other identified contours were discarded. The last continuous contours appear to reasonably capture the bulk of the negative and positive vortices immediately downstream of the cylinder ($X/D \lessapprox 3$). However, the vortex farther downstream is not identified due to the selection of a relatively aggressive initial threshold. The process was then repeated using a less aggressive starting threshold (λ_{2o}) to identify a more diffused vortex core farther downstream as shown in figure 3.7(b). A constraint on the maximum number of expected vortex cores within the field of view was used to limit the number of iterations of λ_{2o}.

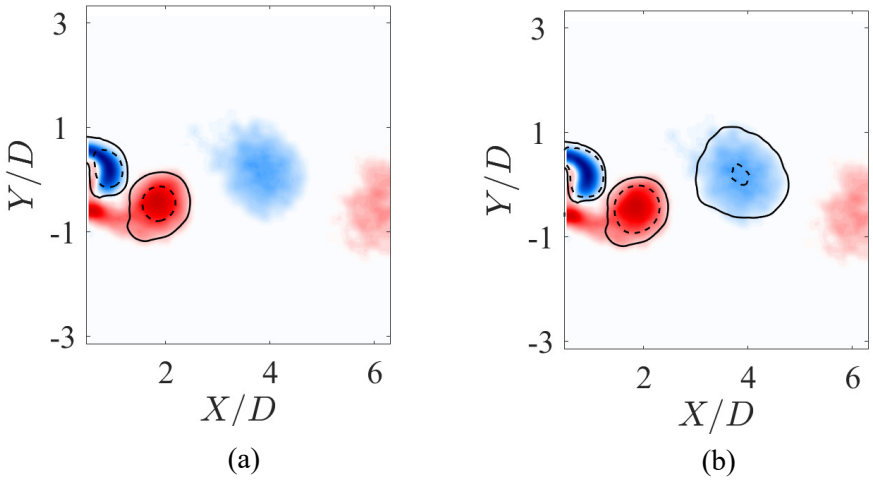

Figure 3.7: Contours of identified vortex boundaries overlaid on contours of spanwise vorticity. (a) Contours using aggressive λ_{2_0} (dotted line) and the associated last continuous contours (solid line), and (b) contours using relaxed λ_{2_0} and associated last continuous contours.

Chapter 4

Freestream turbulence effects on quasi-steady vortex-induced vibrations

The effect of moderate elevation of freestream turbulence intensity from the baseline level is investigated on the quasi-steady response of a low mass-damping VIV system. The most prominent effects of eFST on quasi-steady VIV response are observed towards the end of the lower branch and through desynchronization along with the inter-branch transition regions. Conversely, eFST is found to minimally affect quasi-steady VIV response within the initial and upper response branches. To elucidate this relative robustness of VIV to eFST, comparisons are made between eFST effects on the wake of a stationary cylinder and VIV with very low oscillation amplitudes. The results reveal a distinct change in the separated shear layer characteristics with free vibration that contribute towards the robustness of VIV to eFST.

4.1 Amplitude and frequency response

Figure 4.1 shows the amplitude and frequency response of the cylinder with and without eFST. The amplitude response is characterized by the average of all amplitude peaks in a given time series (A^*_{mean}) with the uncertainty in mean amplitude accommodated by the marker size. The baseline amplitude response (shown in black circles) is typical for systems with comparable mass-damping ratios (e.g., [62], [63]), featuring the initial ($4.0 \lessapprox U^* \lessapprox 5.3$), upper ($5.3 \lessapprox U^* \lessapprox 6.5$), and lower branches ($6.5 \lessapprox U^* \lessapprox 10.0$) of response followed by desynchronization. The identified branch boundaries, range of synchronization, and frequency response characteristics agree well with those reported in literature (e.g., [83], [62]) for similar mass ratios. An example, representing A^*_{max} from [62] is shown in blue open circles in figure 4.1(a) with $m^* = 8.63$ and $\zeta = 0.00151$. A^*_{max} from [62] is expectedly higher than A^*_{mean} from the current experiments in the initial and upper branches due to the higher degree of amplitude modulations in these branches compared to the relatively stable oscillation in the lower branch (see next section). Apart from this, differences in the upper-to-lower branch transition and the U^* corresponding to desynchronization could be a result of the different Re and/or differences in the experimental setups.

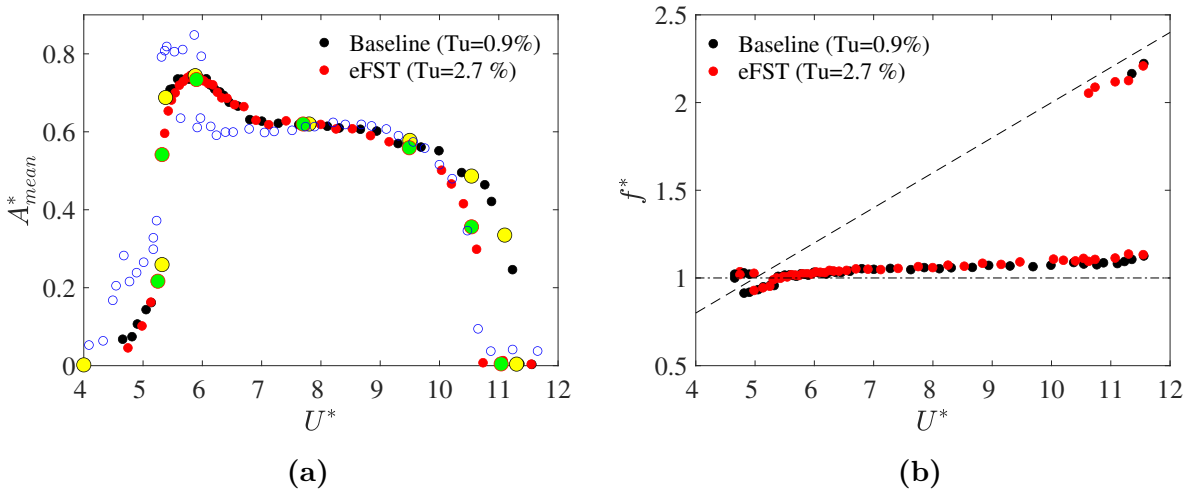

Figure 4.1: (a) Amplitude response of system. Green and yellow circled markers indicate locations where PIV data were collected for the eFST and baseline cases, respectively. Blue open markers correspond to data from [62] for comparison at similar mass-damping. (b) Frequency response of the system. The dashed line represents a Strouhal number of $St = 0.205$.

The results show that the introduction of eFST leads to premature desynchronization of the system. Additionally, differences in baseline and eFST response can be observed around

the transition between the initial and upper branches. However, over the majority of the initial and upper branch, eFST does not significantly modify the system response, where differences in A^*_{mean} between the cases are within the measurement uncertainty. Towards the end of the lower branch, lower mean amplitudes of oscillation are observed in the eFST case beginning at $U^* \approx 8.5$. This difference in amplitudes progressively increases with increasing reduced velocity, eventually resulting in earlier desynchronization for the eFST case. Negligible amplitudes of oscillation are first observed around $U^* \approx 10.7$ in the eFST case, compared to $U^* \approx 11.2$ for the baseline. This is confirmed in the frequency response shown in figure 4.1(b), where a secondary peak is observed close to the Strouhal frequency at lower reduced velocities for the eFST case. Increasing FST also appears to affect the transition between the branches of response. Notably, near the transition between the initial and upper branch ($U^* \approx 5.3$), the distinct increase in amplitudes for the eFST cases is lower (from approximately $0.3D$ to $0.55D$) than the baseline case (from approximately $0.3D$ to $0.65D$) in figure 4.1(a). To explore cycle-to-cycle variations in the structural response, histograms of the peak amplitudes measured over approximately one thousand cycles of oscillation are shown in figure 4.2 for the baseline and eFST case. The insets display a representative time trace of cylinder displacement. The histograms reveal distinct changes in amplitude response characteristics across the different branches. In the initial branch (figure 4.2(a)), a relatively broad histogram is observed. This is attributed to substantial modulations in the cylinder displacement seen in the inset signal trace and also reported in previous studies (e.g., [83]). In the upper branch (figures 4.2(b) and 4.2(c)), the histogram narrows notably; however, intermittent switching between vortex shedding modes [123] contributes to the variance in peak amplitudes, reflected in the inset displacement traces. The histograms pertaining to the lower branch (figures 4.2(d),4.2(e)) feature a relatively narrow peak and the lowest standard deviation across all response branches. This is a consequence of the relatively stable cylinder oscillations seen in the insets and reported in earlier studies for the lower branch (e.g., [62]). System desynchronization (figure 4.2(f)) is characterized by increasing variance in peak amplitudes which are related to the emergence of multiple wake structures as the system transitions from lock-in to a desynchronized wake [132].

The trends observed in the baseline case are also apparent for the eFST case. Similar to the mean system response characteristics, the main effects of freestream turbulence are largely confined to the transition between the initial and upper branch ($U^* \approx 5.3$), where the eFST case displays higher variance, and when the system is desynchronizing ($U^* \approx 10.5$), where the case with eFST exhibits a more complex distribution with higher variance than the baseline case. In contrast, the effect on cycle-to-cycle variations within the main branches of response is marginal. This contrasting behavior is likely related to and reflected in the flow dynamics which is explored in the following section.

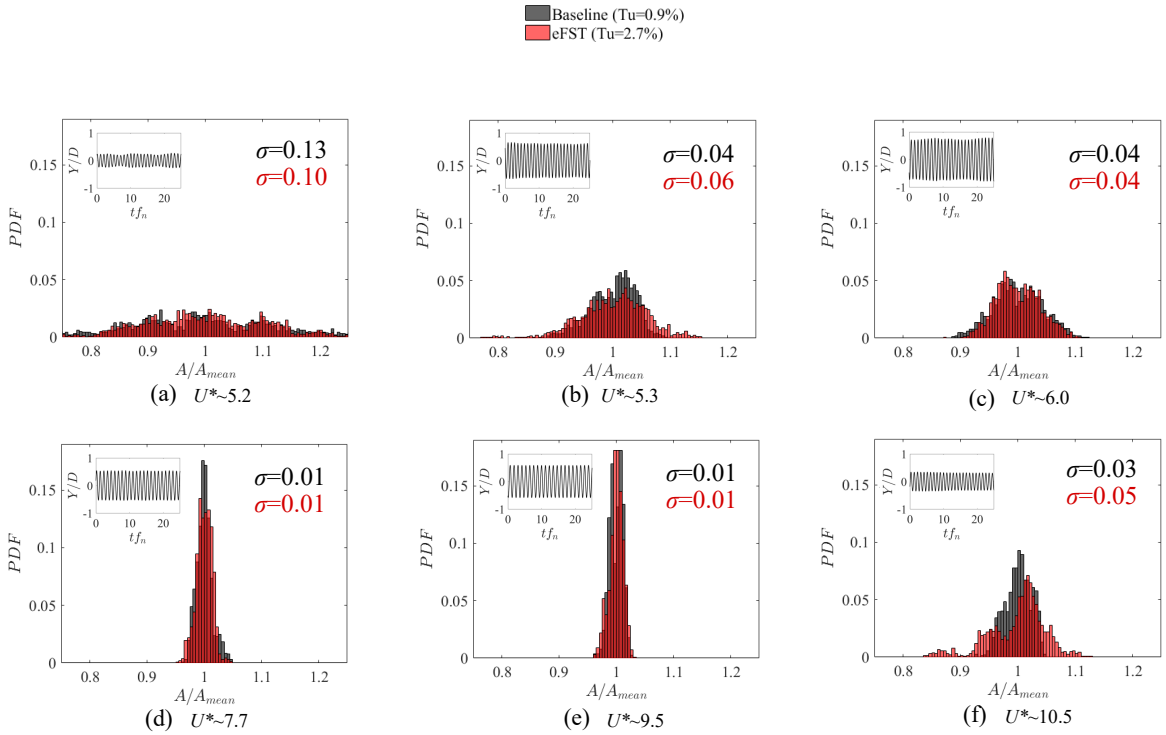

Figure 4.2: Histograms of peak amplitudes across the synchronization region. Insets show typical time traces of response along with the corresponding color coded standard deviation. The peaks are normalized by the mean of all peaks in the dataset.

.

4.2 Mean flow topology and vortex shedding modes

Mean streamwise velocity fields at representative U^* spanning all response regimes along with the corresponding phase averaged spanwise vorticity fields are presented in figure 4.3. Phase averaging was performed based on the cylinder position, and the results are shown for the cylinder positioned at the maximum positive displacement (θ =90°). In the initial branch ($U^* \approx 5.2$, figure 4.3(a)), the expected 2S mode of vortex shedding is observed in the wake, where vortices of opposite sign are shed from each shear layer in an alternating fashion [62]. The mean flow features a symmetric recirculation region immediately downstream of the cylinder base (marked by deep blue contours) where a significant wake velocity deficit is observed. In the initial branch, the introduction of eFST has minimal effect on both the vortex shedding characteristics and the mean flow topology.

In the upper branch ($U^* \approx 6.0$, figure 4.3(b)), $2P_0$ shedding is observed [123], with two vortices, one primary, and one weaker counter-rotating secondary vortex, shed in each half cycle. The change in the shedding mode is also accompanied by a 180° phase shift in shedding compared to the initial branch, consistent with previous observations (e.g., [62]). The increase of the oscillation amplitude in this response branch leads to the formation of

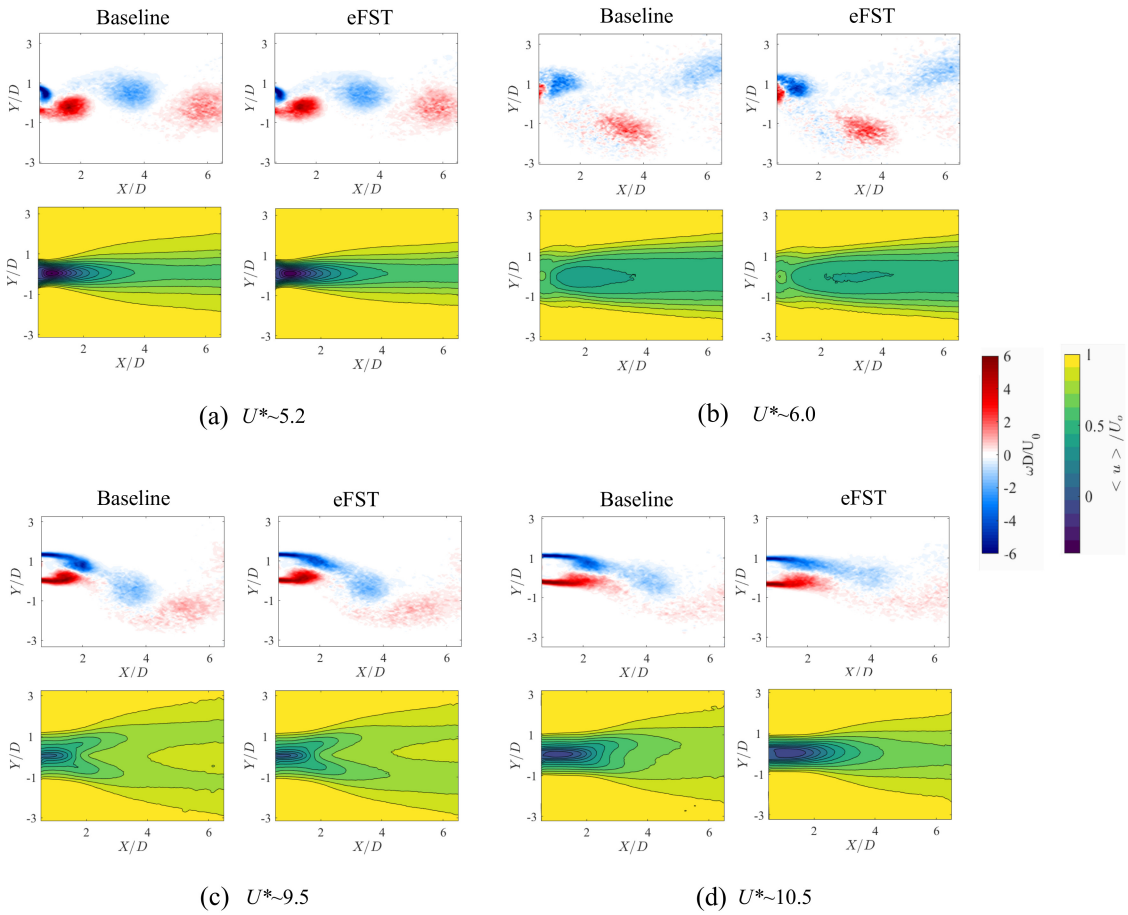

Figure 4.3: Mean streamwise velocity and phase averaged spanwise vorticity contours.

a wider wake compared to that seen for the initial branch. However, the local wake velocity deficit is lower on average, and no reverse flow is observed downstream of the cylinder. When eFST is introduced, the mean flow topology and vortex shedding mode remain relatively unchanged, however, the phase averaged vorticity contours indicate the shedding of stronger primary vortices. This is particularly evident for the negative vortex about to be shed from the cylinder (compare vortices at approximately $X/D \approx 1.5$ in figure 4.3(b)).

In the lower branch ($U^* \approx 9.5$, figure 4.3(c)), a pair of counter-rotating vortices of roughly equal strength is shed in each half cycle, characteristic of the expected 2P shedding [62]. It should be noted that $U^* \approx 9.5$, while still representative of the lower branch, is situated towards the end of the lower branch and close to the transition to desynchronization. The change in the vortex shedding mode from $2P_0$ to 2P produces a distinct dual-lobe topology in the mean wake contours for the lower branch, characterized by an increase in the maximum velocity deficit in this region compared to the upper branch. Similar to other branches of response, increasing eFST does not alter the wake topology significantly in the lower branch. However, a subtle difference is noticeable in the separation process

between the two like-signed vortices. In the baseline case (figure 4.3(c)), the two negative vortices are separated more distinctly, with minimal vorticity present between the two cores, whereas the separation between the like-signed vortices in the eFST case is not readily apparent. Additionally, the upstream negative vortex in the eFST case is more elongated compared to the baseline case, where the roll-up of the vortex is more apparent. These differences in the vortex shedding characteristics are found to be particularly important as the system desynchronizes, and are discussed further in section 4.4.

As the system desynchronizes ($U^* \approx 10.5$, figure 4.3(d)), and the oscillation amplitudes decrease markedly, 2P shedding is gradually replaced by 2S shedding [132]. Wake desynchronization from the cylinder oscillation results in a phase averaged field that approaches time averaged statistics, with vorticity concentrated primarily in the shear layers. The mean wake velocity increasingly resembles that of the initial branch, with a notable increase in maximum velocity deficit and the reappearance of a prominent recirculation region. The changes to the phase averaged vorticity and mean velocity fields are more apparent with the introduction of eFST, as expected from the structural response. The baseline case at $U^* \approx 10.5$ (figure 4.3(d)) is at an early stage of desynchronization and resembles the eFST case from figure 4.3(c), characterized by the less apparent separation between like-signed vortices, and more elongated vortex shapes.

As expected from the structural response results, the main effect of eFST on wake development is seen in the onset of and progression to desynchronization. The sensitivity of the initial-upper branch transition to eFST may be ascribed to the sensitivity of associated vortex shedding mode changes to variations in test conditions, including FST. However, the overall robustness of wake development to changes in free stream turbulence is strikingly different from the significant effect of eFST on stationary cylinder wakes at similar Re [82]. This is explored in the following section, followed by a more detailed examination of the desynchronization region.

4.3 Wake reorganization with small-amplitude cylinder vibrations

To explore the general robustness of VIV wake development to eFST, it is instructive to examine in more detail the effect of eFST on stationary cylinder wakes at similar Re, where previous literature has reported significant modifications to the wake (e.g., [82]). The flow dynamics associated with freely vibrating cylinders in the initial branch and when the system is desynchronized are similar to the flow across stationary cylinders in that the vortex shedding modes are 2S, and the mean flow topology in all cases features a recirculation zone bounded by separated shear layers and a topological saddle point. These similarities allow for a comparison of the contrasting effects of eFST on stationary and vibrating cylinder wakes.

To this end, two VIV cases were chosen: $U^* \approx 4.0$, $f_n \approx 1.45\ Hz$ (Initial branch), and $U^* \approx 11.2$, $f_n \approx 0.54\ Hz$ (Desynchronized). Both reduced velocities are characterized by very small mean oscillation amplitudes ($\approx 0.01D$) with a relatively large separation between the associated natural frequencies. The wakes in the VIV cases are compared to the stationary cylinder wake, achieved by anchoring the tip of the cylinder model to the end plate.

Figure 4.4 displays contours of the mean streamwise velocity for the selected cases with and without eFST. The bottom row depicts the differential wake (eFST-baseline) to better illustrate the differences between each case. Figure 4.5 highlights the variation of key statistics (4.5(a): mean streamwise velocity, 4.5(b) rms streamwise velocity fluctuations $u_{rms} = \sqrt{\overline{u'^2}}$, and 4.5(c) rms transverse velocity fluctuations $v_{rms} = \sqrt{\overline{v'^2}}$) along the wake centerline. The measured wake statistics for the baseline stationary cylinder case fall within the scatter reported in previous studies at similar Re [46, 89, 107, 138]. The variance between individual studies is typically ascribed to differences in the Reynolds number, aspect ratio, and/or blockage effects [129, 131, 181]. For the stationary cylinder, increasing FST leads to a marked decrease in the streamwise extent of the recirculation region. Specifically, the wake closure point, defined as the point where zero mean velocity is attained along the wake centerline, moves upstream from $2.18D$ for the baseline case to $1.35D$ when eFST is introduced. Accompanying this wake contraction is a notable increase ($\approx 18\%$) in the magnitude of v_{rms} directly downstream of the cylinder, along with an upstream shift in the location of peak v_{rms} and u_{rms}, in line with previous observations (e.g., [130]).

For VIV at $U^* \approx 4.0$, eFST marginally affects the near wake, involving minimal changes to the wake closure point, as well as minimal modification to both location and magnitude of peak v_{rms} and u_{rms}. At $U^* \approx 11.2$, eFST induces a more notable upstream movement of the wake closure point from 2.49 D to 2.16 D. Although the peak rms magnitudes are not changed appreciably with eFST, contrary to $U^* \approx 4.0$ case, their locations move upstream, indicating an upstream movement of the vortex formation region. However, this effect is less prominent than in the stationary cylinder case.

Significant quantitative differences between eFST and baseline cases can be extracted from figure 4.5. Specifically, differences can be observed in the location and magnitude of the minimum streamwise velocity along the wake centerline (u_{min}) seen in figure 4.5(a). For the stationary cylinder u_{min} = -0.28U_0 at X/D = 1.66, while u_{min} = -0.21U_0 at X/D = 1.51 for $U^* \approx 4.0$, and u_{min} = -0.29U_0 at X/D = 1.82 and for $U^* \approx 11.2$. Thus, it is evident that free vibration of the cylinder at both reduced velocities ($U^* \approx 4.0$ and 11.2) results in unique mean wake characteristics irrespective of the FST level. The observed differences in baseline mean wake characteristics are expected to be related to changes in vortex shedding between the cases, which is explored further for the baseline cases.

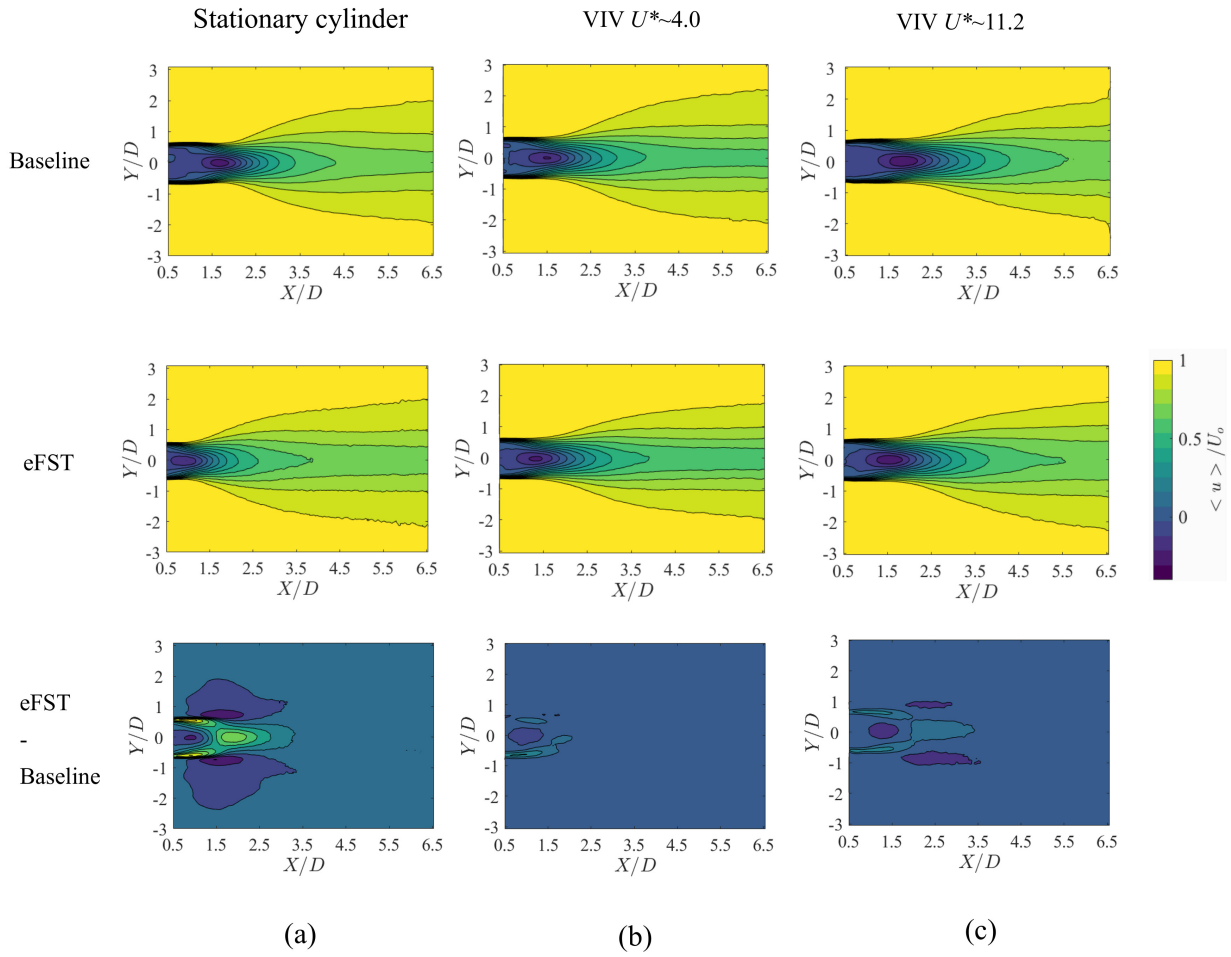

Figure 4.4: Effect of eFST on the mean streamwise velocity for (a) stationary cylinder, (b) low-amplitude cylinder vibration at $U^* \approx 4.0$, and (c) low-amplitude cylinder vibration at $U^* \approx 11.2$. Bottom row depicts the differential wake (eFST-baseline) to better illustrate the changes.

Spectral analysis of the transverse velocity component along the wake centerline at the location of peak v_{rms} for all the baseline cases are presented in figure 4.6(a). Compared to the expected Strouhal shedding (St_{vs}) for the stationary cylinder, the VIV cases exhibit a distinct reduction ($\approx 8\%$ with a more broadband distribution at $U^* \approx 11.2$) in the dominant wake Strouhal number (marked by the red dashed lines in figure 4.6(a)). This is also reflected in the structural response spectra shown in figures 4.6(b) and 4.6(c) for baseline cases at $U^* \approx 4.0$ and 11.2, respectively. Both cases reveal two dominant frequencies in the structural response–one close to the structure's natural frequency (black dashed line marked St_n), and one centered around the modified vortex shedding frequency (red dashed line). The reduction in dominant wake frequencies that is also reflected in the structural response points to a coupled fluid-structure response, even at very low oscillation amplitudes and two distinct natural frequencies. The introduction of eFST is seen to minimally affect the

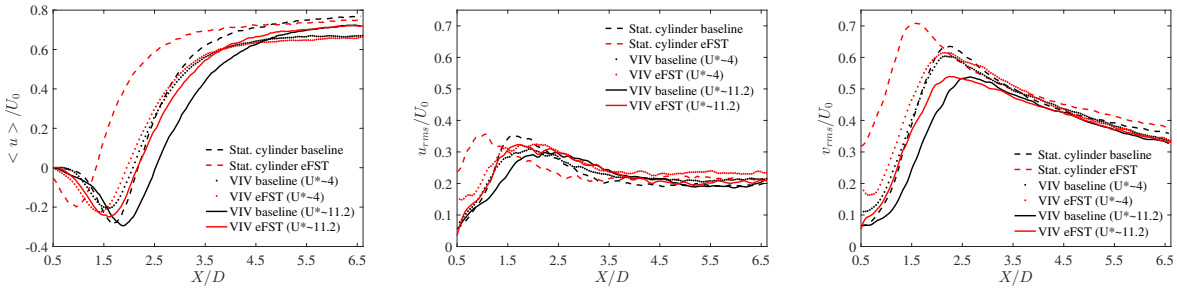

(a) **(b)** **(c)**

Figure 4.5: Velocity statistics along wake centerline (a)Mean streamwise velocity, (b) rms streamwise velocity fluctuations, and (c) rms transverse velocity fluctuations.

dominant frequencies for all tested cases and is not shown here for brevity.

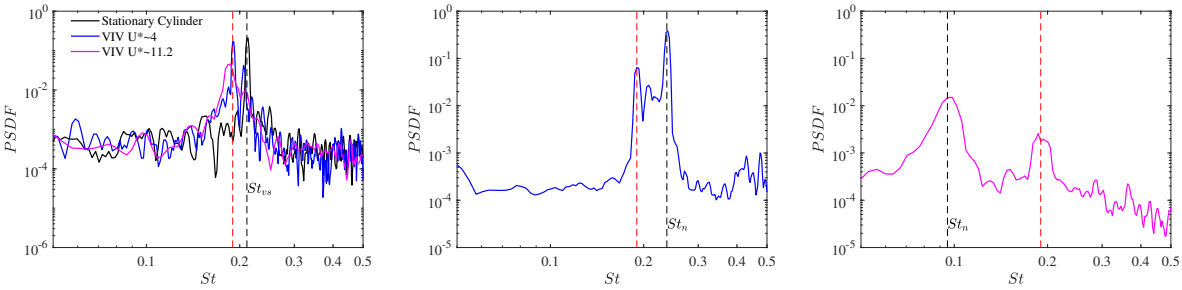

(a) **(b)** **(c)**

Figure 4.6: (a) PSDF of transverse velocity along wake centerline for baseline cases. (b) Spectra of cylinder displacement at $U^* \approx 4.0$ (c) Spectra of cylinder displacement at $U^* \approx 11.2$. Red dotted lines indicate the modified vortex shedding frequency.

The fluid-structure coupling evidenced through common dominant frequencies in wake and structure response (figure 4.6), and associated distinct baseline wake characteristics at $U^* \approx 4.0$ and 11.2 (figure 4.5) is speculated to contribute to the robustness of VIV cases to eFST when compared to stationary cylinder wakes. For stationary cylinders, the observed drastic changes with the introduction of eFST are related to the effect of external perturbations on the separated shear layers. In particular, eFST promotes the breakdown of coherent structures in shear layers thereby resulting in premature laminar-to-turbulent transition [82] that further precipitates the contraction of the wake (figure 4.4(a)). The transition to turbulence in the shear layers partly contributes to increased Reynolds stresses along the shear layers [46] and this is explored further for the selected cases.

Figure 4.7 displays contours of Reynolds shear stress in the wakes of the stationary and vibrating cylinders with and without eFST. The results for all baseline cases feature distinct

"lobes" that do not extend up to the cylinder and are antisymmetric with respect to the wake centerline. For the baseline stationary cylinder, the notable initial Reynolds stress levels in the shear layers are attributed to the shear layer instability and transition expected at the investigated Reynolds number, as well as shear layer flapping due to vortex roll-up [46]. When eFST is introduced, aside from the wake contraction and increase in fluctuating velocity magnitudes previously observed (figure 4.5), there is a marked increase ($\approx 35\%$) in Reynolds shear stress along the shear layers, with the lobes now extending farther upstream towards the cylinder. This increase may result from a combination of earlier shear layer transition [82], and more vigorous shear layer flapping [140] due to roll-up moving closer to the cylinder base. Conversely, for both VIV cases, eFST does not induce appreciable changes in the magnitudes of Reynolds shear stress along the shear layers. Thus, while stationary cylinder shear layers at the current $\boldsymbol{Re}$ are highly sensitive to external perturbations, the fluid-structure coupling in the VIV cases appears to desensitize the shear layers to elevated free-stream perturbations, thereby contributing to the general robustness of the flow development and structural response to eFST.

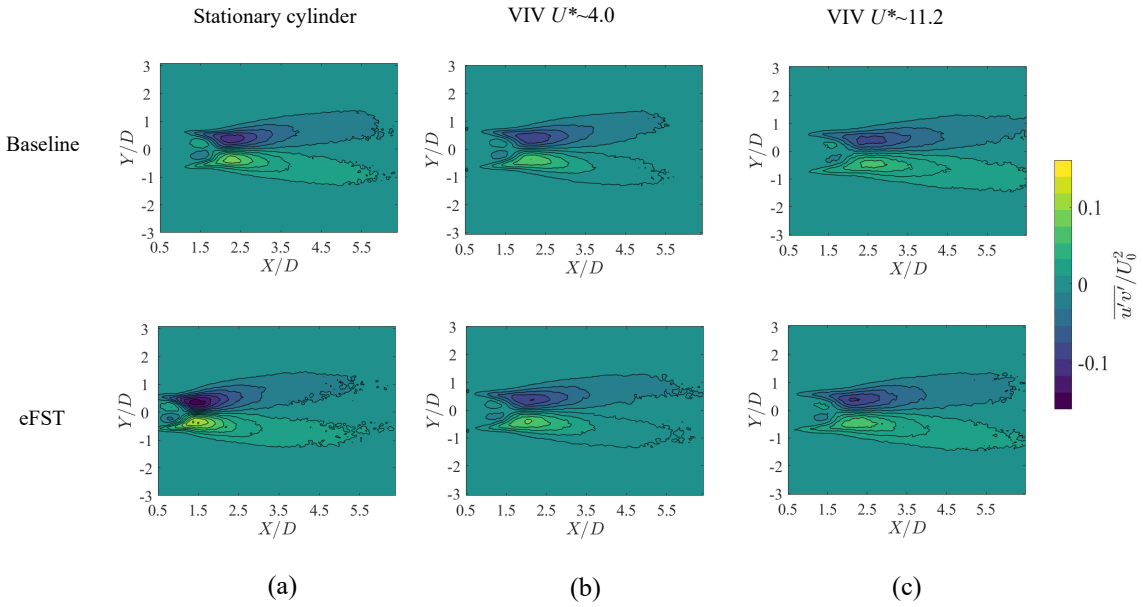

Figure 4.7: Reynolds shear stress in the wake for (a) stationary cylinder, (b) low-amplitude cylinder vibration at $U^* \approx 4.0$, and (c) low-amplitude cylinder vibration at $U^* \approx 11.2$.

4.4 Desynchronization analysis

This section explores the evolution of the coherent structures in the wake leading to and during desynchronization. Snapshot proper orthogonal decomposition (POD) [172] is employed here for this purpose. Figure 4.8 displays the first and third streamwise POD

spatial modes (ϕ_1^u, ϕ_3^u) for the baseline and eFST cases through the transition from the end of the lower branch ($U^* \approx 9.5$) and into desynchronization ($U^* \approx 11.0$ for baseline and $U^* \approx 10.5$ for eFST). Given that POD modes are found to exist in pairs for large-scale convective-dominated flows such as the present cases [109], the first and third modes here are representative of the first two mode pairs. The third column in both cases corresponds to different reduced velocities that produce comparable amplitude response for the baseline and eFST cases in desynchronization.

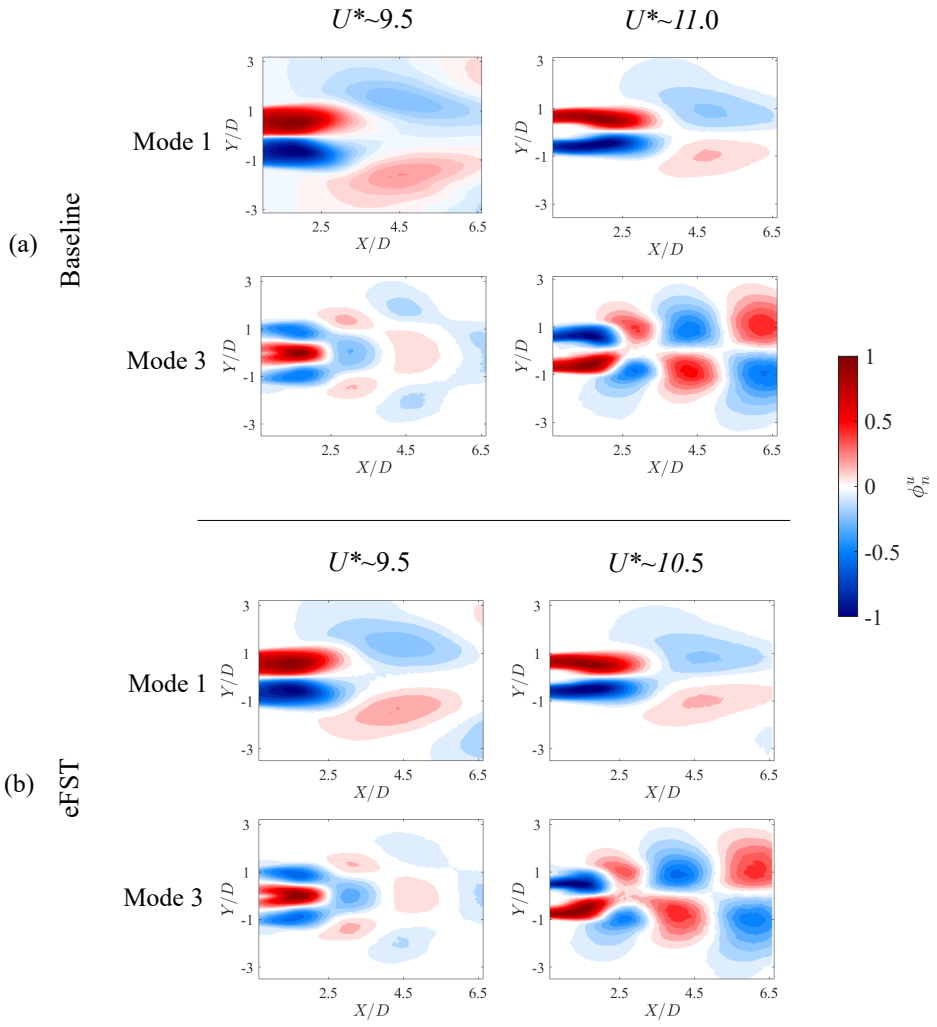

Figure 4.8: POD streamwise spatial mode contours of the first and third mode for (a) baseline and (b) eFST cases.

.

At $U^* \approx 9.5$, both baseline and eFST cases exhibit similar spatial mode structures for both first and third modes, characteristic of the expected 2P shedding [155] in the lower branch. As the cylinder undergoes desynchronization, both baseline ($U^* \approx 11.0$) and eFST

($U^* \approx 10.5$) cases exhibit a distinct third mode. The structure of the third mode resembles the first mode pair found in the initial branch, where 2S shedding is observed [153]. This 2S mode becomes the dominant mode for both baseline and eFST cases with an increase in reduced velocity [155] (not shown here for brevity), highlighting the transition from 2P lock-in to 2S desynchronized wake. The existence of nearly identical mode structures as the wake transitions from 2P to 2S affirms similarities in the desynchronization process between baseline and eFST cases. However, despite similarities in the structure of the spatial modes, some differences were identified in their relative energy contributions, particularly in cases where the 2P mode of shedding is dominant. Figure 4.9 shows the relative energy contribution of the six most energetic modes for both baseline and eFST cases at $U^* \approx 9.5$. The introduction of eFST results in a distinct redistribution of relative energy between the mode pairs. In all cases, the relative contribution of the first mode pair is higher with eFST, while the relative contribution of the subsequent two mode pairs decreases. This redistribution likely reflects a modification of the 2P vortex shedding process since other potential influencing parameters such as amplitude and frequency response at $U^* \approx 9.5$ are nearly identical between baseline and eFST cases.

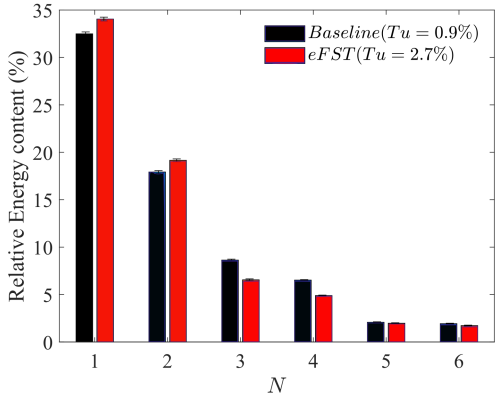

Figure 4.9: Relative energy of first six POD modes associated with 2P shedding near the onset of desynchronization at $U^* \approx 9.5$.

A low order model (LOM) of the wake is employed here to illustrate the differences in wake development between baseline and eFST cases associated with the relative energy distributions seen in figure 4.9. The LOM utilizes the six most energetic modes ($N = 6$ in equation 3.3), consistent with previous investigations where a minimum of six modes were required to reconstruct the 2P shedding phenomenon [69]. Figure 4.10 compares the phase averaged spanwise vorticity reconstruction of the wake using the LOM for baseline and eFST cases at $U^* \approx 9.5$. A notable difference is observed in the like-signed vortex separation between the two cases. In particular, the baseline case is characterized by an apparent separation between the two negative vortex cores and a defined roll-up of the upstream vortex. Conversely, the like-signed vortex separation and upstream vortex roll-up in the

eFST case are less prominent. Additionally, differences in the shape of the two positive vortices are also apparent between the two cases, with the eFST case exhibiting more elongated shapes. The differences in like-signed vortex separation were first observed in the original phase averaged vorticity fields (figure 4.3), and are featured more prominently in the LOM reconstruction. Overall, the LOM reconstructions show clear differences in the vortex roll-up and like-signed vortex separation process between baseline and eFST cases that are associated with the modal energy redistribution seen in figure 4.9.

The changes to the vortex roll-up and separation process seem to be reflective of the system transitioning from the lower branch to desynchronization, involving the change from 2P lock-in to 2S desynchronized state. Similar behavior is also observed for the baseline case at higher reduced velocities. As seen in the phase averaged images from figure 4.3, the baseline case also exhibits a less apparent like-signed vortex separation and vortex roll-up between figures 4.3(c) and (d). The introduction of eFST advances this process, thereby promoting earlier desynchronization.

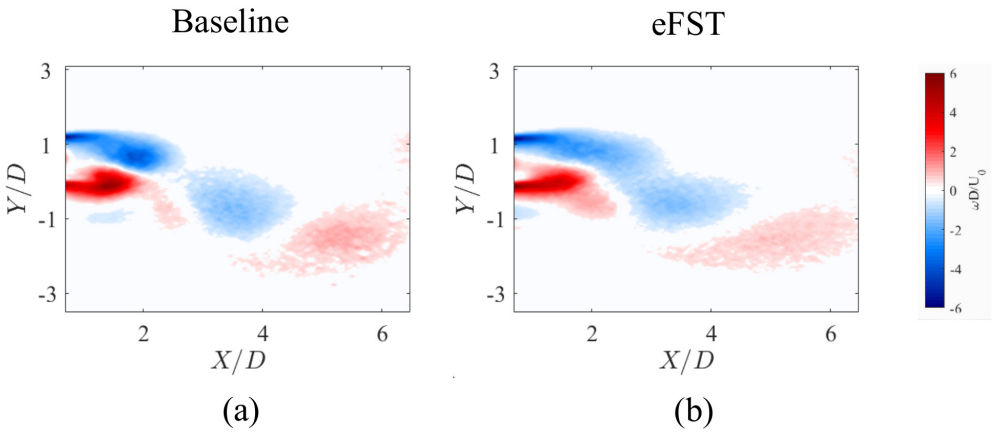

Figure 4.10: Phase-averaged spanwise vorticity with the cylinder at maximum positive amplitude for (a) baseline and (b) eFST cases using a LOM of six modes at $U^* \approx 9.5$.

4.5 Concluding remarks

The present study examined the influence of eFST on the response characteristics of VIV through simultaneous displacement and flow field measurements. A 1-DOF system with low mass-damping ($0.0084 < m^*\zeta < 0.0145$) was considered for a range of reduced velocities ($3.9 < U^* < 12.7$) at a constant Reynolds number of approximately 4400. Freestream turbulence (eFST) was generated using a biplanar grid of square cross sections that increased the turbulence intensity from $Tu = 0.9\%$ to $Tu = 2.7\%$ at the cylinder location. In addition, a reference case of a stationary cylinder was considered at the same Reynolds number and

the two levels of free-stream turbulence.

The results show that eFST at the tested intensity and Re predominantly modifies the response at larger reduced velocities, particularly inducing earlier desynchronization. In contrast, eFST is found to minimally affect mean and dynamic VIV response within the main branches of synchronization with the exception of the inter-branch transitions. Consequently, the main effect on the flow development is also confined to the earlier onset of desynchronization induced by eFST.

The contrasting robustness of VIV and sensitivity of a stationary cylinder wakes to eFST has been explored by considering stationary cylinder flow and VIV with minor amplitudes ($\approx 1\%$ of cylinder diameter at $U^* \approx 4$, 11.2). The results show drastic changes to the near wake of the stationary cylinder with eFST, notably resulting in a contraction of the near wake, while the wakes in the VIV cases were minimally affected. For stationary cylinders, the changes to the near wake are associated with the earlier transition of the shear layers with the introduction of eFST. Conversely, for freely vibrating cylinders, the fluid-structure coupling apparently desensitizes the shear layers to elevated freestream turbulence, thus contributing to the robustness of the limit cycle oscillations.

Proper orthogonal decomposition was employed to explore the wake structures through the end of the lower branch and into desynchronization for both baseline and eFST cases. The results show similarities between baseline and eFST cases in the spatial structure of the POD modes through desynchronization, but notable differences in the associated relative energy content, particularly when the wake is dominated by 2P shedding. The impact of the relative energy modification on the wake structure was investigated by creating a low order model (LOM) of the wake using the six most energetic POD modes. The LOM showed differences between baseline and eFST cases in the vortex roll-up and like signed vorticity separation that is characteristic of the 2P mode. In particular, the presence of eFST results in less apparent vortex separation and less distinct vortex roll-ups. Similar behavior is also observed for the baseline case at higher reduced velocities, thus indicating that eFST primarily promotes premature desynchronization while minimally modifying the underlying physical processes.

The relative robustness of VIV to the moderate level of eFST tested in the present work agrees with the work of Goswami et. al. [61] who also explored VIV in moderate eFST conditions and at similar Re. The present work links the change in shear layer behavior with cylinder oscillations that to the robustness of VIV to eFST. The present results indicate that VIV at low mass-damping remain relatively unaffected by eFST at Re that correspond to the earlier stages of the shear layer transition regime for stationary cylinders. Significant changes are expected at larger Re and more intense turbulence where boundary layer transition takes place. This is supported by the results from Pasto [139] who observed a decrease in oscillation amplitudes for Re near the end of the shear layer transition regime and at higher turbulence intensities.

Chapter 5

Transient vortex-induced vibrations of a cylinder released from rest in a steady freestream

The VIV setup at FMRL is modified to enable a release from rest into a steady freestream at various reduced velocities spanning the different response branches. The results show distinct responses across the response branches including an amplitude overshoot in the initial branch and a continuous increase in amplitudes in the upper and lower branches. Analysis of the forcing signals is used to identify the onset of nonlinear lock-in behavior characteristic of VIV following cylinder release. Additionally, differences in the transient amplitude growth rates are found across the response branches, with these differences being linked to the forcing characteristics on the cylinder. Quantitative analysis of the wake is used to relate the changes in forcing characteristics with the timing of vortex shedding along with identification of the changing wake topologies during the transients.

5.1 Quasi-steady state system characteristics

The quasi-steady system amplitude response (A^*_{mean}), frequency response (f^*), and mean vortex force phase difference (ϕ_v) are presented in figures 5.1(a-c), respectively. The amplitude response features the initial branch (IB, $4.0 \lessapprox U^* \lessapprox 5.3$), upper branch (UB, $5.3 \lessapprox U^* \lessapprox 6.5$), lower branch (LB, $6.5 \lessapprox U^* \lessapprox 10.5$), and desynchronization regimes ($U^* \gtrapprox 10.5$) expected for a low-mass damping system [83]. Dashed vertical lines roughly delineate the boundaries between the branches. The amplitude response (figure 5.1(a)) in the initial branch is characterized by relatively low amplitudes of oscillation ($0.08 \lessapprox A^*_{mean} \lessapprox 0.25$). The frequency response (figure 5.1(b)) reveals two dominant frequencies near the von Kármán shedding frequency (sloped dashed line) and the structure's natural frequency for $U^* \lessapprox 4.8$. This early initial branch is referred to as the quasi-periodic regime [83] and is not of significant interest in the present work. A single lock-in frequency lower than the structure's natural frequency ($f^* < 1$) is attained towards the end of the initial branch (figure 5.1(b)). The vortex force phase difference (figure 5.1(c)) following lock-in to a single frequency is positive and close to 0°. The upper branch is characterized by the largest oscillation amplitudes ($0.68 \lessapprox A^*_{mean} \lessapprox 0.73$). The nondimensional oscillation frequency is slightly greater than one, and ϕ_v settles close to 180°. As expected, oscillation amplitudes in the lower branch ($0.5 \lessapprox A^*_{mean} \lessapprox 0.62$) are smaller than those in the upper branch. Here, the nondimensional frequency and vortex force phase difference remain greater than one and close to 180°, respectively. Increasing the reduced velocity beyond $U^* \approx 10.5$ brings the system to the desynchronization regime, where a dual frequency response (around the natural and von Kármán shedding frequencies) reappears. The amplitudes of oscillation are reduced substantially in this regime. The identified branch boundaries, oscillation amplitudes, and frequency/phase response characteristics agree well with those reported in literature, for example, [62] and [83] for similar mass-damping ratios.

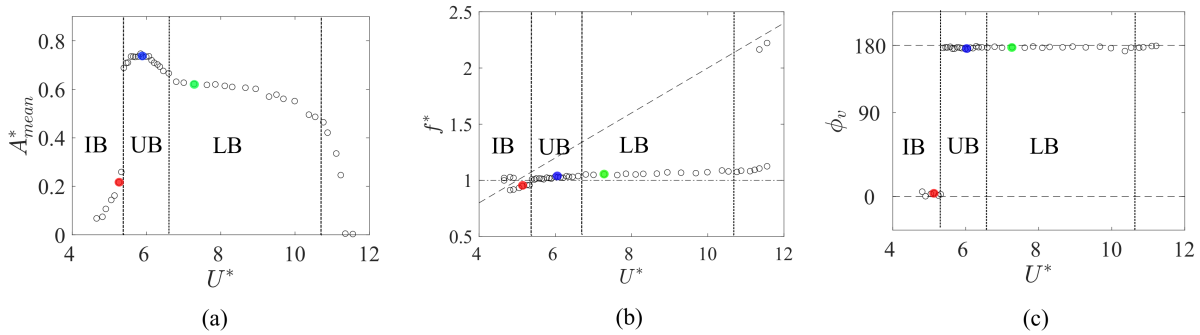

Figure 5.1: Quasi-steady state system characteristics. (a) Mean amplitude response calculated as the mean of all peaks in a time series, (b) frequency response calculated using spectral analysis of the displacement signal, and (c) mean vortex force phase difference obtained through the application of the Hilbert transform [83]. The uncertainty in all quantities is accommodated by the marker sizes. The red, green, and blue markers indicate U^* which are analyzed in further detail using both PIV measurements and detailed force analysis.

The quasi-steady state wake topology varies significantly across the response branches, as depicted by phase-averaged spanwise vorticity contours presented in figures 5.2(a-c) for the initial ($U^* \approx 5.2$), upper ($U^* \approx 6.0$), and lower ($U^* \approx 7.2$) branches, respectively. For phase averaging, the cylinder position was used as the reference signal, with 0° corresponding to the instant when the cylinder crosses its equilibrium position and is moving in the positive Y direction. The velocity fields were segregated into 15° bins for averaging, with each bin comprising approximately eighty individual snapshots. For each case in figure 5.2, the cylinder is located at the top dead center of oscillation The initial branch flow field (figure 5.2(a)) features the expected 2S mode [62] characterized by the alternate shedding of oppositely-signed vortices. In the upper branch, (figure 5.2(b)) the wake topology resembles that of the $2P_0$ mode [62], however, the weaker secondary vortex is not clearly identifiable in the phase-averaged vorticity contours. The characteristic jump in ϕ_v accompanying the initial-upper branch transition (figure 5.1(c)) is reflected in a nearly 180° change in the phase of vortex shedding in figure 5.2(b) compared to figure 5.2(a). In the lower branch (figure 5.2(c)), the 2P mode [62] is identified by pairs of counter-rotating vortices of roughly equal strength being shed at each half-cycle [123].

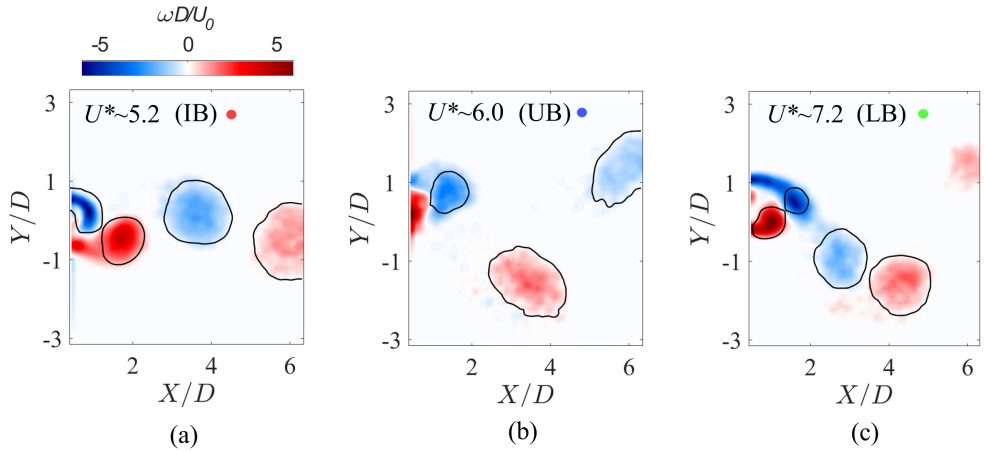

Figure 5.2: Phase-averaged spanwise vorticity contours at locations marked by the colored symbols (figure 5.1 in the (a) initial, (b) upper, and (c) lower branches, respectively. The cylinder is at top dead center of oscillation cycle in all cases.

5.2 Transient amplitude response

Figure 5.3 depicts the transient amplitude response for final reduced velocities $U^* \approx 5.2$, 6.0, and 7.2, corresponding to the initial, upper, and lower branches of quasi-steady end state. Figure 5.3(a) displays a time series of the cylinder displacement for a single trial overlaid with the amplitude envelope across the time series. Figure 5.3(b) displays the amplitude envelopes across 15 trials. For all cases, $tf_n = 0$ corresponds to the instant of cylinder release. The results show that amplitude envelopes exhibit similar trends for each reduced velocity, with the transient envelopes appearing to be shifted in time (this is particularly evident at $U^* \approx 7.2$). Accordingly, cross-correlation analysis of the corresponding time series was used to estimate a "time lag" (τ) between the individual trials in each set. This time lag was computed relative to the trial with the earliest transient onset in each data set. To align the trials, each trial was temporally shifted by the difference between its individual time lag relative to the leading trial and the mean time lag across all trials. An ensemble average of all shifted trials was obtained with the results presented in figure 5.3(c). The resulting profiles reveal the system's mean amplitude progression (solid black line) at each reduced velocity. The slopes of the envelopes represent the amplitude growth rate. The gray-shaded region represents ± one standard deviation of amplitude envelopes between the shifted trials and provides an estimate of the variability in dynamics between the temporally shifted trials.

The mean amplitude progression (figure 5.3(c)) at $U^* \approx 5.2$ is characterized by a distinct amplitude overshoot followed by a steady amplitude decay to quasi-steady state. In particular, amplitudes of around $A/D \approx 0.4$ are achieved within approximately 11-12 cycles ($(t-\tau)f_n$) of cylinder release, followed by a reduction in amplitudes until quasi-steady state is attained at $(t-\tau)f_n \approx 25$ where $A/D \approx 0.23$. Relatively low trial-to-trial variability (gray-shaded region) is observed during the transient growth in amplitude, with a noticeable

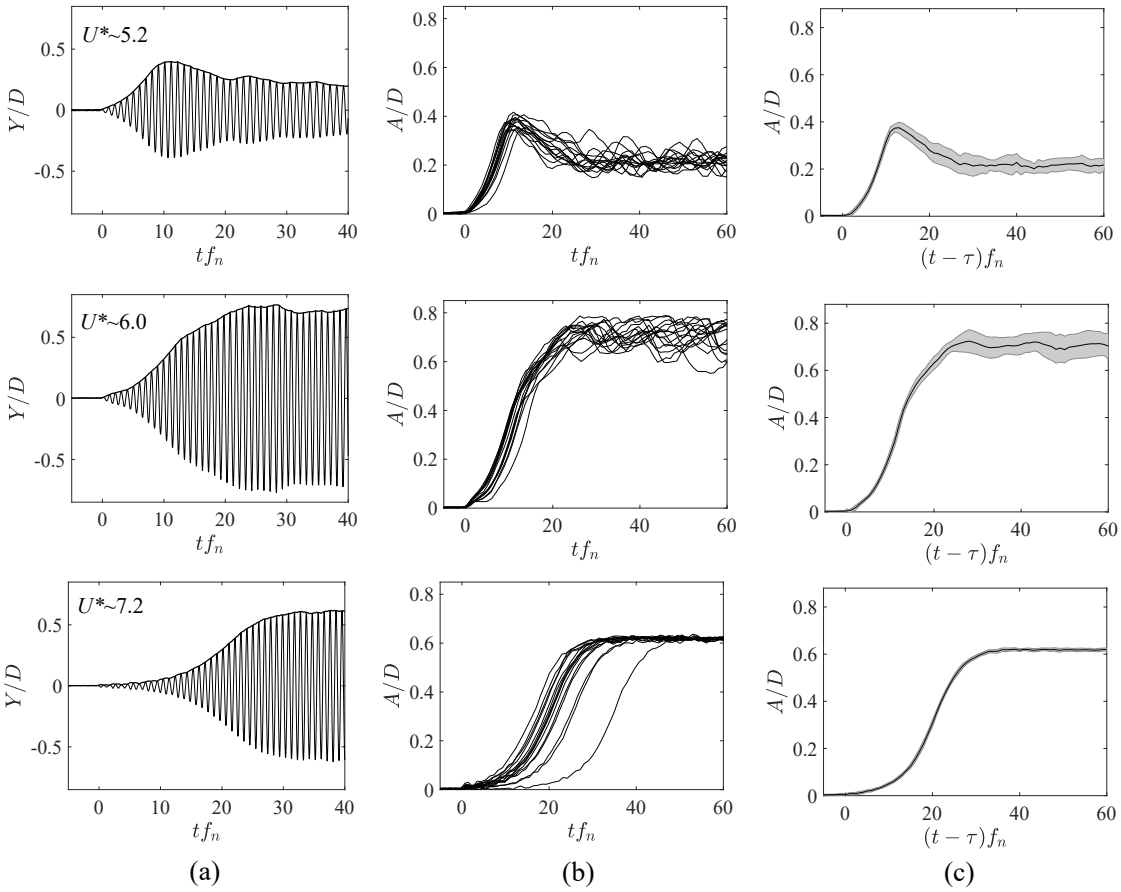

Figure 5.3: Transient amplitude response across the branches. (a) Representative time series response at marked locations in figure 5.1, (b) envelope of peak amplitudes across 15 trials, and (c) ensemble average of all trials shifted by estimated time lag τ.

increase in trial-to-trial variability beyond the peak amplitude. The maximum time delay τ between different trials is within 3.5 cycles (figure 5.3(b)). At $U^* \approx 6.0$, the amplitudes steadily increase with low trial-to-trial variability up to $(t-\tau)f_n \approx 15$. Beyond this, the amplitudes continue to increase, however, there is a noticeable decrease in the slope of the envelope along with increasing trial-to-trial variability until quasi-steady state is attained at $(t-\tau)f_n \approx 22$. The mean amplitude envelope in the upper branch resembles a sigmoid-type profile. The maximum time delay τ between different trials is within 4.5 cycles. At $U^* \approx 7.2$, a relatively smooth sigmoid-type envelope is observed. Aside from a significant increase in the time lag between the trials (figure 5.3(b)), transient response in the adjusted envelope (figure 5.3(c)) shows the lowest variability in this case. Quasi-steady state is achieved in approximately 34 cycles.

Ensemble-averaged transient amplitude envelopes for six reduced velocities (one additional U^* in each response branch) are presented in figure 5.4(a). The mean amplitude envelopes reinforce the trends outlined previously, namely, the overshoot in the initial branch and

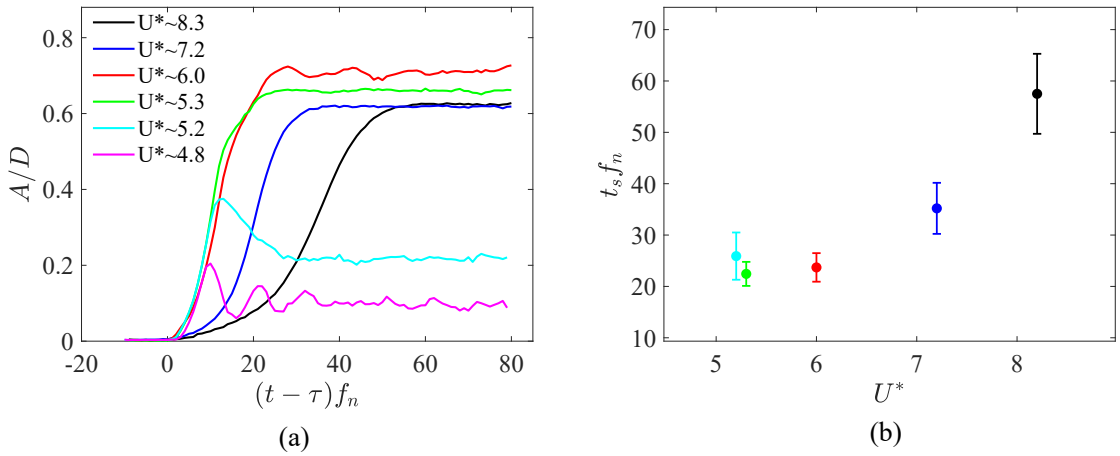

Figure 5.4: (a) Ensemble-average of all trials across the synchronization regime, and (b) associated settling time at each U^*. The settling time is determined as per the algorithm described in text.

sigmoid-type profiles in the upper and lower branches. Additionally, notable differences in the growth rates (slopes) are observed with changing reduced velocities, with the largest growth rates near the end of the initial branch ($U^* \approx 5.2$), and at the start of the upper branch ($U^* \approx 5.3$). Growth rates decline with increasing reduced velocities, particularly beginning from $U^* \approx 6.0$ in the upper branch. The time taken to attain quasi-steady state also increases, similar to the observations in [30]. A "settling time (t_s)" is defined at each U^* to quantify the time taken to attain quasi-steady state by identifying the first instance when a moving average of the amplitude envelope over a prescribed window for each trial falls within a given threshold. Specifically, at each U^*, the mean (A_{mean}) and standard deviation (A_σ) of all amplitude envelopes at quasi-steady state are calculated over approximately 500 cycles. A limiting threshold is then defined as $A_{mean} \pm A_\sigma$. Following this, a moving average and moving standard deviation are calculated for each trial using a window length of approximately five oscillation cycles. The first instance where the moving average falls within the limiting threshold and the moving standard deviation is within 10 % of A_σ is defined as the settling time t_s. Figure 5.4(b) presents the resulting nondimensional $t_s f_n$ for all tested reduced velocities except $U^* \approx 4.8$, where the system exhibits a beating-type response (quasi-periodic regime, [83]) and does not "settle". The error bars represent ± one standard deviation of $t_s f_n$ across all trials. The upper branch cases at $U^* \approx 5.3$ and 6.0 exhibit the fastest settling times (approximately $23 - 24$ cycles) and relatively low standard deviations ($\approx 2 - 3$ cycles). The settling time for $U^* \approx 5.2$ is comparable to the two upper branch cases ($t_s f_n \approx 25$ cycles). With increasing U^* in the lower branch, both the settling time and the standard deviation increase rapidly, reaching $t_s f_n \approx 35 \pm 5$ at $U^* \approx 7.2$, and $t_s f_n \approx 57 \pm 7$ at $U^* \approx 8.3$.

The preceding discussion of transient amplitude response highlights notable similarities and differences across the response branches. The similarity of the observed transient response

across different trials for a given U^*, particularly during the periods of most prominent amplitude growth (figure 5.3(c)), indicates persistent mechanisms governing the system transient dynamics. However, the time lag between trials (figure 5.3(b)) points to a notable variability in the onset of the substantial amplitude growth. Further, in contrast to the upper and lower branches, where the amplitude envelopes indicate continuous positive energy transfer to the cylinder during the transient response (figure 5.4(a)), the amplitude overshoot in the initial branch indicates a switch in the sign of energy transfer to the cylinder.

To elucidate the underlying mechanisms responsible for the observed transient dynamics, the transient frequency response, forcing on the cylinder, and wake PIV measurements are considered further. First, analysis of the transient system frequency response is used to identify the onset of fluid-structure interactions that trigger amplitude growth and lock-in behavior (section 5.3). Following this, an analysis of the forcing on the cylinder is employed to elucidate the energy transfer mechanisms governing varying growth rates and differences in the nature of amplitude envelopes between the initial and upper/lower branches (section 5.4). Finally, the attendant transient wake characteristics are explored in section 5.5 to highlight the underlying physical mechanisms associated with the different responses.

5.3 Transient frequency response and the onset of lock-in

The transition from forcing at the expected von Kármán shedding frequency before cylinder release to the final lock-in frequency at quasi-steady state (figure 5.1(b)) was examined through wavelet analysis of the vortex force. Figure 5.5 presents ensemble-averaged signal energy (modulus square of the wavelet transform) of the force acting on the cylinder at $U^* \approx 5.2$, 6.0, and 7.2, respectively. At each time instance, the signal energy is normalized by the total energy across all scales considered. The maximum energy magnitude is plotted in green, while the red line represents the equivalent maximum in the ensemble-averaged signal energy of displacement. The horizontal dashed and dashed-dotted black lines identify the von Kármán vortex shedding frequency and the structural natural frequency, respectively.

At $U^* \approx 5.2$ (figure 5.5(a)), the von Kármán shedding frequency is within 5 % of the natural frequency, and within two cycles following release at $(t-\tau)f_n = 0$, the dominant force and displacement frequencies are both identified at a common value that is slightly below the structural natural frequency (dashed-dotted black line), indicating lock-in behavior. This initial lock-in continues up to $(t-\tau)f_n \approx 6$. Afterward, the forcing frequency exhibits a distinct decrease, reaching a local minimum at $(t-\tau)f_n \approx 10$ before settling on the final lock-in value ($f^* \approx 0.94$) attained near $(t-\tau)f_n \approx 13$, while the displacement frequency exhibits a continuous gradual reduction to the final lock-in value. The dominant frequencies throughout the transient are lower than the structure's natural frequency as a consequence of the vortex force phase difference (ϕ_v) being lower than 90° thereby contributing to a

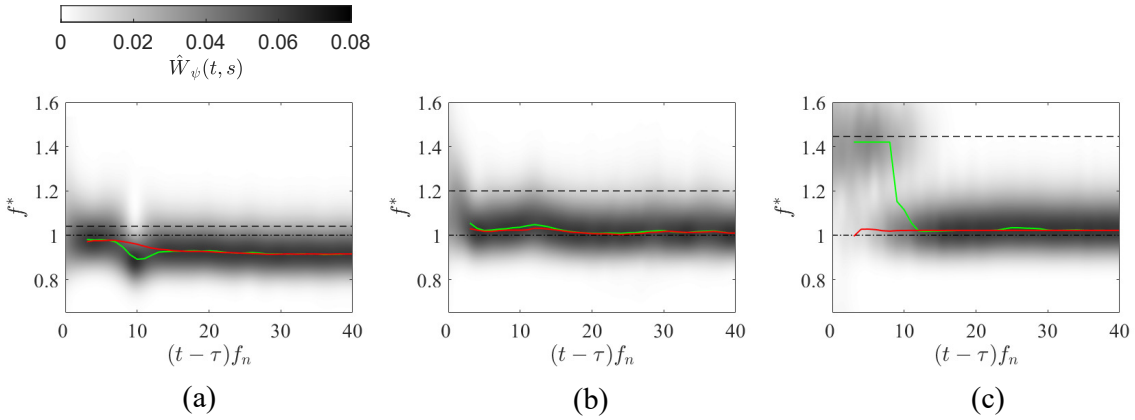

Figure 5.5: Ensemble-averaged normalized wavelet scalograms of force at (a) $U^* \approx 5.2$ (initial), (b) $U^* \approx 6.0$ (upper), and (c) $U^* \approx 7.2$ (lower branches). The green solid lines represent locus of maximum in force scalogram magnitude, red represents the locus of maximum in displacement scalogram magnitude, dashed black indicates von Kármán frequency, and the dashed-dotted black line represents the structure's natural frequency.

positive effective added mass. This is explored further in section 5.4.

At $U^* \approx 6.0$ (figure 5.5(b)), the von Kármán shedding frequency is separated from the natural frequency by approximately 20%. Near $(t-\tau)f_n \approx 4$, both the forcing and displacement frequencies assume a common value ($f^* \approx 1.02$), which is higher than the natural frequency. Both the forcing and displacement frequency increase up to $(t-\tau)f_n \approx 14$ before settling near the final lock-in value $f^* \approx 1.01$ near $(t-\tau)f_n \approx 20$. At $U^* \approx 7.2$ (figure 5.5(c)), the von Kármán shedding frequency is well separated from the natural frequency ($\approx 40\%$), and notable energy content in the forcing signal is observed at the von Kármán frequency up to $(t-\tau)f_n \approx 6$. Between $(t-\tau)f_n \approx 6$ and 13, notable energy content is observed around both von Kármán and structure natural frequencies. At $(t-\tau)f_n \approx 14$, lock-in is attained at a value higher than the structure's natural frequency ($f^* \approx 1.03$). Note that, in contrast to the transient for the initial branch, at both $U^* \approx 6.0$ and 7.2, the lock-in frequencies are greater than the natural frequency throughout the transient and at quasi-steady state due to the vortex force phase differences being between $90 < \phi_v < 180$ ([83] with ϕ values shown in section 5.4). For all the cases presented in figure 5.5, the detection of notable signal energy for the forcing near the structure's natural frequency following cylinder release (albeit at different instances) signifies a modification of forcing characteristics due to nonlinear fluid-structure interaction. While lock-in is observed relatively early ($(t-\tau)f_n \lessapprox 4$) at $U^* \approx 5.2$ and 6.0 (figures 5.5(a-b)), forcing at $U^* \approx 7.2$ (figure 5.5(c)) exhibits a dual frequency response near natural and von Kármán shedding frequencies prior to lock-in. A closer examination of this initial period is required to gain insight into transient system lock-in. For this purpose, linear system response theory is employed to model the initial system response after cylinder release.

The general solution to a linear spring-mass-damper excited by a constant sinusoidal force $F(t) = F_0 sin(\omega t)$ can be expressed as a sum of homogeneous and particular solutions to the equation of motion (equation 2.1):

$$y(t) = \underbrace{\frac{F_0}{4\pi^2 m\sqrt{(f_n^2 - f^2)^2 + (2\zeta f f_n)^2}} sin(2\pi f t - \alpha)}_{\text{Particular Solution}} + \overbrace{Be^{-\zeta 2\pi f_n t} sin(2\pi f_n t\sqrt{1-\zeta^2} + \beta)}^{\text{Homogeneous solution}}, \quad (5.1)$$

where B and β are constants that depend on the initial conditions. The general solution exhibits a dual frequency response at the forcing frequency f and the damped natural frequency $f_d = f_n\sqrt{1-\zeta^2}$) through the particular and homogeneous (decaying) solutions, respectively. The homogeneous solution decay rate is proportional to the damping and persists for $O(100)$ cycles for the damping ratio representative of the present system, $\zeta \approx O(10^-4)$. Thus for a cylinder released from rest where it is subjected to forcing at von Kármán frequency prior to release, the initial structural response is expected to feature both von Kármán and structure natural frequencies while forcing remains at von Kármán shedding frequency. Evidence of a brief period of linear system response matching that of equation 5.1 is observed at $U^* \approx 7.2$, where the von Kármán and natural frequencies are sufficiently separated. An example is presented in figure 5.6, where figure 5.6(a) displays time traces of nondimensional displacement and forcing for approximately 50 cycles, and figure 5.6(b) shows the normalized wavelet scalogram of the forcing signal during the same time period. The scalogram in figure 5.6(b) indicates significant energy at the von Kármán shedding frequency and negligible energy near natural frequency for $tf_n \lessapprox 9$. The left inset of vortex force time history in figure 5.6(a) shows strongly periodic fluctuations for this initial period following the release of the cylinder. Here, the cylinder exhibits relatively minor oscillations that are modulated as a result of the dual-frequency response (equation 5.1 and verified through spectral analysis). At $tf_n \approx 11$, notable energy content appears at the structure's natural frequency in figure 5.6(b). Beyond $tf_n \approx 11$, the forcing time history becomes relatively noisy (see right inset in figure 5.6) which is also reflected in a significant broadening of the energy spectrum (figure 5.6(b)). The amplitude response shows increasing oscillation amplitudes and the beginning of sustained amplitude growth. Beyond $tf_n \approx 30$, the forcing exhibits periodic oscillations with minimal noise. The onset of nonlinear forcing, characterized by the emergence of a notable component of forcing near the structure's natural frequency at $tf_n \approx 11$, is critical for sustained amplitude growth. In particular, it can be shown that for continuous net positive energy transfer to the cylinder, there must be a component of forcing at the structural oscillation frequency (analogous to resonance in a linear system). If forcing persisted only at von Kármán frequency, the amplitudes in the lower branch would remain less than approximately 1 % of the cylinder diameter, as seen in figure 5.6(a) for $tf_n \lessapprox 9$.

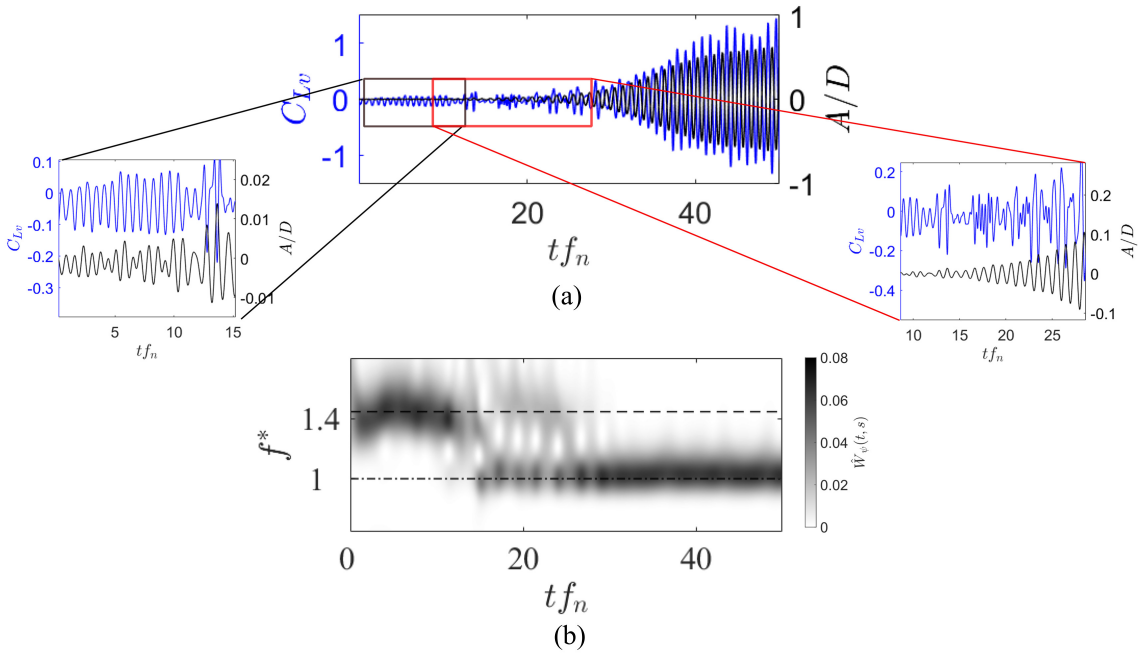

Figure 5.6: Onset of nonlinear behavior for a single trial at $U^* \approx 7.2$. (a) Nondimensional displacement and vortex force and (b) normalized wavelet scalogram of vortex force. The left inset displays the time period featuring periodic forcing at predominantly von Kármán frequency and the right inset displays a period of noisy forcing signal characterized by frequency components around both von Kármán and structure natural frequency along with the associated growth in oscillation amplitudes.

To further investigate the onset of transient fluid structure interactions leading to lock-in, energy contributions around each of the pertinent frequencies are extracted from a single trial (figure 5.6(b)). Specifically, the total normalized wavelet magnitude is extracted from a band of frequencies (± 10 %) bounding the natural and von Kármán frequencies at each time instance ($\hat{E}_s = \sum_{s=s_1}^{s_2} \hat{W}_\psi$). The time history of the respective energy bands normalized by total energy across all scales is plotted in figure 5.7. A significant difference in the extracted energy content is observed between the natural and von Kármán bands for $tf_n \lessapprox 9$. Following this, the natural frequency component begins to increase, coinciding with a decay of the energy content around the von Kármán frequency up to lock-in. The time series of energy content around natural and von Kármán frequency reveals a high degree of negative correlation. This suggests an energy exchange between the two dominant forcing mechanisms, with the natural frequency component gradually superseding the von Kármán frequency, signifying the transition to a lock-in state.

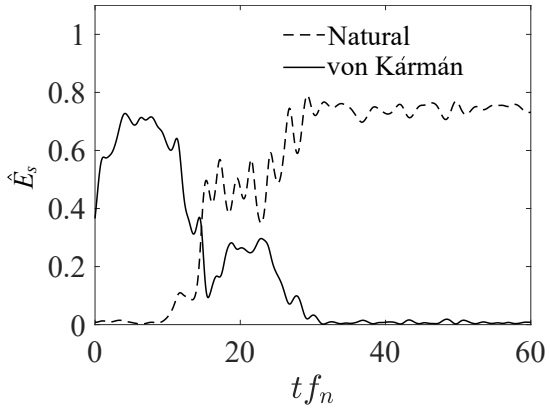

Figure 5.7: Time history of energy concentrated around a band of ±10% of the von Kármán and natural frequency components at $U^* \approx 7.2$ for a single trial (figure 5.6).

The onset of lock-in behavior has been observed for all three representative U^*. While the proximity of the initial von Kármán frequency and structure natural frequency promotes relatively early lock-in for $U^* \approx 5.2$ and 6.0 (figure 5.5), a brief period of linear system behavior is observed at $U^* \approx 7.2$ where the two frequency components are more separated. The onset of substantial forcing near the structure's natural frequency, marking the beginning of nonlinear system behavior, is critical for sustained amplitude growth. However, the onset of forcing at the structure's natural frequency was observed to exhibit significant trial-to-trail variability, particularly in the lower branch. The associated differences in the onset of lock-in and the beginning of prominent growth in vibrations amplitudes are postulated to be the underlying reason for the notable variations in time lag τ (figure 5.3(b)) between different trials. Next, the mechanisms driving the differences in amplitude growth rate and natures of the amplitude curves (figure 5.4(a)) are explored through analysis of the transient forcing characteristics and energy transfer between the fluid and the cylinder.

5.4 Transient forcing characteristics and energy analysis

Figure 5.8 presents the ensemble-averaged nondimensional vortex force (C_{Lv}, top row), the phase difference between vortex force and displacement (ϕ_v, middle row), and the nondimensional energy transferred to the cylinder over each cycle of oscillation (E^*, bottom row) at $U^* \approx 5.2$, 6.0, and 7.2. E^* is estimated through numerical integration of the nondimensional force and cylinder velocity over each cycle of oscillation, as discussed in section 3.3.3. The shaded regions in all figures represent ± one standard deviation around the mean (solid lines). The force magnitude plots are overlaid with ensemble-averaged transient amplitude (from figure 5.3(c)) and the phase plots are overlaid with the loci of maxima in force and displacement frequencies (from figure 5.5). To minimize the noise in the phase estimation due to the presence of multiple frequencies (e.g., figure 5.5(c)), the displacement data were band-pass filtered around the natural frequency for the estimation of ϕ_v.

At $U^* \approx 5.2$ (figure 5.8(a)), the vortex force magnitude increases up to $(t-\tau)f_n \approx 7$, followed by a notable decrease and then recovery to quasi-steady values. The vortex force phase difference (ϕ_v) remains relatively stable at a value slightly below 90° for around 6 cycles. This is followed by a small overshoot and a significant reduction in ϕ_v that coincides with the reduction in forcing frequency. Between $11 \lessapprox (t-\tau)f_n \lessapprox 22$, ϕ_v remains negative ($\phi_v \approx -5°$) before recovering to a positive value ($\phi_v \approx 3°$) at quasi-steady state. The vortex force phase difference is critical to the energy transfer from the fluid to the cylinder since the net magnitude of energy transferred to the cylinder over a cycle depends on both the force magnitude and $sin(\phi_v)$ (e.g., equation 2.5 for quasi-steady state). A value of $\phi_v = 90°$ implies that the vortex force is in phase with the velocity, enabling maximum energy input over an oscillation cycle. Conversely, $\phi_v = 0$ or 180 ° results in net zero energy input over one cycle. At $U^* \approx 5.2$, E^* increases to its peak value at $(t-\tau)f_n \approx 8$ (bottom row, figure 5.8(a)). The rising energy transfer in this time period is due to a combination of increasing force magnitude and ϕ_v remaining relatively close to 90°. The significant drop in ϕ_v beyond $(t-\tau)f_n \approx 8$ results in decreasing E^*, with negative E^* expectedly observed for negative ϕ_v. Negative E^* implies that energy is being transferred from the cylinder to the fluid, which leads to decreasing vibration amplitudes (see gray plot in top row). During the period of negative energy transfer, the force magnitudes are near their quasi-steady value (figure 5.8(a)), highlighting the importance of phase difference to the energy transfer. From $(t-\tau)f_n \gtrapprox 20$, E^* gradually recovers to near zero values, coinciding with the leveling of ϕ_v at 0°.

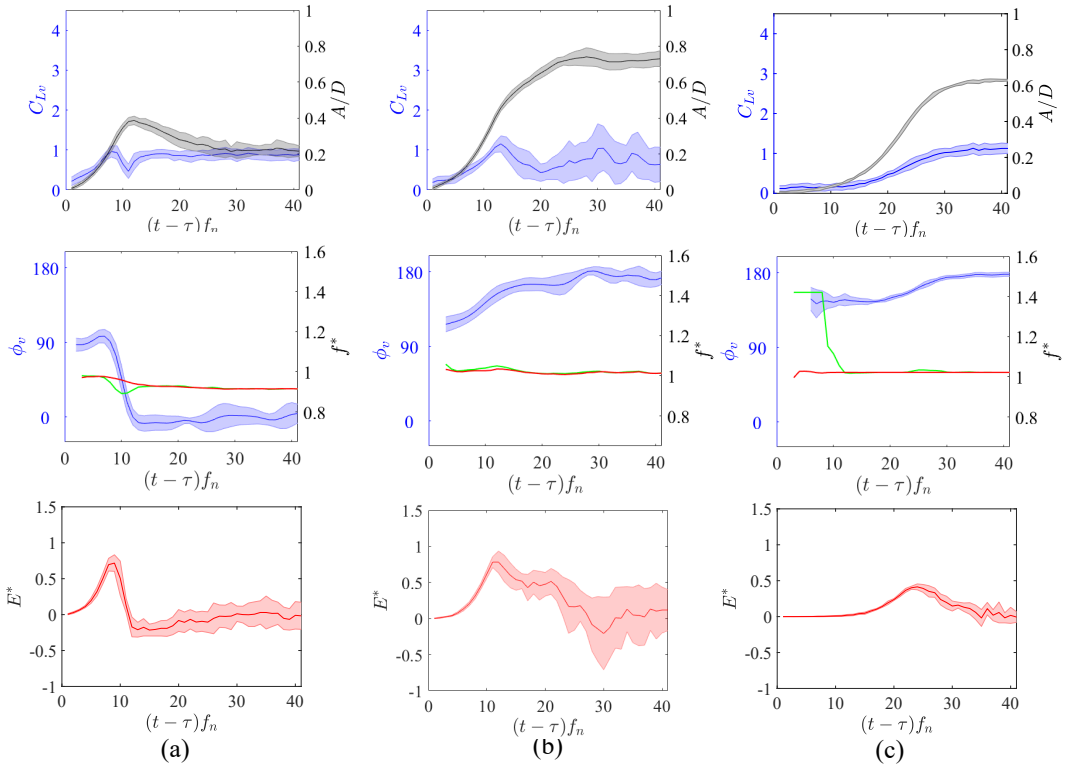

Figure 5.8: Ensemble-averaged nondimensional vortex force (top row, C_{Lv}), vortex force phase difference (middle row, ϕ_v), and nondimensional energy transfer to the cylinder over each oscillation cycle (bottom row, E^*) for representative U^* in (a) initial, (b) upper, and (c) lower branches, respectively. The force plots are overlaid with ensemble-averaged amplitude, and the phase plots are overlaid with loci of force and displacement frequencies from figure 5.5.

At $U^* \approx 6.0$ (figure 5.8(b)), the vortex force magnitude initially increases and peaks at $(t-\tau)f_n \approx 12$. Following this, the force magnitude reduces and then recovers to the quasi-steady state level. Shortly following cylinder release, the forcing phase $\phi_v \approx 115°$ and increases up to 160° near $(t-\tau)f_n \approx 12$. The phase difference then remains nearly constant up until $(t-\tau)f_n \approx 20$, when it begins to converge to the quasi-steady value where ϕ_v is close to 180°. A continuous increase in E^* (bottom row) is observed following cylinder release up to $(t-\tau)f_n \approx 11$. The slope of the E^* curve during this period is lower than that at $U^* \approx 5.2$, which is partly a consequence of the higher ϕ_v values relative to the optimal 90°. Beyond $(t-\tau)f_n \approx 11$, E^* decreases until $(t-\tau)f_n \approx 14$, followed by a relative plateau in E^* up to $(t-\tau)f_n \approx 20$. Note that for $28 \lessapprox (t-\tau)f_n \lessapprox 32$, E^* briefly becomes negative, which coincides with ϕ_v increasing slightly beyond 180°. Once the system attains quasi-steady state, ϕ_v remains close to and below 180°. However, ϕ_v associated with individual trials exhibits regular excursions across the 180° threshold that result in a modulated amplitude response (figure 5.3(b)).

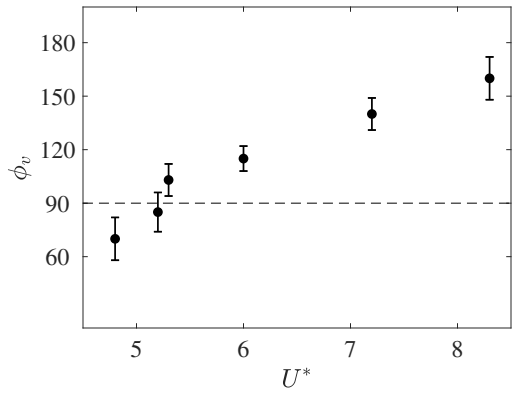

Figure 5.9: Vortex force phase difference ϕ_v immediately after lock-in for all tested U^*. The dotted line represents 90°.

At $U^* \approx 7.2$ (figure 5.8(c)), the force magnitude remains relatively constant up to $(t-\tau)f_n \approx 13$ and then increases continuously up to quasi-steady state. Approximately five cycles following cylinder release, ϕ_v is identified close to 140° and remains relatively constant up to $(t-\tau)f_n \approx 20$. This is followed by a steady increase in ϕ_v to the quasi-steady state where ϕ_v is close to 180 °. Negligible positive values of E^* are observed up to $(t-\tau)f_n \approx 13$ coinciding with the period of relatively constant force magnitude and phase difference. Beyond $(t-\tau)f_n \approx 13$, E^* increases up to its peak value near $(t-\tau)f_n \approx 23$, followed by a gradual decay towards quasi-steady state. The increase of E^* to its peak value is attributed to rising force magnitude despite the growing separation of ϕ_v from 90° up to $(t-\tau)f_n \approx 23$. Beyond this point, the decreasing component of forcing in phase with velocity (due to increasing ϕ_v) results in E^* gradually reducing to zero.

Further analysis of the results showed that, across all U^*, the vortex force magnitudes during the first few cycles of oscillation are of a similar order. However, the initial vortex force phase difference immediately following the onset of lock-in was found to vary significantly with U^*. This is shown in figure 5.9 where ϕ_v is obtained immediately after lock-in, identified as the instant when the contribution of the ensemble-averaged wavelet energy band around natural frequency first reaches 50 % of the total energy content. The results show that ϕ_v increases from approximately 70° at $U^* \approx 4.8$ to $\phi_v \approx 160$ at $U^* \approx 8.3$. The vortex force phase difference ϕ_v is related to the timing of vortex shedding with respect to the oscillation cycle [100]. Thus, the results imply that, at the onset of lock-in, the timing of vortex shedding relative to the cylinder oscillation varies with U^*. The initial ϕ_v after lock-in is closest to 90° for $U^* \approx 5.2$ and 5.3. Consequently, since $\phi_v = 90$ yields the highest energy transfer rate to the cylinder, the largest initial amplitude growth rates are observed in this region (figure 5.4(a)). At other U^*, particularly in the lower branch, increasing separation of the initial ϕ_v from 90° results in lower rates of energy transfer and subsequently lower amplitude growth rates.

Apart from implications on the energy transfer, the vortex force phase difference also influences the value of the lock-in frequency with respect to the structural natural frequency. The relationship between oscillation frequency and the vortex force phase difference has been shown previously [62] and is obtained through substitution of the expressions for force and displacement (equation 2.2) into the equation of motion (equation 2.1). After rearrangement, this gives:

$$\frac{F_v cos(\phi_v)}{kA} = 1 - (f^*)^2 \tag{5.2}$$

Thus, as the vortex force phase difference ϕ_v passes through 90°, the nondimensional frequency f^* will pass through 1. This is seen when examining the initial and final phase differences after lock-in (figures 5.9 and 5.8). At $U^* \approx 5.2$, ϕ_v is initially slightly below 90° implying a negligible component of forcing in phase with the cylinder displacement ($F_{0v} cos(\phi_v) \approx 0, \phi_v \approx 90$) and a minimal change to the effective added mass. Consequently, the initial oscillation frequency is close to the natural frequency ($f^* \approx 0.98$). The final lock-in frequency ($f^* \approx 0.94$) is further below the structure's natural frequency, which is attributed to a significant component of forcing in phase with the cylinder displacement ($F_{0v} cos(\phi_v) \approx F_{0v}, \phi_v \approx 0$), thereby contributing to a positive effective added mass. Conversely, at $U^* \approx 6.0$ and 7.2, ϕ_v remains greater than 90° throughout the system response and the associated lock-in frequencies (f^*) are above 1 (figure 5.5(b-c)).

The examination of the vortex forcing and energy characteristics improves our understanding of the differences in the transient amplitude response curves across the different response branches. Next, the wake dynamics associated with the outlined forcing characteristics and lock-in behavior are explored.

5.5 Attendant transient wake dynamics

Transient wake dynamics is examined through PIV measurements ensemble-averaged across five trials for the cylinder converging to quasi-steady state VIV in the initial, upper, and lower branches for $U^* \approx 5.2$, 6.0, and 7.2, respectively. Qualitative and quantitative assessments of the transient wake development are performed using vortex identification via the methodology outlined in section 3.3.4. The shedding of each tracked vortex in the ensemble-averaged transient sequence is defined as the moment when vortex circulation Γ reaches a peak value, with circulation estimated through integration of the ensemble-averaged vorticity field inside the identified vortex contour (section 3.3.4). The downstream distance at which a given vortex attains a maximum circulation provides an estimate of the vortex formation length (L_f), measured from the origin to the streamwise location of the shed vortex centroid. The phase of the cylinder oscillation cycle (θ) at which a given vortex sheds can also be identified, with $\theta = 0°$ corresponding to the instant when the cylinder crosses the equilibrium point in the positive Y direction. Note that θ is distinct from ϕ_v, with the former representing the absolute phase of cylinder oscillation and the latter representing the phase difference between cylinder oscillation and vortex force.

Figure 5.10 presents the ensemble-averaged spanwise vorticity contours overlaid with the identified vortex boundaries for $U^* \approx 5.2$ at four instances during the transient. The corresponding instances are marked in the transient ensemble-averaged displacement time series in figure 5.10(a). For all the depicted vorticity contours, the cylinder is at the bottom dead center of an oscillation cycle. The nondimensional vortex formation length and oscillation phase of the cylinder at shedding are presented in figure 5.11. At $(t-\tau)f_n \approx 3$, the wake exhibits an alternating pattern of oppositely signed vortices similar to quasi-steady 2S shedding from a stationary cylinder. At $(t-\tau)f_n \approx 6$, the wake continues to exhibit a similar alternating pattern of vortices; however, the shear layer roll-up takes place closer to the cylinder compared to that seen at $(t-\tau)f_n \approx 3$. Additionally, the positive shear layer has a more pronounced deflection in the direction opposite to the cylinder displacement when compared to $(t-\tau)f_n \approx 3$ (compare figures 5.10(c) and 5.10(b)). Near the peak oscillation amplitude at $(t-\tau)f_n \approx 10$ (figure 5.10(d)), a more significant deflection of the positive shear layer is observed along with a weaker negative vortex roll-up near the cylinder base ($X/D \approx 0.75$) compared to the flow development seen at $(t-\tau)f_n \approx 6$. Additionally, a weaker vortex is shed from the positive shear layer and trails the negative vortex at $X/D \approx 1$ (figure 5.10(d)), resembling the $2P_0$ shedding mode. The $2P_0$ mode is more evident in wake vorticity data from individual runs (not shown here for brevity) near peak oscillation amplitudes. At $(t-\tau)f_n \approx 15$ (figure 5.10(e)), the wake closely resembles a quasi-steady 2S pattern, but negative vortex roll-up near the base of the cylinder is evidently delayed in this same oscillation phase (compare figures 5.10(e) and 5.10(d)). Specifically, the negative vortex at $X/D \approx 2$ in figure 5.10(e) is still attached to the shear layer whereas the negative vortex at a similar streamwise location in figure 5.10(d) has already been shed. This highlights a change in the shedding phase during the transient.

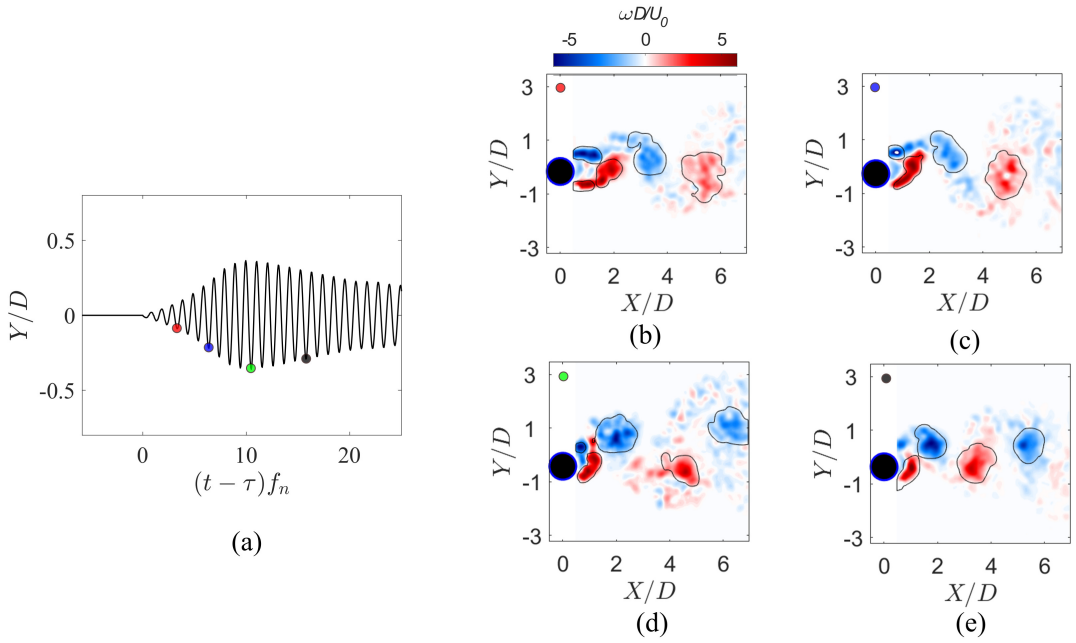

Figure 5.10: (a) Ensemble-averaged time series and spanwise vorticity at $U^* \approx 7.2$ for (b) $(t-\tau)f_n \approx 3$, (c) $(t-\tau)f_n \approx 6$, (d) $(t-\tau)f_n \approx 10$, and (e) $(t-\tau)f_n \approx 15$. The solid black lines in (b-e) indicate the vortex boundaries identified through the methodology outlined in 3.3.4.

The shortening of the near wake with increasing oscillation amplitudes observed in figure 5.10 is reflected in the vortex formation lengths trend captured in figure 5.11(a). The dashed line in the plot represents the formation length for a stationary cylinder estimated using the same methodology. The dotted line represents the formation lengths obtained from phase-averaged vorticity fields in quasi-steady state VIV. The results show that the formation length reduces during the onset of vibrations, reaching a local minimum when the amplitude of vibrations peaks at $(t-\tau)f_n \approx 10$, following which it recovers to the quasi-steady state value $L_f/D \approx 2.2$. For approximately 10 cycles, the oscillation phase at shedding (θ, figure 5.11(b)) is approximately 40° for the positive vortex and 215° for the negative vortex. Thus, the positive vortex is shed when the cylinder is moving towards positive Y and is located between the equilibrium and top dead center positions, while the negative vortex sheds roughly 180° after that. After $(t-\tau)f_n \approx 11$, positive and negative vortices are shed at $\theta \approx 130°$ and $\theta \approx 300°$, respectively, which constitutes a 90° phase shift compared to the earlier portion of the transient. Here, the negative vortex is shed as the cylinder is moving from the bottom dead center towards the equilibrium position, and the positive vortex sheds roughly 180° later as the cylinder is moving down from its top dead center towards the equilibrium position.

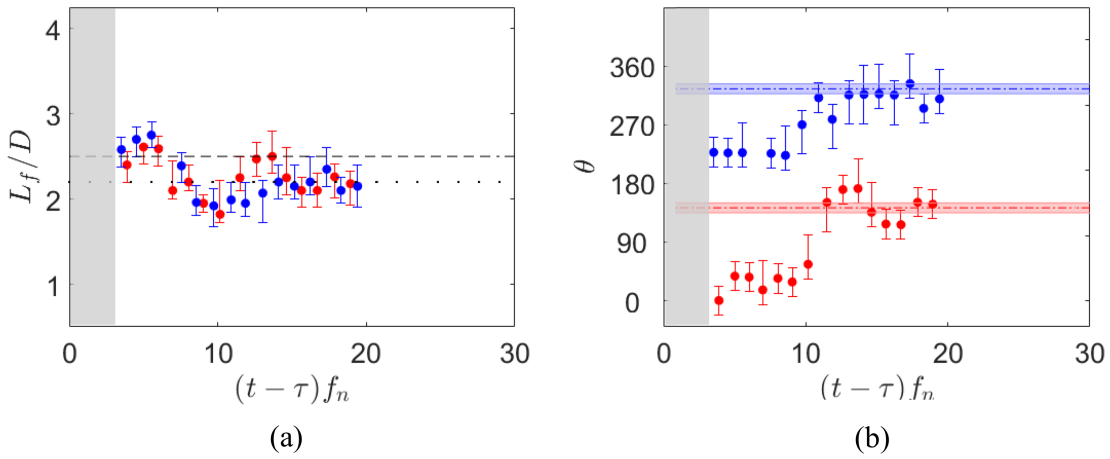

Figure 5.11: Transient wake characteristics at $U^* \approx 5.2$. (a) Vortex formation lengths and (b) phase of oscillation at vortex shedding. Dashed, dotted lines in (a) represent the formation lengths obtained from the stationary cylinder and quasi-steady, phase-averaged VIV cases, respectively. Dashed lines in (b) indicate the quasi-steady, phase-averaged θ with the shaded regions indicating the methodological uncertainty. Gray areas identify regions where estimations are unreliable due to the absence of lock-in and/or low-amplitude oscillation preventing accurate phase estimation.

It is instructive to contrast the development of vortex shedding at the onset of cylinder oscillation with that for a stationary cylinder. For the latter, vortex pinch-off (shedding) results primarily from a growing vortex drawing the opposing shear layer across the wake that ultimately cuts off the supply of vorticity to the growing vortex [60]. For VIV, the onset of cylinder oscillation induces shear layer deflection. As observed in the vorticity field snapshots (figure 5.10 (b-c)), the deflected positive shear layer impinges on the negative shear layer, which affects the vortex pinch-off process. This is supported by the fact that shedding of oppositely signed vortices is separated by 180° in terms of the phase of cylinder oscillation, thus linking the pinch-off process to the cylinder motion. Increasing oscillation amplitudes leads to larger deflections of the shear layer (compare figures 5.10(b) and (d)) and a subsequent shortening of the vortex formation region. As the cylinder reaches the overshoot amplitudes ($(t-\tau)f_n \approx 10$) and the shear layers exhibit the largest deflections, a rapid change in the shedding phase ensues, with the associated change in θ comparing well with that in ϕ_v at the same time (figure 5.8). It can be deduced that, near the peak oscillation amplitude, the combination of large shear layer deflections and short formation lengths inhibits opposite shear layer impingement, thereby causing the change in the vortex shedding phase and transition to the new equilibrium state at the end of the transient.

Figures 5.12 and 5.13 present the ensemble-averaged spanwise vorticity contours and the associated quantitative metrics for $U^* \approx 6.0$. At $(t-\tau)f_n \approx 8$ (figure 5.12(b)), the wake exhibits alternating shedding of single vortices similar to the initial wake topology for $U^* \approx$

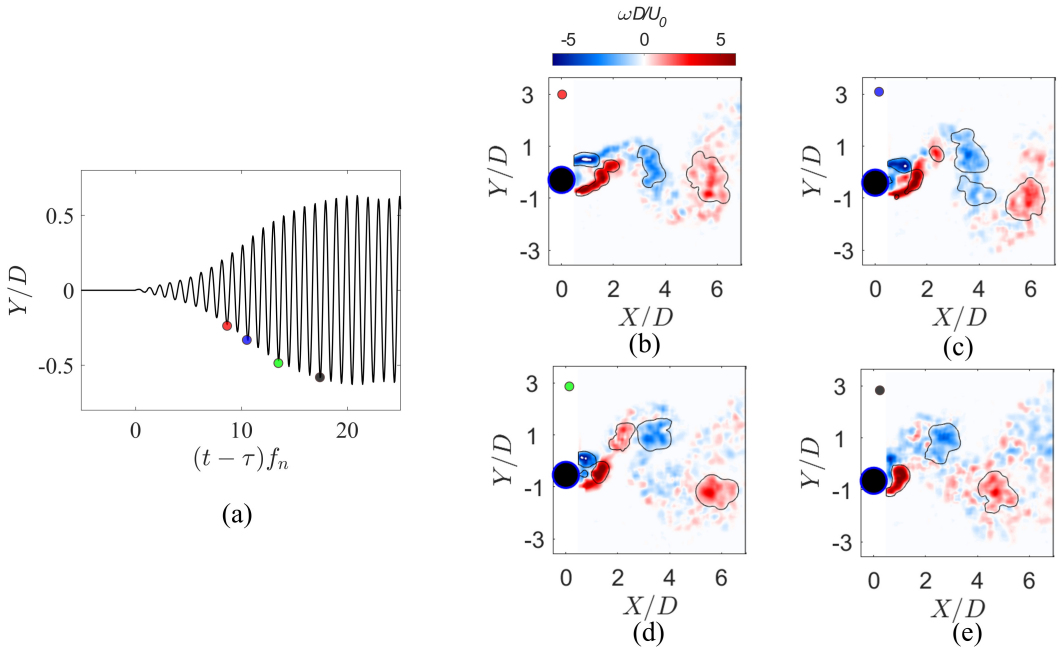

Figure 5.12: (a) Ensemble-averaged time series and spanwise vorticity at $U^* \approx 6.0$ for (b) $(t-\tau)f_n \approx 8$, (c) $(t-\tau)f_n \approx 10$, (d) $(t-\tau)f_n \approx 13$, and (e) $(t-\tau)f_n \approx 18$. The black solid lines in (b-e) indicate the vortex boundaries identified through the methodology outlined in 3.3.4.

5.2 (figure 5.10(a)). As the amplitude of oscillations increases, a distinct change in wake topology is identified at $(t-\tau)f_n \approx 10$ (figure 5.12(c)), where a counter-rotating pair of vortices is shed ($X/D \approx 3$), similar to 2P shedding. At $(t-\tau)f_n \approx 13$ (figure 5.12(d)), the 2P pattern persists and is accompanied by the reduction in the formation length. At $(t-\tau)f_n \approx 18$ (figure 5.12(e)), the positive shear layer is significantly deflected due to the relatively large oscillation amplitudes, and the 2P mode is no longer identifiable in the near wake. At quasi-steady state, the $2P_0$ mode can be identified in the data from individual runs (not shown), but the weaker secondary vortex cannot be discerned in the ensemble-averaged images due to cycle-to-cycle variations in shedding phase alignment.

To enable consistent vortex tracking during the periods of changing wake topology through the transient, attention in this transient case is focused on the leading vortex in each vortex pair (e.g., negative vortex at $X/D \approx 3.5$ in figure 5.12(d)). The vertical lines in figure 5.13(b) are used to approximate the shedding regimes observed in phase-averaged sequence. The vortex formation length (figure 5.13(a)) shows a continuous reduction from $L_f \approx 3D$ to approximately $1.8D$ at quasi-steady state. Note, that the formation length is noticeably higher than that for the stationary cylinder case (dashed line) for $(t-\tau)f_n \lessapprox 10$, despite relatively small amplitudes of vibrations. With the lock-in frequency being notably lower than the von Kármán frequency for the stationary cylinder (figure 5.5(b)), the increased formation length may be in part attributed to the longer shedding period allowing more significant downstream advection of the forming vortex prior to pinch-off. Around 5 cycles

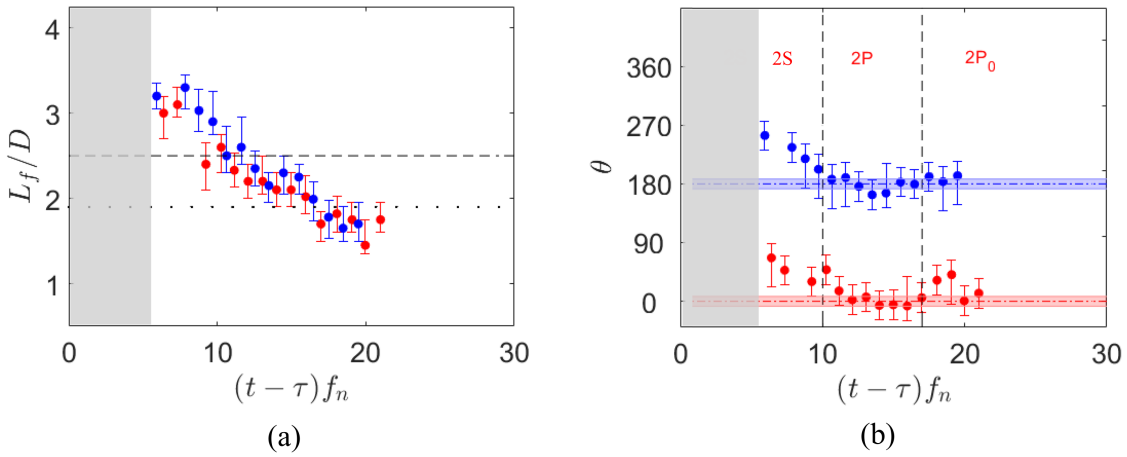

Figure 5.13: Transient wake characteristics at $U^* \approx 6.0$. (a) Vortex formation lengths and (b) phase of cylinder oscillation at the instant of vortex shedding. Refer to figure 5.11 for interpretation of lines and shaded regions.

after cylinder release, the shedding phase of positive and negative vortices is $\theta \approx 40°$ and $\theta \approx 210°$, respectively, and a steady reduction in the shedding phase is observed up to $(t-\tau)f_n \approx 13$. Beyond this time, θ remains relatively stable near the quasi-steady state value. The observed change in θ between $5 \lessapprox (t-\tau)f_n \lessapprox 13$ mimics that in ϕ_v during the transient (figure 5.8).

Figures 5.14 and 5.15 present the ensemble-averaged spanwise vorticity contours and the associated quantitative metrics at $U^* \approx 7.2$. Prior to lock-in ($(t-\tau)f_n \lessapprox 14$, figure 5.5), distinct coherent structures can be only identified in the immediate vicinity of the cylinder (figure 5.14(b)), with no particular topological features identifiable beyond $X/D \approx 2.5$ due to run-to-run variation in the wake development. At $(t-\tau)f_n \approx 18$ (figure 5.14(c)), an alternately signed vorticity pattern is identified in the wake, resembling the 2S shedding mode. At $(t-\tau)f_n \approx 27$ (figure 5.14(d)), the wake exhibits the 2P topology which persists to quasi-steady state ($(t-\tau)f_n \approx 33$, figure 5.14(e)).

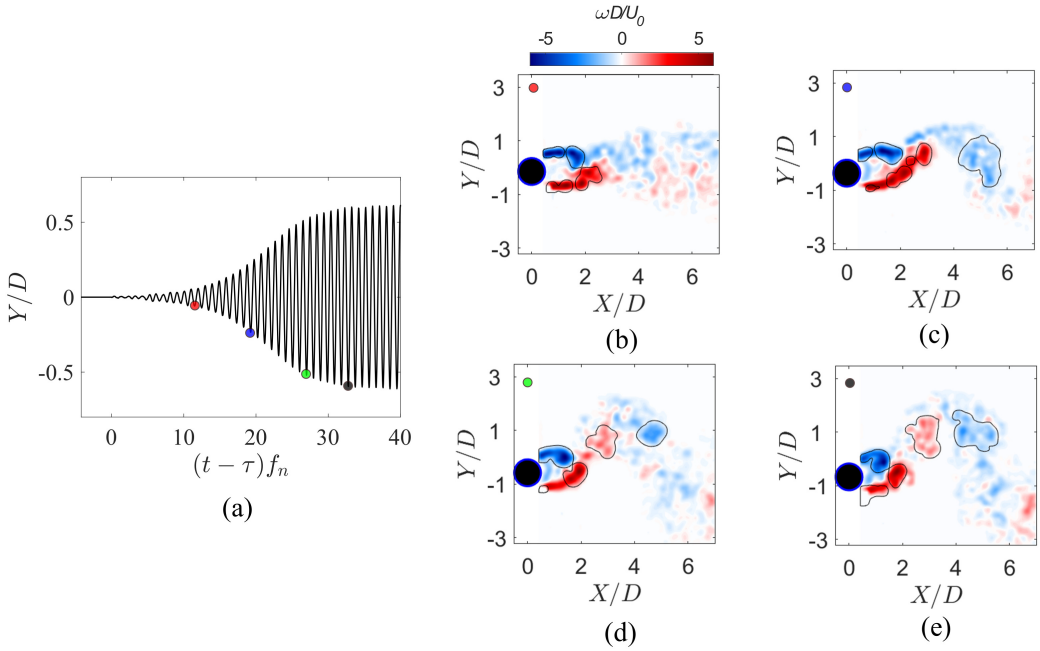

Figure 5.14: (a) Ensemble-averaged time series and spanwise vorticity at $U^* \approx 7.2$ for (b) $(t-\tau)f_n \approx 10$, (c) $(t-\tau)f_n \approx 18$, (d) $(t-\tau)f_n \approx 27$, and (e) $(t-\tau)f_n \approx 33$.The black solid lines in (b-e) indicate the vortex boundaries identified through the methodology outlined in 3.3.4.

Following lock-in, the ensemble-averaged wake characteristics are estimated based on the leading vortex tracking in each vortex pair, similar to the $U^* \approx 6.0$ case. Between $14 \lessapprox (t-\tau)f_n \lessapprox 21$, where the wake topology resembles 2S shedding, consistent tracking of the vortex cores was not possible, and no wake metrics are provided. Beyond $(t-\tau)f_n \approx 21$, the vortex formation length, on the average, shows a decrease from above $L_f/D \approx 3.0$ to the quasi-steady state value $L_f/D \approx 2.75$. The leading positive and negative vortices are shed at a relatively constant $\theta \approx$ -10° and 170° in the resolved later stages of the transient wake response.

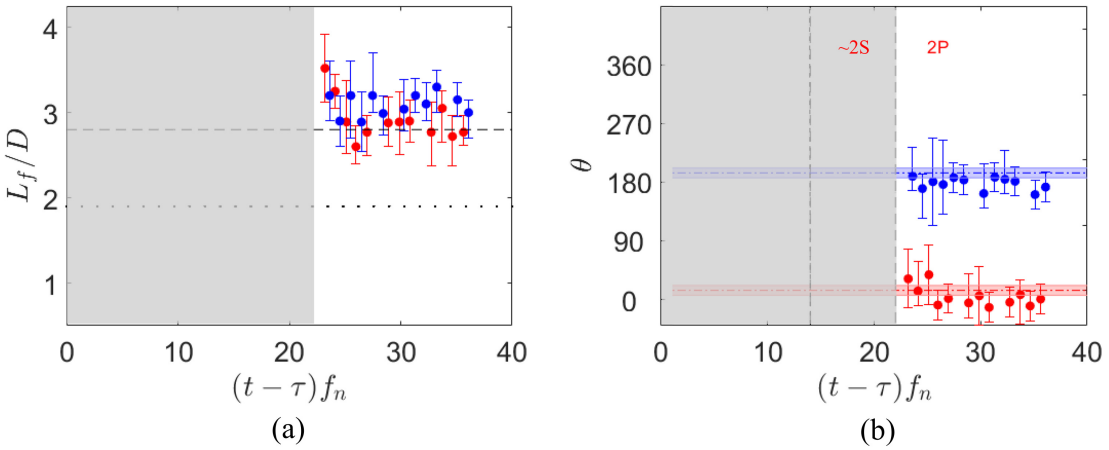

Figure 5.15: Transient wake characteristics at $U^* \approx 7.2$. (a) Vortex formation lengths and (b) phase of cylinder oscillation at the instant of vortex shedding. Refer to figure 5.11 for interpretation of lines and shaded regions.

The analysis of the ensemble-averaged wake characteristics is useful in identifying the transient changes in wake topology and characteristics. However, transient wake dynamics during the onset of lock-in behavior can be illustrated better through the examination of wake characteristics in individual runs. This is particularly true in the lower branch case, where the ensemble-averaged wake downstream of $X/D \approx 3$ during the initial transient period ($(t-\tau)f_n \lessapprox 14$, figure 5.14(b)) is smeared out as a result of the different times at which lock in is attained in different trials. Figure 5.16 depicts normalized wavelet scalograms of the vortex force (top row), and the corresponding transverse velocity signal along the wake centerline at $X/D \approx 4$ for individual trials at $U^* \approx 5.2$, 6.0, and 7.2, respectively. In all cases, the location of the sampled for the velocity signal is downstream of the vortex formation region throughout the transient.

For all the cases considered, prior to cylinder release, the dominant wake frequency is identified near the von Kármán frequency prior to release ($tf_n < 0$, bottom row). For $U^* \approx 5.2$ (figure 5.16(a)), a slight decrease in dominant frequency is observed almost immediately following cylinder release. Beyond $tf_n > 0$, the trend observed in the vortex forcing scalogram (top row) is closely reflected in the velocity scalogram (bottom row) including the significant reduction in dominant frequency near $tf_n \approx 10$. The larger separation between the natural and von Kármán frequencies at $U^* \approx 6.0$ compared to $U^* \approx 5.2$ allows for a more distinct identification of the change in dominant wake frequency at $tf_n \approx 4$ (figure 5.16(b), bottom row). After $tf_n \gtrapprox 4$, the velocity wavelet is more modulated than the forcing wavelet, however, the general trend remains similar with the dominant frequency remaining close to the natural frequency throughout the rest of the transient.
The wavelet scalogram of vortex force at $U^* \approx 7.2$ (figure 5.16(c), top row) indicates the emergence of a significant energy content near the structural natural frequency at $tf_n \approx$

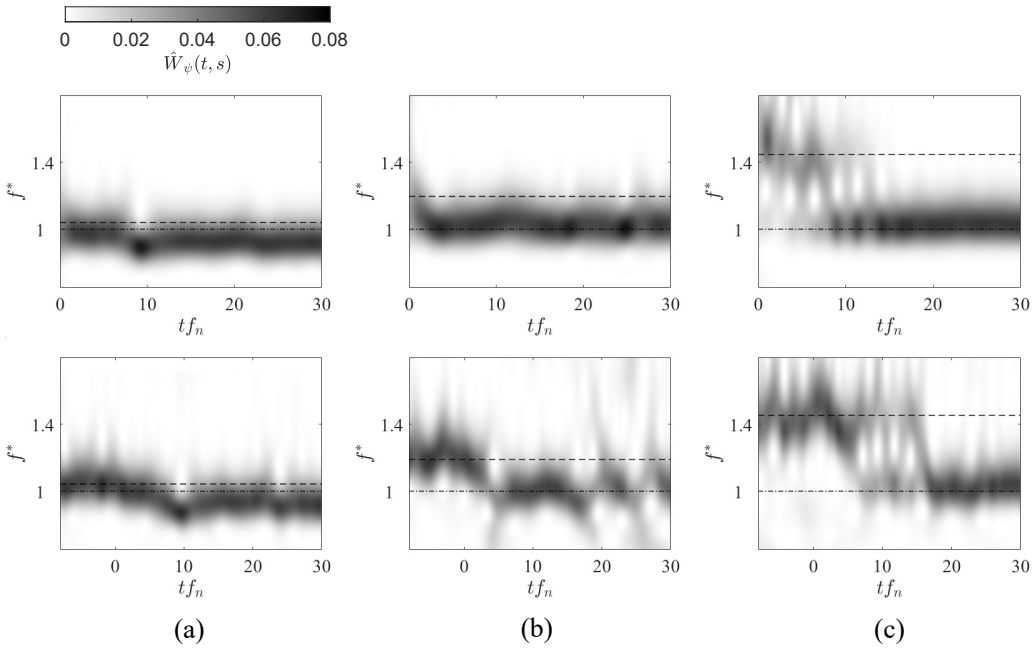

Figure 5.16: Single realization transient of the normalized wavelet scalogram of vortex forcing (top row), and normalized wavelet scalogram of transverse velocity signal (bottom row) at $X/D \approx 4$ for (a) $U^* \approx 5.2$, (b) $U^* \approx 6.0$, and (c) $U^* \approx 7.2$, respectively.

8, prior to a full lock-in at $tf_n \approx 13$. During the time interval between $8 \lessapprox tf_n < 13$, both the von Kármán and natural frequency components appear in the results. The scalogram is comparable to figure 5.6, highlighting a gradual changeover from the von Kármán to the natural frequency forcing mechanisms. A similar distribution of energy is observed in the wavelet scalogram of the wake velocity in the bottom row of figure 5.16(c). Since the chosen point is downstream of the vortex formation region, and velocity fluctuations resulting directly from cylinder oscillations are minimal for $tf_n \lessapprox 13$ (where the amplitude of oscillations are less than $0.1D$), the occurrence of distinct energy bands at both natural and von Kármán frequencies indicates the passage of wake structures at both frequencies. It can be deduced that in the time period prior to complete lock-in ($tf_n \approx 13$ in this case), the cylinder motion induces shear layer deflection that disrupts the von Kármán shedding mechanism and promotes the shedding of structures at frequencies near the structure's natural frequency. The shedding of these structures contributes to positive energy transfer to the cylinder and amplitude growth. The larger shear layer deflections associated with amplitude growth increasingly influence the vortex shedding, culminating in lock-in, where opposite shear layer impingement dominates the shedding mechanism.

5.6 Discussion

The examination of the wake dynamics (section 5.5), in conjunction with the forcing characteristics (section 5.4) and transient frequency response (section 5.3), provides an insight into

the fluid-structure interactions throughout the transient system response. As seen in figures 5.16 (bottom row) for $tf_n < 0$, the dominant frequency in the wake is associated with von Kármán shedding prior to cylinder release. Across all branches, nonlinear forcing is initiated at different times after cylinder release, resulting in a response that differs from a linear system response (equation 5.1). The forcing experienced by the cylinder at von Kármán frequency prior to release (figure 5.16, bottom row for $tf_n < 0$) results in an initial displacement that disrupts the prevailing von Kármán pinch-off mechanism. For $U^* \approx 5.2$ (initial branch), the proximity of the von Kármán and natural frequencies (figure 5.5(a)) promotes rapid lock-in within a few cycles where the vortex pinch-off is facilitated through the impinging shear layers. The phase difference between vortex forcing and displacement (figure 5.8(a)) is initially slightly below 90°, leading to a lock-in frequency below natural frequency ($f^* \approx 0.98$). Further, $\phi_v \approx 90°$ enables near maximum net energy input to the cylinder per cycle that results in the largest initial amplitude growth rates (figure 5.4(a)) during the transients in the initial branch of VIV. Near peak oscillation amplitudes (figure 5.10(a), $(t-\tau)f_n \approx 10$), a change in the timing of vortex shedding results in a brief period of negative energy transfer and subsequently a new equilibrium state at the end of the transient. While the wake topology remains similar to 2S throughout the transient, a brief period of $2P_0$ shedding is observed near peak oscillation amplitudes, prior to the change in timing of vortex shedding.

For $U^* \approx 6.0$ (upper branch), despite an increased separation between von Kármán and natural frequencies ($\approx 20\%$), lock-in is established within approximately four cycles (figure 5.5(b)). Following lock-in, ϕ_v increases from approximately 120° to 160° (figure 5.8(b)). Consequently, the lock-in frequency exceeds the natural frequency ($f^* > 1$) throughout the transient, and the amplitude growth rates are lower than those for the initial branch case (figure 5.4(a)). With increasing oscillation amplitudes, the initial 2S shedding is eventually replaced by the 2P mode, along with a notable reduction in the vortex formation length. As the oscillation amplitudes increase and the formation length decreases further, the trailing vortex strength gradually diminishes.

For $U^* \approx 7.2$ (lower branch), the larger separation between natural and von Kármán frequencies (approximately 40 %, figure 5.5(c)) results in a notably delayed onset of lock-in ($(t-\tau)f_n \approx 14$). The vortex force phase difference continuously increases from approximately 140° following lock-in to the quasi-steady value close to 180° (figure 5.8(c)). Similar to the $U^* \approx 6.0$ case, the lock-in frequency consistently exceeds the natural frequency ($f^* > 1$) throughout the transient. However, the amplitude growth rates are notably lower than those in the upper branch (figure 5.4(c)) owing to the increased separation of ϕ_v from the optimal value of 90 °. Similar to the transient in the upper branch, as the cylinder oscillations increase in amplitude, 2P shedding begins, and the vortices form progressively closer to the cylinder, with the 2P mode persisting until quasi-steady state.

For all the cases examined, wavelet analysis of the transverse velocity fluctuations at the wake centerline for individual trials revealed a good match with the forcing frequency behavior (figure 5.16), establishing a link between the large-scale vortex shedding and

forcing behavior on the cylinder. Moreover, the onset of lock-in behavior is more readily identified through analysis of the dynamics in a single realization, particularly for the lower branch case. Specifically, the time period prior to lock-in ($(t-\tau)f_n \lessapprox 14$ for $U^* \approx 7.2$, figure 5.16(c)) is characterized by the presence of two dominant frequencies centered around the natural and von Kármán frequencies in both the forcing and velocity signals. A gradual changeover from the more dominant von Kármán to the natural frequency component takes place up to lock-in (figure 5.7). Physically, the progressive increase in deflection of the shear layers accompanying the growing oscillation amplitudes results in a more pronounced effect on the timing of vortex pinch-off and diminishes the importance of the von Kármán shedding mechanism [60].

The transient structural and wake characteristics have been examined for all response branches. However, in the context of practical applicability, the prediction of transient VIV response is important. While transient response prediction has been briefly explored in previous studies for example [125] and [115], it remains to be investigated in more detail. Morse and Williamson [125] and Menon and Mittal [115] used energy maps created from forced vibration data to predict free vibration response. Specifically, for a given combination of vibration amplitude A and frequency f, the average energy extracted from the flow over one forced oscillation cycle (E^*) is calculated. Subsequently, detailed contour maps can be generated that show how E^* varies with A and f. Through nondimensionalization using cylinder diameter and flow velocity, E^* can be expressed as a function of A^* and a wavelength parameter $\lambda^* = U/fD = U^*/f^*$. In the present experiments, the range of amplitudes and frequencies encountered during the transient response across all branches falls within the bounds of the detailed contour maps from Morse and Williamson[123], thereby allowing for a comparison of the energy extracted at each A^* and λ^*. To this end, the transient response at each representative U^* is first mapped onto the amplitude-wavelength plane. Specifically, the ensemble-averaged peak amplitude (A/D, figure 5.3(c)), and associated oscillation frequency (f^*, figure 5.5) are extracted at each cycle. These values are then plotted on the amplitude-wavelength plane as shown in figure 5.17(a) in red dots. For all reduced velocities, the red dots outline the system state trajectory starting from rest ($A = 0$, approximate location marked in blue dots in figure 5.17(a)) up to the respective quasi-steady states. In other words, each circle represents the location of the system in the amplitude-wavelength plane during the transient.

For $U^* \approx 5.2$, the trajectory expectedly captures the amplitude overshoot, however, there is a noticeable increase in wavelength through the trajectory due to the decreasing frequency between the initial and final lock-ins (figure 5.5). In contrast, the trajectories for $U^* \approx 6.0$ and 7.2 map a relatively straight path up to quasi-steady state owing to the relatively stable lock-in frequencies. Using the mapped trajectories, the energy extracted by the cylinder between successive points (red dots) can be obtained from figure 5.8. The results are presented in figures 5.17(b-d) and compared to estimates obtained from quasi-steady forced vibrations at the same point in the amplitude-wavelength plane by interpolating values of $C_Y sin(\phi)$ from the maps of [123], and applying equation 2.5. The results show

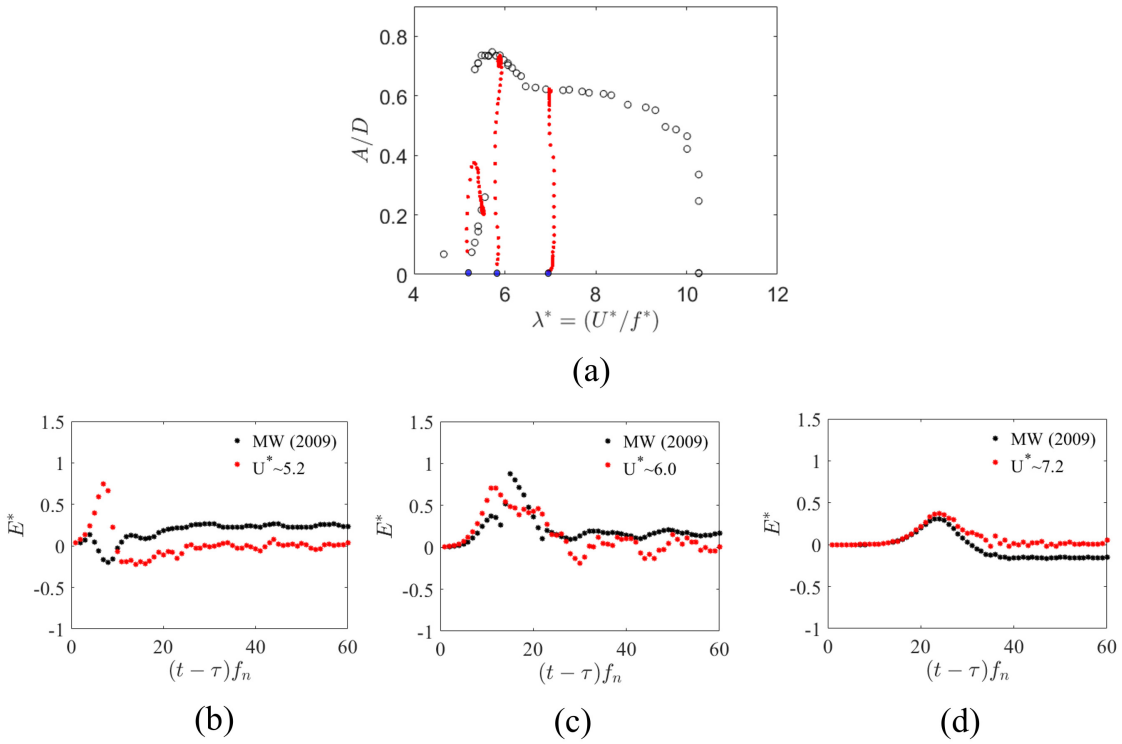

Figure 5.17: Energy transferred over one cycle through the cylinder's trajectory in the amplitude-wavelength plane. (a) Trajectory at all representative U^* with the start identified through blue markers and (b-d) comparison of energy extracted with forced vibration data from [124].

that for $U^* \approx 5.2$ (initial branch), the predictions based on quasi-steady forced vibration (black dots) differ significantly from the actual transient. Conversely, for $U^* \approx 6.0$ and 7.2, a progressively closer match is observed.

For $U^* \approx 5.2$, the forced vibration data indicates predominantly negative energy extraction within $2 \lessapprox (t-\tau)f_n \lessapprox 11$. The negative values result from the trajectory entering regions of negative excitation for forced vibrations. For $U^* \approx 6.0$, the forced vibration data shows continuous positive energy transfer during the initial transient, but notable differences are still observed. In particular, the slope of the graph is larger in the transient experiments compared to predictions, resulting in a delayed energy peak. For $U^* \approx 7.2$, the energy input to the cylinder, including the timing and magnitude of the peak, matches relatively well with predictions. The non-zero energy values at quasi-steady state in the forced vibration data for all cases are speculated to be due to the differing Re between the present experiments ($Re \approx 4{,}400$) and the forced vibration data ($Re = 4,000$), since zero-energy isoline positioning is sensitive to Re [123]. The progressive improvement of the agreement between actual data and estimates from quasi-steady results correlates with the increase in the duration of the transient from the initial to lower branches of response. For the

initial branch case ($U^* \approx 5.2$), the largest amplitude growth rates are observed, leading to a relatively rapid transient and more dynamic changes to the wake characteristics. As the growth rates decrease in the upper branch and the duration of the transient increases, a better agreement with the quasi-steady predictions is attained. Ultimately, the best match is observed in the lower branch, where a slower transient process facilitates a better agreement with quasi-steady state-based estimates.

5.7 Concluding remarks

This study conducted an experimental investigation into the transient dynamics of an elastically mounted cylinder released from a stationary state in a steady freestream flow. The cylinder's motion was constrained to one degree of freedom transverse to the incoming flow. The Reynolds number was maintained at approximately 4,400, while reduced velocities were varied within $4.5 < U^* < 11.5$ by adjusting the structure's natural frequency. Simultaneous cylinder displacement and two-component velocity field measurements were used in conjunction with force estimation to characterize reference quasi-steady states, and transient system responses. The transient development of VIV was investigated for a range of reduced velocities spanning the three response branches.

For the transient response in the initial branch, a notable overshoot of amplitude is observed approximately ten cycles after cylinder release, followed by a gradual convergence to quasi-steady state. Conversely, for transients in the upper and lower branches, a continuous growth of amplitudes to quasi-steady state is observed with the amplitude envelopes resembling sigmoid curves. Within each response branch, different trials exhibit similar trends, particularly during the periods of most significant amplitude growth. However, the timing of the onset of sustained amplitude growth differs between the trials, resulting in the amplitude envelopes being separated by a time delay, and the variability in the onset of substantial amplitude growth, on the average, increases with increasing U^*. Further, the time to attain quasi-steady state increases, while the maximum amplitude growth rate decreases, with increasing U^*.

The analysis of the results shows that lock-in behavior, characterized by the dominant forcing and displacement frequencies assuming a common value, occurs within two and up to a maximum of four cycles following cylinder release for the initial and upper branch transients, respectively. This is linked to the relatively small separation between the initial von Kármán shedding frequency and the natural frequency of the structure in these branches. In contrast, in the lower branch, as the natural and von Kármán frequencies become more separated, the vortex forcing exhibits a dual-frequency response for a longer time period, delaying the onset of lock-in. The departure of forcing from primarily von Kármán frequency marks the onset nonlinear forcing, associated with lock-in, which is shown to be crucial for sustained amplitude growth.

The observed changes in the growth rate of vibrations amplitude in different response branches are shown to be linked to distinct changes in both the vortex force magnitude and phase difference with respect to cylinder oscillations, with the latter playing a more dominant role. Specifically, near the transition between the initial and upper branches, the vortex force phase difference ϕ_v is initially close to 90°, facilitating the most efficient energy transfer to the structure and, hence, the fastest increase in vibration amplitudes compared to the other U^*. The decrease in transient amplitude growth rates with increasing U^* is attributed to increasing separation of initial vortex force phase difference from the optimal 90° following lock-in.

Analysis of the wake flow development was employed to establish a relationship between the transient wake dynamics and the associated structural responses in each response branch. Specifically, the vortex force phase difference is linked to the timing of vortex shedding with respect to the cylinder oscillation cycle, with changes in the timing of shedding shown to mimic the changes in ϕ_v. Additionally, the onset of nonlinear forcing is identified through the emergence of wake vortex shedding near the structural natural frequency in addition to the dominant von Kármán shedding. The onset of cylinder oscillation results in shear layer deflections that disrupt the von Kármán shedding mechanism by promoting opposite shear layer impingement. With growing oscillation amplitude, more significant deflections of the shear layers increasingly affect the vortex shedding process, progressively diminishing the significance of the von Kármán shedding mechanism up to lock-in. Further, the transition between different vortex shedding modes is identified throughout the transients in each response branch.

The possibility of modeling the transient response based on available data for quasi-steady forced vibrations was explored. The results show a significant difference in cycle-to-cycle energy extraction predictions compared to experimental measurements for the transients in the initial branch. However, the agreement with experiments progressively improves for the transients in the upper and lower branches. This is associated with the increase of the transient duration and decrease in transient amplitude growth rates with increasing $U*$. Thus, employing existing quasi-steady state databases is expected to provide notably better modeling capabilities of the transient system response for the upper and particularly lower branch, compared to the initial branch.

Chapter 6

Transient vortex-induced vibrations of a cylinder in unsteady freestream conditions

Experiments are conducted at LTRAC to evaluate system behavior when subjected to various ramp up/down changes in the freestream velocity. The results indicate a departure of system characteristics from quasi-steady behavior when the freestream transient period is on the order of tens of cylinder oscillation cycles. Quantitative analysis of the wake and structural response reveals a relatively fast initial response to the changes (within approximately 20 cycles of oscillation), with the subsequent transient response closely related to the forcing characteristics (primarily phase difference) and consequently, the energy transfer between the fluid and the structure. Topological changes to the wake are identified through the transients. Additionally, significantly slower variations in the freestream ($O(100)$ cycles) allowed the system to approach quasi-steady behavior.

6.1 Quasi-steady state system characteristics

The quasi-steady system amplitude response (A^*_{mean}), frequency response (f^*), and mean vortex force phase difference (ϕ_v) are presented in figures 6.1(a-c), respectively. Data collected while increasing U^* incrementally are shown in black circles, while the gold square markers represent the system characteristics for decreasing U^*. The amplitude response (figure 6.1(a)) features the expected response branches for a low mass-damping system, including the initial branch (IB, $3.9 \lessapprox U^* \lessapprox 5.3$), upper branch (UB, $4.9 \lessapprox U^* \lessapprox 6.5$), lower branch (LB, $6.5 \lessapprox U^* \lessapprox 9.5$), and desynchronization regimes (Dsnc, $U^* \gtrapprox 9.5$). Details of the response characteristics within each branch are described in Section 5.1. Additionally, hysteresis was observed in the IB-UB transition region during the LTRAC experiments [1], similar to previous studies (e.g., [83]). In particular, for increasing U^* (black markers), the initial branch persists up to $U^* \approx 5.3$ with mean amplitudes reaching up to $A^*_{mean} \approx 0.3$ (figure 6.1(a)). Additionally, the mean phase difference remains close to 0° (figure 6.1(c)) and $f^* < 1$ (figure 6.1(b)) up to $U^* \approx 5.3$. Conversely, for decreasing U^* (gold square markers), high-amplitude oscillations ($A^* \gtrapprox 0.65$) persist for U^* as low as 4.9. While the oscillation amplitudes remain high, the nondimensional frequency indicates a switch to $f^* < 1$ towards the end of the hysteresis curve for decreasing U^* (gold square markers within $4.9 \lessapprox U^* \lessapprox 5.1$). This indicates a switch in mean vortex force phase difference to near 0°, however, mean phase estimations were unreliable in this region due to phase slips [47] which are discussed later. The hysteretic region is discussed in more detail in Appendix B. Overall, the oscillation amplitudes, range of synchronization, and frequency/phase characteristics agree well with previous literature at similar $m^*\zeta$ (e.g., [83]).

6.2 Transient amplitude response

Figure 6.2 depicts the transient amplitude response of the system when subjected to a fast ramp in freestream velocity (see section 3.2.4 for details on the fast ramp) for all cases investigated. The black lines represent the envelopes of peak oscillation amplitudes for individual trials, the green lines represent the ensemble average of the envelopes across all the trials, and the red lines indicate the associated quasi-steady state response (figure 6.1(a)) for the imposed velocity changes. Additionally, the vertical dashed lines indicate the start and end of the freestream velocity ramp period (freestream transient). The top and bottom rows depict increasing and decreasing U^* cases, respectively.

Across all of the cases examined except the UB-IB case, it is apparent that the system transient behavior deviates from the associated quasi-steady responses (red lines). The IB-UB case (figure 6.2(a)) reveals a continuous amplitude increase between the two quasi-steady

[1] The experiments at FMRL did not reveal hysteresis behavior likely due to the way U^* was changed. Specifically, to achieve a change in U^*, the structure was brought to rest following which the position of the springs was changed. This change in the system state presumably negated any hysteresis effect.

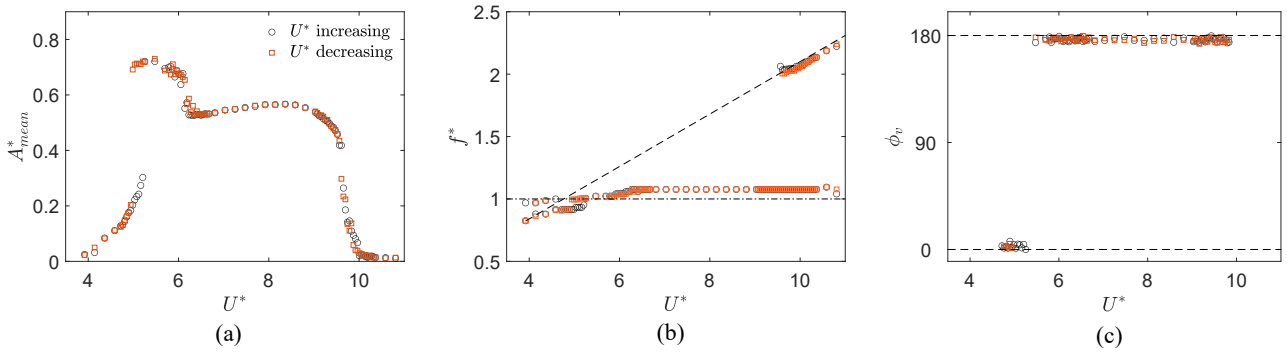

Figure 6.1: Quasi-steady state system characteristics. (a) Mean amplitude response calculated as the mean of all peaks in a time series, (b) frequency response calculated using spectral analysis of the displacement signal, and (c) mean vortex force phase difference obtained through the application of the Hilbert transform [83]. The uncertainty in all quantities is accommodated by the marker sizes. Black markers signify increasing U^* while gold markers signify decreasing U^*.

end states, with the envelopes exhibiting a sigmoidal shape and the different trials appearing to be separated by a relatively small time delay. Most of the amplitude growth occurs within the free stream transient period (between the vertical dashed lines). The associated quasi-steady response (red line) shows the drastic jump in mean amplitudes characteristic of the quasi-steady IB-UB transition (figure 6.1(a)). Conversely, the transient response indicates a more gradual and continuous increase in amplitudes. The UB-IB transition (figure 6.2(d)) reveals two distinct behaviors. In most trials, the cylinder exhibited a small amplitude drop and remained in a high-amplitude hysteresis state ($A^* \approx 0.65$) found at the end of the IB-UB transition for reducing U^* (gold square markers in figure 6.1(a)). Conversely, in approximately 10% of all trials, the oscillation amplitudes continued to decay until they reached the corresponding initial branch quasi-steady state ($A^* \approx 0.17$). The timing of the onset of this second reduction in amplitude varied significantly. The seemingly spontaneous amplitude decay to the initial branch suggests that the high-amplitude state may be in unstable equilibrium. It is worth noting that the quasi-steady end state after the freestream transient is situated towards the end of the hysteresis loop for decreasing U^* in the quasi-steady state response (figure 6.1(a)). Moreover, this region falls within the unstable equilibrium zone identified in a previous study based on energy maps [124]. For the UB-IB case, the ensemble average (green line) was calculated based only on the trials that remained at the high-amplitude state through the data collection period. The ensemble average matches well with the quasi-steady response curve (red line).

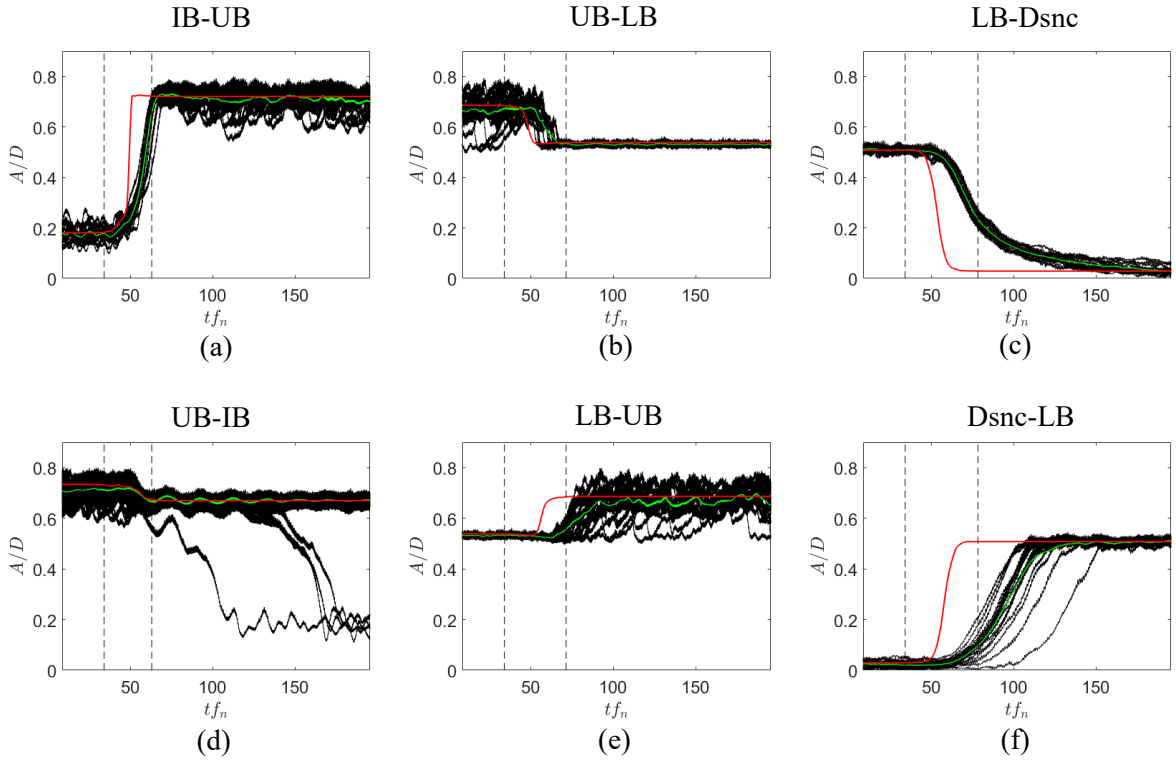

Figure 6.2: Transient amplitude envelopes across all trials for the fast ramp cases (see section 3.2.4 for details on the fast ramp). The red lines represent the quasi-steady amplitudes at the corresponding freestream velocities. The green lines represent the ensemble averages of all trials. The vertical dashed lines demarcate the period of freestream velocity change (freestream transient).

The UB-LB transition case (figure 6.2(b)) shows a relatively rapid amplitude decay for all trials within the freestream transient period. While the rate of decay appears similar between the trials, the onset of the decay occurs at slightly different times. Notably, this behavior is similar to what is observed during intermittent switching reported in the quasi-steady upper branch [203]. This is illustrated by examining the envelopes of two trials that exhibit this amplitude decay from UB to LB values before the start of the freestream transient ($tf_n \approx 15$ and 20 in figure 6.2(b)). The rate of amplitude decay in these two instances is similar to that observed in all trials during the freestream transient. The amplitude decay for all trials occurs after the quasi-steady response reaches its end state (red line). For the LB-UB case(figure 6.2(e)), all the trials show a gradual increase in amplitudes to the upper branch. The amplitude growth rate remains similar across all trials. Contrary to the UB-LB case, the onset of amplitude growth for all trials in the LB-UB case occurs near or after the end of the freestream transient when the quasi-steady state amplitudes have already reached their end state. The amplitude growth rate is similar to that observed in the intermittent switching behavior in the upper branch. The similarities between transient responses for both UB-LB and LB-UB cases and intermittent switching behavior are further explored during the discussion of the transient forcing characteristics

(section 6.3).

The transients in the LB-Dsnc case (figure 6.2(c)) reveal a steady amplitude decay across all trials, with the envelopes exhibiting an inverse sigmoid curve. The onset of amplitude decay occurs within the freestream transient period around the time that the quasi-steady response is near its end state. The amplitude decay rate decreases asymptotically with the decay continuing well after the end of the freestream transient. The Dsnc-LB case (figure 6.2(f)) reveals a continuous amplitude growth across all trials with the envelopes resembling sigmoid curves. The onset of significant amplitude growth occurs either toward the end or after the freestream transient. Additionally, the periods of most significant amplitude growth occur after the quasi-steady response has reached its end state. Contrasting with the low variance in the onset of amplitude decay across different trials in the LB-Dsnc case, the onset of sustained amplitude growth for different trials in the Dsnc-LB case shows a substantial variability.

Figure 6.3 shows the transient amplitude responses of the system when subjected to the slow ramp in freestream velocity (up to 20 times slower than the fast ramp cases). In general, the transient responses are observed to follow the quasi-steady responses more closely compared to the fast ramp cases. Additionally, the transient amplitude changes occur well within the bounds of the freestream transients (dashed vertical lines). The IB-UB transition (figure 6.3(a)) shows the envelopes attaining larger amplitudes in the initial branch ($A^* \approx 0.3$, compared to $A^* \approx 0.25$ in the fast ramp case) before the rapid increase in amplitude to upper branch values. The UB-IB (figure 6.3(d)) transition shows all the trials remaining in the high-amplitude hysteresis state following the freestream transient. The UB-LB (figure 6.3(b)) case reveals an amplitude decay similar to the fast ramp cases that also occurs after the quasi-steady response attains lower branch amplitudes. Additionally, for the trials with the most delayed onset of the amplitude decay, a period of relatively stable amplitudes in between the two quasi-steady states is observed ($500 \lessapprox t f_n \lessapprox 600$). The LB-UB (figure 6.3(e)) case reveals a gradual increase in oscillation amplitudes with the trend closely resembling the quasi-steady response. Finally, the LB-Dsnc and Dsnc-LB cases (figures 6.3(c,f)) follow the quasi-steady curves relatively well.

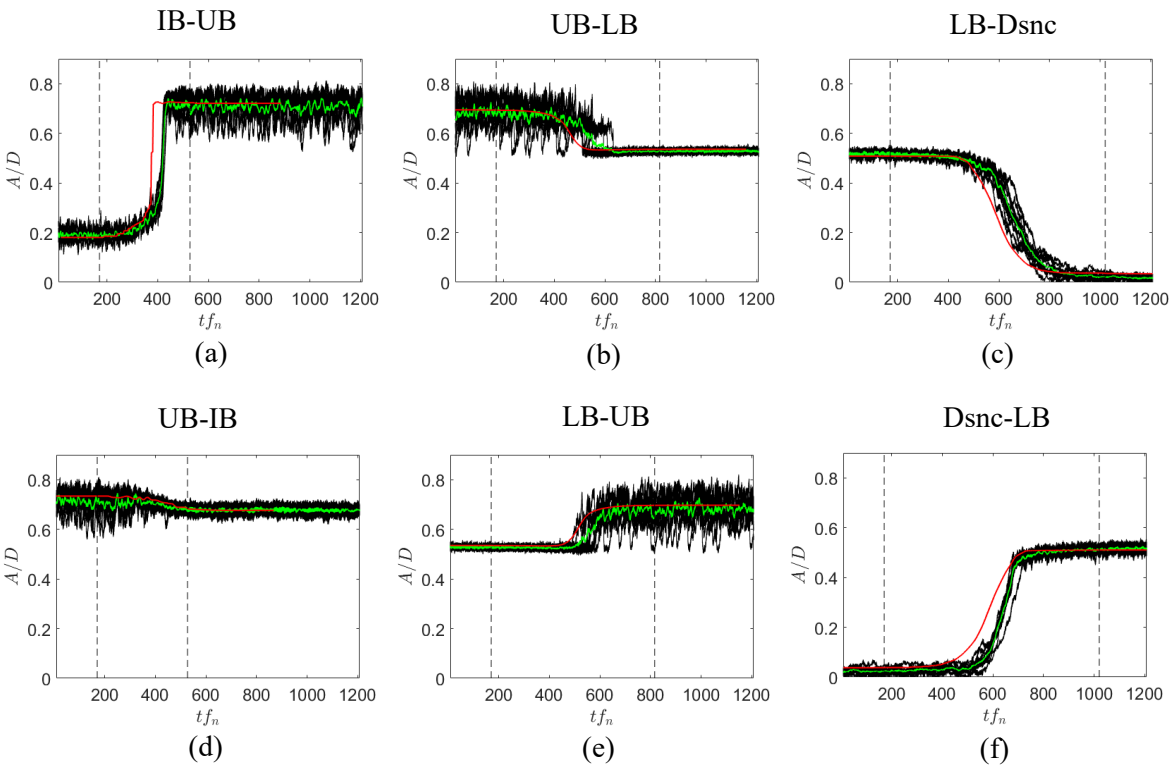

Figure 6.3: Transient amplitude envelopes for all trials across the branches for slow ramp cases (see section 3.2.4 for details on the slow ramp). The red lines represent the quasi-steady amplitudes at the corresponding freestream velocities. The green lines represent the ensemble averages of all trials. The vertical dashed lines demarcate the freestream transient period.

In addition to the different transient behaviors outlined above, it is of interest to estimate the time taken by the system to transition between two quasi-steady states in response to a change in freestream conditions. To this end, a "transient time" was estimated for each case. Specifically, the mean (A_{mean}) and standard deviation (A_σ) of all amplitude peaks at the initial and end quasi-steady states are calculated over approximately 400 cycles of quasi-steady VIV. Limiting thresholds between the quasi-steady end states are then defined as $A_{mean} \pm 2 \times A_\sigma$. Following this, a moving average is calculated for each transient trial using a temporal window length of approximately five oscillation cycles. The transient time (t_t) is defined as the period when the moving average lies between the two quasi-steady thresholds. Figures 6.4(a) and (b) depict the nondimensional transient start and end times for all the cases except the UB-IB case for the fast and slow ramp cases, respectively. The start times are represented using open symbols while the end times are shown by filled symbols. Figures 6.4(c) shows the total transient time for both fast (yellow) and slow (magenta) ramps while figure 6.4(d) shows the transient time as a percentage of the corresponding quasi-steady transient time. Transient times for the UB-IB case did not yield reasonable results using this method primarily due to the proximity of the two quasi-steady end states. Each case in figures 6.4(a) and (b) consists of three elements:

- The freestream transient duration (the period between the vertical dashed lines in figures 6.2 and 6.3), represented here as yellow (fast ramp) and magenta (slow ramp) shaded regions.
- Start and end times for the quasi-steady response (red lines in figures 6.2 and 6.3). These are obtained using the methodology described above and marked by dashed-dotted lines.
- Start and end times for the actual response. These are shown as open and filled markers, respectively, and the error bars represent one standard deviation of the start and end times across all trials.

The subsequent discussion will include elements from all four plots in figure 6.4. The discussion of start and end times of the transient and quasi-steady responses pertain to figures 6.4(a) and (b). The total transient time of the response (time between the markers) is presented in figure 6.4(c). Finally, figure 6.4(d) presents the transient time estimates normalized by the quasi-steady transient time.

A brief examination of the mean transient start and end times for the fast ramp (open and closed markers in figure 6.4(a)) reveals significant variance across all the examined cases. The mean end time (upper closed marker) for the IB-UB case is located just outside the end of the freestream transient periods (yellow-shaded region). The mean start time (lower open marker) is near its corresponding quasi-steady transient start time (lower dashed-dotted line). However, the total transient time of approximately 16 cycles (figure 6.4(c)) is notably larger than the associated quasi-steady transient time (approximately five times longer, figure 6.4(d)). The shorter transient time for the quasi-steady response is reflective of the distinct jump between the initial and upper branches. The actual transient response, however, is characterized by a more gradual, continuous growth of oscillation amplitudes between the two end states. Additionally, the relatively small standard deviations (approximately 2 cycles) reflect a tight window between the onset and end of the transient response across all trials.

The mean start and end times in the UB-LB fast ramp case (figure 6.4(a)) are within the freestream transient period, however, the start time lies above the associated quasi-steady end time. Notably, the total transient time (7 cycles figure 6.4(c)) is shorter than the corresponding quasi-steady transient time (figure 6.4(d)). Here, the switch from the upper to lower branch is similar to intermittent switching behavior characterized by a relatively rapid drop in amplitudes. Conversely, the quasi-steady response for UB-LB is characterized by a comparatively gradual reduction in oscillation amplitudes. Finally, the larger standard deviations (between 5 and 7 cycles) compared to the IB-UB case indicate a larger variability in the onset of the transient behavior (intermittent switching) across all trials. The LB-UB case (figure 6.4(a)) shows the mean start time near the end of the freestream transient and a total transient time of approximately 10 cycles (figure 6.4(c)), which is about 25% longer than the corresponding quasi-steady transient time (figure 6.4(d)). Similar to the UB-LB

case, the transient behavior resembles intermittent switching, with the amplitude growth rate lower than the quasi-steady growth rate for the associated freestream velocity change, thus resulting in slightly longer transient times. In this case, the standard deviations are relatively large (approximately 10 cycles).

The LB-Dsnc fast ramp case shows the longest mean transient times (nearly 70 cycles, figure 6.4(c)) with the onset of the transient (lower open marker) near the end time for the quasi-steady response (upper dashed line). The transients across all trials are initiated within approximately 4 cycles of each other, signifying a nearly consistent response to the changing freestream. However, the end time has a larger standard deviation (approximately 13 cycles, figure 6.4(a)). This is due to the system transitioning into desynchronization where the cylinder exhibits significant amplitude modulations relative to the mean amplitudes. Consequently, different trials cross the lower quasi-steady thresholds at different times. Overall, the LB-Dsnc fast ramp case has the longest relative transient time (approximately 6 times longer than the associated quasi-steady response, figure 6.4(d)). The Dsnc-LB fast ramp case also exhibits a relatively long transient time (45 cycles, figure 6.4(c)) with the largest standard deviation (15 cycles, figure 6.4(a)) in both the mean start and end time. The relative transient time is over four times the associated quasi-steady response (figure 6.4(d)). The mean start times are near the end of the freestream transient when the quasi-steady response has already reached its end state. While the trend in the transient amplitude growth remains similar across all trials (figure 6.2(f)), the large spread in transient times is attributed to the differences in the timing of onset of sustained amplitude growth (figure 6.2(f)).

For the slow ramp cases, the mean start and end times (figure 6.4(b)) fall well within the bounds of the freestream transients (magenta shaded region). While the total transient times in all cases are longer than those from the fast ramp cases (figure 6.4(c)), the relative transient times in the IB-UB, LB-Dsnc, and Dsnc-LB cases are closer to 100%, reflecting the increasingly quasi-steady nature of the responses. While both UB-LB and LB-UB slow ramp cases also indicate behavior that signifies a more quasi-steady response, the current estimations of transient time do not reflect that due to the adopted methodology. As an example, consider the transient amplitude response in the slow ramp for the UB-LB case (figure 6.3(b)). The ensemble-averaged amplitude envelopes (green line) indicate a steady decrease in mean amplitudes before the rapid drop associated with intermittent switching while the quasi-steady response (red line) is still decreasing in amplitude. This small decrease in mean amplitudes still falls within the quasi-steady threshold for upper branch oscillations ($A_{mean} \pm 2 \times A_{\sigma}$), thus not registering as the start of the transient. However, the increasingly quasi-steady nature of the response in the UB-LB and LB-UB cases is more apparent in the subsequent discussion (associated with figure 6.5).

Overall, the transient time estimates affirm the qualitative trends observed in the amplitude responses for the fast and slow ramp cases (figures 6.2 and 6.3). Specifically, the longest transient times are observed in the LB-Dsnc and Dsnc-LB cases for both fast and slow

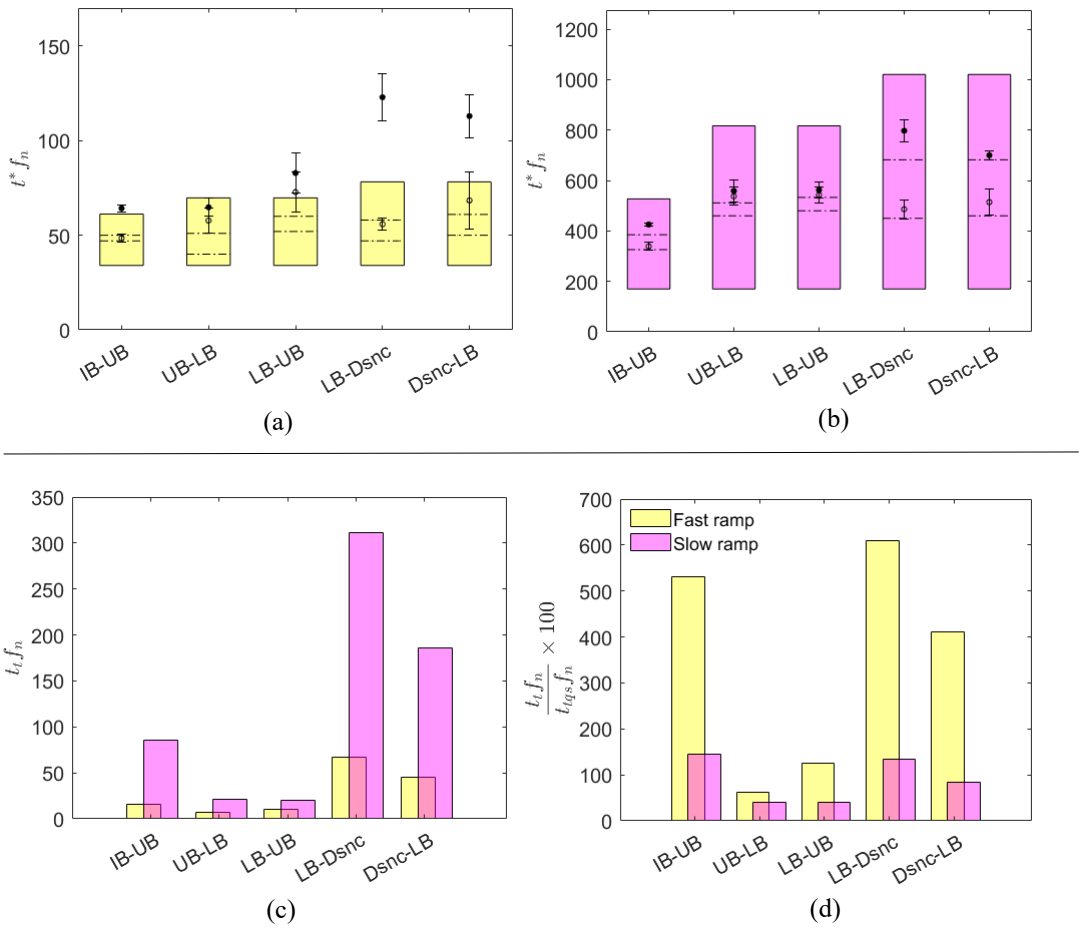

Figure 6.4: Estimations of transient start (open symbols) and end times (filled symbols) for (a) fast ramp and (b) slow ramp cases, respectively. The shaded regions indicate the freestream transient period with the yellow representing the fast ramp and the magenta representing the slow ramp. The dashed-dotted lines indicate the transient time of the quasi-steady response, estimated using the same methodology. (c) The total nondimensional transient time for each case, and (d) transient time as a percentage of the associated quasi-steady transient time.

ramps. Conversely, the shortest times are observed in the UB-LB and LB-UB cases, due to the proximity of the mean amplitudes at the two end states along with the nature of the transient responses exhibiting behavior similar to intermittent switching. While the relative transient time provided evidence of some of the cases (IB-UB, LB-Dsnc, and Dsnc-LB) exhibiting increasingly quasi-steady responses for the slow ramp cases, the UB-LB and LB-UB transient times estimates did not follow this trend due to the limitations of the estimation methodology.

Examination of the transient amplitude responses in both fast and slow ramp cases revealed the different ways in which the system transitions between two quasi-steady end states.

However, it is of interest to visualize the extent to which system behavior deviates from quasi-steady behavior when subjected to changing freestream conditions. To this end, the system response is mapped onto the $A^* - U^*$ plane for both fast and slow ramp cases. Specifically, at each instant in time, the nondimensional ensemble-averaged amplitude is plotted against the reduced velocity corresponding to the instantaneous freestream velocity. The resulting locus of points maps the "trajectory" of the system in the $A^* - U^*$ plane. Figure 6.5 presents the resulting system trajectories for both the fast ramp (yellow lines) and the slow ramp (magenta lines) cases, respectively. In all cases except the UB-IB transition, the slow ramp trajectories (magenta lines) fall closer to the quasi-steady response markers (open symbols) through the transient. Notably, the increasingly quasi-steady nature of the response to the slow ramp in the UB-LB and LB-UB cases is also captured here. Overall, slower changes in freestream velocity allow more time for the system to adjust to its new state, thus more closely approximating quasi-steady behavior. However, the results show that the transient response does not completely match the quasi-steady response for the slow ramp case. Specifically, for the current system ($m^* \approx 10$), even relatively slow rates of change in freestream velocity (change in U^* of 1 per approximately 600 oscillation cycles) result in transient responses that differ from quasi-steady state. For the fast ramp cases (yellow lines), the deviation from quasi-steady curves is more pronounced. This is most evident in the LB-Dsnc and Dsnc-LB cases. In particular, the shapes of the trajectories signify minimal change in A^* while U^* is rapidly changing during the initial transient period. A similar but less exaggerated deviation from quasi-steady response is observed in the UB-LB and LB-UB fast ramp transients. The IB-UB fast ramp transient also deviates from quasi-steady response more than the slow ramp case. The UB-IB case for both fast and slow ramps shows the closest match to the quasi-steady response.

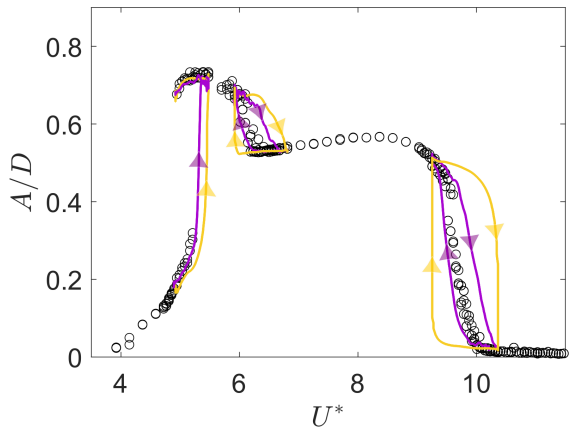

Figure 6.5: Transient system trajectories in the $A^* - U^*$ plane. The yellow lines depict the fast ramp cases while the magenta lines depict the slow ramp cases.

In summary, examination of the transient amplitude responses in the fast ramp cases revealed the different ways in which the system transitions from one quasi-steady state to another (e.g., intermittent switching in UB-LB, inverse sigmoid in Dsnc-LB). Moreover, decreasing the mean acceleration rates (slow ramp) showed that, while the system transients increasingly approached quasi-steady behavior, the nature of the responses between the two quasi-steady end states remained similar to the fast ramp cases. Estimations of the transient times provided quantitative evidence of the different trends outlined in the amplitude responses. To shed more light on the mechanisms driving the different responses across all the examined cases, an analysis of the forcing characteristics is carried out next. From this point, attention will be paid to only the fast ramp cases as the inferences drawn can be extended to the slow ramp cases.

6.3 Transient forcing characteristics

Figure 6.6 displays the ensemble-averaged forcing characteristics for all cases except the UB-IB transition (the dual response nature of this case is explored separately in the subsequent discussion). The procedure for ensemble averaging utilized the similarity in the nature of the transient amplitude responses (figure 6.2) across all trials for each case by temporally shifting each trial to a common datum. Specifically, cross-correlation analysis of individual time series was used to estimate the "time lag" (τ) between the transient responses across individual trials in each case. This time lag was computed relative to the trial with the earliest transient onset in each data set. To align the trials, each trial was temporally shifted by the difference between its individual time lag relative to the leading trial and the mean time lag across all trials. This ensemble averaging procedure is the same as the one used during the release from rest experiments (section 5.2), and provides a reliable statistical representation of the dynamics observed within each realization.

The left column in figure 6.6 displays the ensemble-averaged nondimensional vortex forcing magnitude (blue color) along with the ensemble-averaged cylinder displacement (gray). The ensemble-averaged phase difference between the vortex force and cylinder displacement is presented in the middle column, and the last column displays the ensemble-averaged signal energy (modulus square of the wavelet transform) of the vortex forcing signal. The signal energy at each instant is normalized by the total energy across all scales. The maximum energy magnitude is plotted in green, while the red line represents the equivalent maximum in the ensemble-averaged signal energy of displacement. In the first two columns, the shaded region represents ± one standard deviation based on the ensemble averaging.

The force magnitudes in the IB-UB case (left column in figure 6.6(a)) gradually increase after the onset of the freestream transient (first vertical dashed line). This is followed by a relatively sharp drop in force magnitudes at $(t-\tau)f_n \approx 55$, near the end of the freestream transient (right vertical dashed line). The drop in force magnitudes coincides with the period of most significant amplitude growth. Concurrently, the vortex force phase difference

(middle column) exhibits a rapid increase from near 0° to near 180°. The continuous positive values of the phase difference and passage through 90° (phase difference for most efficient energy transfer) promote sustained net positive energy transfer to the cylinder, resulting in rapid amplitude growth (equation 2.6). Prior to the freestream transient, the dominant force and displacement frequencies (green and red lines, last column in figure 6.6(a)) are well below the structure's natural frequency ($f^* \approx 0.92$) as a consequence of the phase difference being near 0°. During the period of most significant amplitude growth, the dominant forcing frequency exhibits a distinct overshoot followed by settling near the quasi-steady value where $f^* > 1$. The end quasi-steady state lock-in frequency is slightly higher than the structure's natural frequency as a consequence of a change in the sign of the effective added mass resulting from the change in forcing phase difference (equation 5.2). During the transient, The dominant displacement frequency (red line) gradually increases from the initial branch quasi-steady lock-in value ($f^* \approx 0.92$) to the final quasi-steady lock-in value.

The force magnitudes in the UB-LB case (figure 6.6(b), left column) continuously increase for approximately 15 cycles after the onset of the freestream transient. At $(t-\tau)f_n \approx 55$, the force magnitudes exhibit a distinct spike that coincides with the amplitude decay from the upper to the lower branch. Following the spike, the force magnitudes settle on a value larger than the quasi-steady upper branch force magnitudes. The drop in amplitudes also coincides with a slight overshoot of the phase difference (middle column) above 180°. This overshoot signifies a brief period of negative excitation, resulting in the amplitude decay. Following the overshoot, the phase difference stabilizes slightly below the 180° threshold, with a lower variance that is characteristic of the stable oscillations in the lower branch. The dominant forcing and displacement frequencies (figure 6.6(b), right column) increase from $f^* \approx 1.02$ to 1.05 near the drop in amplitudes. The increased separation of the lock-in frequency from the structural natural frequency is a consequence of larger forcing magnitudes on the cylinder while the phase remains close to 180°, thereby reducing the effective added mass (equation 5.2).

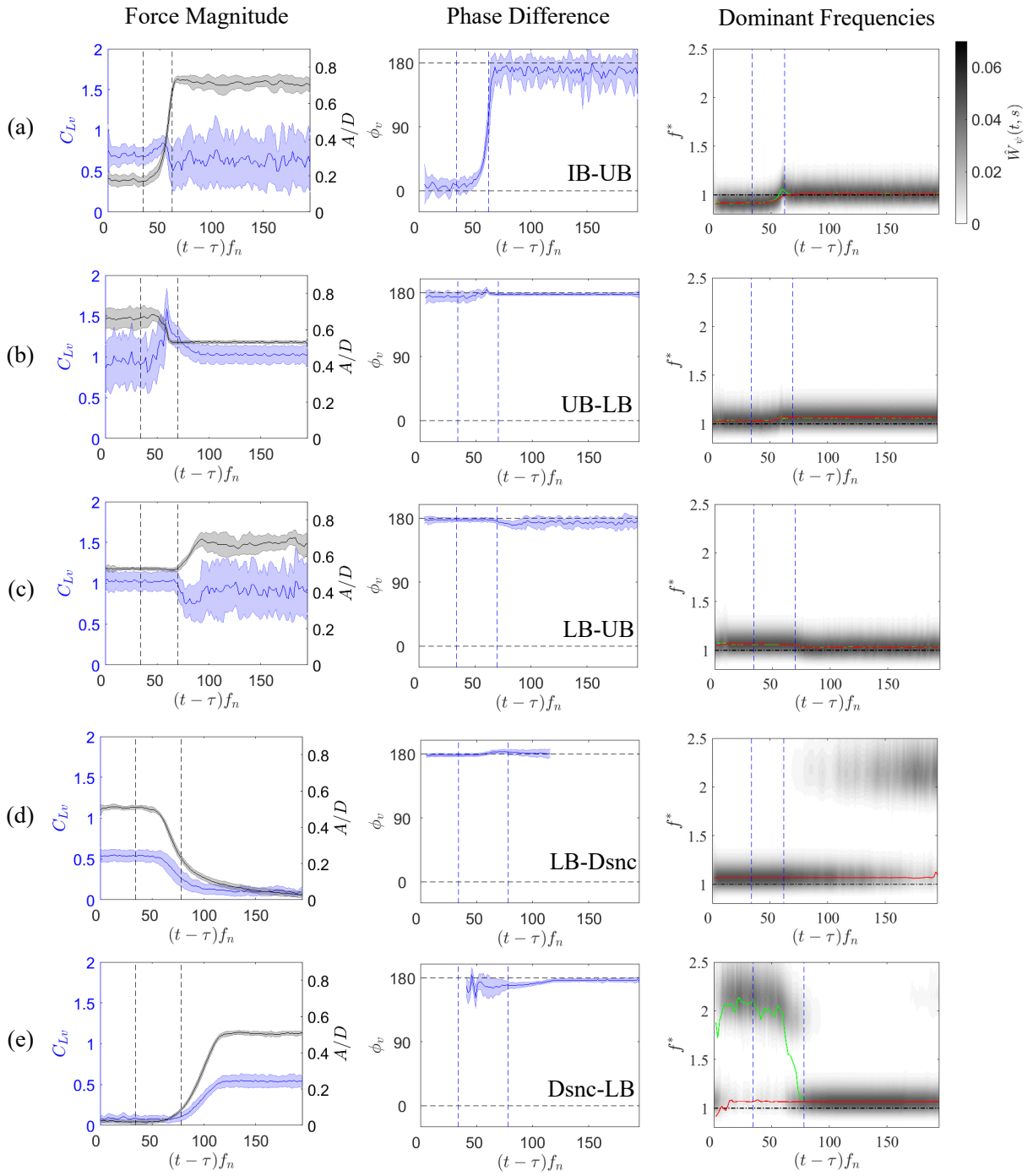

Figure 6.6: Forcing characteristics for all cases except the UB-IB transition. The left column depicts the ensemble-averaged normalized force magnitude in blue along with the ensemble-averaged cylinder displacement in gray. The middle column depicts the vortex force phase difference, and the right column depicts the ensemble-averaged and normalized signal energy of vortex forcing. The vertical dashed lines in all plots demarcate the freestream transient period.

For the LB-UB case (figure 6.6(c)), the force magnitudes (left column) remain stable until the end of the freestream transient where they exhibit a rapid drop. This drop coincides with the onset of cylinder amplitude growth, with the force magnitudes remaining near the lower value during the amplitude growth. Following this, the forcing recovers to the final quasi-steady state value. The vortex force phase difference (middle column) exhibits a small but noticeable reduction below the lower branch quasi-steady values that enable net positive energy transfer to the cylinder during the period of amplitude growth. As the amplitudes reach their final quasi-steady state, the phase difference recovers to a quasi-steady value closer to the 180° threshold while exhibiting the larger variance typical of the upper branch. The dominant forcing and displacement frequencies (right column) gradually reduce to values closer to the structure's natural frequency as a result of the forcing changes as discussed in the UB-LB case. Similarities in the amplitude responses between the UB-LB and LB-UB cases and intermittent switching behavior in the quasi-steady upper branch were briefly discussed in section 6.2. This similarity is explored later through analysis of the forcing characteristics of individual realizations in both UB-LB and LB-UB cases.

The LB-Dsnc case force magnitudes (figure 6.6(d), left column) exhibit a gradual reduction starting slightly after the amplitude of vibrations begins to decrease. Both the amplitude and forcing continue to decay well after the end of the freestream transient. The onset of amplitude decay coincides with the phase difference increasing and remaining slightly above 180°, resulting in a continuous net negative energy transfer to the cylinder. The signal energy of forcing (right column) reveals the emergence of a second component of forcing around $f^* \approx 2.1$ near the end of the freestream transient while the cylinder amplitudes continue to decay. This dual frequency response is reflective of the emergence of forcing at von Kármán frequency in addition to that at the structure's natural frequency. The von Kármán component gradually strengthens and becomes dominant as the cylinder reaches its final quasi-steady state. The dominant displacement frequency remains near structural natural frequency throughout the transient.

The Dsnc-LB case (figure 6.6(e)) force magnitudes increase at a rate slower than the amplitude growth rate starting from near the end of the freestream transient. The phase difference (middle column), before the end of the freestream transient, is close to 170° and remains relatively stable until the end of the freestream transient, where it starts gradually growing towards the quasi-steady state value close to 180°. The proximity of the phase difference to 180° results in a relatively slow amplitude growth rate (figure 6.2(f)). The forcing signal energy (right column) reveals a dual frequency response similar to the LB-Dsnc case with a larger contribution from the von Kármán component until near the end of the freestream transient, where a relatively sudden lock-in is established. Notably, sustained cylinder amplitude growth is only observed following the onset of lock-in (first column, figure 5.8(e)). Additionally, the timing of the onset of lock-in was found to vary between trials, resulting in the large variance between transient start times for this case (figure 6.4).

The UB-IB case (figure 6.2(d)) exhibited a dual-response, where approximately 90% of trial remained at the high-amplitude hysteresis quasi-steady state while the remaining trials returned to initial branch amplitudes. Figure 6.7 depicts two trials of the UB-IB case showing (a) a trial that remained in the high-amplitude state and (b) a trial that returned to the initial branch. Individual realizations are considered due to unreliable ensemble-averaged phase difference estimations due to "phase slips" as discussed further. For the trial that remained at high amplitude (figure 6.7(a)), the force magnitudes decrease to $C_{Lv} \approx 0.25$ and exhibit lower variance shortly following the onset of the freestream transient. The new mean value is lower than the quasi-steady values for both IB and UB (see figure 6.6(a)). The phase difference (middle column) exhibits unique behavior compared to the previously discussed cases. Before the onset of the freestream change (first vertical dashed line), the phase difference is close to the 180° threshold. During the freestream transient, the phase difference decreases rapidly toward 0°, however, there are distinct spikes in the phase difference. These spikes (phase slips) are related to frequency modulations in the forcing that result in intermittent lock-in behavior [47]. Evidence of this can be found in the signal energy of the forcing (right column) which shows the dominant forcing frequency (green line) exhibiting significant modulations while the displacement frequency is relatively stable and below natural frequency. The mean phase difference (apart from the phase slips) is slightly higher than that observed in quasi-steady IB (see figure 5.8(a)), oscillating near $\phi_v \approx 15$. This larger value of ϕ_v ensures sufficient positive energy transfer to the cylinder to support the large amplitude oscillations (equation 2.6) despite the lower values of forcing. Additionally, since the phase difference remains between 0 and 180° through the transient, the cylinder continuously extracts positive energy from the flow, however; the drop in force magnitudes results in the reduction of mean amplitudes from $A^*_{mean} \approx 0.72$ to 0.65.

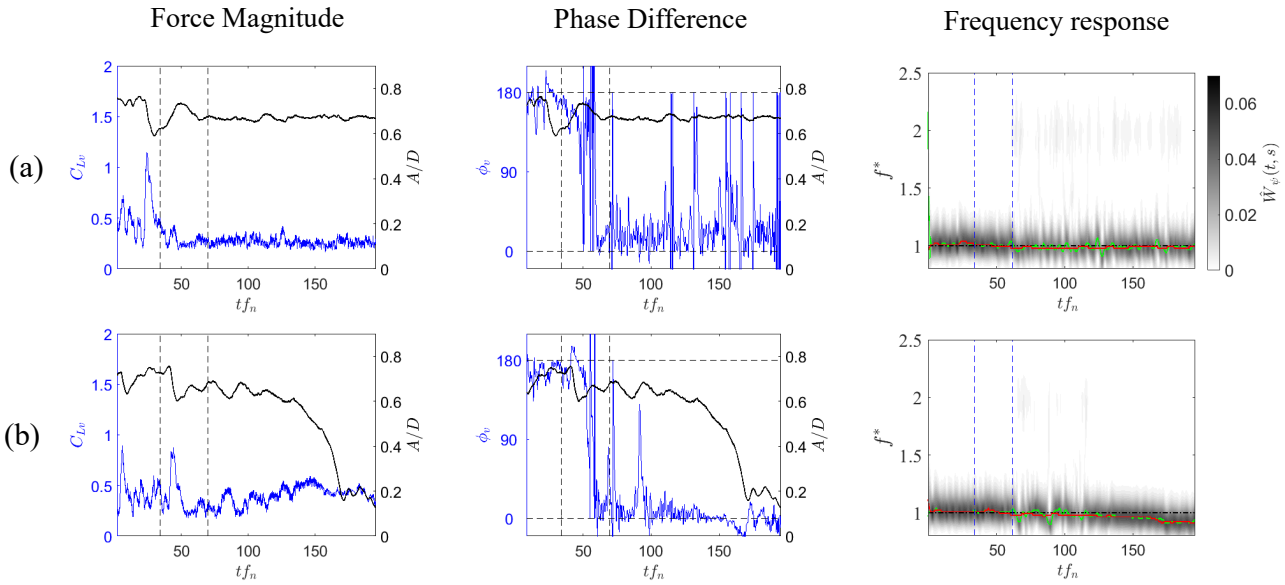

Figure 6.7: Forcing characteristics of individual realizations for the UB-IB transition with (a) remaining in the high-amplitude state and (b) returning to the initial branch.

For the trial during UB-IB transition that returns to the initial branch (figure 6.7(b)), marked differences in the forcing characteristics are observed compared to the trial that remained at high-amplitude oscillations. Specifically, after the freestream transient, the forcing magnitude exhibits larger modulations. Additionally, the force magnitudes gradually increase beyond $tf_n \approx 100$ until the onset of the most significant amplitude decay near $tf_n \approx 130$. The phase difference (middle column) also differs from the previous case in that the mean phase values are closer to the 0° threshold, particularly for $tfn \gtrapprox 100$. Consequently, the energy input to the cylinder is unable to balance the energy lost to damping, and the amplitudes exhibit a generally decaying trend for $tf_n \gtrapprox 100$. Beyond $tf_n \approx 130$, the phase difference regularly drops below 0° and the amplitude decay rates increase. The periods of most significant amplitude decay coincide with the lowest phase difference values. Once the system attains the final quasi-steady state values, the phase oscillates slightly above 0° (not visible with the current axis limits). The signal energy shows the switch in dominant frequencies from $f^* > 1$ before the freestream transient to $f^* < 1$ after the freestream transient. As the oscillation amplitude decays to the final quasi-steady state values and the force magnitudes increase, the dominant frequencies move further below the natural frequency and settle near $f^* \approx 0.92$.

The amplitude decay in the UB-LB case (figures 6.2(b)) and the steady amplitude growth in the LB-UB case (figures 6.2(e)) resemble intermittent switching behavior found in quasi-steady upper branch vibrations. To elucidate the similarities, individual realizations of both transient cases (UB-LB, LB-UB) are presented in figure 6.8. The first column depicts the force magnitude and vortex force phase difference associated with a single trial of the UB-LB case while the second column shows the same plots for a single trial in the LB-UB

case. In the UB-LB and the LB-UB cases, the amplitude response shows the existence of intermittent switching behavior for $20 \lessapprox tfn \lessapprox 40$ and $120 \lessapprox tf_n \lessapprox 150$, respectively. In both instances, the system is in the quasi-steady upper branch state, under steady freestream conditions (outside the dashed lines). For both cases, amplitude decay coincides with a significant spike in the force magnitudes and a small but noticeable excursion of the phase difference above 180°. In the UB-LB case (left column), the amplitudes begin increasing almost immediately following the rapid amplitude decay. The forcing magnitudes decrease and remain relatively low during the amplitude growth while the phase difference exhibits a reduction to lower values before returning closer to 180° as the cylinder amplitude increases. In the LB-UB case (right column), the amplitude remains close to the lower branch values ($A^* \approx 0.56$) for $120 \lessapprox tf_n \lessapprox 130$. Beyond this, the amplitudes grow to typical UB values, and the forcing magnitude and phase difference follow the same trend outlined in the UB-LB case.

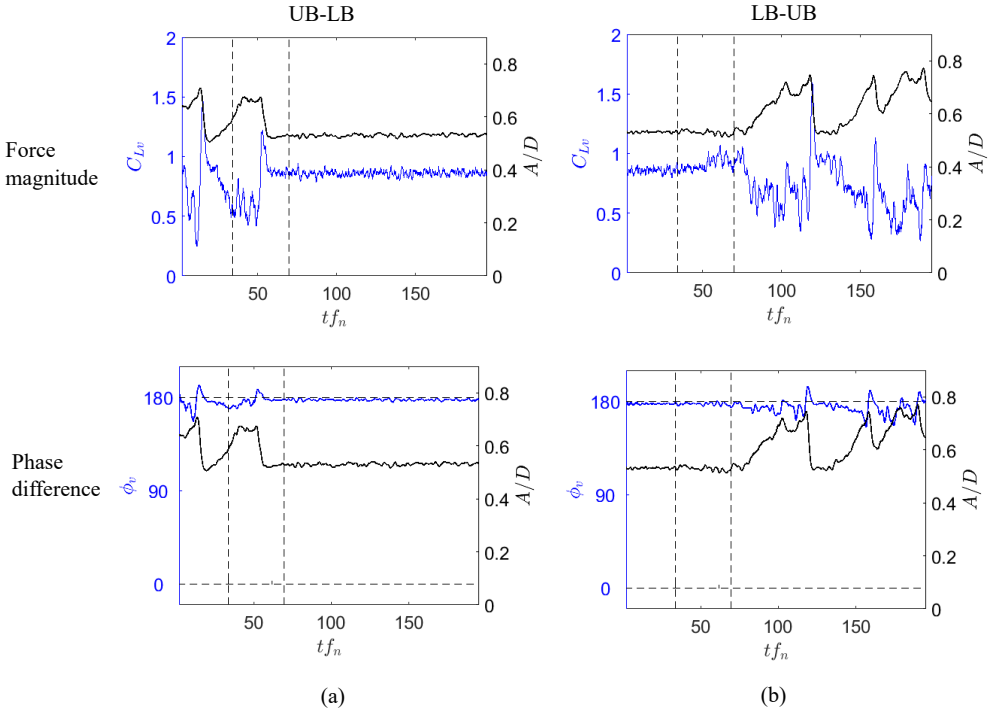

Figure 6.8: Forcing magnitude (top row) and phase difference (bottom row) of individual realizations for the (a) UB-LB and (b) LB-UB cases, respectively.

The system characteristics described above for intermittent switching in the upper branch under steady freestream conditions match those observed during the freestream transients for both UB-LB and LB-UB cases. Specifically, the force magnitudes and phase difference both spike during the amplitude drop in the UB-LB case, and the force magnitudes and phase difference values decrease prior to the amplitude growth period for the LB-UB case. Moreover, the amplitude decay rate in the UB-LB case, and the amplitude growth rate during the LB-UB transition are similar to those observed during intermittent switching for

quasi-steady VIV in UB. The changing freestream conditions appear to promote intermittent switching behavior in the UB-LB case during the freestream transient. In the LB-UB case, the amplitude growth is initiated only near the end of the freestream transient. However, slightly larger modulations in the forcing magnitude during the freestream transient (starting at $tf_n \approx 55$, figure 6.8(b)) point to changes in wake dynamics. Ultimately, the system characteristics during the amplitude growth (growth rate, forcing characteristics) resemble those of a system already in the upper branch. It is thus speculated that the wake characteristics are modified during the freestream transient and resemble a system in the low-amplitude state of upper branch intermittent switching near the end of the freestream transient.

The foregoing discussion of the forcing characteristics for all cases has provided more insight into the underlying mechanisms resulting in different amplitude responses (figure 6.2) and transient times (figure 6.4). While the forcing magnitude and phase difference are both important in transient behavior, the latter is critical to the energy transfer to the cylinder (equation 2.6) and consequently the amplitude growth/decay rate. Next, the transient wake dynamics associated with the outlined responses are discussed.

6.4 Attendant transient wake characteristics

The dominant modes of vortex shedding in the initial, upper, and lower branches include the expected 2S,2P$_0$, and 2P modes, respectively. The characteristic features of each mode along with mean wake development in each response branch are detailed in previous chapters (see sections 4.2 and 5.1). The same modes of shedding are observed during the present experiments, albeit with minor changes to the topology likely arising from the difference in Reynolds numbers. In addition to the shedding characteristics in the initial, upper, and lower response branches, the flow development in the hysteresis region is discussed in Appendix B. The transient wake dynamics are examined through PIV measurements ensemble-averaged over five trials for all cases. The ensemble averaging methodology is the same as that used for the forcing analysis (section 6.3). Additionally, the two responses in the UB-IB case are treated by conditionally averaging trials that exhibit the distinct type of response, and the results are discussed in section 6.4.1. Ensemble-averaged PIV measurements enable the identification of the changing coherent structures throughout the transient. Additionally, the dynamic response of the wake to the changing freestream is examined in two ways. First, the wavelet analysis (section 3.3.2) of the transverse velocity signal along the wake centerline at $X/D \approx 2.5$ downstream of the cylinder is used to identify temporal changes to the dominant wake frequencies. Second, the rms of an instantaneous "error field" is constructed to quantify the temporal evolution of the near wake characteristics from the initial quasi-steady state. While a universal definition of the near wake is lacking, the region between $0.5 < X/D < 3$ and $-1.5 < Y/D < 1.5$ is adopted as the near wake here since the vortex formation and shedding process for all cases occurs within this domain. The moving average of the streamwise velocity within this domain is constructed

by employing a temporal window of approximately six oscillation cycles in length (approximately 150 PIV snapshots). At each instant, this moving average is subtracted from the initial quasi-steady mean streamwise velocity field in this domain estimated over approximately 200 cycles before the start of the freestream transient. The rms of this "error field" at each instant then represents the statistical deviation of the near wake from its initial state.

Figure 6.9 depicts the ensemble-averaged spanwise vorticity at four instances through the transient for the IB-UB case. The corresponding instances are marked in the transient ensemble-averaged displacement time series figure 6.9(a)[2]. In all the cases, the cylinder is at the top dead center of an oscillation cycle. At $(t-\tau)f_n \approx 46$ (figure 6.9(b)), the wake exhibits an alternately signed pattern of vortices representative of 2S shedding. At $(t-\tau)f_n \approx 56$ (figure 6.9(c)), the wake continues to exhibit 2S shedding with the positive vortex at $X/D \approx 1.75$ still attached to the shear layer. As the cylinder oscillations continue to grow in amplitude, distinct changes are observed in the wake. At $(t-\tau)f_n \approx 62$ (figure 6.9(d)), the wake still exhibits the alternating pattern of vortices. However, the positive vortex at $X/D \approx 2$ has already been shed with evidence of a weak negative trailing vortex at $X/D \approx 0.6$. The shedding of the positive vortex by this point in the oscillation cycle signifies a switch in the timing of vortex shedding. This is further supported by the rapid change in the vortex force phase difference from 0° to 180° around the same time (figure 6.6(a)). The switch in vortex shedding timing, along with evidence of a weak trailing vortex, is indicative of the transition from 2S to $2P_0$ shedding. As the system reaches its final quasi-steady state at $(t-\tau)f_n \approx 70$ (figure 6.9(e)), the wake continues to exhibit the $2P_0$ mode.

[2]Note that the freestream transient limits are not provided in this figure and subsequent amplitude figures due to the differing x-axis scales employed for clarity.

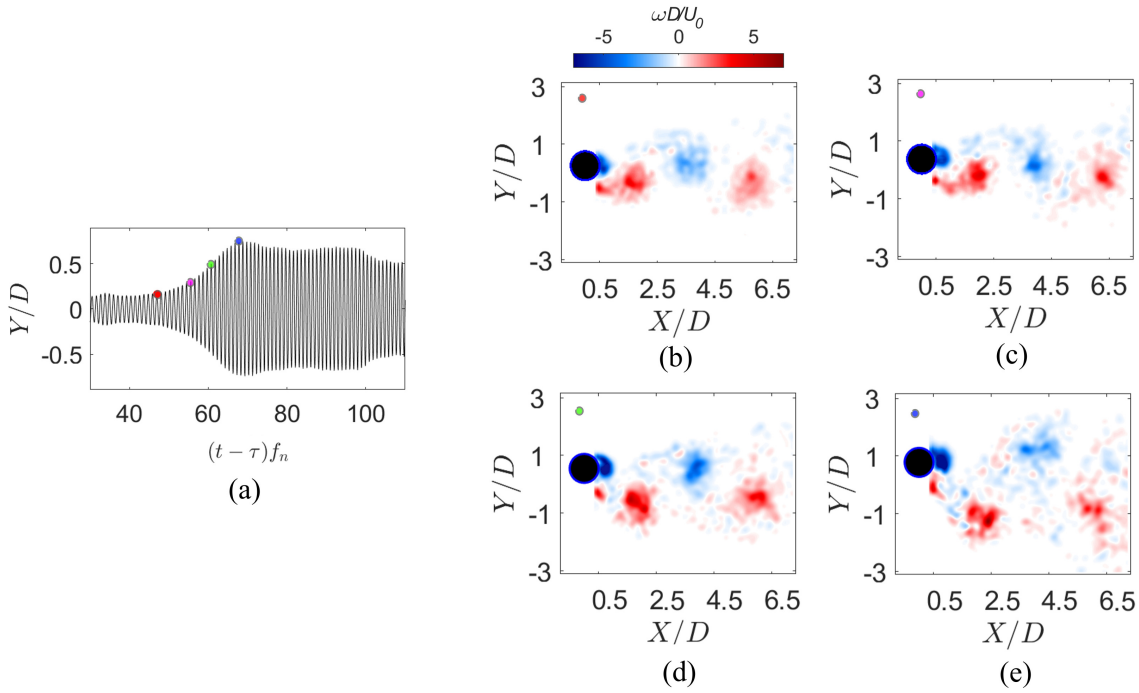

Figure 6.9: (a) Ensemble-averaged time series and spanwise vorticity for the IB-UB case at (b) $(t-\tau)f_n \approx 46$, (c) $(t-\tau)f_n \approx 56$, (d) $(t-\tau)f_n \approx 62$, and (e) $(t-\tau)f_n \approx 70$.

Figure 6.10(a) depicts the ensemble-averaged signal energy of the transverse velocity along the wake centerline at $X/D \approx 2.5$. The signal energy at each instant is normalized by the total energy across all scales. The vertical dashed lines demarcate the freestream transient period. The dashed-dotted line represents the structure's natural frequency and the dashed line represents the expected von Kármán shedding frequency based on the instantaneous freestream velocity. Before the freestream transient (first vertical dashed line), the dominant wake frequency ($f^* \approx 0.92$) remains well below the structure's natural frequency. Beyond $(t-\tau)f_n \approx 55$, the dominant frequency exhibits a significant increase and settles near $f^* = 1$ towards the end of the freestream transient. Beyond this point, the normalized signal energy is significantly diminished, signifying a broadening of the energy spectrum. The wake dominant frequency matches well with the dominant forcing frequency (figure 5.8(a)). Figure 6.10(b) depicts the ensemble-averaged rms error of the near wake with respect to the initial quasi-steady state. Before the start of the freestream transient, the rms error is below 5% of the freestream velocity. Following the onset of the freestream transient, the rms error gradually increases, particularly beyond $(t-\tau)f_n \approx 40$, indicating a steady departure of the near wake from the initial quasi-steady state. The steady increase in rms error coincides with the increase in forcing magnitudes during the same period (figure 6.6(a)). Beyond $(t-\tau)f_n \approx 55$, the rms error rapidly increases to its final value near 25% of the freestream velocity at the final quasi-steady state. The rapid growth in rms error coincides with the period of most significant amplitude growth (figure 6.2(a)). Notably, while the wake begins to depart from its initial state soon after the onset of the freestream transient, the shedding

frequency remains relatively stable until the periods of most significant amplitude growth.

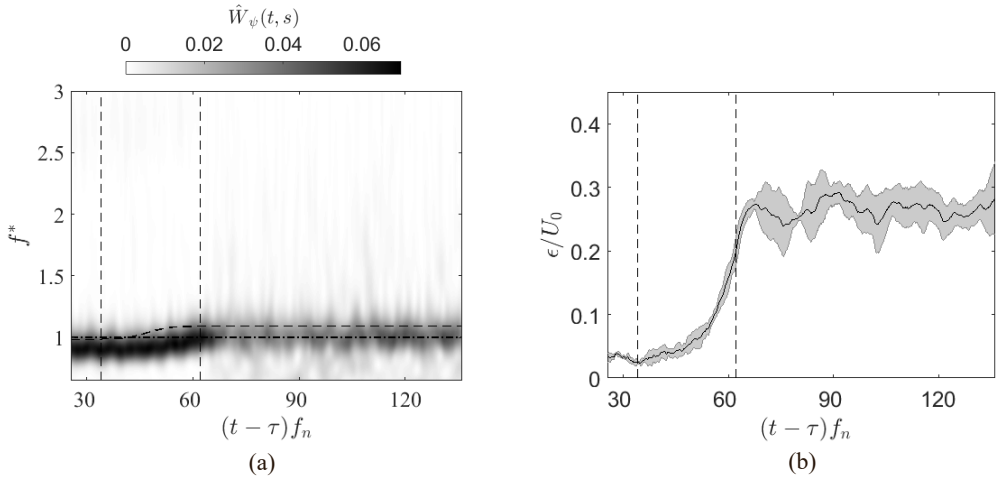

Figure 6.10: Transient wake dynamics for the IB-UB case. (a) Ensemble-averaged normalized signal energy of the transverse velocity along the wake centerline at $X/D \approx 2.5$ and (b) ensemble-averaged rms error of the near wake with respect to the initial quasi-steady state.

Figure 6.11 presents the ensemble-averaged spanwise vorticity contours at four instances during the transient in the UB-LB case. At $(t-\tau)f_n \approx 40$ (figure 6.11(b)), the wake exhibits $2P_0$ shedding. With the cylinder at the top dead center, only a negative vortex roll-up is visible near the cylinder base at $X/D \approx 0.6$. At $(t-\tau)f_n \approx 48$ (figure 6.11(c)), the wake still exhibits a topology that resembles $2P_0$ shedding, however, the negative vortex roll-up occurs farther downstream compared to the previous instance. As the oscillation amplitudes decrease, the wake at $(t-\tau)f_n \approx 55$ (figure 6.11(d)) shows evidence of both positive and negative vortex roll-ups moving farther upstream. The wake farther downstream begins to show signs of 2P shedding, as evidenced by the counter-rotating vortex pair seen between $1.5 \lessapprox X/D \lessapprox 3.75$. As the system approaches its final quasi-steady state, the wake at $(t-\tau)f_n \approx 62$ (figure 6.11(e)) exhibits a clear 2P pattern of shedding, characterized by the counter-rotating pair of roughly equal strength. Additionally, both negative and positive vortex roll-ups are apparent near the cylinder.

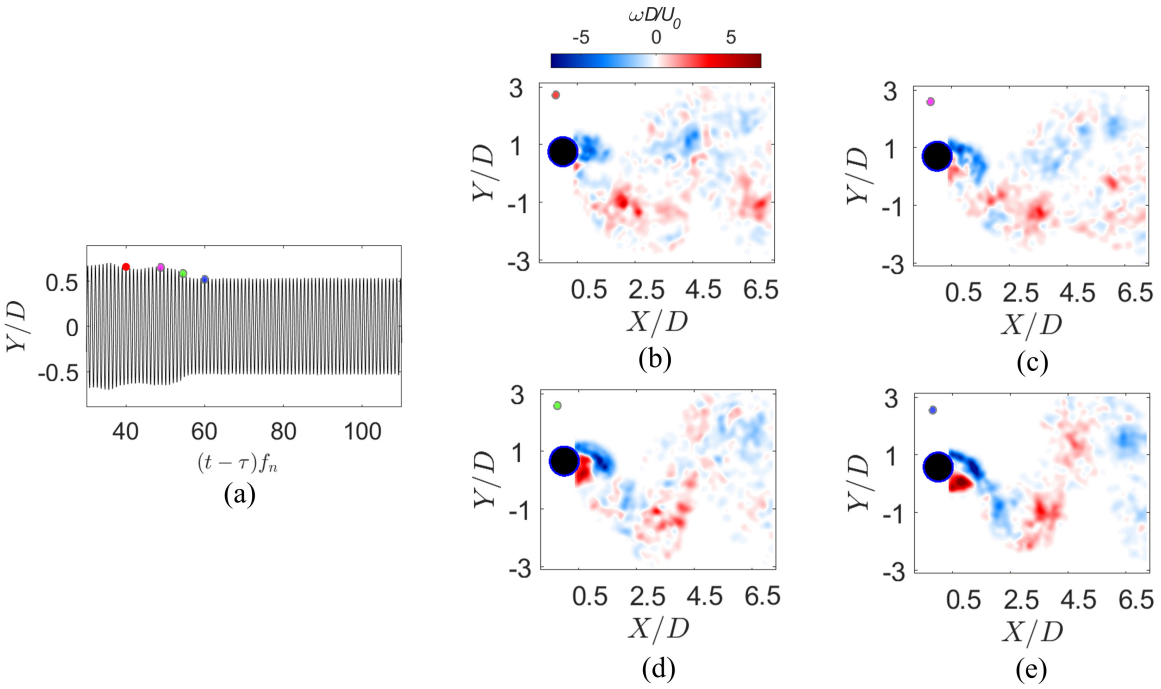

Figure 6.11: (a) Ensemble-averaged time series and spanwise vorticity for the UB-LB case at (b) $(t-\tau)f_n \approx 40$, (c) $(t-\tau)f_n \approx 48$, (d) $(t-\tau)f_n \approx 55$, and (e) $(t-\tau)f_n \approx 62$.

The ensemble-averaged signal energy of the transverse velocity (figure 6.12(a)) shows the dominant frequency located near the structure's natural frequency with relatively low magnitudes for $(t-\tau)f_n \lessapprox 55$. Beyond this, the normalized signal energy increases, signifying a narrower spectral distribution, and the dominant frequency shifts above the structural natural frequency. The rms error (figure 6.12(b)) begins to depart from the initial quasi-steady state within 5-7 cycles after the freestream transient is initiated. The increase in rms error mirrors the increase in forcing magnitudes during the same period (figure 6.6(b)). Beyond $(t-\tau)f_n \approx 55$, the rms error rapidly increases, coinciding with the drop in oscillation amplitudes and the spike in forcing magnitudes.

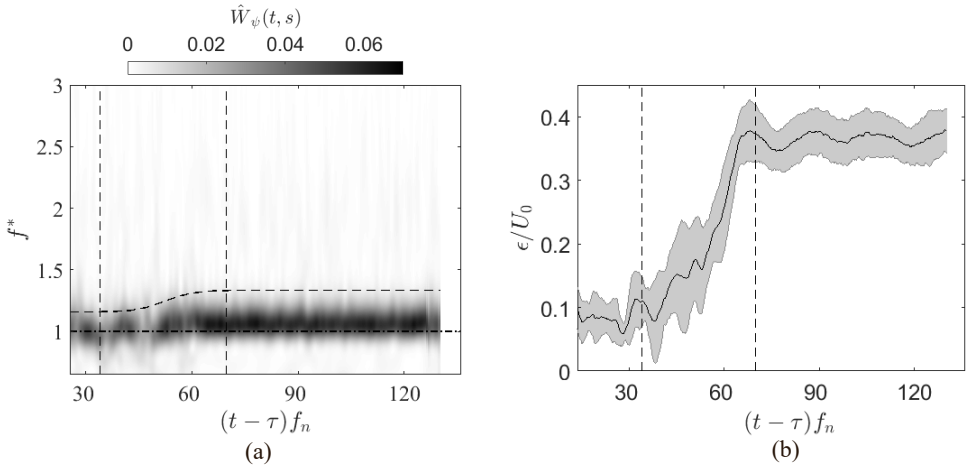

Figure 6.12: Transient wake dynamics for the UB-LB case. (a) Ensemble-averaged normalized signal energy of the transverse velocity along the wake centerline at $X/D \approx 2.5$ and (b) ensemble-averaged rms error of the near wake with respect to the initial quasi-steady state.

Figure 6.13 presents the ensemble-averaged spanwise vorticity contours at four instances during the transient in the LB-UB case. At $(t-\tau)f_n \approx 63$ (figure 6.13(b)), the wake exhibits the 2P mode of shedding. At $(t-\tau)f_n \approx 70$ (figure 6.13(c)), near the beginning of cylinder amplitude growth, the wake continues to resemble the 2P mode. However, a slight reduction in formation length is observed, as evidenced by the less apparent roll-up of the positive vortex near the cylinder base at $X/D \approx 0.6$ compared to the previous instance (compare figures 6.13(c) and (b)). As the oscillation amplitudes continue to grow (figure 6.13(d), $(t-\tau)f_n \approx 76$)), the reduction in formation length becomes more apparent. In particular, the negative vortex roll-up occurs much closer to the base of the cylinder and the positive vortex roll-up is not identified within the current field of view. Around this time, the 2P mode transitions to $2P_0$, as evidenced by the diminishing trailing vortex strengths. The $2P_0$ shedding mode persists as the system approaches quasi-steady state (figure 6.13(e), $(t-\tau)f_n \approx 83$).

The dominant wake frequency in the LB-UB case (figure 6.14(a)) remains above the structure's natural frequency before and throughout the freestream transient period. Concurrent with the period of oscillation amplitude growth, the dominant frequency exhibits a noticeable decrease to values below the structure's natural frequency before increasing slightly above $f^* = 1$ and settling there. The near wake rms error (figure 6.14(b)) remains below 5% for $(t-\tau)f_n \approx 50$ before exhibiting an increase to approximately 13% towards the end of the freestream transient. The rise in rms error between $50 \lessapprox (t-\tau)f_n \lessapprox 70$ (figure 6.14(b)) is linked in part to the reducing formation length before the rise in amplitudes. In contrast to the previous two cases (IB-UB and UB-LB), the initial increase in rms error during the freestream transient is not reflected in the ensemble-averaged forcing signal for the LB-UB case (figure 6.6(c)). However, the forcing signal in the individual trial analysis (figure 6.8(b))

showed a slight increase in the forcing modulation during this period. Beyond $(t-\tau)f_n \approx 70$, the error increases significantly, coinciding with the rising oscillation amplitudes and the transition from 2P to $2P_0$ shedding.

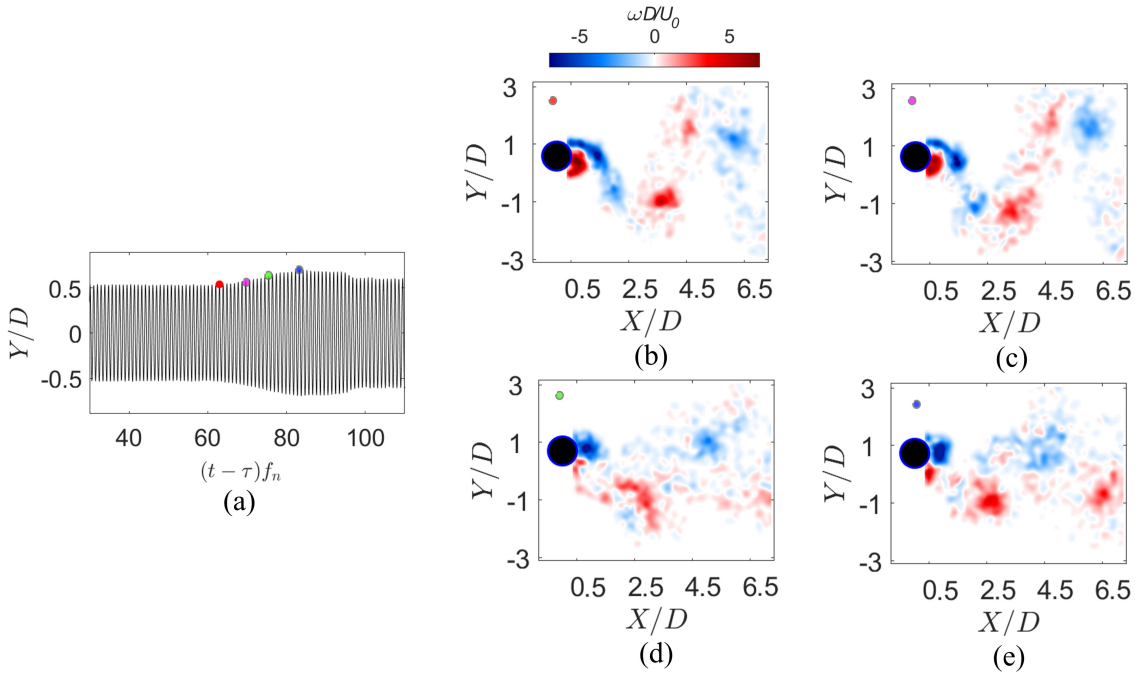

Figure 6.13: (a) Ensemble-averaged time series and spanwise vorticity for the LB-UB case at (b) $(t-\tau)f_n \approx 63$, (c) $(t-\tau)f_n \approx 70$, (d) $(t-\tau)f_n \approx 76$, and (e) $(t-\tau)f_n \approx 83$.

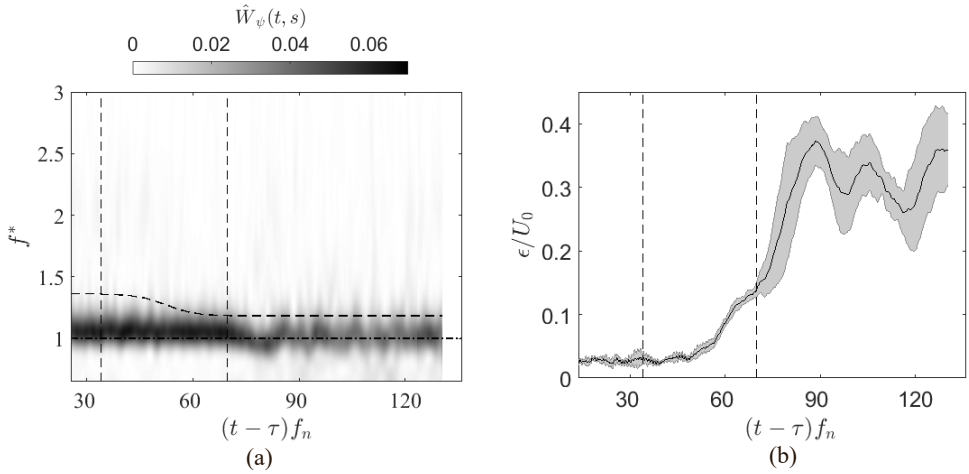

Figure 6.14: Transient wake dynamics for the LB-UB case. (a) Ensemble-averaged normalized signal energy of the transverse velocity along the wake centerline at $X/D \approx 2.5$ and (b) ensemble-averaged rms error of the near wake with respect to the initial quasi-steady state.

The ensemble-averaged vorticity contours during the transient for the LB-Dsnc case are presented in figure 6.15. At $(t-\tau)f_n \approx 44$ (figure 6.15(b)), the wake exhibits the 2P mode of shedding. Note that the 2P shedding topology at this reduced velocity differs from the 2P quasi-steady state at the end of the UB-LB transition, particularly in the streamwise vortex spacing and the vortex strength. At $(t-\tau)f_n \approx 60$ (figure 6.15(c)), the wake continues to exhibit the 2P mode. As the amplitude of vibrations decay, the wake topology at $(t-\tau)f_n \approx 70$ (figure 6.15(d)) begins to exhibit an alternating pattern of vorticity similar to 2S shedding. This shedding pattern persists as the cylinder moves into the desynchronization regime ((figure 6.15(e)), $(t-\tau)f_n \approx 89$).

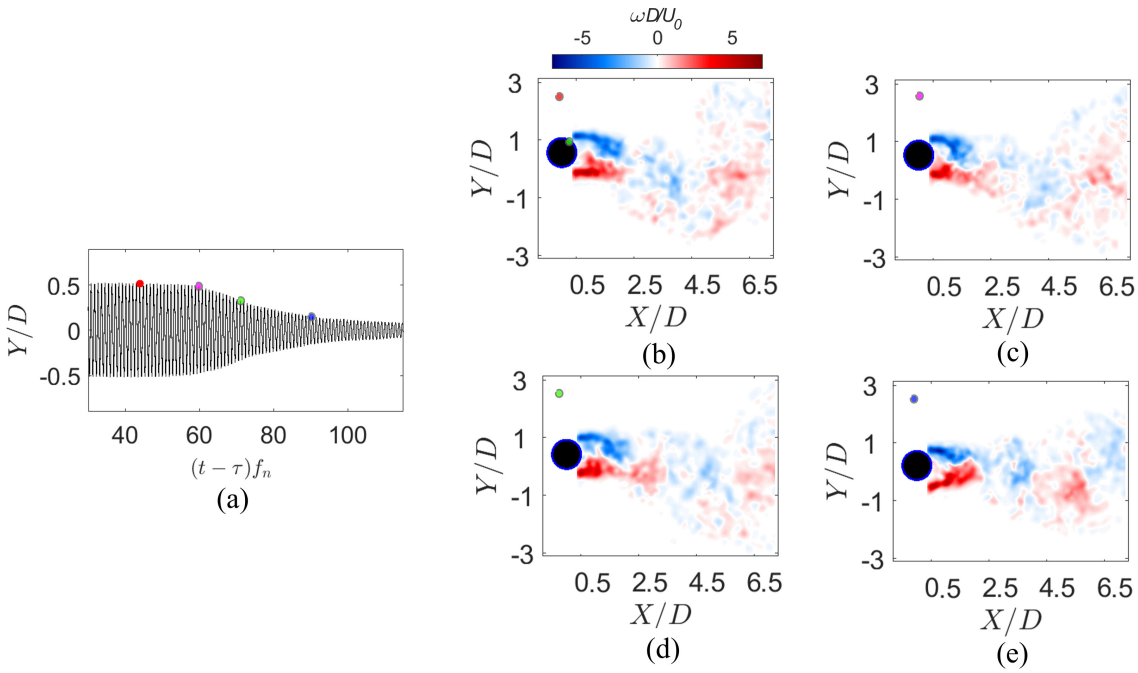

Figure 6.15: (a) Ensemble-averaged time series and spanwise vorticity for the LB-Dsnc case at (b) $(t-\tau)f_n \approx 44$, (c) $(t-\tau)f_n \approx 60$, (d) $(t-\tau)f_n \approx 70$, and (e) $(t-\tau)f_n \approx 89$.

The dominant wake frequency in the LB-Dsnc case for $(t-\tau) \lessapprox 70$ exhibits the lock-in frequency above $f^* = 1$ (figure 6.16(a)). Between $70 \lessapprox (t-\tau) \lessapprox 90$, a dual frequency activity centered near the von Kármán and structure natural frequencies emerges. Notably, the von Kármán frequency is very close to the first harmonic of the oscillation frequency. This, coupled with the fact that the temporal shift for ensemble averaging in the LB-Dsnc case is minimal (figure 6.2(c)), results in minimal phase-smearing during the ensemble averaging. Consequently, the identification of the coherent 2S-like structures in figures 6.15(d-e) is possible. Beyond $(t-\tau)f_n \approx 90$, the von Kármán frequency becomes dominant. The near wake rms error (figure 6.16(b)) increases steadily with a relatively large standard deviation (gray shaded region) for $(t-\tau)f_n \lessapprox 60$. During this initial period of the freestream transient, neither the forcing magnitudes nor the oscillation amplitudes change appreciably (figure 6.8(d)). This is similar to the results during the initial freestream transient period

for the LB-UB case. Beyond $(t-\tau)f_n \approx 60$, the rms error asymptotically increases up to quasi-steady state, coinciding with the decrease in forcing magnitudes and amplitude decay. The standard deviation of the rms error is minimal during the periods of amplitude decay (figure 6.16(b)).

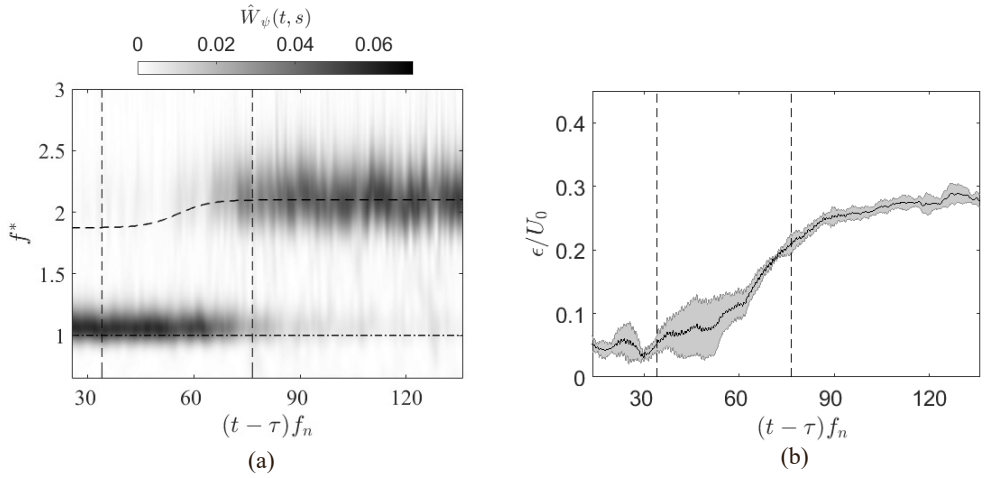

Figure 6.16: Transient wake dynamics for the LB-Dsnc case. (a) Ensemble-averaged normalized signal energy of the transverse velocity along the wake centerline at $X/D \approx 2.5$ and (b) ensemble-averaged rms error of the near wake with respect to the initial quasi-steady state.

The Dsnc-LB case ensemble-averaged vorticity contours are presented in figure 6.17. At $(t-\tau)f_n \approx 50$ and $(t-\tau)f_n \approx 70$ (figure 6.17(b-c)), distinct coherent structures are only identified near the cylinder, and no distinct topological features can be identified beyond $X/D \approx 2.5$. The 2P mode of shedding is identified as the cylinder amplitude continues to grow (figure 6.17(d), $(t-\tau)f_n \approx 90$) and persists through quasi-steady state (figure 6.17(e), $(t-\tau)f_n \approx 107$).

The dominant wake frequency (figure 6.18(a)) closely follows the von Kármán frequency (dashed line) for $(t-\tau)f_n \lessapprox 90$. Starting from $(t-\tau)f_n \approx 69$, notable energy content is identified near the structure's natural frequency. Between $69 \lessapprox (t-\tau)f_n \lessapprox 95$, both von Kármán and natural frequencies are identified. The emergence of a component near the natural frequency coincides with the onset of significant amplitude growth. Contrasting with the LB-Dsnc case (figure 6.16(a)), the von Kármán frequency at the end of the freestream transient is not near the first harmonic of the oscillation frequency. Thus, the ensemble averaging is affected by significant phase smearing during the initial period of amplitude growth where both von Kármán and natural frequency components are detected in the wake ($69 \lessapprox (t-\tau)f_n \lessapprox 95$). The near wake rms error (figure 6.18(b)) remains relatively low for $(t-\tau) \lessapprox 60$, beyond which a continuous increase in rms error is observed until a small plateau near the end of the freestream transient. Similar to the LB-UB and

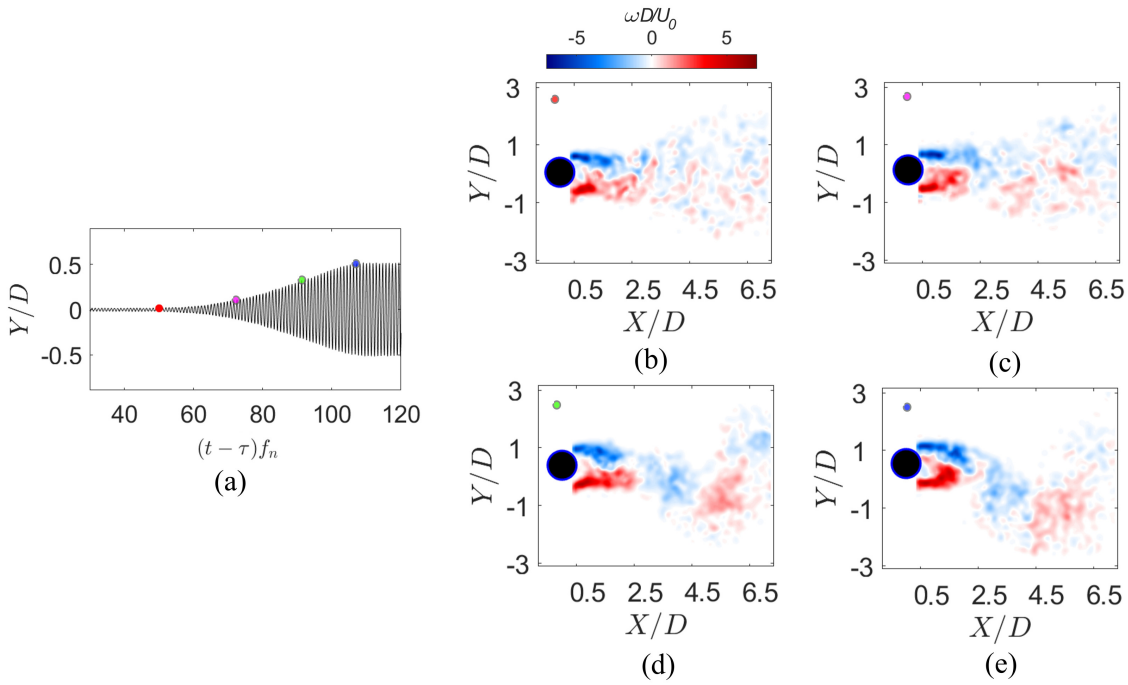

Figure 6.17: (a) Ensemble-averaged time series and spanwise vorticity for the Dsnc-LB case at (b) $(t-\tau)f_n \approx 50$, (c) $(t-\tau)f_n \approx 70$, (d) $(t-\tau)f_n \approx 90$, and (e) $(t-\tau)f_n \approx 107$.

LB-Dsnc cases, the oscillation amplitudes and forcing magnitudes do not change appreciably during this period (figure 6.6(e)). Coinciding with the period of most significant oscillation amplitude growth ($(t-\tau)f_n \gtrapprox 80$), the rms error rapidly increases up to approximately 30% at quasi-steady state (figure 6.18(b)).

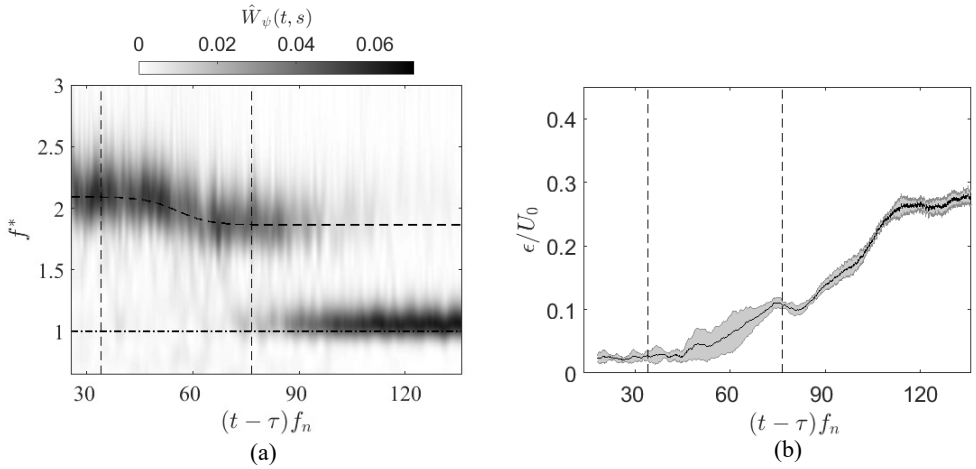

Figure 6.18: Transient wake dynamics for the Dsnc-LB case. (a) Ensemble-averaged normalized signal energy of the transverse velocity along the wake centerline at $X/D \approx 2.5$ and (b) ensemble-averaged rms error of the near wake with respect to the initial quasi-steady state.

6.4.1 UB-IB dual response

The wake dynamics for the dual-response observed in the UB-IB case are explored further. Figure 6.19 depicts four instances during the transient for the case that remains in the high-amplitude state (top set of images), and the trials that return to the initial branch (bottom set of images). For the former case, five PIV trials were used for ensemble averaging. Only three PIV trials were captured for ensemble averaging in the case that returned to the IB due to the lower frequency of occurrence for this mode. For the high-amplitude case, the instances at $(t-\tau)f_n \approx 40$ and 46 (figure 6.19(b-c)) are within the freestream transient period, and the wake resembles the $2P_0$ mode of shedding. Near the end of the freestream transient (figure 6.19(d), $(t-\tau)f_n \approx 62$), slight changes are observed in the wake topology. Specifically, while the shedding pattern still resembles $2P_0$, the vortices appear to have moved upstream by as much as one diameter. This is also evidenced by the fact that, in the previous two instances, four vortices (two on each side of the wake centerline) can be identified within the field of view, while an additional negative vortex is visible towards the end of the field of view at $(t-\tau)f_n \approx 62$. This new topology persists at $(t-\tau)f_n \approx 72$ (figure 6.19(e)).

For the trials that returned to the IB, the reduction in oscillation amplitudes occurred after an extended period at the high-amplitude state ($60 \lessapprox (t-\tau)f_n \lessapprox 120$, figure 6.19(f)). The wake topology during this period (e.g., figure 6.19(g), $(t-\tau)f_n \approx 120$) is similar to that seen in figures 6.19(d-e) for oscillations at the high-amplitude state. At $(t-\tau)f_n \approx 135$ (figure 6.19(h)), it can be seen that the positive vortex at $X/D \approx 2$ remains attached to the shear layer, signifying changes in vortex shedding timing. This becomes more apparent as the oscillation amplitudes decay further (figure 6.19(i), $(t-\tau)f_n \approx 160$), signifying a switch in the timing of shedding. At $(t-\tau)f_n \approx 160$, the wake topology begins to resemble

2S shedding, characterized by the lower transverse distance between the vortices. The vortex formation region moves farther upstream, as evidenced by the upstream movement of the last negative vortex at $X/D \approx 6$, now well within the field of view. The end state quasi-steady 2S shedding is observed at $(t - \tau)f_n \approx 180$ (figure 6.19(j)).

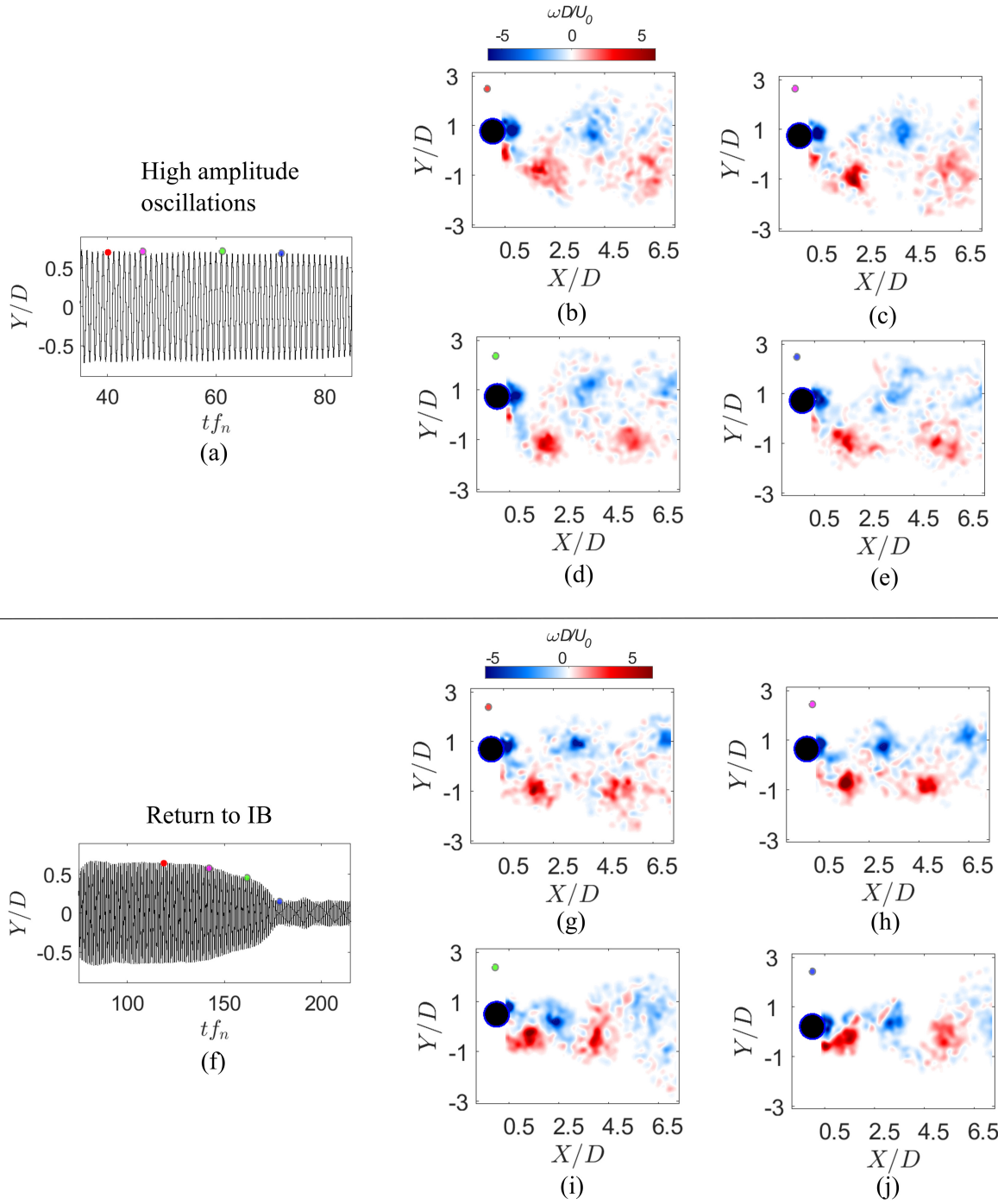

Figure 6.19: (a) Ensemble-averaged time series and spanwise vorticity for the UB-IB. case that remains at a high-amplitude state at (b) $(t-\tau)f_n \approx 40$, (c) $(t-\tau)f_n \approx 46$, (d) $(t-\tau)f_n \approx 62$, and (e) $(t-\tau)f_n \approx 72$. (f) Ensemble-averaged time series and spanwise vorticity for the UB-IB. case that returns to the initial branch at (g) $(t-\tau)f_n \approx 120$, (h) $(t-\tau)f_n \approx 135$, (i) $(t-\tau)f_n \approx 160$, and (j) $(t-\tau)f_n \approx 180$.

Figures 6.20(a-b) present the ensemble-averaged signal energy of the transverse velocity and near wake rms error for the trials that remain at high-amplitude oscillations in the UB-IB case. Figures 6.20(c-d) present the same for the trials that returned to the initial branch. Before the end of the freestream transient, the dominant wake frequency for the high-amplitude case (6.20(a)) is centered around the structural natural frequency. After the freestream transient, the dominant wake frequency decreases below the structural natural frequency. The near wake rms error (figure 6.20(b)) shows a nearly immediate increase following the onset of the freestream transient. The maximum value of the rms error (approximately 15 %) attained towards the end of the freestream transient, is relatively low compared to previous cases due to the similarity in the wake topology between the initial and final states (figure 6.9). The ensemble-averaged transverse velocity signal energy for the trials that return to the initial branch (figure 6.20(c)) shows that the dominant wake frequency primarily remains below $f^* = 1$ for $(t-\tau)f_n \lessapprox 160$. A notable increase in signal energy is seen for $(t-\tau)f_n \gtrapprox 130$. Additionally, a decrease of the dominant frequency to well below $f^* = 1$ is observed near $(t-\tau)f_n \approx 180$, coinciding with the period of most significant amplitude decay (figure 6.19(f)). The near wake rms error (figure 6.20(d)) is approximately 15%, for $(t-\tau)f_n \lessapprox 130$, similar to the end state in figure 6.20(b). Beyond this, a steady increase in rms error is observed until $(t-\tau)f_n \approx 160$, where the error saturates near 20%. The steady increase in rms error coincides with the onset of gradual amplitude decay and a change in shedding mode to 2S shedding (figure 6.19(i)).

For all the cases considered, qualitative analysis of the transient wake development helped identify the topological changes to the wake during system transients. Time-frequency analysis of the dominant wake frequencies matched them to those of the forcing on the cylinder, affirming the link between the large-scale shedding in the wake and the forcing on the cylinder. Additionally, the near wake rms error provided a measure of the deviation of the near wake from its initial state, with the start of the increase in rms error signaling the onset of the wake transient response. For the IB-UB, UB-LB, and Dsnc-LB. cases, a departure from the initial quasi-steady state is observed within approximately five cycles after the onset of the freestream transient. Concurrently, changes are also identified in the forcing characteristics for the IB-UB and UB-LB cases. This suggests that the forcing on the cylinder in the initial and upper branches is sensitive to relatively small changes in the wake characteristics. Conversely, in the LB-UB and LB-Dsnc cases, relatively minor changes to the forcing characteristics are observed despite significant changes to the wake characteristics within the freestream transient periods. The decreased sensitivity of the forcing to changes in the wake is speculated to stem in part from the larger vortex formation lengths in the lower branch compared to the initial and upper branches. In other words, the farther the vortices (low-pressure regions) are from the cylinder base, the lower the sensitivity of forces to similar changes in the near wake characteristics.

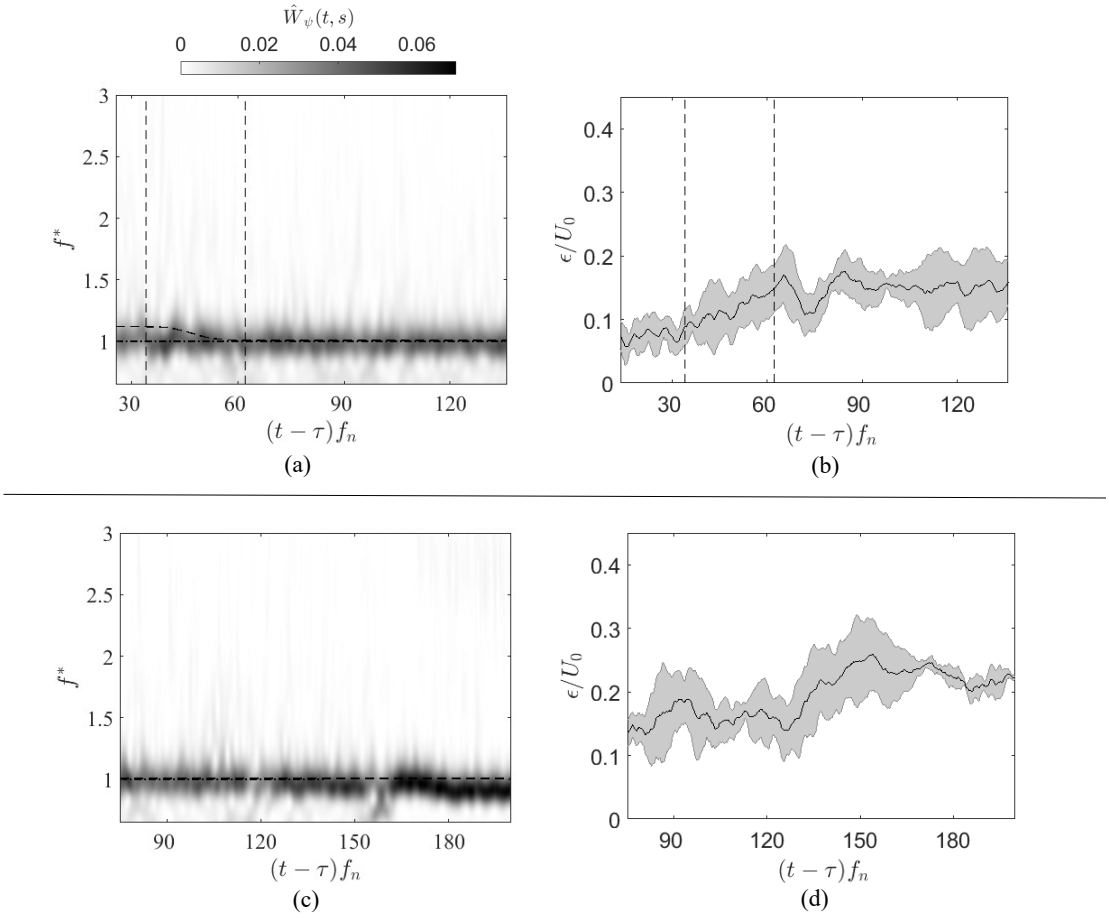

Figure 6.20: Transient wake dynamics for the UB-IB. cases. The top row depicts the trials the remain in high-amplitude oscillations, while the bottom row depicts trials that returned to the initial branch. (a) Ensemble-averaged normalized signal energy of the transverse velocity along the wake centerline at $X/D \approx 2.5$ and (b) ensemble-averaged rms error of the near wake with respect to the initial quasi-steady state.

6.5 Discussion

The combined analysis of the transient wake response with the forcing characteristics (section 6.3) and the amplitude response (section 6.2) provides a holistic outlook on transient VIV response in the unsteady freestream conditions considered in the present study.

The onset of the continuous increase in near wake rms errors approximately marks the start of the transient wake response and is observed within a maximum of nearly 20 cycles after the onset of the freestream transient for all cases. However, there is a considerable variance in the timing of onset of wake response between the different cases. Nevertheless, the start of the system transient amplitude response (transient start time in figure 6.4(a)) occurs later than the start of the corresponding transient wake response for

all cases. While different methods were adopted for quantifying the wake and system responses, the results suggest that the initial structural response lags the initial wake response.

Following the onset of the structural response, the paths taken by the system between the two quasi-steady states and the total transient times are closely related to the energy transfer between the fluid and the structure. The largest rates of oscillation amplitude growth (figure 6.2) are observed in the IB-UB case, where large rates of net positive energy transfer are enabled by the phase difference passing between 0 and 180° through 90°. Conversely, the slowest transients are observed in the LB-Dsnc and Dsnc-LB cases, where the phase differences remain close to 180°. These findings are similar to the ones from the release from rest experiments, where a gradual increase in initial lock-in phase differences was observed with increasing U^* (figure 5.9), resulting in slower transients with increasing U^*. Additionally, the results from a previous study [30] considering a large mass ratio ($m^* \approx 1590$) flexible cylinder released from rest also indicate a similar trend. Specifically, the fastest transient responses were found near the end of the initial branch and the maximum amplitude growth rate decreased with increasing U^*. This suggests that the trends in phase difference, and subsequently energy transfer rates vs U^* remain similar over a wide range of mass ratios.

The two distinct behaviors observed in the UB-IB case (with most trials remaining at a high-amplitude state and approximately 10% of trials returning to the initial branch) also provide evidence of the importance of phase difference to the transient dynamics. For trials where the system remained in the high-amplitude state, the vortex force magnitudes are significantly lower than those in either quasi-steady upper or initial branches. Additionally, the mean phase differences are more separated from 0° compared to quasi-steady IB, enabling sufficient net positive energy transfer to the cylinder despite the lower forcing magnitudes (figure 6.7(a)). The trials that returned to the initial branch exhibited a period where the mean phase difference decreased to values closer to 0°. Despite the phase difference being positive, the energy transferred to the cylinder is insufficient to sustain the high-amplitude oscillations (energy input does not balance energy lost to damping) and a gradual amplitude decay commences. The underlying mechanisms that trigger the decrease in amplitudes to IB in some trials remain unanswered.

The current study has presented results pertaining to the simultaneous examination of the structure and wake dynamics for a low mass-damping system subjected to two distinct freestream accelerations. The nature of the system responses along with some of the key underlying mechanisms have been elucidated. However, the utility of the presented results to the broader engineering community remains to be addressed. To this end, some of the potential questions that may arise for various engineering considerations are briefly discussed:

1. How applicable are the studied freestream accelerations to real-world VIV?

Two distinct mean freestream acceleration rates were considered within this study. The fast ramp case consisted of freestream transients that lasted between approximately 30 and

45 cycles of cylinder oscillation, while the slow ramp case lasted between approximately 360 and 900 cycles. These ranges cover operating conditions that are experienced by many engineering applications as seen in figure 2.4. Thus, the results from the present study can directly inform transient behavior prediction for systems of comparable mass ratios ($m^* \approx 10$) for a wide range of freestream accelerations within the tested limits.

2. How can the present results be extended to systems with significantly different mass ratios?

While a comprehensive investigation needs to be undertaken to satisfactorily answer this question, a comparison of the present results with those from relevant studies can provide some initial insight. This is particularly true when trying to estimate the freestream acceleration rate required to elicit near quasi-steady system behavior. For the current mass ratio ($m^* \approx 10$), nondimensional mean accelerations of the freestream corresponding to a change in U^* of 1 over approximately 600 oscillation cycles ($\Delta U^*/(\Delta t f_n) \approx 1/600$) resulted in the system approaching close to quasi-steady behavior. A previous study considering unsteady freestream effects on flexible cylinders of mass ratio $m^* \approx 1$ [150], found near quasi-steady behavior for nondimensional mean accelerations of $\Delta U^*/(\Delta t f_n) \approx 1/50$. This constitutes a nearly 10 times increase in mean accelerations from the current experiment for an order of magnitude decrease in m^*. Further, results from another study conducted on flexible cylinders of mass ratio $m^* = 1{,}590$ [94] subjected to mean accelerations of $\Delta U^*/(\Delta t f_n) \approx 1/360$ showed significant transient effects. The deviations from the quasi-steady curve are more exaggerated than those found in the present study (compare figures 6.5 and figure 2.5). Additionally, release-from-rest experiments conducted on the same flexible cylinder setup revealed the number of oscillation cycles taken to attain quasi-steady state from rest was approximately 100 times those found in the present study ($m^* \approx 18$, Chapter 5) at similar reduced velocities (figure 5.4). Overall, a comparison of the different results indicates a weakly linear relationship between transient behavior (for e.g, transient time) and mass ratio. However, the actual mean acceleration required is expected to vary based on the quasi-steady start and end states.

3. While slower transients will elicit more quasi-steady responses, how will system transients behave for faster mean flow accelerations than those considered in the present study?

For the fast ramp case, it can be shown that the local accelerations are at least two orders of magnitude lower than the largest convective accelerations. In other words, the pressure gradients introduced by the flow acceleration are not expected to appreciably influence the system response. It is speculated that the trends in system responses described for the fast ramp case will remain similar for faster freestream accelerations provided the local accelerations are still significantly lower than the convective accelerations, particularly for systems with mass ratios of the same order or larger. Consider that the outlined transient behaviors between the two end states involve coupled changes to the wake and structural

dynamics that are driven by the energy transfer between the fluid and the structure. Thus, while faster freestream accelerations will likely promote faster initial wake and structural responses, the paths taken by the system between the two end states depend on the rates of energy transfer and the system inertia. Evidence for this can be also found in the present results for the LB-Dsnc and Dsnc-LB cases, where the majority of changes in system dynamics occur after the freestream transient has ended. As mentioned previously, the trends in energy transfer rates hold for a wide range of mass ratios, thus allowing for a first-order estimate of transient behavior in the case of faster ramps and for different mass ratios.

6.6 Concluding remarks

The present study experimentally investigated the transient response of an elastically-mounted cylinder ($m^* = 9.4$, $\zeta \approx 1{\times}10^{-}3$) subjected to unsteady freestream conditions. The system was forced to transition between adjacent response branches by varying the freestream velocity in sigmoidal profiles between the two associated end states. The cases considered include transitions between the initial and upper branches (IB↔UB), upper and lower branches (UB↔LB), and lower branch to desynchronization (LB↔Dsnc). Simultaneous cylinder displacement, forces, and two-dimensional velocity field measurements were acquired. Two mean acceleration rates were considered: a fast ramp where $\Delta U^*/(\Delta t f_n) \approx 1/50$, signifying a change in reduced velocity of 1 over approximately 50 oscillation cycles, and a slow ramp where $\Delta U^*/(\Delta t f_n) \approx 1/600$.

The transient response in all cases subjected to the fast ramp lags the associated quasi-steady response (response based on the instantaneous freestream velocity), with the transient responses exhibiting similar behavior between multiple trials within each case. A notable exception is the UB-IB case where a dual response was observed, where a majority of the trials (approximately 90%) remained at a high-amplitude hysteretic state while a smaller fraction of trials returned to the initial branch. The transient time (time spent between the two end states) varied significantly between the different cases. In particular, the shortest transient times were observed in the UB-LB and LB-UB cases, primarily due to the proximity of the steady state amplitudes between the two end states, while the longest transient times were found in the LB-Dsnc and Dsnc-LB cases. The largest rates of change in the amplitude were found in the IB-UB case. Plotting the system trajectories on an $A^* - U^*$ map indicated the degree to which the transient responses deviate from the quasi-steady curve on the same map. As expected, transient responses for the slow ramp case indicated a closer match with the quasi-steady state response, while the fast ramp cases showed significant deviations from the quasi-steady results.

The forcing characteristics (magnitude and phase difference with respect to cylinder displacement) were used to elucidate the underlying mechanics responsible for the different

transient behaviors in the fast ramp conditions. The phase difference, in particular, was shown to be critical in determining the system response. Generally, net positive energy transfer to the cylinder resulting in growing oscillations requires the phase difference to lie between 0 and 180° with sustained periods outside those thresholds resulting in amplitude decay. The fastest growth rates in the IB-UB transition were linked to the phase difference passing between 0 and 180° through 90°. Conversely, the slowest amplitude growth/decay rates (LB↔ Dsnc) were associated with the phase difference continually being close to 180° resulting in low rates of energy transfer. Wavelet analysis of the forcing signal was used to identify the changes to the dominant lock-in frequencies through the transient with these behaviors linked to the forcing phase difference.

Analysis of the wake flow development enabled identification of the different wake states and topologies encountered during the transition between different end states. The onset of the changes in the wake was shown to precede the onset of significant changes in the amplitude response for all cases, signifying a lag in the initial system response. Additionally, the changes in the near wake velocity field were shown to closely correlate with trends in the system forcing for the cases starting in the initial and upper branches, particularly during periods of insignificant amplitude change. This points to an increased sensitivity of the forcing to the near wake characteristics for the initial and upper branches. Conversely, the lower branch exhibited a decreased sensitivity to changes in the near wake. Finally, the comparative analysis of the results from the present study and those from previous investigations highlighted the importance of both the mass ratio and the mean acceleration rate to the transient system response characteristics.

Chapter 7

Conclusions & Recommendations

The main findings from this work are summarized and recommendations for future studies are provided.

7.1 Conclusions

In this thesis, a series of experimental investigations were carried out to explore the structure and wake dynamics of a circular cylinder undergoing 1-DOF VIV subjected to two flow conditions commonly encountered in real-world flows: elevated freestream turbulence and unsteady freestream conditions. In contrast to most previous work related to these two flow conditions, a key objective of this work was to simultaneously explore the structure and wake dynamics to better elucidate the physical mechanisms at play. Experiments were conducted at two different free-surface water channel facilities on carefully manufactured VIV setups. Additionally, an array of measurement techniques including simultaneous displacement, force, and non-intrusive flow measurements were employed.

The two flow conditions considered in this thesis give rise to changes in both the quasi-steady and transient system characteristics, with eFST primarily modifying the quasi-steady response and unsteady freestream conditions giving rise to distinct transient dynamics. Transient VIV behavior is also encountered in steady freestream conditions when there are changes to the system's structural properties. The dynamics of transient VIV in both steady and unsteady flows are closely related to the energy transfer between the fluid and the structure. Since steady flows pose fewer experimental challenges, this case was studied first to understand key transient system behavior.

The investigation of the effects of eFST on quasi-steady VIV is presented in Chapter 4. A turbulence grid placed upstream of the cylinder was used to raise the freestream turbulence intensity from a baseline of 0.9% to 2.7% at the cylinder location. Elevated FST was found to primarily affect the quasi-steady response towards the end of the lower branch and at the transitions between the main response branches. In particular, an earlier onset of desynchronization was observed with eFST. In contrast, the responses within the initial and upper branches were minimally affected. Analysis of the wake dynamics affirmed the marginal effects of eFST through most of the synchronization region. This insensitivity was in stark contrast to the drastic changes observed in stationary cylinder wake at the same conditions. A comparison of stationary cylinder wakes and VIV wakes at low oscillation amplitudes (early initial branch and desynchronization region) revealed distinct changes to the shear layer characteristics in the VIV cases. In particular, for the Reynolds number considered in the study, stationary cylinder shear layers are highly susceptible to transition, with eFST promoting this transition process. Conversely, the separated shear layers in the VIV cases were found to be largely insensitive to the eFST perturbations. This change in shear layer behavior likely resulted from the coupled fluid-structure interactions when the cylinder is free to oscillate, thereby serving as perturbations to the separated shear layers. The fluid-structure coupling was highlighted through spectral analysis of the wake signals which revealed distinct modifications to the shedding frequency that were also reflected in the displacement signals. Finally, a low order model constructed from the six most energetic POD modes of the wake near the end of the lower branch revealed subtle changes to the 2P shedding process that are reflective of an earlier onset of desynchronization.

Specifically, less pronounced like-signed vortex separation was observed in the presence of eFST, highlighting the change from 2P to 2S shedding at desynchronization.

In Chapter 5, the results from experiments detailing the dynamics of a cylinder released from rest were presented. The setup remained the same as that used for the eFST experiments with the addition of a system designed to release the cylinder when triggered. Exploring the dynamics of a system released from rest was critical to understanding the onset of nonlinear coupling behavior characteristic of VIV. In particular, the transition from the initial forcing induced by von Kármán shedding to nonlinear forcing was examined through the analysis of the forcing and displacement signals. In all cases, immediately after release, the cylinder is displaced due to the forcing imposed by von Kármán shedding. This displacement subsequently disrupts the von Kármán shedding mechanism. For reduced velocities where the von Kármán shedding frequency and structural natural frequency are close, relatively large initial cylinder displacements result in a rapid switch in the vortex pinch-off and shedding mechanism. Specifically, opposite shear layers are forced to interact due to their deflection, resulting in changes to the vortex pinch-off and shedding. Shear layer deflection progressively increases with cylinder amplitude growth further promoting this pinch-off mechanism until lock-in is established.

For reduced velocities within the synchronization region, lock-in is eventually established, and the subsequent amplitude growth is closely related to the energy transfer between the fluid and the cylinder. The phase difference between vortex force and cylinder displacement was shown to be critical to the net energy transfer, and consequently, the oscillation amplitude growth rate. In particular, net positive energy transfer to the cylinder was observed only when the phase difference was between 0 and 180°, with energy transfer maximized at 90°, when the cylinder velocity and forcing are in phase. Additionally, a close relationship was found between the timing of vortex shedding and the phase difference. Notably, the initial phase difference after lock-in progressively increased with reduced velocity, resulting in slower amplitude growth at larger reduced velocities. In addition to the energy transfer implications, the phase difference was shown to influence the system lock-in frequency by modifying the effective added mass.

Chapter 6 examined the transient dynamics of a circular cylinder undergoing VIV subjected to various ramp changes in freestream velocity. The experiments were conducted at a different facility with a different 1-DOF VIV setup from the one considered for Chapters 4 and 5. Two different rates of freestream velocity change were studied: a “fast ramp” case where the total freestream transient time was within 45 cycles of cylinder oscillation, and a “slow ramp” case, with the freestream transient lasting up to approximately 900 oscillation cycles. A total of six cases were examined that correspond to a transition between the main response branches. The results from the fast ramp cases revealed distinct transient dynamics that deviated substantially from the expected quasi-steady response. The transient responses lagged behind the expected quasi-steady responses to varying degrees. Further, the onset of the changes in the wake was shown to precede the onset of

significant changes in the amplitude response for all cases, signifying a lag in the initial system response. While the initial wake response was relatively rapid in all the examined cases (within 20 cycles following the start of the freestream velocity change), the transient progression to the new quasi-steady state differed significantly between the different cases. The longest transients lasted more than six times the expected quasi-steady response based on the velocity change. The transient dynamics in unsteady freestream were closely related to the phase difference between forcing and displacement (and consequently energy transfer) throughout the transient, similar to the results from Chapter 5. The slowest rates of amplitude change were attained near the end of the lower branch, where the phase differences were close to 180° throughout the transient. The fastest oscillation amplitude change rates were observed at lower reduced velocities (initial-upper transition region).

System transient dynamics approached quasi-steady behavior for the slower freestream variations. Although additional measurements are required to determine the required mean freestream accelerations to promote quasi-steady behavior, a comparative analysis of the present results and those of previous studies on VIV in unsteady flows point to the importance of the mass ratio in system response to unsteady flows. In particular, the rate of change of freestream velocity required to elicit near quasi-steady behavior is seen to scale approximately inversely with the mass ratio. In other words, the larger the mass ratio, the slower the freestream variation is required for quasi-steady behavior.

Overall, this thesis extends the body of knowledge regarding VIV behavior in two key real-world flow conditions through simultaneous consideration of structural and flow dynamics. Additionally, new insights are gained into the onset of nonlinear system behavior that is characteristic of VIV. The key takeaways from this work include the robustness of the shedding dynamics for cylinders free to vibrate at the tested eFST levels and $\boldsymbol{Re}$, and the prominent role that phase dynamics play in transient VIV behavior.

7.2 Recommendations

The results obtained in this thesis have given rise to several research questions that warrant further exploration in future studies. A few of the most pertinent suggestions for future work are listed below.

- Extension of the current 1-DOF system to different 2-DOF VIV (constant/variable amplitude, flexible cylinder) subjected to the same freestream conditions will help further our understanding of real-world VIV. The results from the transient cases indicated similarities in behavior with previous studies considering 2-DOF flexible systems (e.g., slower amplitude growth rates with increasing reduced velocity). However, studies of 2-DOF VIV in eFST have reported contrasting results, prompting the need for further investigation.

- Only a relatively moderate level of elevated freestream turbulence intensity was employed in this thesis. While the reported results are expected to hold for slightly higher levels of turbulence intensity and Re within the early shear layer transition regime, it is essential to study the effect of larger turbulence intensities as well as at higher Re pertaining to the later stages of shear layer transition and boundary layer transition regimes. It is speculated that earlier boundary layer transition that may be induced at such conditions will result in decreased loading and oscillation amplitudes compared to a baseline case. In addition to the turbulence intensity, the turbulence integral length scale effects need to be considered.

- Analysis of boundary layer and separated shear layer development for a cylinder undergoing minor vibrations may provide insights into the physical mechanisms underlying the decreased sensitivity to external perturbations of eFST. To this end, higher-resolution measurements in the shear layer region are needed. These measurements would also enable the identification of the small-scale shear layer structures and their behavior. The results from such a study may find use in flow control applications where forced vibrations of the cylinder may be used to target desirable near wake behavior.

- Near wake measurements may also be employed to offer additional insights into the mechanisms leading up to lock-in for a structure released from rest in the synchronization region.

- Quantitative analysis focused on relating specific topological flow features to the forcing on the cylinder is required. The force partitioning method [147] presents a viable option for this, with its application to experimental data in complex separated flows recently demonstrated [220]. Such a targeted forcing analysis would enhance understanding of the importance of the different flow regions (e.g., shear layers, formation region, far wake) on the forcing characteristics. Among other possibilities, such a study would enable more informed flow control strategies.

- The importance of the mass ratio to the transient response behavior was briefly discussed in Chapter 6. A parametric study focused on transient VIV considering a wide range of mass ratios is required to generalize the present results to a wider range of systems encountered in real-world applications (section 2.4). The importance of other parameters such as the damping and the Reynolds number must also be considered for a comprehensive understanding of transient VIV.

References

[1] (EC1), E. 1. 2004 Actions on structures–general actions–part 1-4: wind actions

[2] Aarnes, J. R., Andersson, H. I., & Haugen, N. E. L. 2018 Numerical investigation of free-stream turbulence effects on the transition-in-wake state of flow past a circular cylinder. *Journal of Turbulence* **19** (3), 252–273

[3] Abernathy, F. H. & Kronauer, R. E. 1962 The formation of vortex streets. *Journal of Fluid Mechanics* **13** (1), 1–20

[4] Adrian, R. J. & Westerweel, J. 2011 *Particle image velocimetry*, number 30. Cambridge university press

[5] Ahlborn, B., Seto, M. L., & Noack, B. R. 2002 On drag, strouhal number and vortex-street structure. *Fluid dynamics research* **30** (6), 379

[6] Anagnostopoulos, P. 1994 Numerical investigation of response and wake characteristics of a vortex-excited cylinder in a uniform stream. *Journal of Fluids and Structures* **8** (4), 367–390

[7] Anagnostopoulos, P. & Bearman, P. 1992 Response characteristics of a vortex-excited cylinder at low reynolds numbers. *Journal of Fluids and Structures* **6** (1), 39–50

[8] Archer, C. L. & Jacobson, M. Z. 2005 Evaluation of global wind power. *Journal of Geophysical Research: Atmospheres* **110** (D12)

[9] ARIE, M., KIYA, M., SUZUKI, Y., HAGINO, M., & TAKAHASHI, K. 1981 Characteristics of circular cylinders in turbulent flows. *Bulletin of JSME* **24** (190), 640–647

[10] Assi, G. R. & Bearman, P. W. 2018 Vortex-induced vibration of a wavy elliptic cylinder. *Journal of Fluids and Structures* **80**, 1–21

[11] Assi, G. R., Srinil, N., Freire, C. M., & Korkischko, I. 2014 Experimental investigation of the flow-induced vibration of a curved cylinder in convex and concave configurations. *Journal of Fluids and Structures* **44**, 52–66

[12] Aswathy, M. & Sarkar, S. 2019 Effect of stochastic parametric noise on vortex induced vibrations. *International Journal of Mechanical Sciences* **153**, 103–118

[13] Aswathy, M. & Sarkar, S. 2020 Nonlinear dynamics of circular cylinders undergoing vortex induced vibrations in presence of stochastic noise. *Dynamics and Control of Energy Systems* 195–214

[14] Azad, R. S. 1993 *The atmospheric boundary layer for engineers*, vol. 17. Springer Science & Business Media

[15] Badger, J., Hahmann, A., Larsén, X. G., Badger, M., Kelly, M., Olsen, B. T., & Mortensen, N. G. 2015 The global wind atlas: an eudp project carried out by dtu wind energy

[16] Bardal, L. M. & Sætran, L. R. 2016 Wind gust factors in a coastal wind climate. *Energy Procedia* **94**, 417–424

[17] Barros, D. C., Duan, Y., Troolin, D. R., & Longmire, E. K. 2021 Air-filled soap bubbles for volumetric velocity measurements. *Experiments in Fluids* **62**, 1–12

[18] Bearman, P. W. 1984 Vortex shedding from oscillating bluff bodies. *Annual review of fluid mechanics* **16** (1), 195–222

[19] Bearman, P. 2011 Circular cylinder wakes and vortex-induced vibrations. *Journal of Fluids and Structures* **27** (5-6), 648–658

[20] Berdahl, C. & Thompson, D. 1993 Eduction of swirling structure using the velocity gradient tensor. *AIAA journal* **31** (1), 97–103

[21] Berger, E. & Wille, R. 1972 Periodic flow phenomena. *Annual Review of Fluid Mechanics* **4** (1), 313–340

[22] Berkooz, G., Holmes, P., & Lumley, J. L. 1993 The proper orthogonal decomposition in the analysis of turbulent flows. *Annual review of fluid mechanics* **25** (1), 539–575

[23] Bishop, R. E. D. & Hassan, A. 1964 The lift and drag forces on a circular cylinder oscillating in a flowing fluid. *Proceedings of the Royal Society of London. Series A. Mathematical and Physical Sciences* **277** (1368), 51–75

[24] Blackburn, H. & Melbourne, W. 1996 The effect of free-stream turbulence on sectional lift forces on a circular cylinder. *Journal of Fluid Mechanics* **306**, 267–292

[25] Blevins, R. D. & Coughran, C. S. 2009 Experimental investigation of vortex-induced vibration in one and two dimensions with variable mass, damping, and reynolds number. *Journal of Fluids Engineering* **131** (10)

[26] Bloor, M. S. 1964 The transition to turbulence in the wake of a circular cylinder. *Journal of Fluid Mechanics* **19** (2), 290–304

[27] Bosbach, J., Kühn, M., & Wagner, C. 2009 Large scale particle image velocimetry with helium filled soap bubbles. *Experiments in fluids* **46**, 539–547

[28] Bouard, R. & Coutanceau, M. 1980 The early stage of development of the wake behind an impulsively started cylinder for 40< re< 10 4. *Journal of Fluid Mechanics* **101** (3), 583–607

[29] Bourguet, R. & Mathis, R. 2023 A wind tunnel investigation of the effects of end and laminar/turbulent inflow conditions on cylinder vortex-induced vibrations. *Journal of Fluids and Structures*

[30] Brika, D. & Laneville, A. 1993 Vortex-induced vibrations of a long flexible circular cylinder. *Journal of Fluid Mechanics* **250**, 481–508

[31] Brown, C. W., Connor, L. N., Lillibridge, J. L., Nalli, N. R., & Legeckis, R. V. 2005 An introduction to satellite sensors, observations and techniques. In *Remote Sensing of Coastal Aquatic Environments: Technologies, Techniques and Applications*, pp. 21–50. Springer

[32] Carniel, S., Sclavo, M., Kantha, L., & Clayson, C. 2005 Langmuir cells and mixing in the upper ocean. *Il nuovo cimento C* **28** (1), 33–54

[33] Chakraborty, P., Balachandar, S., & Adrian, R. J. 2005 On the relationships between local vortex identification schemes. *Journal of fluid mechanics* **535**, 189–214

[34] Chakraborty, S., Lin, T.-W., & Chern, M.-J. 2018 Vortex motions around a vertically vibrating cylinder in oscillatory flows. *Journal of Marine Science and Technology* **26** (6), 7

[35] Chang, C.-C. 1992 Potential flow and forces for incompressible viscous flow. *Proceedings of the Royal Society of London. Series A: Mathematical and Physical Sciences* **437** (1901), 517–525

[36] Chen, W.-L., Zhang, Q.-Q., Li, H., & Hu, H. 2015 An experimental investigation on vortex induced vibration of a flexible inclined cable under a shear flow. *Journal of Fluids and Structures* **54**, 297–311

[37] Chong, M. S., Perry, A. E., & Cantwell, B. J. 1990 A general classification of three-dimensional flow fields. *Physics of Fluids A: Fluid Dynamics* **2** (5), 765–777

[38] Christensen, R. M., Nielsen, M. G., & Støttrup-Andersen, U. 2017 Effective vibration dampers for masts, towers and chimneys. *Steel Construction* **10** (3), 234–240

[39] D'Asaro, E. A. 2014 Turbulence in the upper-ocean mixed layer. *Annual review of marine science* **6**, 101–115

[40] Daniels, S. J., Castro, I. P., & Xie, Z.-T. 2016 Numerical analysis of freestream turbulence effects on the vortex-induced vibrations of a rectangular cylinder. *Journal of Wind Engineering and Industrial Aerodynamics* **153**, 13–25

[41] Davies, M. 1976 A comparison of the wake structure of a stationary and oscillating bluff body, using a conditional averaging technique. *Journal of Fluid Mechanics* **75** (2), 209–231

[42] Deepakkumar, R., Jayavel, S., & Tiwari, S. 2017 A comparative study on effect of plain-and wavy-wall confinement on wake characteristics of flow past circular cylinder. *Sādhanā* **42**, 963–980

[43] Deng, H., Jiang, Q., Li, F., & Wu, Y. 2011 Vortex-induced vibration tests of circular cylinders connected with typical joints in transmission towers. *Journal of wind engineering and industrial aerodynamics* **99** (10), 1069–1078

[44] Derbunovich, G., Zemskaya, A., Repik, E., & Sosedko, Y. P. 1982 Use of screens for controlling the structure of flow turbulence in wind tunnels. *Uch. Zap. TsAGI* **13** (11)

[45] Dickey, T. D. & Bidigare, R. R. 2005 Interdisciplinary oceanographic observations: the wave of the future. *Scientia Marina* **69** (S1), 23–42

[46] Dong, S., Karniadakis, G., Ekmekci, A., & Rockwell, D. 2006 A combined direct numerical simulation–particle image velocimetry study of the turbulent near wake. *Journal of Fluid Mechanics* **569**, 185–207

[47] Dorogi, D. & Baranyi, L. 2020 Identification of upper branch for vortex-induced vibration of a circular cylinder at re= 300. *Journal of Fluids and Structures* **98**, 103135

[48] Dykes, K., Damiani, R., Roberts, O., & Lantz, E. 2018 Analysis of ideal towers for tall wind applications. In *2018 Wind Energy Symposium*, p. 0999

[49] Ellingsen, Ø. M., Flamand, O., Amandolese, X., Coiffet, F., & Hémon, P. 2022 Field tests on a full-scale steel chimney subjected to vortex-induced vibrations. *Structural Engineering International* **32** (1), 55–61

[50] Emes, M. J., Arjomandi, M., Ghanadi, F., & Kelso, R. M. 2017 Effect of turbulence characteristics in the atmospheric surface layer on the peak wind loads on heliostats in stow position. *Solar Energy* **157**, 284–297

[51] Epps, B. 2017 Review of vortex identification methods. In *55th AIAA aerospace sciences meeting*, p. 0989

[52] Fage, A. & Falkner, V. 1931 Further experiments on the flow around a circular cylinder. r. & m. no. 1369. *British AR C*

[53] Fage, A. & Warsap, J. 1929 The effects of turbulence and surface roughness on the drag of a circular cylinder. r & m. no. 1283. *British ARC*

[54] Feng, C. 1968 *The measurement of vortex induced effects in flow past stationary and oscillating circular and D-section cylinders*. PhD thesis, University of British Columbia

[55] Flemming, F. & Williamson, C. 2005 Vortex-induced vibrations of a pivoted cylinder. *Journal of Fluid Mechanics* **522**, 215

[56] Fu, B., Zou, L., & Wan, D. 2018 Numerical study of vortex-induced vibrations of a flexible cylinder in an oscillatory flow. *Journal of Fluids and Structures* **77**, 170–181

[57] Fukuda, K., Balachandar, R., & Barron, R. 2017 Development of vortex structures in the wake of a sharp-edged bluff body. *Physics of Fluids* **29** (12)

[58] Gargett, A. E. 1989 Ocean turbulence. *Annual Review of Fluid Mechanics* **21** (1), 419–451

[59] Gerich, D. & Eckelmann, H. 1982 Influence of end plates and free ends on the shedding frequency of circular cylinders. *Journal of Fluid Mechanics* **122**, 109–121

[60] Gerrard, J. 1966 The mechanics of the formation region of vortices behind bluff bodies. *Journal of fluid mechanics* **25** (2), 401–413

[61] Goswami, I., Scanlan, R. H., & Jones, N. P. 1993 Vortex-induced vibration of circular cylinders. i: experimental data. *Journal of Engineering Mechanics* **119** (11), 2270–2287

[62] Govardhan, R. & Williamson, C. 2000 Modes of vortex formation and frequency response of a freely vibrating cylinder. *Journal of Fluid Mechanics* **420**, 85–130

[63] Govardhan, R. & Williamson, C. 2006 Defining the 'modified griffin plot'in vortex-induced vibration: revealing the effect of reynolds number using controlled damping. *Journal of fluid mechanics* **561**, 147–180

[64] Hearst, R. J. & Lavoie, P. 2014 Decay of turbulence generated by a square-fractal-element grid. *Journal of Fluid Mechanics* **741**, 567–584

[65] Hommema, S. E. & Adrian, R. J. 2003 Packet structure of surface eddies in the atmospheric boundary layer. *Boundary-Layer Meteorology* **106**, 147–170

[66] Honji, H. & Taneda, S. 1969 Unsteady flow past a circular cylinder. *Journal of the physical society of Japan* **27** (6), 1668–1677

[67] Hu, W., Letson, F., Barthelmie, R., & Pryor, S. 2018 Wind gust characterization at wind turbine relevant heights in moderately complex terrain. *Journal of Applied Meteorology and Climatology* **57** (7), 1459–1476

[68] Huang, M., Zhang, B., Guo, Y., Huan, R., & Lou, W. 2021 Prediction and suppression of vortex-induced vibration for steel tubes with bolted joints in tubular transmission towers. *Journal of Structural Engineering* **147** (9), 04021128

[69] Huera-Huarte, F. J. & Vernet, A. 2010 Vortex modes in the wake of an oscillating long flexible cylinder combining pod and fuzzy clustering. *Experiments in fluids* **48** (6), 999–1013

[70] Hunt, J. C., Wray, A. A., & Moin, P. 1988 Eddies, streams, and convergence zones in turbulent flows. *Studying turbulence using numerical simulation databases, 2. Proceedings of the 1988 summer program*

[71] Hussain, A. F. 1986 Coherent structures and turbulence. *Journal of Fluid Mechanics* **173**, 303–356

[72] Hutchins, N., Chauhan, K., Marusic, I., Monty, J., & Klewicki, J. 2012 Towards reconciling the large-scale structure of turbulent boundary layers in the atmosphere and laboratory. *Boundary-layer meteorology* **145** (2), 273–306

[73] Immas, A., Do, N., & Alam, M.-R. 2021 Real-time in situ prediction of ocean currents. *Ocean Engineering* **228**, 108922

[74] Inman, D. J. & Singh, R. C. 1994 *Engineering vibration*, vol. 3. Prentice Hall Englewood Cliffs, NJ

[75] Jauvtis, N. & Williamson, C. 2004 The effect of two degrees of freedom on vortex-induced vibration at low mass and damping. *Journal of Fluid Mechanics* **509**, 23

[76] Jeon, D. & Gharib, M. 2004 On the relationship between the vortex formation process and cylinder wake vortex patterns. *Journal of Fluid Mechanics* **519**, 161–181

[77] Jeong, J. & Hussain, F. 1995 On the identification of a vortex. *Journal of fluid mechanics* **285**, 69–94

[78] Jungo, P., Goyette, S., & Beniston, M. 2002 Daily wind gust speed probabilities over switzerland according to three types of synoptic circulation. *International Journal of Climatology: A Journal of the Royal Meteorological Society* **22** (4), 485–499

[79] Kaasen, K. E., Lie, H., Solaas, F., & Vandiver, J. K. 2000 Norwegian deepwater program: analysis of vortex-induced vibrations of marine risers based on full-scale measurements. In *Offshore Technology Conference*, OTC–11997. OTC

[80] Kaja, K., Zhao, M., Xiang, Y., & Cheng, L. 2016 Three-dimensional numerical simulations of vortex-induced vibrations of tapered circular cylinders. *Applied Ocean Research* **60**, 1–11

[81] Kelly, K. A., Dickinson, S., McPhaden, M. J., & Johnson, G. C. 2001 Ocean currents evident in satellite wind data. *Geophysical Research Letters* **28** (12), 2469–2472

[82] Khabbouchi, I., Fellouah, H., Ferchichi, M., & Guellouz, M. S. 2014 Effects of free-stream turbulence and reynolds number on the separated shear layer from a circular cylinder. *Journal of Wind Engineering and Industrial Aerodynamics* **135**, 46–56

[83] Khalak, A. & Williamson, C. H. 1999 Motions, forces and mode transitions in vortex-induced vibrations at low mass-damping. *Journal of fluids and Structures* **13** (7-8), 813–851

[84] Khalak, A. & Williamson, C. 1996 Dynamics of a hydroelastic cylinder with very low mass and damping. *Journal of fluids and structures* **10** (5), 455–472

[85] Kim, J., Moin, P., & Moser, R. 1987 Turbulence statistics in fully developed channel flow at low reynolds number. *Journal of fluid mechanics* **177**, 133–166

[86] Kiya, M., Suzuki, Y., Arie, M., & Hagino, M. 1982 A contribution to the free-stream turbulence effect on the flow past a circular cylinder. *Journal of Fluid Mechanics* **115**, 151–164

[87] Kozakiewicz, A., Sumer, B. M., Fredsøe, J., & Hansen, E. A. 1997 Vortex regimes around a freely vibrating cylinder in oscillatory flow. *International Journal of Offshore and Polar Engineering* **7** (02)

[88] Kozmar, H. 2011 Wind-tunnel simulations of the suburban abl and comparison with international standards. *Wind and Structures, An International Journal* **14** (1), 15–34

[89] Kravchenko, A. G. & Moin, P. 2000 Numerical studies of flow over a circular cylinder at re d= 3900. *Physics of fluids* **12** (2), 403–417

[90] Krogstad, P.-Å. & Davidson, P. 2011 Freely decaying, homogeneous turbulence generated by multi-scale grids. *Journal of fluid mechanics* **680**, 417–434

[91] Kumar, S., Navrose, & Mittal, S. 2016 Lock-in in forced vibration of a circular cylinder. *Physics of Fluids* **28** (11), 113605

[92] Kurian, T. & Fransson, J. H. 2009 Grid-generated turbulence revisited. *Fluid dynamics research* **41** (2), 021403

[93] Kwok, K. C. 1986 Turbulence effect on flow around circular cylinder. *Journal of engineering mechanics* **112** (11), 1181–1197

[94] Lague
, F. d. r. & Laneville, A. 2002 Vortex-induced vibrations of a flexible cylinder in a slowly varying flow: experimental results. In *ASME International Mechanical Engineering Congress and Exposition*, vol. 36592, pp. 259–265

[95] Lavoie, P., Djenidi, L., & Antonia, R. 2007 Effects of initial conditions in decaying turbulence generated by passive grids. *Journal of Fluid Mechanics* **585**, 395–420

[96] Lavoie, P., Djenidi, L., & Antonia, R. A. 2006 Effect of initial conditions on the generation of coherent structures in grid turbulence. *J. Fluid Mech* **346**, 201–237

[97] Laws, E. & Livesey, J. 1978 Flow through screens. *Annual review of fluid mechanics* **10** (1), 247–266

[98] Lawson, T., Anthony, K., Cockrell, D., Davenport, A., Flint, A., Freeston, D., Harris, R., Lyons, R., Mayne, J., Melling, R., *et al.* 1986 Mean forces, pressures and flow field velocities for circular cylindrical structures: single cylinder with two-dimensional flow

[99] Lee, Y., Rho, J., Kim, K. H., & Lee, D.-H. 2011 Fundamental studies on free stream acceleration effect on drag force in bluff bodies. *Journal of mechanical science and technology* **25**, 695–701

[100] Leontini, J. S., Thompson, M. C., & Hourigan, K. 2006 The beginning of branching behaviour of vortex-induced vibration during two-dimensional flow. *Journal of Fluids and Structures* **22** (6-7), 857–864

[101] Li, Z., Wang, Z., Li, J., & Liu, S. 2023 Experimental study on vortex-induced vibration of steel tubes in transmission towers at various inflow conditions. *Buildings* **13** (1), 252

[102] Lie, H. & Kaasen, K. 2006 Modal analysis of measurements from a large-scale viv model test of a riser in linearly sheared flow. *Journal of fluids and structures* **22** (4), 557–575

[103] Lighthill, J. 1986 Fundamentals concerning wave loading on offshore structures. *Journal of Fluid Mechanics* **173**, 667–681

[104] Lilly, J. M. 2017 Element analysis: a wavelet-based method for analysing time-localized events in noisy time series. *Proceedings of the Royal Society A: Mathematical, Physical and Engineering Sciences* **473** (2200), 20160776

[105] Lilly, J. M. & Olhede, S. C. 2012 Generalized morse wavelets as a superfamily of analytic wavelets. *IEEE Transactions on Signal Processing* **60** (11), 6036–6041

[106] Livanos, D. 2018 Investigation of vortex induced vibrations on wind turbine towers. *Delft University of Technology* 1–86

[107] Lourenco, L. 1994 Characteristics of the plate turbulent near wake of a circular cylinder. a particle image velocimetry study. *In Unpublished, results taken from Beaudan and Moin*

[108] Lumley, J. L. 1967 The structure of inhomogeneous turbulent flows. *Atmospheric turbulence and radio wave propagation* 166–178

[109] MA, X., Karamanos, G.-S., & Karniadakis, G. 2000 Dynamics and low-dimensionality of a turbulent near wake. *Journal of fluid mechanics* **410**, 29–65

[110] MacEnri, J., Reed, M., & Thiringer, T. 2013 Influence of tidal parameters on seagen flicker performance. *Philosophical Transactions of the Royal Society A: Mathematical, Physical and Engineering Sciences* **371** (1985), 20120247

[111] Mannini, C., Massai, T., & Marra, A. M. 2018 Unsteady galloping of a rectangular cylinder in turbulent flow. *Journal of Wind Engineering and Industrial Aerodynamics* **173**, 210–226

[112] Marble, E. 2018 *Structural Response and Wake Vortex Dynamics of Cylindrical Structures Undergoing VIV with Elliptic Trajectories*. MA thesis, University of Waterloo

[113] Maryami, R., Showkat Ali, S. A., Azarpeyvand, M., & Afshari, A. 2020 Turbulent flow interaction with a circular cylinder. *Physics of Fluids* **32** (1), 015105

[114] Mehta, R. D. & Bradshaw, P. 1979 Design rules for small low speed wind tunnels. *The Aeronautical Journal* **83** (827), 443–453

[115] Menon, K. & Mittal, R. 2019 Flow physics and dynamics of flow-induced pitch oscillations of an airfoil. *Journal of Fluid Mechanics* **877**, 582–613

[116] Menon, K. & Mittal, R. 2021 On the initiation and sustenance of flow-induced vibration of cylinders: insights from force partitioning. *Journal of Fluid Mechanics* **907**, A37

[117] Milne, I. A., Sharma, R. N., Flay, R. G., & Bickerton, S. 2013 Characteristics of the turbulence in the flow at a tidal stream power site. *Philosophical Transactions of the Royal Society A: Mathematical, Physical and Engineering Sciences* **371** (1985), 20120196

[118] Moffat, R. J. 1988 Describing the uncertainties in experimental results. *Experimental thermal and fluid science* **1** (1), 3–17

[119] Mohamed, M. S. & Larue, J. C. 1990 The decay power law in grid-generated turbulence. *Journal of Fluid Mechanics* **219**, 195–214

[120] Moin, P. & Kim, J. 1985 The structure of the vorticity field in turbulent channel flow. part 1. analysis of instantaneous fields and statistical correlations. *Journal of Fluid Mechanics* **155**, 441–464

[121] Monin, A. 1970 The atmospheric boundary layer. *Annual Review of Fluid Mechanics* **2** (1), 225–250

[122] Monty, J., Chong, M., Hutchins, N., & Marusic, I. 2006 Surface shear stress fluctuations in the atmosheric surface layer. In *Proceedings of the 11th Asian Congress of Fluid Mechanics*

[123] Morse, T. & Williamson, C. 2009 Fluid forcing, wake modes, and transitions for a cylinder undergoing controlled oscillations. *Journal of Fluids and Structures* **25** (4), 697–712

[124] Morse, T. & Williamson, C. 2009 Prediction of vortex-induced vibration response by employing controlled motion. *Journal of Fluid Mechanics* **634**, 5–39

[125] Morse, T. & Williamson, C. 2010 Steady, unsteady and transient vortex-induced vibration predicted using controlled motion data. *Journal of Fluid Mechanics* **649**, 429

[126] Morton, B. 1984 The generation and decay of vorticity. *Geophysical & Astrophysical Fluid Dynamics* **28** (3-4), 277–308

[127] Morton, C. & Yarusevych, S. 2014 On vortex shedding from low aspect ratio dual step cylinders. *Journal of Fluids and Structures* **44**, 251–269

[128] Niemann, H., Lupi, F., & Hoeffer, R. 2014 Vibrations of chimneys under the action of the wind. In *u Proceedings of the 9th international conference on structural dynamics, Portugal*, vol. 30

[129] NOKA, F. 1998 Vortex formation length of a circular cylinder (300< re< 4,000) using dpiv. In *ASME Fluid Engineering Division Summer Meeting, FEDSM*, pp. 98–5149

[130] Norberg, C. 1987 Effects of reynolds number and a low-intensity freestream turbulence on the flow around a circular cylinder. *Chalmers University, Goteborg, Sweden, Technological Publications* **87** (2), 1–55

[131] Norberg, C. 1994 An experimental investigation of the flow around a circular cylinder: influence of aspect ratio. *Journal of Fluid Mechanics* **258**, 287–316

[132] O'Neill, C. M., Riches, G., & Morton, C. 2021 Wake dynamics and heuristic modelling in the desynchronization region of 1-dof viv. *International Journal of Heat and Fluid Flow* **88**, 108729

[133] Oertel Jr, H. 1990 Wakes behind blunt bodies. *Annual Review of Fluid Mechanics* **22** (1), 539–562

[134] Of Civil Engineers, A. S. 2013 Minimum design loads for buildings and other structures. In American Society of Civil Engineers

[135] Okajima, A. 1982 Strouhal numbers of rectangular cylinders. *Journal of Fluid mechanics* **123**, 379–398

[136] Osalusi, E., Side, J., & Harris, R. 2009 Reynolds stress and turbulence estimates in bottom boundary layer of fall of warness. *International Communications in Heat and Mass Transfer* **36** (5), 412–421

[137] Osalusi, E., Side, J., & Harris, R. 2009 Structure of turbulent flow in emec's tidal energy test site. *International Communications in Heat and Mass Transfer* **36** (5), 422–431

[138] Parnaudeau, P., Carlier, J., Heitz, D., & Lamballais, E. 2008 Experimental and numerical studies of the flow over a circular cylinder at reynolds number 3900. *Physics of Fluids* **20** (8), 085101

[139] Pastò, S. 2008 Vortex-induced vibrations of a circular cylinder in laminar and turbulent flows. *Journal of Fluids and structures* **24** (7), 977–993

[140] Perret, L. 2009 Piv investigation of the shear layer vortices in the near wake of a circular cylinder. *Experiments in fluids* **47**, 789–800

[141] Perrin, R., Braza, M., Cid, E., Cazin, S., Barthet, A., Sevrain, A., Mockett, C., & Thiele, F. 2007 Obtaining phase averaged turbulence properties in the near wake of a circular cylinder at high reynolds number using pod. *Experiments in Fluids* **43**, 341–355

[142] Perrotta, G. & Jones, A. R. 2018 Quasi-steady approximation of forces on flat plate due to large-amplitude plunging maneuvers. *AIAA Journal* **56** (11), 4232–4242

[143] Pope, S. B. 2001 Turbulent flows

[144] Pope, S. B. & Pope, S. B. 2000 *Turbulent flows*. Cambridge university press

[145] Prasanth, T. & Mittal, S. 2008 Vortex-induced vibrations of a circular cylinder at low reynolds numbers. *Journal of Fluid Mechanics* **594**, 463–491

[146] Provansal, M., Mathis, C., & Boyer, L. 1987 Bénard-von kármán instability: transient and forced regimes. *Journal of Fluid Mechanics* **182**, 1–22

[147] Quartapelle, L. & Napolitano, M. 1983 Force and moment in incompressible flows. *AIAA journal* **21** (6), 911–913

[148] Raffel, M., Willert, C. E., Scarano, F., Kähler, C. J., Wereley, S. T., & Kompenhans, J. 2018 *Particle image velocimetry: a practical guide*. Springer

[149] Rahman, S., Jain, A. K., Bharti, S., & Datta, T. 2020 Comparison of international wind codes for across wind response of concrete chimneys. *Journal of Wind Engineering and Industrial Aerodynamics* **207**, 104401

[150] Resvanis, T. L. 2014 *Vortex-induced vibration of flexible cylinders in time-varying flows*. PhD thesis, Massachusetts Institute of Technology

[151] Resvanis, T. L., Vandiver, J. K., & Fu, S. 2015 Ramp tests: a novel approach to viv model testing of flexible cylinders using continuously varying towing speeds. In *International Conference on Offshore Mechanics and Arctic Engineering*, vol. 56482, V002T08A059. American Society of Mechanical Engineers

[152] Reynolds, W. & Hussain, A. 1972 The mechanics of an organized wave in turbulent shear flow. part 3. theoretical models and comparisons with experiments. *Journal of Fluid Mechanics* **54** (2), 263–288

[153] Riches, G., Martinuzzi, R., & Morton, C. 2018 Proper orthogonal decomposition analysis of a circular cylinder undergoing vortex-induced vibrations. *Physics of Fluids* **30** (10), 105103

[154] Riches, G. & Morton, C. 2018 One degree-of-freedom vortex-induced vibrations at constant reynolds number and mass-damping. *Experiments in Fluids* **59** (10), 157

[155] Riches, G. P. 2018 *Experimental investigation of vortex-induced vibrations using a cyber-physical system*. MA thesis, Graduate Studies

[156] Roach, P. 1987 The generation of nearly isotropic turbulence by means of grids. *International Journal of Heat and Fluid Flow* **8** (2), 82–92

[157] Rockwood, M. P., Taira, K., & Green, M. A. 2017 Detecting vortex formation and shedding in cylinder wakes using lagrangian coherent structures. *AIAA journal* **55** (1), 15–23

[158] Roshko, A. 1955 On the wake and drag of bluff bodies. *Journal of the aeronautical sciences* **22** (2), 124–132

[159] Roshko, A. 1993 Perspectives on bluff body aerodynamics. *Journal of Wind Engineering and Industrial Aerodynamics* **49** (1-3), 79–100

[160] Ruiz, S. A. G., Barriga, J. E. C., & Martinez, J. A. 2021 Wind power assessment in the caribbean region of colombia, using ten-minute wind observations and era5 data. *Renewable Energy* **172**, 158–176

[161] Sadeh, W. Z. & Brauer, H. J. 1980 A visual investigation of turbulence in stagnation flow about a circular cylinder. *Journal of Fluid Mechanics* **99** (1), 53–64

[162] Sadeh, W. Z., Sutera, S. P., & Maeder, P. F. 1970 An investigation of vorticity amplification in stagnation flow. *Zeitschrift für angewandte Mathematik und Physik ZAMP* **21** (5), 717–742

[163] Saffman, P. G. 1995 *Vortex dynamics*. Cambridge university press

[164] Sarkar, D., Osborne, M. A., & Adcock, T. A. 2018 Prediction of tidal currents using bayesian machine learning. *Ocean Engineering* **158**, 221–231

[165] Sarpkaya, T. 1991 Nonimpulsively started steady flow about a circular cylinder. *AIAA journal* **29** (8), 1283–1289

[166] Sarpkaya, T. 2004 A critical review of the intrinsic nature of vortex-induced vibrations. *Journal of fluids and structures* **19** (4), 389–447

[167] Scarano, F., Ghaemi, S., Caridi, G. C. A., Bosbach, J., Dierksheide, U., & Sciacchitano, A. 2015 On the use of helium-filled soap bubbles for large-scale tomographic piv in wind tunnel experiments. *Experiments in Fluids* **56**, 1–12

[168] Scarano, F. & Riethmuller, M. L. 2000 Advances in iterative multigrid piv image processing. *Experiments in Fluids* **29** (1), S051–S060

[169] Scharnowski, S., Bross, M., & Kähler, C. J. 2019 Accurate turbulence level estimations using piv/ptv. *Experiments in Fluids* **60** (1), 1–12

[170] Sciacchitano, A., Neal, D. R., Smith, B. L., Warner, S. O., Vlachos, P. P., Wieneke, B., & Scarano, F. 2015 Collaborative framework for piv uncertainty quantification: comparative assessment of methods. *Measurement Science and Technology* **26** (7), 074004

[171] Sejdić, E., Djurović, I., & Jiang, J. 2009 Time–frequency feature representation using energy concentration: an overview of recent advances. *Digital signal processing* **19** (1), 153–183

[172] Sirovich, L. 1987 Turbulence and the dynamics of coherent structures. i. coherent structures. *Quarterly of applied mathematics* **45** (3), 561–571

[173] So, R., Wang, X., Xie, W.-C., & Zhu, J. 2008 Free-stream turbulence effects on vortex-induced vibration and flow-induced force of an elastic cylinder. *Journal of fluids and structures* **24** (4), 481–495

[174] Solari, G. & Kareem, A. 1998 On the formulation of asce7-95 gust effect factor. *Journal of Wind Engineering and Industrial Aerodynamics* **77**, 673–684

[175] Son, H. A., Lee, S., & Lee, J. 2020 Numerical analysis of drag force acting on 2d cylinder immersed in accelerated flow. *Water* **12** (6), 1790

[176] Soti, A. K., Zhao, J., Thompson, M. C., Sheridan, J., & Bhardwaj, R. 2018 Damping effects on vortex-induced vibration of a circular cylinder and implications for power extraction. *Journal of Fluids and Structures* **81**, 289–308

[177] Sumer, B. & Fredsoe, J. 1988 Transverse vibrations of an elastically mounted cylinder exposed to an oscillating flow

[178] Supradeepan, K. & Roy, A. 2014 Characterisation and analysis of flow over two side by side cylinders for different gaps at low reynolds number: a numerical approach. *Physics of Fluids* **26** (6)

[179] Surry, D. 1972 Some effects of intense turbulence on the aerodynamics of a circular cylinder at subcritical reynolds number. *Journal of Fluid Mechanics* **52** (3), 543–563

[180] Sutera, S. P. 1965 Vorticity amplification in stagnation-point flow and its effect on heat transfer. *Journal of Fluid Mechanics* **21** (3), 513–534

[181] Szepessy, S. & Bearman, P. 1992 Aspect ratio and end plate effects on vortex shedding from a circular cylinder. *Journal of Fluid Mechanics* **234**, 191–217

[182] Taira, K., Brunton, S. L., Dawson, S. T., Rowley, C. W., Colonius, T., McKeon, B. J., Schmidt, O. T., Gordeyev, S., Theofilis, V., & Ukeiley, L. S. 2017 Modal analysis of fluid flows: an overview. *Aiaa Journal* **55** (12), 4013–4041

[183] Taylor, G. I. 1938 The spectrum of turbulence. *Proceedings of the Royal Society of London. Series A-Mathematical and Physical Sciences* **164** (919), 476–490

[184] Thorsen, M. J., Sævik, S., & Larsen, C. M. 2016 Time domain simulation of vortex-induced vibrations in stationary and oscillating flows. *Journal of Fluids and Structures* **61**, 1–19

[185] Toebes, G. H. 1969 The unsteady flow and wake near an oscillating cylinder

[186] Tognarelli, M., Slocum, S., Frank, W., Campbell, R., *et al.* 2004 Viv response of a long flexible cylinder in uniform and linearly sheared currents. In *Offshore Technology Conference*. Offshore Technology Conference

[187] Truitt, A. & Mahmoodi, S. N. 2013 A review on active wind energy harvesting designs. *International Journal of Precision Engineering and Manufacturing* **14** (9), 1667–1675

[188] Unit, E. S. D. 1985 Characteristics of atmospheric turbulence near the ground. part ii: single point data for strong winds (neutral atmosphere)

[189] Van Oudheusden, B., Scarano, F., Van Hinsberg, N., & Watt, D. 2005 Phase-resolved characterization of vortex shedding in the near wake of a square-section cylinder at incidence. *Experiments in Fluids* **39** (1), 86–98

[190] Vandiver, J. K. 2012 Damping parameters for flow-induced vibration. *Journal of fluids and structures* **35**, 105–119

[191] Vandiver, J., Marcollo, H., Swithenbank, S., & Jhingran, V. 2005 High mode number vortex-induced vibration field experiments. In *Offshore technology conference*, OTC–17383. OTC

[192] Viré, A., Derksen, A., Folkersma, M., & Sarwar, K. 2020 Two-dimensional numerical simulations of vortex-induced vibrations for a cylinder in conditions representative of wind turbine towers. *Wind Energy Science* **5** (2), 793–806

[193] Vollmers, H., Kreplin, H., & Meier, H. 1983 Separation and vortical-type flow around a prolate spheroid-evaluation of relevant parameters. *Tech. rep.*, DEUTSCHE FORSCHUNGS-UND VERSUCHSANSTALT FUER LUFT-UND RAUMFAHRT EV ...

[194] Wang, H., Zhai, Q., & Chen, K. 2019 Vortex-induced vibrations of an elliptic cylinder with both transverse and rotational degrees of freedom. *Journal of Fluids and Structures* **84**, 36–55

[195] Wang, X., So, R., Xie, W.-C., & Zhu, J. 2008 Free-stream turbulence effects on vortex-induced vibration of two side-by-side elastic cylinders. *Journal of fluids and structures* **24** (5), 664–679

[196] Wei, T. & Smith, C. 1986 Secondary vortices in the wake of circular cylinders. *Journal of Fluid Mechanics* **169**, 513–533

[197] Weiss, J. 1991 The dynamics of enstrophy transfer in two-dimensional hydrodynamics. *Physica D: Nonlinear Phenomena* **48** (2-3), 273–294

[198] Westerweel, J. 1997 Fundamentals of digital particle image velocimetry. *Measurement science and technology* **8** (12), 1379

[199] Westerweel, J. & Scarano, F. 2005 Universal outlier detection for piv data. *Experiments in fluids* **39** (6), 1096–1100

[200] Willert, C. E. & Gharib, M. 1991 Digital particle image velocimetry. *Experiments in fluids* **10** (4), 181–193

[201] Williamson, C. H. 1989 Oblique and parallel modes of vortex shedding in the wake of a circular cylinder at low reynolds numbers. *Journal of Fluid Mechanics* **206**, 579–627

[202] Williamson, C. H. 1996 Vortex dynamics in the cylinder wake. *Annual review of fluid mechanics* **28** (1), 477–539

[203] Williamson, C. H. & Govardhan, R. 2004 Vortex-induced vibrations. *Annu. Rev. Fluid Mech.* **36**, 413–455

[204] Williamson, C. H. & Roshko, A. 1988 Vortex formation in the wake of an oscillating cylinder. *Journal of fluids and structures* **2** (4), 355–381

[205] Williamson, C. 1996 Three-dimensional wake transition. *Journal of Fluid Mechanics* **328**, 345–407

[206] WMO, G. 1996 Guide to meteorological instruments and methods of observation

[207] Wood, C. 1967 Visualization of an incompressible wake with base bleed. *Journal of Fluid Mechanics* **29** (2), 259–272

[208] Wu, T. & Kareem, A. 2012 An overview of vortex-induced vibration (viv) of bridge decks. *Frontiers of Structural and Civil Engineering* **6** (4), 335–347

[209] Wyngaard, J. C. 1992 Atmospheric turbulence. *Annual Review of Fluid Mechanics* **24** (1), 205–234

[210] Yamazaki, H. & Osborn, T. R. 1988 Review of oceanic turbulence: implications for biodynamics. *Toward a theory on biological-physical interactions in the world ocean* 215–234

[211] Yan, B., Chan, P., Li, Q., He, Y., Cai, Y., Shu, Z., & Chen, Y. 2022 Characterization of wind gusts: a study based on meteorological tower observations. *Applied Sciences* **12** (4), 2105

[212] Zdravkovich, M. 1969 Smoke observations of the formation of a kármán vortex street. *Journal of Fluid Mechanics* **37** (3), 491–496

[213] Zdravkovich, M. 1981 Review and classification of various aerodynamic and hydrodynamic means for suppressing vortex shedding. *Journal of Wind Engineering and Industrial Aerodynamics* **7** (2), 145–189

[214] Zdravkovich, M. 1990 Conceptual overview of laminar and turbulent flows past smooth and rough circular cylinders. *Journal of wind engineering and industrial aerodynamics* **33** (1-2), 53–62

[215] Zdravkovich, M. M. 1997 *Flow around circular cylinders: Volume 1: Fundamentals*, vol. 1. Oxford university press

[216] Zdravkovich, M. M. 1997 *Flow around circular cylinders: Volume 2: Applications*, vol. 2. Oxford university press

[217] Zhao, M., Cheng, L., & Zhou, T. 2013 Numerical simulation of vortex-induced vibration of a square cylinder at a low reynolds number. *Physics of Fluids* **25** (2)

[218] Zhao, M., Kaja, K., Xiang, Y., & Yan, G. 2013 Vortex-induced vibration (viv) of a circular cylinder in combined steady and oscillatory flow. *Ocean engineering* **73**, 83–95

[219] Zhou, J., Adrian, R. J., Balachandar, S., & Kendall, T. 1999 Mechanisms for generating coherent packets of hairpin vortices in channel flow. *Journal of fluid mechanics* **387**, 353–396

[220] Zhu, Y., Lee, H., Kumar, S., Menon, K., Mittal, R., & Breuer, K. 2023 Force moment partitioning and scaling analysis of vortices shed by a 2d pitching wing in quiescent fluid. *arXiv preprint arXiv:2301.13373*

Appendices

Appendix A
Uncertainty analysis

Uncertainty quantification is critical to ensure reliable interpretations of results, particularly considering the experimental nature of the present work. Here, uncertainty is estimated using the methodology outlined by Moffat [118]. Specifically, the total uncertainty ϵ_β for a quantity β is expressed as the root-sum-square of n sources of errors ϵ_i over a 95% confidence interval:

$$\epsilon_\beta = \pm \left(\sum_{i=1}^{n} \epsilon_i^2 \right)^{1/2} \tag{A.1}$$

While it is not practical to estimate all the sources of error, the investigator must account for the most dominant error sources.

For quantities that are not measured directly (derived quantities), two approaches were adopted to estimate the uncertainty propagated from the measured to the derived quantity. First, if the relationship between the derived quantity β and the measured quantities α is known through a defined function, i.e. $\beta = f(\alpha_1, \alpha_2, ...\alpha_n)$, then the propagated uncertainty is estimated as:

$$\epsilon_\beta = \pm \left[\sum_{i=1}^{n} \left(\frac{\partial \beta}{\partial \alpha_i} \epsilon_{\alpha_i} \right)^2 \right]^{1/2} \tag{A.2}$$

Often, the derivatives in equation A.2 are tedious to evaluate or impossible to compute. In these cases, the propagated uncertainty is estimated through the sequential perturbation method [118]. Briefly, the uncertainty in the measured quantities α_i is propagated to β as follows:

1. Estimate the nominal value of the derived quantity β_0 from α_i without accounting for the uncertainty.
2. Sequentially perturb each α_i by increasing its value by its uncertainty interval and recording the associated uncertainty β_i^+.
3. Repeat the previous step by reducing each α_i by the uncertainty interval and recording β_i^-. The total propagated uncertainty from each measured quantity α_i is $|\beta_i^+ - \beta_i^-|$.
4. Calculate the total uncertainty in β using equation A.1.

Table A.1 presents the uncertainties of all quantities in the present work rounded to the first decimal. At both FMRL and LTRAC, the cylinder diameter was measured at multiple locations using a digital vernier with a resolution of 0.01 mm. The associated relative uncertainties in the diameter at FMRL and LTRAC are ±0.03% and ±0.026%, respectively. The submerged cylinder length was measured using a tape measure with a resolution of 1 mm corresponding to relative uncertainties of ±0.24% and ±0.13%, respectively. The propagated uncertainty using equation A.2 to the aspect ratios are ±0.24% and ±0.16%, respectively. The uncertainty in the mass ratio is propagated through the structural mass and the displaced fluid mass. The mass of each component was measured using digital scales with resolutions of 0.001 kg. The propagated uncertainty in the mass of the displaced fluid

considered the uncertainty in the density, submerged length, and diameter. The density was calculated indirectly through the temperature measured using a thermometer with resolution 1°C. The overall propagated uncertainty to the mass ratios are 0.4% and 0.5% at FMRL and LTRAC, respectively. The propagated uncertainty to the Reynolds numbers accounts for the uncertainties in the freestream velocity, diameter, and kinematic viscosity. The uncertainty in kinematic viscosity was calculated indirectly using the temperature with a resulting relative uncertainty of ±2.5% at both facilities. The uncertainty in the freestream velocity was calculated using the correlation statistics method [170] resulting in an uncertainty of ±1.5% of the mean freestream velocity. The propagated uncertainty to the Reynolds numbers was less than 2.9 and 3.3% at FMRL and LTRAC, respectively. The propagated uncertainty to the reduced velocity accounted for uncertainties in the freestream velocity, diameter, and system natural frequency in still water. The natural frequency was determined through impulse tests in still water and spectral analysis of the resulting displacement signal. The signal was divided into equal windows of length $2{\times}10^{15}$ with a 50% overlap, corresponding to a frequency resolution of 0.0153 Hz. The overall propagated uncertainty to the reduced velocity was less than 6.6% at FMRL and 7.4% at LTRAC.

The uncertainties in the cylinder position ($\pm 0.003D$, based on a sensor resolution of $20\mu m$ and linearity of 0.1% of full scale), and the cylinder diameter were propagated to the nondimensional amplitude A^* resulting in total uncertainties less than 2.7% in all cases. Similarly, the uncertainties in the nondimensional frequency are propagated from the uncertainty in the frequency measurement and the system natural frequency, giving values less than 1.2% at FMRL and less than 0.4% at LTRAC. The higher uncertainty in the FMRL experiments is a consequence of the changing system natural frequency giving rise to larger relative uncertainties at lower natural frequencies. The uncertainties in the streamwise velocities and rms velocities are estimated using the correlation statistics method and are typically highest in the wake regions. The associated values for each case are presented in table A.1. The uncertainty in the forcing was estimated using two methods. At FMRL, the total uncertainty in the numerically derived vortex forcing magnitude and vortex force phase difference was estimated through sequential perturbation of the individual contributors (displacement, velocity, acceleration, mass, spring constant, and the system damping) with their associated uncertainties. The uncertainty in the spring constants was propagated from the mass and system natural frequency. The uncertainty in the damping was propagated from the nondimensional damping (estimated through the log-decrement method, equation 3.1), the spring constant, and the mass. Following this, the uncertainty in the forcing magnitude, freestream velocity, density, and frontal area were propagated to the final nondimensional forcing using equation A.2. The total propagated uncertainty in the nondimensional mean force at quasi-steady state was found to be within ±16% and ±3% for the phase difference. AT LTRAC, the forces were measured directly using a six-axis ATI-mini force sensor with a resolution of 0.005 N. The propagated uncertainty to the nondimensional force was calculated to be less than 3.1% of the mean force and less than 0.9% of the vortex force phase difference at quasi-steady state.

Parameter	Chapter 4	Chapter 5	Chapter 6	Methodology
AR	±0.2%	±0.2%	±0.2%	Eq. A.2
m^*	±0.4%	±0.4%	±0.5%	Eq. A.2
U^*	< ±6.6%	< ±6.6%	< ±7.4%	Eq. A.2
Re	±2.9%	±2.9%	< ±3.3%	Eq. A.2
A^*	< ±2.7%	< ±2.7%	< ±2.7%	Eq. A.2
f^*	< ±1.2%	< ±1.2%	< ±0.4%	Eq. A.2
Tu	±0.05%	-	-	[169]
$\|u\|/U_0$	< ±12%	< ±10%	< ±13.5%	Eq. A.2
u_{rms}	< 8.4% of max u_{rms}	-	-	Eq. A.2
v_{rms}	< 7.6% of max v_{rms}	-	-	Eq. A.2
$\overline{\|C_{Lv}\|}$	-	< ±16%	< ±3.1%	Sequential perturbation, Eq.A.2
$\overline{\|\phi_v\|}$	-	< ±3%	< ±0.9%	Sequential perturbation, Eq.A.2
L_f/D	-	< ±0.25D	-	section A.1
θ	-	< ±35°	-	section A.1

Table A.1: Maximum uncertainty estimates of measured and derived quantities. All uncertainty estimates are provided over a 95% confidence interval.

A.1 Uncertainty in vortex shedding dynamics

In Chapter 5, the instant of peak circulation of a vortex was used to identify the vortex formation length, and the cylinder phase at shedding. However, estimating the associated methodological uncertainty in peak identification presents unique challenges. The first step involves estimating the uncertainty in the circulation estimates, a nontrivial task owing to the lack of a universal definition of the vortex boundary. To illustrate the method adopted in the present work, an example of the phase-averaged shedding in the quasi-steady initial branch is provided. Identification of the vortex boundary in the present work involved an iterative process that searches for the last continuous contour of λ_2 that encloses a given vortex (see section 3.3.4 for details). To estimate the methodological uncertainty in the circulation arising from differences in the identified boundary, the iterative procedure was also conducted using the contours of the Q criterion. Figure A.1 compares the identified last continuous contours of the phase-averaged vorticity fields in the wake of the cylinder using the (a) λ_2 contours, and the (b) Q contours. It can be seen that both vortex identification methods capture essentially the same regions of vorticity with minor differences between the contours.

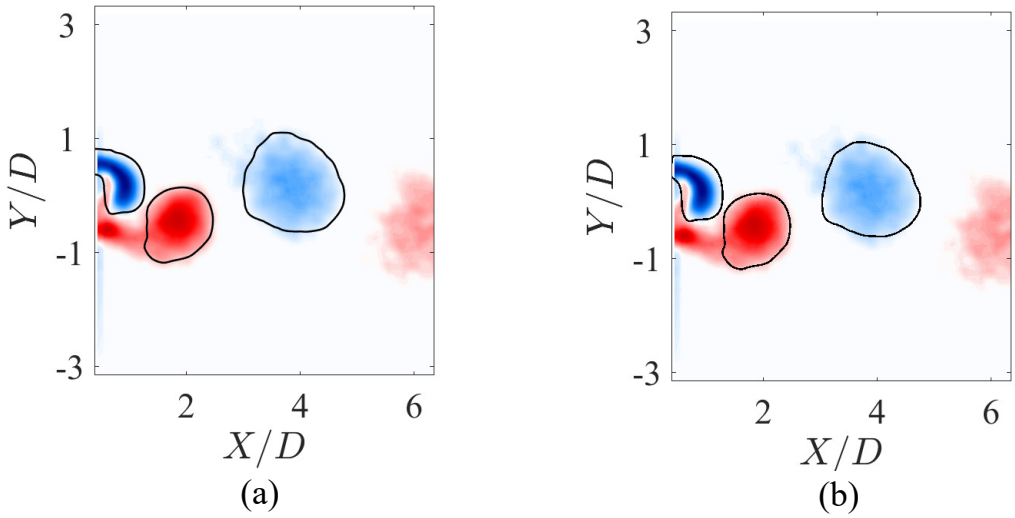

Figure A.1: Vortex boundaries identified using the last continuous threshold method (see section 3.3.4) employing contours of (a) λ_2 criterion and (b) Q criterion.

Once the vortex boundaries are identified, the rms of the difference between the circulations estimated using the λ_2 and Q criterion over a complete cycle of oscillation is used as a measure of the uncertainty in the circulation (multiplied by 2 for 95% confidence). These are shown as errorbars in figure A.2 which depicts the estimated circulation of the positive and negative vortex as functions of the cylinder oscillation phase θ. Next, the peak circulation is identified for the positive and negative vortices as the intersection of linear fits to the periods of growing and decaying vorticity (shown as solid blue and red lines in figure A.2). For each of the growth/decay phases of the vortex (e.g., $30° \lessapprox \theta \lessapprox 130°$), the root mean square error of the measured circulations with the linear fit is calculated. For 95% confidence, the error is multiplied by two. The total uncertainty is then calculated as the root-sum-square (equation A.1) of the rms error from the linear fit (fit error) and the methodological uncertainty in circulation (Q vs λ_2). This is done separately for the individual growth and decay phases. Finally, the total uncertainty in the circulation is then translated to an uncertainty in the shedding phase by substitution into the equations for the linear fit.

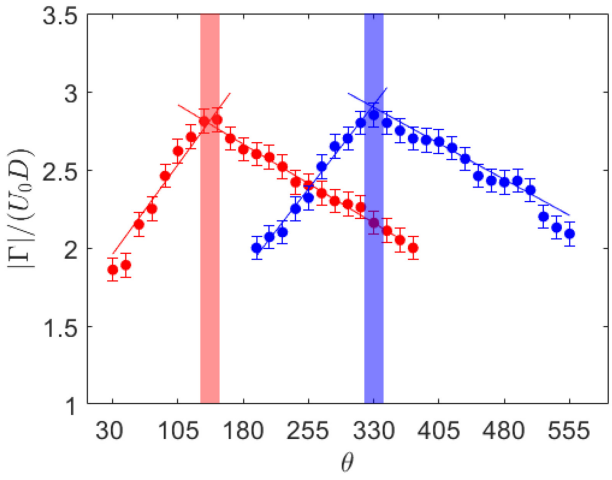

Figure A.2: Circulation estimates from phase-averaged vorticity contours versus cylinder oscillation phase.

Appendix B

Additional measurements of the hysteresis in the initial↔upper branch transition

The hysteretic transition between the initial and upper branches is examined in more detail. For decreasing U^*, a switch in the mean vortex force phase difference from near 180° to near 0° is observed despite sustained high-amplitude oscillations typical of the upper branch. In this high-amplitude state, distinct changes are observed in the wake topology compared to a typical upper branch case, including the shedding of more coherent vortices. Moreover, the switch in phase difference is not related to a distinct switch in the timing of vortex shedding but is speculated to be linked to a change in the phase of the pressure fluctuations with respect to the cylinder oscillation due to the modified vortex shedding characteristics.

The existence of hysteresis in the transition between initial and upper branches is well established in literature (e.g., [83]). However, to the best of the author's knowledge, a detailed characterization of the structure and wake dynamics within this region has not been undertaken. To this end, an additional set of measurements was conducted at LTRAC by imposing small variations in the freestream velocity near the hysteretic region corresponding to $\Delta U^* \approx 0.03$. The resulting amplitude response, rms vortex force coefficient, and nondimensional frequency are presented in figure B.1 where the black and red markers represent increasing and decreasing U^*, respectively. The amplitude response for increasing U^* (black markers, figure B.1(a)) indicates a notable increase in oscillation amplitudes for $U^* \lessapprox 5.25$, with peak amplitudes reaching $A^*_{10} \approx 0.4$. The jump in amplitudes to $A^*_{10} \approx 0.75$ beyond this point indicates the switch from the initial to the upper branch. The rms force magnitudes (figure B.1(b)) are seen to increase gradually up to $U^* \approx 5.05$ followed by a brief plateau and then a small decrease up to the end of the initial branch. Following the switch to the upper branch, the rms force magnitudes increase with U^*. The system oscillation frequency (figure B.1(c)) shows a gradual increase in frequencies from $f^* \approx 0.9$ to 0.95 before the transition to the upper branch, where $f^* > 1$. The switch in the position of the lock-in frequency with respect to system natural frequency is related to the switch in vortex force phase difference from near 0° to near 180° (equation 5.2).

While decreasing U^* down to approximately 4.95, the oscillation amplitudes remain notably high ($A^* \gtrapprox 0.68$, figure B.1(a)). The rms vortex force magnitudes (figure B.1(b)) exhibit a continuous decrease until the end of the high-amplitude region, with the values notably lower than those in both both quasi-steady initial and upper branches. The nondimensional frequency (figure B.1(c)) indicates a switch in the lock-in frequency from $f^* > 1$ to $f^* < 1$ at $U^* \approx 5.1$. This switch in the lock-in frequency to $f^* < 1$ is not typical of the upper branch system behavior where f^* remains greater than 1. The subsequent discussion is focused on the decreasing U^* case owing to its unique dynamics.

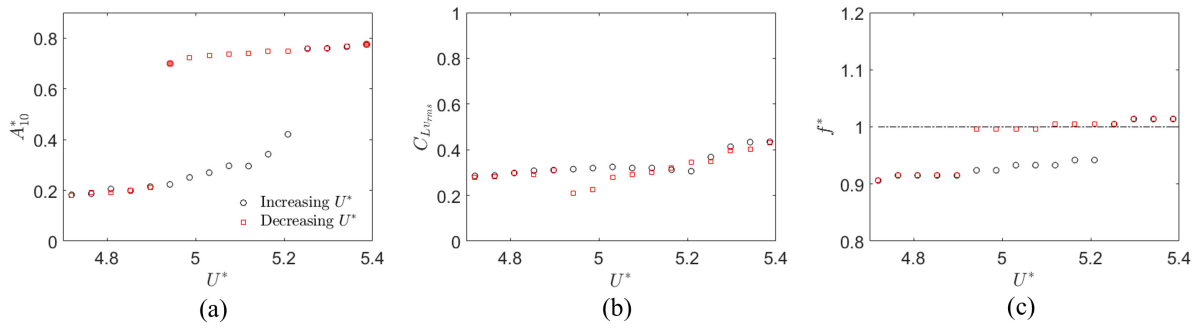

Figure B.1: Measurements between $4.7 \lessapprox U^* \lessapprox 5.5$.(a) Top ten percent of amplitude peaks, (b) rms vortex force coefficient, and (c) nondimensional frequency ratio with the dashed-dotted line demarcating system natural frequency.

To elucidate the changes to the system dynamics with decreasing U^*, two representative U^* (4.95 and 5.4) on either side of the frequency switch (figure B.1(c)) are explored further. These cases are depicted as filled markers in figure B.1(a). In both cases, the system exhibits high-amplitude oscillations. This is seen in figure B.2(a) where the left column depicts a time series of oscillations in the upper branch, and the right column depicts the system at the high-amplitude hysteresis state. The amplitude modulations for the hysteresis case are notably lower. The corresponding time trace of vortex forcing is shown in figure B.2(b). Apart from the magnitude of forcing being significantly lower for the hysteresis case, notably lower modulations in forcing are also observed, similar to the amplitude response. The vortex force phase difference (figure B.2(c)) shows a switch in the mean phase from near 180° in the quasi-steady UB state to near 0° in the hysteresis state. Additionally, both quasi-steady and hysteresis states exhibit phase slips [47]. These phase slips are due to brief periods where the forcing and displacement frequency are not locked in. These "lock-out" periods are evidenced in the normalized signal energy (modulus square of the wavelet transform) of the forcing signal (figure B.2(d)), where the green line is the locus of maximum in signal energy and the red line is the locus of maximum in the corresponding displacement signal energy. The hysteresis case (right column) exhibits larger and more frequent modulations of the forcing frequency. Additionally, the dominant frequencies (force and displacement) predominantly lie below $f^* = 1$ due to the mean vortex phase difference switch from near 180° to near 0°.

Overall, notable differences in system dynamics are encountered as the reduced velocity is decreased from reduced velocities in the upper branch. The drastic switch in the vortex force phase difference is typically associated with the transition between the initial and upper branches, simultaneously accompanied by a distinct change in oscillation amplitudes. Moreover, this transition is typically reflective of a switch in the timing of vortex shedding [62]. The wake and shedding dynamics are explored next.

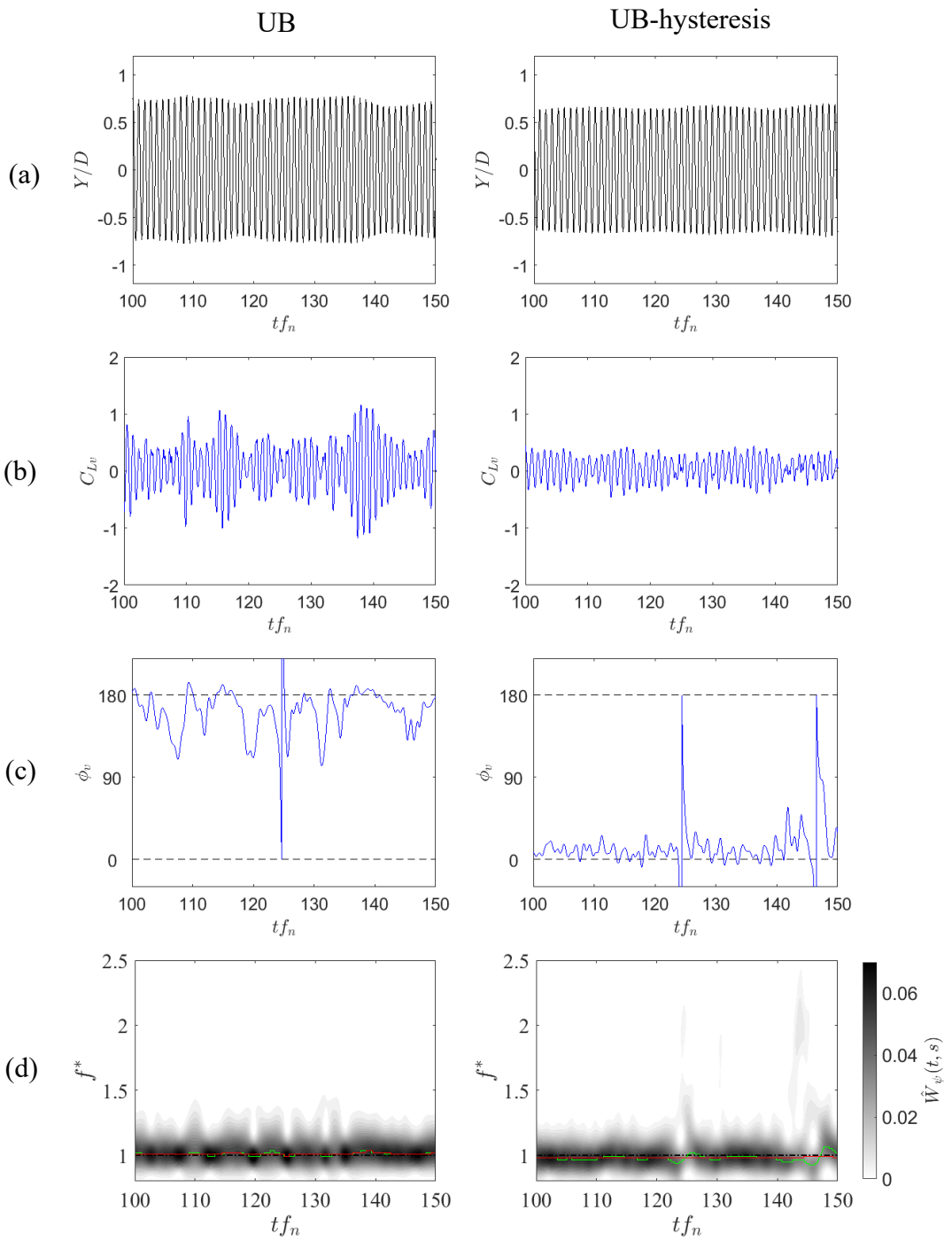

Figure B.2: System characteristics in the upper branch (left column) and the high-amplitude hysteresis state (right column). (a) Time series of cylinder displacement, (b) Time series of the vortex forcing, (c), (d) vortex force phase difference, and (e) normalized signal energy of the vortex force overlaid with the maximum locus of the forcing (green) and displacement (red) signal energies, respectively.

Figure B.3 presents the phase-averaged spanwise vorticity contours for the cylinder at its top dead position or the upper branch oscillations (left column) and the high-amplitude hysteresis state (right column), respectively. The vortex shedding mode in both cases is $2P_0$. This is more evident in figure B.3(b) where a weak trailing vortex is being shed near the positive vortex at $X/D \approx 1.5$. However, the vortices in the hysteresis case are significantly more coherent. Additionally, the hysteresis case indicates a lower mean vortex advection speed, evidenced by the increased number of vortices contained within the same field of view (five vortices in the hysteresis case compared to four in the upper branch case, not counting the weak trailing vortex). The lower vortex advection speed is presumably in part linked to the lower freestream velocities for the hysteresis case (approximately 10% lower than the upper branch case). Near the cylinder base ($X/D \approx 0.5$), there is a change in the structure of the positive shear layer, with that in the hysteresis case angled away from the cylinder compared to the upper branch case. Finally, in both the upper branch and hysteresis cases, the first positive vortex ($X/D \approx 2$) has already been shed at the depicted instant (cylinder at top dead center), indicating that despite the change in vortex force phase difference, there appears to be minimal change to the timing of vortex shedding.

Figure B.4 presents the mean streamwise velocity contours for the upper branch oscillations (left column) and the high-amplitude hysteresis state (right column). A larger velocity deficit is observed in the hysteresis case (right column) presumably resulting from the slightly lower oscillation amplitudes. The lack of change in the timing of vortex shedding accompanying the shift in mean vortex force phase differences is in stark contrast to previously examined cases (e.g., transient release from rest for all response branches, chapter 5) where a close relationship between both quantities was observed. It is speculated that, in the hysteresis region, the changes to the vortex shedding characteristics and wake topology (described above) facilitate a change in the phase of the surface pressure fluctuations with respect to the cylinder oscillation, resulting in the switch of phase difference between vortex force and cylinder displacement. A further reduction of U^* results in a switch in the timing of shedding and a drop in amplitudes to the initial branch (see figure 6.19). To the best of the author's knowledge, the switch in the vortex force phase difference independent of the timing of shedding has not been reported previously.

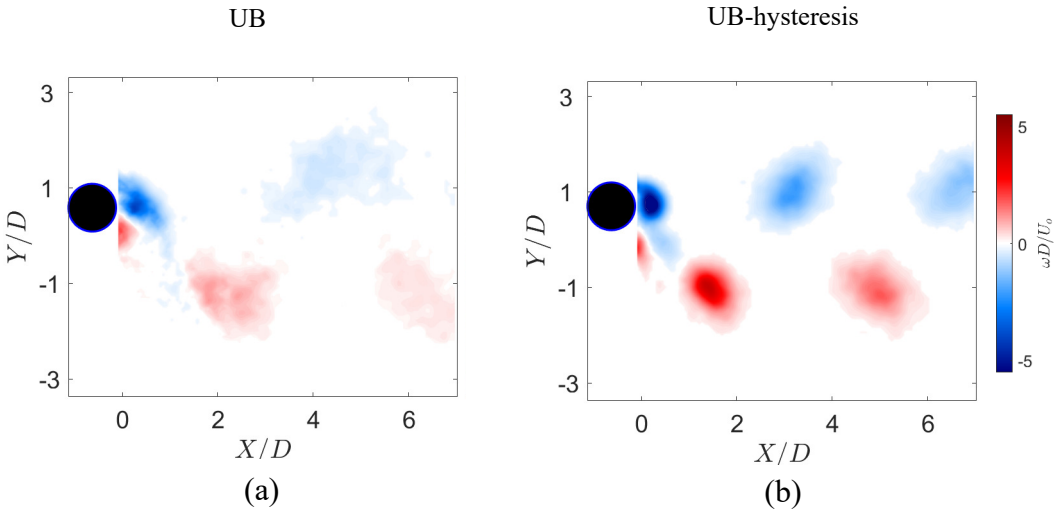

Figure B.3: Phase-averaged spanwise vorticity contours (top row) for the (a) upper branch and (b) high-amplitude hysteresis cases.

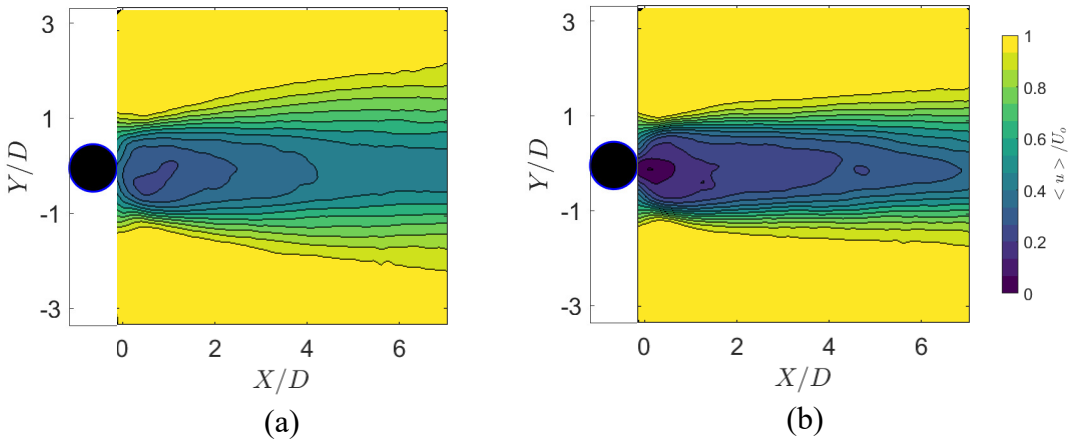

Figure B.4: Mean streamwise velocity contours (top row) for the (a) upper branch and (b) high-amplitude hysteresis cases.